

Konfigurationswechselwirkung und Spin-Bahn-Kopplung: Neue Methoden zur Behandlung großer Moleküle

INAUGURAL-DISSERTATION

zur

Erlangung des Doktorgrades der
Mathematisch-Naturwissenschaftlichen Fakultät
der Heinrich-Heine-Universität Düsseldorf

vorgelegt von

MARTIN KLEINSCHMIDT

aus Kiel

Juni 2006

Aus dem Institut für Theoretische Chemie und Computerchemie
der Heinrich-Heine-Universität Düsseldorf

Gedruckt mit der Genehmigung der Mathematisch-Naturwissenschaftlichen Fakultät
der Heinrich-Heine-Universität Düsseldorf

Referentin: Frau Prof. Dr. Christel M. Marian
Korreferent: Herr Priv. Doz. Dr. Timo Fleig

Tag der mündlichen Prüfung: 3. Juli 2006

Inhalt

Inhalt	5
1 Einführung	7
2 Theoretischer Teil	9
2.1 Relativistik und Spin-Bahn-Kopplung	9
2.2 Spin-Bahn-Operatoren	10
2.3 Spinfreie Methoden	12
2.3.1 Korrelation	12
2.3.2 MRCI	12
2.3.3 DFT	13
2.3.4 DFT/MRCI	14
3 Methodenentwicklung und Implementierung	17
3.1 Erzeugung der Spinkopplungen	18
3.1.1 Erzeugung der Spinfunktionen	19
3.1.2 Erzeugung der Kopplungsfelder	20
3.1.3 Abspeicherung als gepackte Matrizen	21
3.1.4 Erweiterung auf den Zweielektronen-Spin-Bahn-Operator	32
3.2 Spin-Bahn-Kopplung von DFT/MRCI Wellenfunktionen	36
3.2.1 Programmtechnischer Teil	36
3.2.2 Vergleich HF- und KS-basierter MRCI-Entwicklungen	37
3.2.3 Berechnung von g -Tensoren mit SPOCK	48
3.3 Spin-Bahn CI	61
3.3.1 Programmtechnischer Teil	61
3.3.1.1 Aufbau der Startvektoren	61
3.3.1.2 Berechnung des Matrix-Vektor-Produkts	61
3.3.1.3 Diagonalisierung der komplexen Matrix	62
3.3.2 Orthogonalitätsprobleme	63
3.3.3 Testrechnungen und Anwendungen	63
3.3.3.1 Dithiosuccinimid	64
3.3.3.2 Pyranthion	64
4 Anwendungen	83
4.1 Thiophen	83
4.2 Uracil	84
4.3 Dithiosuccinimid	96

4.4	Psoralene	124
4.5	Porphin	137
4.5.1	Metallporphyrine	137
4.5.2	Lebensdauern im freien Porphin	138
5	Zusammenfassung	141
6	Anhang	143
6.1	Inputbeschreibung	143
6.2	Dateien und Datentransfer zu anderen Programmen	147
	Literatur	151

1

Einführung

In der Natur hat das Licht der Sonne großen Einfluss auf alles Leben. Die Gewinnung von Energie über Photosynthese in Pflanzen und Bakterien, die Synthese wichtiger Verbindungen über Photoreaktionen, die Beschaffung von Informationen über die Umgebung durch Augen oder andere Photosensoren, aber auch der Schutz der Zellbestandteile vor schädlichem Einfluss des Sonnenlichts sind hier zu nennen. Allen diesen Effekten gemeinsam ist ihr Ablauf auf chemischer Ebene über elektronisch angeregte Zustände. Durch die Energie des Lichts wird ein Molekül aus seinem Grundzustand heraus angeregt. Die im angeregten Zustand gespeicherte Energie kann nun zu einer Reaktion dieses Moleküls selbst führen, sie kann an andere Moleküle weitergegeben werden, die dann ihrerseits im angeregten Zustand Reaktionen eingehen, oder sie kann als Schwingungsenergie, also als einfache Wärme in die Umgebung gelangen.

Zum Verständnis der Vorgänge in biologischen Zellen bei Anregung durch Licht ist zunächst ein Verständnis der zugrunde liegenden elementaren Prozesse auf der chemischen Ebene in einzelnen Molekülen vonnöten. Im kürzlich an der Heinrich-Heine-Universität Düsseldorf neu eingerichteten Sonderforschungsbereich „Molekulare Antwort nach elektronischer Anregung“ (SFB 663) werden diese Phänomene interdisziplinär mit der ganzen Breite der Methoden von der Biologie über die Biochemie, Bioanorganische, Organische und Physikalische Chemie bis hin zur Theoretischen Chemie untersucht.

Oftmals ist der erste Schritt der auf eine Bestrahlung folgenden Vorgänge eine Umwandlung eines angeregten Moleküls in einen anderen angeregten Zustand des gleichen Moleküls. Die Anregung findet dabei typischerweise aus einem Singulett-Grundzustand statt, und führt zu einem angeregten Zustand, der ebenfalls ein Singulett ist. Der Übergang zu einem Triplettzustand ist in der nichtrelativistischen Betrachtung verboten. Tatsächlich können Übergänge in einen Triplettzustand jedoch beobachtet werden. Die Wahrscheinlichkeit für einen solchen spinverbotenen Übergang kann errechnet werden, wenn die spezielle Relativitätstheorie in geeigneter Weise mit berücksichtigt wird. Entscheidend ist dabei die Spin-Bahn-Kopplung, also die Kopplung des Spindrehimpulses eines Elektrons mit dem Bahndrehimpuls eines anderen oder des gleichen Elektrons.

Relativistische Effekte in Molekülen werden in der theoretischen Chemie schon seit geraumer Zeit untersucht. Es gibt etablierte Methoden und Programme zum Einbezug dieser Effekte und zur Berechnung daraus abgeleiteter Eigenschaften. Skalarrelativistische Effekte stellen dabei kein besonderes Hindernis dar. Ihre Behandlung ist auch für große

1. EINFÜHRUNG

Moleküle über relativistische Kernpotentiale oder durch Verwendung eines entsprechenden Einelektronenoperators von der Rechenzeit her problemlos.

Anders sieht es aus beim Einbezug der Spin-Bahn-Kopplung und daraus abgeleiteter Eigenschaften. Zwar kann durch die Einführung einer Einelektronen-Näherung für den Spin-Bahn-Hamiltonoperator der Aufwand drastisch reduziert werden. Die zusätzlichen Kopplungen zwischen verschiedenen Symmetrien, Multiplizitäten und Multiplettkomponenten bedingen jedoch eine derartige Steigerung in der Komplexität, dass für große Moleküle mit herkömmlichen Methoden keine sinnvolle Behandlung der Spin-Bahn-Kopplung möglich ist. Die bestehenden Programmpakete sind zwar in der Lage, Atome und zwei- oder dreiatomige Moleküle mit sehr guter Genauigkeit zu beschreiben. Auch mehratomige Moleküle sind mit etwas verringrigerer Genauigkeit untersuchbar. Moleküle, wie sie in biologischen Systemen vorkommen, mit dutzenden Atomen und dutzenden oder gar einigen hundert Elektronen bleiben jedoch verschlossen.

Die Berechnung von Geometrien, Energien und Eigenschaften größerer Moleküle stellt auch in Zeiten ständig wachsender Rechenleistungen moderner Computer immer noch eine Herausforderung dar. Große Schritte sind, wegen des mit der Systemgröße polynomiell wachsenden Aufwands, nicht allein durch schnellere Computersysteme oder mehr Speicher erzielbar, sondern können nur durch Fortschritte in der Methodenentwicklung erreicht werden.

Das Ziel dieser Arbeit war die Entwicklung eines Programmpakets, mit dem die Spin-Bahn-Kopplung, sowie daraus abgeleitete Eigenschaften in organischen Molekülen oder Komplexen schwerer Elemente mit mehreren Liganden bis zu einer Grenze von etwa 200 Valenzelektronen berechnet werden können.

Als Grundlage dienen dabei das Programm DFT/MRCI und die Spin-Bahn-Integrale in der Einzentren-*mean-field* Näherung. Das DFT/MRCI-Programm wurde von Stefan Grimme und Mirko Waletzke an der Rheinischen Friedrich-Wilhelms-Universität Bonn entwickelt.[1] Es erlaubt durch die geschickte Kombination von Dichtefunktionaltheorie und Multi-Referenz-Konfigurationswechselwirkung die Berechnung elektronisch angeregter Zustände für die in Frage kommenden Moleküllklassen mit einer Genauigkeit von etwa 0.2 eV. Durch den Einsatz moderner Programmiertechniken und Näherungsmethoden können derartige Rechnungen innerhalb von Stunden bis hin zu wenigen Tagen auf einem normalen Personal Computer durchgeführt werden. Die *mean-field* Näherung von Bernd Heß *et. al.*[2] wurde von Bernd Schimmelpfennig im sehr effizienten Programm AMFI[3] umgesetzt.

2

Theoretischer Teil

2.1 Relativistik und Spin-Bahn-Kopplung

Die spezielle Relativitätstheorie fordert eine Gleichbehandlung von räumlichen und zeitlichen Koordinaten in der Beschreibung der Natur (Lorentzkovarianz). Diese Forderung ist von der nichtrelativistischen zeitabhängigen Schrödinger-Gleichung

$$i\hbar \frac{\partial}{\partial t} \Psi = \left(-\sum_i \frac{\hbar^2}{2m} \nabla_i^2 + V \right) \Psi \quad (2.1)$$

nicht erfüllt, da diese eine erste Ableitung nach der Zeit, im kinetischen Energieoperator jedoch eine zweite Ableitung nach den räumlichen Koordinaten enthält. Erst die vierkomponentige Dirac-Gleichung bringt die Quantentheorie mit der Relativitätstheorie in Einklang — zunächst nur für ein einzelnes Elektron. Sowohl der Spin, als auch die Spin-Bahn-Kopplung ergeben sich in der Dirac-Theorie automatisch. Sie müssen nicht über Postulate eingeführt werden, wie es sonst in der nichtrelativistischen Quantenchemie der Fall ist. Daher werden Spin und Spin-Bahn-Kopplung auch als relativistische Effekte bezeichnet. Streng genommen sind jedoch alle relativistischen Effekte, die in Theorien beschrieben werden, in Rechnungen auftauchen, oder zur Erklärung von Abweichungen im Periodensystems der Elemente herangezogen werden keine zusätzlichen Effekte, sondern der Normalzustand der Natur. Sie treten nur zutage, wenn einfachere Resultate der nichtrelativistischen Betrachtung mit Experiment, relativistischer Rechnung oder Theorie verglichen werden.

Das Spektrum des Diracoperators umfasst neben den üblichen elektronischen Zuständen auch ein Kontinuum von Zuständen mit negativer Energie. Der Operator ist also nicht nach unten beschränkt. Die gängige Betrachtungsweise fasst die positronischen Zustände als vollständig besetzten „Dirac-See“ auf. Die vierkomponentigen Lösungen der Dirac-Gleichung werden demnach als zwei elektronische und zwei positronische Freiheitsgrade gedeutet, wobei die zwei elektronischen Freiheitsgrade mit den zwei Komponenten des Spins in Verbindung gebracht werden.

Aufbauend auf der vierkomponentigen Dirac-Gleichung sind nahezu alle verfügbaren Methoden der Quantenchemie in einer vollrelativistischen Version implementiert worden. Als herausragendes Programmpaket soll an dieser Stelle das DIRAC-Projekt[4] genannt werden. Vierkomponentige Rechnungen versprechen die höchste Genauigkeit bei der Behandlung der Relativistik, stellen jedoch teils extreme Anforderungen an Rechenzeit und verfügbaren Speicher. Der Hauptgrund dafür liegt in den hohen Anforderungen an die Basis der

2. THEORETISCHER TEIL

positronischen Komponente, die über die Bedingungen kinetischer Balance im Drehimpuls immer eine Ordnung höher sein muss als die Basis der elektronischen Komponente. Über ein Einfrieren der Spinoren mit negativer Energie für die Korrelationsbehandlung ähnlich der *frozen core* Näherung lässt sich zwar der Aufwand wieder deutlich reduzieren, es bleiben jedoch die Bestimmung der Spinoren und die Transformation der Integrale auf die Spinorbasis als Flaschenhals bestehen.

Da jedoch zwei der vier Komponenten zur Beschreibung der Elektronen eigentlich genügen könnten, ist ein wichtiger Schritt die näherungsweise Abtrennung der positronischen Freiheitsgrade. Hierzu sind eine Reihe von Methoden entwickelt worden (siehe etwa die Übersichtsartikel in [5] und [6]), die gleichzeitig mit der Reduktion auf zwei Komponenten eine Trennung des Hamiltonoperators in einen skalaren und einen magnetischen, also einen Spin-Bahn-Kopplungs-freien und einen Spin-Bahn-Kopplungsterm erreichen.

Für der Behandlung organischer Moleküle, auf die das vorliegende Programm ausgerichtet ist, ist diese weitere Trennung naheliegend. Die Relativistik hat hier nur einen geringen Einfluss auf die Energien und Wellenfunktionen. Diese können also zunächst in einer Spin-Bahn-Kopplungs-freien Rechnung optimiert, und die Spin-Bahn-Kopplung später hinzugefügt werden. Dieser störungstheoretische Ansatz hat seine Stärke in der konzeptuelle Einfachheit und der geringen Rechenzeit für die Spin-Bahn-Kopplung. Die Berechnung der Spin-Bahn-Matrixelemente über die bereits konvergierten CI-Wellenfunktionen benötigt nur eine im Vergleich zur Berechnung der Wellenfunktionen geringe Zeit. Alle weiteren Rechnungen können dann in der kleinen Basis der Wellenfunktionen in vernachlässigbarer Zeit durchgeführt werden. Der Nachteil des störungstheoretischen Ansatzes ist die teils schlechte, teils einfach ungewisse Konvergenz mit der Anzahl berücksichtigter Zustände. Will man hier Verbesserungen erzielen, und viele Zustände berücksichtigen, so verlängert sich die Rechenzeit entsprechend.

Als Ausweg bietet sich an, die vorgenannte Trennung in einen Spin-Bahn-Kopplungs-freien und einen Spin-Bahn-Kopplungsterm wieder aufzuheben. In diesem Fall wird die Spin-Bahn-Kopplung im „Spin-Bahn-CI“ vollständig variationell berücksichtigt. Die Abhängigkeit von der Länge der Zustandssumme entfällt. Der Aufwand für diese Vorgehensweise ist jedoch ungemein größer, da die meisten Symmetrieblockungen entfallen (siehe Abschnitt 3.3).

2.2 Spin-Bahn-Operatoren

Der Breit–Pauli Spin–Bahn–Operator[7]

$$H_{SO}^{BP} = \frac{e^2 \hbar}{2m^2 c^2} \left\{ \sum_i \left(-\nabla_i \left(\sum_\alpha \frac{Z_\alpha}{r_{i\alpha}} \right) \times \mathbf{p}_i \right) \cdot \boldsymbol{\sigma}_i \right\} \quad (2.2)$$

$$+ \sum_i \sum_{j \neq i} \left(\nabla_i \left(\frac{1}{r_{ij}} \right) \times \mathbf{p}_i \right) \cdot \boldsymbol{\sigma}_i \quad (2.3)$$

$$+ 2 \sum_i \sum_{j \neq i} \left(\nabla_j \left(\frac{1}{r_{ij}} \right) \times \mathbf{p}_j \right) \cdot \boldsymbol{\sigma}_i \quad (2.4)$$

hat den Nachteil, nicht von unten beschränkt zu sein — er lässt noch Elektron-Positron-Paarbildungsprozesse zu. Daher ist er prinzipiell nicht geeignet, in variationellen Rechnun-

gen verwendet zu werden, denn es kann nicht ausgeschlossen werden, dass die Lösungen auf unendliche negative Werte fallen. Dieses Problem ist in der Praxis kaum beobachtet worden. Die Ursache dafür ist darin zu sehen, dass in den üblichen korrelierten Rechnungen die innersten Orbitale gefroren werden, und somit die steilsten Exponenten, die ein Abrutschen in die $1/r^3$ -Singularität ermöglichen würden, nicht zur Relaxation zur Verfügung stehen.

Alternativ kann der der *no-pair* Douglas–Kroll[8; 9; 10] Spin–Bahn Operator zum Einsatz kommen:

$$\begin{aligned} H_{SO}^+ &= e^2 \hbar^2 \left\{ \sum_i \sum_{\alpha} Z_{\alpha} \frac{A_i}{E_i + mc^2} \boldsymbol{\sigma}_i \left(\frac{\mathbf{r}_{i\alpha}}{r_{i\alpha}^3} \times \mathbf{p}_i \right) \frac{A_i}{E_i + mc^2} \right. \\ &\quad \left. - \sum_{i \neq j} \frac{A_i A_j}{E_i + mc^2} \left(\frac{\mathbf{r}_{ij}}{r_{ij}^3} \times \mathbf{p}_i \right) \cdot (\boldsymbol{\sigma}_i + 2\boldsymbol{\sigma}_j) \frac{A_i A_j}{E_i + mc^2} \right\} \end{aligned} \quad (2.5)$$

mit

$$E_i = \sqrt{m^2 c^4 + p_i^2 c^2} \quad \text{und} \quad A_i = \sqrt{\frac{E_i + mc^2}{2E_i}}$$

Dabei sind die $1/r_{ij}^3$ und $1/r_{i\alpha}^3$ Singularitäten durch E_i und A_i gedämpft.

Beide in Frage kommenden Operatoren beinhalten Ein- und Zweielektronenbeiträge. Die Berechnung des Zweielektronenbeitrags zur Spin–Bahn Kopplung ist im Vergleich zum Einelektronenbeitrag jedoch extrem aufwendig. Es treten bis zu Vierindexintegrale auf, deren Zahl mit der 4. Potenz der Basissatzgröße wächst. In den angestrebten großen Molekülen werden also Größenordnungen erreicht, bei denen eine Berechnung und Abspeicherung nicht mehr sinnvoll handhabbar sind. Auch die Transformation auf die Molekülorbitalbasis wäre extrem zeitraubend.

Andererseits ist insbesondere in Molekülen mit schweren Atomen der Beitrag des Einelektronenteils des Spin–Bahn Operators bei weitem dominant. Jede Näherung, die es ermöglicht, sich auf einen effektiven Einelektronen–Spin–Bahn–Operator zu beschränken, wird also eine immense Ersparnis der Ressourcen Rechenzeit und Speicherplatz herbeiführen.

Die *mean-field* Spin–Bahn–Näherung folgt einem Ansatz ähnlich dem im Hartree–Fock. Der Einelektronenbeitrag bleibt unverändert, jedoch wird im Zweielektronenteil die explizite Wechselwirkung mit den anderen Elektronen durch eine Wechselwirkung mit einem gemittelten Feld der anderen Elektronen ersetzt.

$$\hat{\mathcal{H}}_{SO}^{\text{eff}}(1) = \hat{\mathcal{H}}_{SO}(1) + \hat{\mathcal{H}}_{SO}^{\text{mf}}(1) \quad (2.6)$$

Alle echten Vierindexintegrale, bei denen alle Indizes unterschiedlich sind, werden vernachlässigt. Der Zweielektronenbeitrag zur Wechselwirkung zwischen Einfachanregungen beinhaltet eine Summierung über die besetzten Orbitale. Gibt man nun eine konkrete Besetzung für die Orbitale vor, beispielsweise die der Hartree–Fock–Determinante, so können die Zweielektronenbeiträge einmalig berechnet und auf die Einelektronenintegrale

aufaddiert werden. In der Basis der Valenzorbitale i und j wird in der Matrixdarstellung des Operators $\hat{\mathcal{H}}_{\text{SO}}^{\text{mf}}(1)$

$$\begin{aligned} \langle i | \hat{\mathcal{H}}_{\text{SO}}^{\text{mf}}(1) | j \rangle = \sum_a \gamma_a & \left\{ \langle ia | \mathcal{H}_{\text{SO}}(2) | ja \rangle - \frac{3}{2} \langle ia | \mathcal{H}_{\text{SO}}(2) | aj \rangle \right. \\ & \left. - \frac{3}{2} \langle ai | \mathcal{H}_{\text{SO}}(2) | ja \rangle \right\} \end{aligned} \quad (2.7)$$

über die besetzten Orbitale a summiert. Der so erhaltene effektive Spin-Bahn-Operator ist ein Einelektronenoperator. Daher reduziert sich der Aufwand zur Berechnung der Integrale und deren Transformation auf die MO-Basis beträchtlich. Weiterhin ist auch die tatsächliche Berechnung der Matrixelemente betroffen. Während der Zweielektronenoperator auch Konfigurationen koppeln kann, die sich um eine Doppelanregung unterscheiden, koppelt dieser Einelektronenoperator nur Konfigurationen, die sich um eine Einfachanregung unterscheiden. Die Zahl der in einem gegebenen Konfigurationsraum zu berücksichtigenden Beiträge wird also ebenfalls drastisch erniedrigt.

2.3 Spinfreie Methoden

2.3.1 Korrelation

In der Hartree-Fock-Theorie wird die Elektron-Elektron Wechselwirkung genähert, indem die einzelnen Elektronen jeweils nur das gemittelte elektrostatische Feld der anderen Elektronen erfahren. Eine explizite Wechselwirkung der einzelnen Elektronen findet keine Berücksichtigung. Diese Näherung verursacht einen Fehler in den berechneten Energien, da sich zwei Elektronen verschiedenen Spins beliebig nahe kommen können, und die dabei wirkende starke Abstoßung unberücksichtigt bleibt. Elektronen gleichen Spins sind durch den Aufbau der Wellenfunktion aus Slaterdeterminanten und die dabei bereits erfolgte Berücksichtigung des Fermi-Lochs am Aufenthalt an gleichem Ort gehindert.

Die Differenz zwischen dem Hartree-Fock-Ergebnis und der exakten Lösung wird als Korrelationsenergie bezeichnet. Dabei bleibt festzuhalten, dass diese Korrelationsenergie keine wirkliche physikalische Relevanz besitzt, sondern lediglich als Artefakt der vorgenommenen Näherung auftritt.

Zur Berechnung des bisher unberücksichtigt gebliebenen Teils der Energie gibt es verschiedene Methoden. Diese gehen teilweise vom Ergebnis der Hartree-Fock-Näherung aus und versuchen, in der Basis der HF-Orbitale die Korrelationsenergie zu beschreiben. Hier sind in erster Linie die Störungstheorie, die Konfigurationswechselwirkungsverfahren und der *Coupled Cluster*-Ansatz zu nennen. Andere Methoden, wie die Dichtefunktionaltheorie, oder auch Methoden mit expliziter Berücksichtigung der Elektron-Elektron-Wechselwirkung (r_{12} -Methoden) versuchen eine direkte Berechnung der Energie ohne den Umweg über die HF-Näherung und seine künstliche Einführung der Korrelationsenergie.

2.3.2 MRCI

Die Konfigurationswechselwirkung (engl. Configuration Interaction, CI) ist die wohl konzeptionell einfachste Methode zur Behandlung der Elektronenkorrelation. Benutzt man alle

in einer gegebenen MO-Basis darstellbaren Besetzungen des Orbitalraums mit den vorhandenen Elektronen, also den gesamten Konfigurationsraum, so erhält man eine vollständige Basis. Dieses *full CI* ergibt die bei gegebenem Operator und Basissatz exakte Lösung. Da die Dimension dieses Ansatzes jedoch schon für kleinste Moleküle die Grenzen der Handhabbarkeit sprengt, wird in der Praxis nur mit eingeschränkten Konfigurationsräumen gearbeitet. Üblicherweise wird der Konfigurationsraum auf Ein- und Zweifachanregungen bezüglich einer Referenzkonfiguration, meist der Hartree-Fock-Determinante, beschränkt. Der Grund dafür ist, dass die Ein- und Zweielektronenoperatoren des Hamiltonoperators höhere Anregungen nicht mit der Referenz koppeln. Somit ist nur ein indirekter Einfluss möglich. Für Zustände, die durch diese einzelne Referenz nicht gut beschrieben sind, die also einen Multikonfigurationscharakter haben, ist ein Multireferenzansatz der nächste Schritt. Es werden dabei Ein- und Zweifachanregungen aus mehreren, bis zu mehreren Hundert Konfigurationen zugelassen. In diesem Ansatz erhält man bei geeigneter Wahl des Referenzraums eine sehr gute Beschreibung der Elektronenkorrelation. Bei einer Analyse der einzelnen Koeffizienten des konvergierten CI-Vektors stellt sich jedoch heraus, dass eine überwältigende Zahl der Konfigurationen nur sehr geringe Beiträge leistet. Abhilfe kann hier ein Selektionsverfahren schaffen, das den Beitrag der einzelnen Konfigurationen bereits vor Durchführung der CI-Rechnung störungstheoretisch abschätzt, und nur Konfigurationen mit einem erwarteten Beitrag über einem vorgegebenen Schwellwert zulässt.

Problematisch bleibt hier die Abschätzung des dabei gemachten Fehlers, also des Beitrags der vernachlässigten Konfigurationen.

Nachteile des CI-Ansatzes sind das schnelle Anwachsen des Konfigurationsraums mit der Größe des behandelten Problems, die relativ langsame Konvergenz der Ergebnisse mit der Größe des berücksichtigten Konfigurationsraums, sowie die fehlende Größenkonsistenz. Letzteres bedeutet, dass die errechnete Energie sich für ein nicht wechselwirkendes Dimer nicht additiv verhält, wie es eigentlich physikalisch gefordert wäre.

2.3.3 DFT

Die Dichtefunktionaltheorie (DFT) geht von der Voraussetzung aus, dass die Elektronendichte eines Moleküls dessen Eigenschaften vollständig festlegt. Die Energie des Systems ergibt sich dann als Funktional der Dichte. Die Bestimmung der Wellenfunktion mit ihren $3N$ Freiheitsgraden ist also durch die Bestimmung der Dichte mit lediglich drei Freiheitsgraden ersetzt.

Diese zunächst unbekannte Dichte wird im Kohn-Sham-Verfahren durch Orbitale dargestellt, die aus den auch in *ab-initio* Methoden gebräuchlichen Basisfunktionen gebildet werden. Im Kohn-Sham DFT werden sie in einem ähnlichen Verfahren wie im Hartree-Fock-SCF optimiert, haben jedoch streng genommen keinerlei physikalische Relevanz und sind nur ein Hilfsmittel zur Darstellung der Dichte. Ebenso wie das Hartree-Fock Verfahren ist das Kohn-Sham-DFT eine Einfachreferenzmethode, also zur Bestimmung von Multikonfigurationszuständen nicht geeignet.

Eines der Hauptprobleme der DFT ist, dass das exakte Austauschkorrelationsfunktional nicht bekannt und auch nicht direkt bestimmbar ist. Das einfachste Funktional, ist das LDA-Funktional (*local density approximation*). Es nähert die Austauschkorrelationsenergie eines Elektrons, indem es sie gleich der in einem homogenen Elektronengas setzt. Mit anderen lokalen Funktionen hat es gemein, dass es nur vom Ort und der Dichte an diesem Ort abhängt. Damit unterscheidet es sich von den Funktionen in der Näherung

2. THEORETISCHER TEIL

generalisierter Gradienten (*generalized gradient approximation*, GGA), in denen auch die Ableitung der Dichte eingeht, um besser der unregelmäßigen Dichteverteilung in Molekülen gerecht zu werden. Eine weitere Abwandlung sind die Hybridfunktionale, in denen ein Teil der Austauschwechselwirkung durch den exakten Term aus der Hartree-Fock-Theorie beschrieben wird.

Die Kohn-Sham-Dichtefunktionaltheorie ist erst einmal eine Methode nur für den elektronischen Grundzustand eines Moleküls. Hier leistet sie gute Dienste und hat weite Verbreitung gefunden zur Bestimmung von Geometrien und Energien, und somit auch zur Berechnung von Reaktionsverläufen, die im Grundzustand stattfinden.

Auch eine Berechnung von angeregten Zuständen ist mittlerweile mit der zeitabhängigen Dichtefunktionaltheorie (*Time-Dependent DFT*, TDDFT) zur Standardmethode geworden. Es wird dabei die Antwort des Moleküls auf eine externe Störung, konkret ein elektromagnetisches Feld ausgewertet. Die Anregungsenergien ergeben sich dabei als Polstellen. TDDFT liefert ordentliche Ergebnisse bei angeregten Zuständen, die als Einfachanregung darstellbar sind, hat jedoch Probleme bei Zuständen mit Doppelanregungscharakter, den sehr diffusen Rydberg-Zuständen, sowie bei Zuständen mit stark unterschiedlicher Ladungsverteilung (*charge-transfer*-Zustände)

Die Stärken der Dichtefunktionaltheorie sind ihre hohe Geschwindigkeit und Genauigkeit insbesondere bei der Berechnung von Grundzuständen. Auch die Forderung nach Größenkonsistenz ist erfüllt. Als Nachteil ist in erster Linie die Beschränkung auf Einfachreferenzzustände zu nennen. Auch ist im Gegensatz zur Konfigurationswechselwirkung keine Systematische Verbesserung der Ergebnisse möglich.

2.3.4 DFT/MRCI

Die gute Eignung der Dichtefunktionaltheorie zur Behandlung der dynamischen Elektronenkorrelation und die große Flexibilität des Multireferenz-CI-Ansatzes wurden von Stefan Grimme und Mirko Waletzke im Programm DFT/MRCI[1] vereinigt. Die Grundidee ist, möglichst viele der Informationen, die das DFT über die dynamische Korrelation in einer Verbindung liefert in eine MRCI-Rechnung einfließen zu lassen, da diese im DFT sehr schnell berechnet werden.

Die Wellenfunktion wird wie im konventionellen CI in Molekülorbitale (MOs) entwickelt, diese werden jedoch aus Kohn-Sham(KS)-Orbitalen gebildet statt aus *ab-initio* Orbitalen. Der exakte Hamiltonoperator wird durch einen empirischen Operator ersetzt. Dieser unterscheidet zwischen diagonalen und außerdiagonalen Matrixelementen:

- Diagonalelemente des effektiven DFT/MRCI Hamiltonians werden aus den Hartree-Fock-Ausdrücken und einem DFT-spezifischen Korrekturterm zusammengesetzt. Die HF-Energien sind ersetzt durch die KS-Energien, Coulomb- und Austauschintegrale werden durch globale Parameter angepasst. Es kommen dabei im Singulettfall drei, und im Triplettfall zwei empirische Parameter zum Einsatz.
- Ein doppeltes Zählen der dynamischen Korrelation wird mittels einer Dämpfung außerdiagonaler Beiträge durch einen exponentiell von der Energiedifferenz der CSFs abhängigen Ausdruck $p_1 e^{-p_2 \Delta E^4_{ww'}}$ mit zwei weiteren Parametern vermieden.
- Außerdiagonale Beiträge von CSFs mit gleichem Raumteil werden exakt berechnet.

2.3. SPINFREIE METHODEN

Die insgesamt 5 empirischen Parameter des DFT/MRCI Hamiltonians sind an einem Satz experimenteller Anregungsenergien geeicht worden. Im Gegensatz zu den meisten semiempirischen Methoden sind diese Parameter unabhängig von den betrachteten Atomen. Lediglich die Multiplizität des Zustands und die Art des verwendeten Dichtefunktionalen gehen ein. Parametersätze existieren derzeit nur für Singuletts und Triplets in Verbindung mit dem BHLYP[11; 12]-Funktional. Eine Anwendung dieser Parametrisierung auf Dupletts wurde erfolglos abgebrochen[13], soll jedoch in Kürze mit einem erweiterten Ansatz erneut bearbeitet werden[14].

Bis hierher bietet der DFT/MRCI-Ansatz noch keine Verbesserung im Rechenaufwand gegenüber einem klassischen MRCI. Da der Einfluss energetisch hoch liegender CSFs durch die exponentielle Dämpfung jedoch ohnehin sehr klein ist, werden die energetisch über einem einstellbaren Schwellwert liegenden nicht in die CI-Entwicklung aufgenommen. Dadurch kann die CI-Entwicklung extrem kurz gehalten werden. Im Gegensatz zur störungstheoretischen Abschätzung des Beitrags einer CSF im selektierenden *ab-initio* MRCI ist die Selektion nach diesem Energiekriterium extrem schnell, da keine Wechselwirkung mit dem Referenzraum berechnet werden muss. Die CI-Entwicklung ist dann nur noch für statische Korrelationseffekte zuständig, während die gesamte dynamische Korrelation durch die DFT in die Rechnung gebracht wird.

Der DFT/MRCI-Ansatz ist seit einigen Jahren sehr erfolgreich eingesetzt worden, und hat dabei seine Robustheit und Güte immer wieder unter Beweis gestellt.

2. THEORETISCHER TEIL

3

Methodenentwicklung und Implementierung

Die Entwicklung des Programmpakets SPOCK ist in große, voneinander weitgehend unabhängige Teile gegliedert:

1. Spin-Bahn-Integrale
2. Spinkopplungskoeffizienten
3. Berechnung von Matrixelementen spinfreier Wellenfunktionen
4. Spin-Bahn-CI
5. Berechnung von Eigenschaften: störungstheoretisch
6. Berechnung von Eigenschaften: über Spin-Bahn-Wellenfunktionen

Die Schnittstelle für die Spin-Bahn-Integrale, sowie die Routinen zur Berechnung von Eigenschaften wurden von Jörg Tatchen im Rahmen seiner Dissertation implementiert[15].

Die Spinkopplungskoeffizienten sind vonnöten, um in einer CSF-basierten Wellenfunktion die Kopplung der Spinfunktionen zu erreichen. Ihre Ausarbeitung und Implementierung ist in Abschnitt 3.1 beschrieben. Das störungstheoretische Modul SPOCK.PT wird zusammen mit einigen beispielhaften Anwendungen in Abschnitt 3.2 vorgestellt. Der letzte Abschnitt 3.3 dieses Methodenteils behandelt den Spin-Bahn-CI-Teil SPOCK.CI des Programmpakets.

3.1 Erzeugung der Spinkopplungen

Bei der Berechnung eines Matrixelements ist neben Integralen über die Raumteile der beteiligten Konfigurationen immer auch die Berechnung der Spinkopplung erforderlich. Im Falle von Slaterdeterminanten ist diese simpel: entweder passt unter einem gegebenen Spinoperator die Besetzung mit α - und β -Elektronen der beiden Determinanten zueinander, dann entspricht die Kopplung einfach dem jeweiligen Effekt des Spinoperators, oder sie passt nicht, dann ist die Kopplung Null. Im Falle der Verwendung von Konfigurationszustandsfunktionen (*Configuration State Functions*, CSFs), also Linearkombinationen von Determinanten, sind die Verhältnisse komplexer. Hier zahlt man den Preis für die Vorteile der CSFs.

Es gibt zur Berechnung dieser Spinkopplung über CSFs ausgereifte Methoden, beispielhaft seien hier der Unitary Group Approach (UGA)[16], der Symmetric Group Approach (SGA)[17], die *symbolic matrix element method* [18], sowie das Table CI [19] genannt. Für diese Ansätze existieren auch jeweils Erweiterungen auf spinabhängige Operatoren: Für das Table CI von Heß[20], für die *symbolic matrix element method* von Yarkony *et. al.* [21], für UGA beispielsweise im COLUMBUS-Paket[22], sowie für SGA von Flocke *et. al.*[23; 24; 25; 26].

Im DFT/MRCI wurde ein älterer, für die Verwendung in einem individuell selektierenden CI bestens geeigneter Ansatz von Wetmore und Segal gewählt[27]. Die Erweiterung dieses Ansatzes auf spinabhängige Einelektronenoperatoren wird in der Veröffentlichung „Efficient generation of matrix elements for one-electron spin-orbit operators“ („Effiziente Erzeugung der Matrixelemente von Einelektronen-Spin-Bahn-Operatoren“) beschrieben[28].

Es wird zunächst gezeigt, dass auch für den *mean-field* Spin-Bahn Operator, als effektivem Einelektronenoperator das Matrixelement als

$$\ell_{ab} \cdot \eta(S, S', \omega, \omega', w, w') \quad (3.1)$$

dargestellt werden kann. Dabei ist ℓ_{ab} das Spin-Bahn-Integral der Einfachanregung $b \rightarrow a$, η der Spin-Kopplungskoeffizient und S/S' ist die Multiplizität der beiden beteiligten Zustände, deren räumliche Konfiguration durch w und w' bezeichnet ist. ω und ω' nummerieren die verschiedenen CSFs. Die Abhängigkeit von M_S ist bereits eliminiert. Matrixelemente über die verschiedenen Multiplettkomponenten werden später mit Hilfe der *scaled 3j-symbols* ermittelt[29; 30]. Weiter wird gezeigt, dass die Abhängigkeit von den Raumteilen w und w' ganz analog zum spinfreien Fall auf Anregungsmuster (*pattern*) zurückzuführen ist, die eine effiziente Speicherung unabhängig vom betrachteten Problem ermöglichen.

Details zur Implementierung wurden nicht veröffentlicht und werden im Folgenden ausgeführt.

Den Ausgangspunkt der Routinen zur Berechnung der Kopplungskoeffizienten bildete das Program ETAGEN.X von S. Grimme. Es wurde jedoch im Laufe der Programmierung vollständig neu geschrieben. Von der ursprünglichen Implementierung ist lediglich das Speicherformat der Kopplungsfelder des Einheitsoperators geblieben, die im spinfreien DFT/MRCI und im SPOCK.CI für den spinfreien Teil des Hamiltonoperators verwendet werden.

Wetmore und Segal schlagen in der ursprünglichen Veröffentlichung vor, die Kopplungskoeffizienten zu bestimmen, indem in einem bereits vorhandenen Programm alle Ein-

3.1. ERZEUGUNG DER SPINKOPPLUNGEN

elektronenintegrale auf Eins und alle Zweielektronenintegrale auf Null gesetzt werden.[27] Dieser Weg wurde auch im ETAGEN.X eingeschlagen.

Zur Erweiterung der Kopplungsfelder auf spinabhängige Operatoren erschien jedoch eine direkte Berechnung der Kopplungen der günstigere, oder zumindest klarere Weg. Hierzu wird auf die einzelnen Determinanten einer CSF explizit mit Vernichtungs- und Erzeugungsoperatoren eingewirkt, und anschliessend der Überlapp mit den CSFs der erzeugten Konfiguration berechnet. Der verwendete Formalismus ist ausführlich in der Veröffentlichung besprochen[28].

3.1.1 Erzeugung der Spinfunktionen

Für die determinantenweise Auswertung der Kopplungsmuster sind zunächst die CSFs zu erzeugen. Im ETAGEN.X wurden die CSFs durch Diagonalisierung der S^2 Matrix erhalten. Dieses Vorgehen führt jedoch zu recht verrauschten CSFs: in den Koeffizienten der Determinanten treten nur wenige und zudem unsaubere Nullen auf. Um am Ende Spin-kopplungsfelder mit möglichst vielen Nullen zu erhalten, die sich also gut packen lassen, wurde auch die Implementierung der CSF-Erzeugung von Grund auf neu geschrieben.

Dabei kommt die Genealogische Konstruktion der Spineigenfunktionen als *branching diagram functions*, gebildet aus *path diagram functions*, wie sie bei R. Pauncz[31] beschrieben ist, zum Einsatz.

Als ersten Schritt benötigt man eine Repräsentation der Determinanten. Üblich ist es, diese über Permutationen zu gewinnen, beispielsweise die Determinanten zu $M_S = 0$ bei vier offenen Schalen als alle Verteilungen von zwei α - und zwei β -Elektronen auf die vier möglichen Positionen.

$$\beta\beta\alpha\alpha \tag{3.2}$$

$$\beta\alpha\beta\alpha \tag{3.3}$$

$$\beta\alpha\alpha\beta \tag{3.4}$$

$$\alpha\beta\beta\alpha \tag{3.5}$$

$$\alpha\beta\alpha\beta \tag{3.6}$$

$$\alpha\alpha\beta\beta \tag{3.7}$$

Dieser Weg war auch im ETAGEN.X implementiert. Im neuen Ansatz wurde ein anderer Weg gewählt: Die Determinanten sind repräsentiert durch binäre Zahlen, wobei die 1 für ein α -, die 0 für ein β -Elektron steht. Im obigen Beispiel also

$$0011 = 3 \tag{3.8}$$

$$0101 = 5 \tag{3.9}$$

$$0110 = 6 \tag{3.10}$$

$$1001 = 9 \tag{3.11}$$

$$1010 = 10 \tag{3.12}$$

$$1100 = 12 \tag{3.13}$$

Die Slaterminanten zu $M_S = 0$ bei vier offenen Schalen ergeben sich also als diejenigen ganzen Zahlen, deren Binärdarstellung vier Stellen hat, und genau zwei Einsen enthält. Dazu wird in einem ersten Schritt zu jeder Zahl zwischen 0 und $(2^{n_{open}} - 1)$ die Zahl der

Einsen in der Binärdarstellung ermittelt, (*nopn* ist hier die maximale Zahl an offenen Schalen, die benötigt wird) und sodann die Determinanten im Feld `msdet1(n, i)` gespeichert, wobei *n* die Anzahl offener Schalen, und *i* die laufende Nummer der Determinanten ist.

Bei der eigentlichen Berechnung der Linearkombination von Determinanten zu CSFs werden die Koeffizienten jeder einzelnen Determinante direkt ermittelt, ohne die Spinfunktionen für eine niedrigere Anzahl offener Schalen kennen zu müssen. Jede einzelne Determinante wird Elektron für Elektron betrachtet, der Koeffizient ergibt sich als Produkt von Brüchen, die durch den bis dahin aufgebauten Teil der Determinanten bestimmt sind. Um möglichst saubere Spinfunktionen zu erhalten, wird so lange wie möglich Ganzzahlarithmetik benutzt. Zähler und Nenner werden getrennt berechnet und erst im letzten Schritt wird der Quotient gebildet und die Wurzel gezogen.

Auf eine Optimierung der Implementierung musste nicht geachtet werden, da der Ansatz ausreichend schnell ist. So dauert beispielsweise die Berechnung der Spinfunktionen für Triplets mit bis zu 14 offenen Schalen lediglich 7 Sekunden auf einem 2.4 GHz Xeon Prozessor. Zudem müssen die Spinfunktionen nur ermittelt werden, wenn die Spinkoppelfelder noch nicht in der Programmabibliothek vorhanden sind.

3.1.2 Erzeugung der Kopplungsfelder

Die Routinen zur Erzeugung der Kopplungsfelder sind gänzlich unabhängig davon, wie die CSFs erzeugt werden, also welche Spinfunktionen verwendet werden. Allerdings hat die Wahl der Spinfunktionen einen Einfluss darauf, wie viele der Kopplungsmatrixelemente von Null verschieden sind, also explizit gespeichert werden müssen.

Die prinzipielle Vorgehensweise zur Errechnung der Kopplungsmatrizen ist in der Veröffentlichung ausführlich beschrieben. Die Grundidee des Anregungsmusteransatzes ist, nur die einfach und variabel besetzten Orbitale zu betrachten. Orbitale, die während der Anregung unverändert leer oder unverändert doppelt besetzt bleiben, können einfach gestrichen werden. Die resultierenden reduzierten Besetzungszahlvektoren werden für Ausgangs- und Endbesetzung verglichen und anhand der unverändert einfach besetzten Orbitale klassifiziert. So erhält man Anregungsmuster (*pattern*) in der Größnordnung von einigen Dutzend. Zu jedem dieser *patterns* ist eine Kopplungsmatrix zu ermitteln, deren Dimension der Anzahl der aus den Konfigurationen zu bildenden CSFs entspricht. Allerdings ist die Einteilung mittels *pattern* noch nicht eindeutig: es bleiben noch jeweils vier Unterfälle unterscheidbar. Ob die Anregung „von links nach rechts“, oder „von rechts nach links“ im Besetzungszahlvektor erfolgt, ist damit nicht unterscheidbar. Ebenso kann nicht zwischen Fällen unterschieden werden, in denen das bewegte Elektron in aus einem einfach besetzten in ein leeres Orbital oder aus einem doppelt besetzten in ein einfach besetztes Orbital angeregt wird. Diese Unterfälle können im Falle des spinfreien und des S_0 -Operators alle durch Transpositionen und Vorzeichenwechsel ineinander überführt werden. Im Falle des S_+ Operators können nur jeweils zwei Unterfälle ineinander überführt werden, so dass doppelt so viele Kopplungsfelder gespeichert sein müssen. Der S_- Operator kann jedoch wiederum durch den S_+ Operator dargestellt werden, so dass unter dem Strich für jeden der drei Spinoperatoren ein Satz Kopplungsfelder vorzuhalten ist.

In der konkreten Implementierung wurden einige Optimierungen vorgenommen. So wird nicht für jedes Anregungsmuster erneut die komplette Anregung $i \rightarrow j$ ausgeführt, sondern die CSFs, in denen Elektron *i* vernichtet wurde, aufgehoben. An allen möglichen Stellen *j* wird sodann nacheinander entweder ein Elektron wieder eingefügt, was zu den

3.1. ERZEUGUNG DER SPINKOPPLUNGEN

Unterfällen *A* führt (gleichbleibende Anzahl offener Schalen), oder ein zweites Elektron vernichtet (dort, wo das erste Elektron eingefügt wird, „verschwindet“ eine offen Schale), um zu den Unterfällen *B* zu gelangen, in denen die Anzahl offener Schalen um zwei abnimmt.

Bei der Vernichtung und Erzeugung von Elektronen kommt der Vorteil der Binärdarstellung zum Tragen. Bei der Erzeugung eines Elektrons müssen alle „links“ davon stehenden Elektronen um eine Position verschoben werden. Dazu genügt es, den unverändert bleibenden Teil mittels einer arithmetischen AND-Operation auszublenden, den Rest mit 2 zu multiplizieren, also um eine binäre Stelle zu verschieben, und anschliessend den unveränderten Teil, sowie das hinzugekommene Elektron zu addieren. Da diese Prozedur mit reinen Rechenoperationen ohne Schleifen oder Sprünge auskommt, ist sie sehr effizient. Die Vorgehensweise zur Vernichtung ist ganz analog, es wird lediglich durch 2 geteilt und so eine Verschiebung in die andere Richtung vorgenommen. Außerdem kommt eine Prüfung hinzu, ob, wenn an Position *i* ein α -Elektron vernichtet werden soll, dort auch tatsächlich eines angetroffen wird. Die weiteren Details zur Berechnung der Kopplungsmatrizen sind in der Veröffentlichung besprochen.

3.1.3 Abspeicherung als gepackte Matrizen

Bei der Betrachtung der berechneten Kopplungsfelder fällt auf, dass sehr viele Einträge Null sind. Daher wurde nach einer Strategie zur kompakteren Abspeicherung gesucht. Eine genauere Inspektion der Felder zeigt einige wenige diagonale Felder, sowie viele Felder, in denen lediglich recht kompakte Blöcke von Null verschieden sind. Bei der Speicherung werden folgende Fälle unterschieden:

- Ist keine Dimension des Feldes größer 9, so wird das Feld, so wie es ist, ungepackt gespeichert. Dies vermeidet einen im Verhältnis zum gesparten Platz unverhältnismässigen Aufwand bei kleinen Feldern. Der Grenzwert ist über einen Parameter einstellbar.
- Diagonale Felder werden gesondert gekennzeichnet, und nur die Diagonale gespeichert.
- In allen anderen Fällen werden die Felder gepackt. Dabei wird nicht für jeden einzelnen von Null verschiedenen Eintrag ein Index gespeichert, sondern zur Ausnutzung der Blockstruktur direkt aufeinander folgende Einträge zusammengefasst. Für jeden Block aufeinanderfolgender Einträge sind also 2 Indizes zu speichern (Startposition und Anzahl). Bei einzelnen Einträgen ist dies unvorteilhaft, da diese nur einen einzelnen Index benötigen würden, für größere Blöcke spart man jedoch. In Tabelle 3.1 ist ersichtlich, dass im Falle sehr dünn besetzter Kopplungsfelder mit vielen einzeln setzenden Einträgen das Indexfeld größer ist, als die Anzahl gespeicherter Werte. während es im Falle einer dichter besetzten Matrix, wie sie bei den Kopplungsfeldern mit Spin-Operatoren vorkommen, kleiner ist.

Als Beispiel ist der Fall der Kopplung von Singulett und Tripletts bei bis zu 12 offenen Schalen in Tabelle 3.1 aufgeführt. Da kleine Felder komplett gespeichert werden, liegt die Zahl der gespeicherten Werte höher als die der von Null verschiedenen. Bei der Berechnung des Speicherbedarfs muss beachtet werden, dass ein Eintrag im Kopplungsfeld 8 byte belegt (`double precision, real*8`), während ein Eintrag im Indexfeld lediglich 4 byte braucht (`integer*4`). Das Packen der Felder ist im Falle der spinabhängigen Operatoren zwar weit

	$\langle S = 1 \hat{1} S = 1 \rangle$	$\langle S = 0 \hat{s}_+ S = 1 \rangle$
Gesamtzahl der Einträge in Feldern	2360577	8286822
Davon Null	2237836	6747851
Nullen in Prozent	94.8%	81.4%
Abgespeicherte Werte	122667	1540154
Größe des Indexfeldes	133468	1280048
Speicherbedarf ungepackt	18.9 MB	66.3 MB
Speicherbedarf gepackt	1.5 MB	17.4 MB
Speicherbedarf gepackt in %	7.9 %	26.3 %

Tabelle 3.1: Dimensionen der gepackten und ungepackten Kopplungsfelder für die Kopplung zweier Triplets mit dem spinfreien Operator, und die Kopplung zwischen Singulett und Triplet mit dem \hat{s}_+ -Operator, jeweils für bis zu 12 offene Schalen.

weniger effizient als im spinfreien Fall, bringt aber immer noch eine Speicherplatzersparnis von rund 75%.

Die gepackte Version wird im SPOCK für die spinabhängigen Kopplungsfelder verwendet. Im DFT/MRCI sind noch die alten ungepackten Felder implementiert. Diese kommen somit auch im SPOCK.CI für die spinfreien Kopplungsfelder zum Einsatz. Weiterhin werden diese neuen Routinen zur Berechnung der spinfreien Kopplungsfelder im Multireferenz-MP2-Programm RIMR von Stefan Grimme verwendet[32].

3.1. ERZEUGUNG DER SPINKOPPLUNGEN



Available online at www.sciencedirect.com



Chemical Physics 311 (2005) 71–79

Chemical
Physics

www.elsevier.com/locate/chemphys

Efficient generation of matrix elements for one-electron spin–orbit operators

Martin Kleinschmidt *, Christel M. Marian

Institute of Theoretical and Computational Chemistry, Heinrich Heine University Düsseldorf, Universitätstr.1, 40225 Düsseldorf, Germany

Received 30 March 2004; accepted 4 October 2004
Available online 6 November 2004

Abstract

We present a procedure for the generation of spin-couplings with effective one-electron spin–orbit operators over spin-symmetry-adapted functions that is independent of the size of the internal space. Extending a spin-free approach by Wetmore and Segal [Chem. Phys. Lett. 36 (1975) 478], we show that all couplings may be precomputed once and stored as a program library. Storage requirements are minimal for up to 10 open shells and become manageable for up to 12 open shells by storing sparse matrices. The procedure has been implemented in the new Spin–Orbit Coupling Kit **Spock**, based on an individually selecting configuration interaction program.

Benchmark and test calculations have been performed on third row atoms and porphyrin derivates.
© 2004 Elsevier B.V. All rights reserved.

1. Introduction

Configuration interaction (CI) calculations with a spin-free Hamiltonian are usually performed in a basis of spin-symmetry-adapted configuration-state functions (CSFs). In contrast to simple Slater determinants, CSFs are eigenfunctions of the total spin operator \hat{S}^2 with eigenvalue $S(S+1)$. Due to spin-symmetry blocking, the dimensionality of the CI matrix in a basis of CSFs is thus reduced compared to that of a determinantal basis. There are also disadvantages of a CSF basis, of course. Compared to a determinantal basis the construction of Hamiltonian matrix elements is significantly more involved.

The spin–orbit interaction leads to a mixing of states with different multiplicities and the advantage of the CSF basis appears to be lost. One might therefore argue that a determinantal basis should be preferable in a two-

component calculation. However, in a determinantly driven spin–orbit CI (e.g. [1,2]) non-zero matrix elements may occur between all determinants with magnetic quantum numbers differing by $M'_S = M_S \pm 0, 1$. In a CSF basis, on the other hand, an additional selection rule applies, i.e., $S' = S \pm 0, 1$ (but not $S' = S = 0$). As a result, large off-diagonal blocks of the Hamiltonian matrix remain zero in a CSF-based spin–orbit CI. The dimension may be reduced further by excluding high multiplicities. Another advantage of the CSF basis is that the resulting wave functions allow for a better physical insight since contributions of individual LS-coupled spin-free states to a spin–orbit mixed state may easily be identified.

To avoid the slow evaluation of matrix elements over CSFs determinant by determinant, various procedures have been proposed for spin-independent operators. In 1975, Wetmore and Segal [3,4] devised an efficient and conceptually simple scheme for the evaluation of spin-couplings between CSFs for spin-independent operators. This scheme relies on the recognition that a matrix element is no more than a weighted sum of one- and

* Corresponding author. Fax: +49 221 811 3466.
E-mail address: [\(M. Kleinschmidt\).](mailto:christel.marian@uni-duesseldorf.de)

3. METHODENENTWICKLUNG UND IMPLEMENTIERUNG

two-electron integrals. These weighting or spin-coupling coefficients are independent of the actual problem. Using “excitation patterns” as a unique identifier, these authors were able to reduce the number of spin-coupling coefficients down to a level which easily facilitates their precomputation and storage as a program library. The same general idea was pursued later in the table CI¹ [5] and the symbolic matrix element method [6]. The symmetric and (graphical) unitary group approaches (SGA and GUGA, see e.g. [7,8]) make use of symmetry selection rules and have to rely on a specific prescription how to generate the CSFs. To our knowledge, extensions to spin-dependent operators exist for the table CI [9], the symbolic matrix element method [10], the unitary group approach [11] and for the symmetric group approach [12–15].

In individually selecting CI procedures, only a small number of all configurations is selected for the calculation. Explicit configuration comparison has to be applied, and the advantages of GUGA and SGA vanish. The pattern approach of Wetmore and Segal does not make any assumptions concerning the completeness of the configuration space and is thus well suited for application in a configuration selecting CI. Recently, it was implemented in the DFT/MRCI program of Grimme and Waletzke [16] and has proven to be very efficient. The DFT/MRCI program utilizes information from a DFT calculation in connection with a multi-reference selecting CI. Typical errors of electronic excitation energies of molecules with a hundred valence electrons lie well below 0.3 eV. In order to incorporate spin-orbit coupling into the DFT/MRCI program, we have extended the approach of Wetmore and Segal to one-electron spin-orbit operators and implemented the resulting coupling matrices in our newly developed Spin-Orbit Coupling Kit **SPOCK**. This program is capable of calculating spin-orbit matrix elements over CI wave functions, as well as directly calculating spin-orbit coupled wave functions via a spin-orbit CI procedure.

2. Separation of space and spin parts

In larger molecules, the use of a full one- and two-electron spin-orbit Hamiltonian – be it the Breit-Pauli or the no-pair Hamiltonian – is prohibitively expensive because of the vast number of two-electron multi-center integrals. On the other hand, the $1/r^3$ dependence of the one- and two-electron operators restricts their action to a fairly local range. Furthermore, the spin-orbit interaction between two states is dominated by single excita-

tions. This does not mean that all two-electron contributions can be neglected. For first-row atoms – the main constituents of organic molecules – the two-electron terms tend to reduce a one-electron spin-orbit matrix element by about 50% [17]. The spin-orbit Hamiltonian utilized here is an effective one-electron operator that consists of the true one-electron spin-orbit Hamiltonian $\hat{\mathcal{H}}_{\text{SO}}(1)$ and $\hat{\mathcal{H}}_{\text{SO}}^{\text{mf}}(1)$, which incorporates the screening by the other electrons in a mean-field approach [18].

$$\hat{\mathcal{H}}_{\text{SO}}^{\text{eff}}(1) = \hat{\mathcal{H}}_{\text{SO}}(1) + \hat{\mathcal{H}}_{\text{SO}}^{\text{mf}}(1). \quad (1)$$

A matrix element of $\hat{\mathcal{H}}_{\text{SO}}^{\text{mf}}(1)$ in the basis of the valence orbitals i, j is given by

$$\langle i | \hat{\mathcal{H}}_{\text{SO}}^{\text{mf}}(1) | j \rangle = \sum_o \gamma_o \left\{ \langle io | \hat{\mathcal{H}}_{\text{SO}}(2) | jo \rangle - \frac{3}{2} \langle io | \hat{\mathcal{H}}_{\text{SO}}(2) | oj \rangle - \frac{3}{2} \langle oi | \hat{\mathcal{H}}_{\text{SO}}(2) | jo \rangle \right\}. \quad (2)$$

Herein, “o” labels occupied core and valence orbitals and $\hat{\mathcal{H}}_{\text{SO}}(2)$ represents the two-electron part of either the Breit-Pauli or no-pair spin-orbit operator. The spin densities for α and β electrons in the orbitals “o” are assumed to be equal and occupation numbers γ_o range between 0 and 2.

As an additional approximation, all multi-center integrals may be neglected. In the latter case, the molecular mean field reduces to a sum of atomic mean fields. Making use of the spherical symmetry in the atomic mean-field integral evaluation step leads to enormous savings of computation time [19].

Any (effective) one-electron spin-orbit operator may be written as a dot product between an effective one-electron angular momentum operator $\vec{\ell}$ and the usual one-electron spin-operator \vec{s} :

$$\hat{\mathcal{H}}_{\text{SO}}^{\text{eff}}(1) = \sum_{k=1}^N \vec{\ell}(k) \cdot \vec{s}(k) = \sum_{\xi \in \{x,y,z\}} \sum_{k=1}^N \hat{\ell}_\xi(k) \cdot \hat{s}_\xi(k). \quad (3)$$

CI wave functions of spin-independent Hamiltonians are computed for a single multiplet component, usually the one with $M_S = S$. Non-vanishing matrix elements of the spin-orbit operator occur for $\Delta S = 0, \pm 1$ and $\Delta M_S = 0, \pm 1$ only. Spin integration is easily performed if the spin operators \hat{s}_{+1} , \hat{s}_{-1} , or \hat{s}_0 are employed in their irreducible tensor representation. The spatial part of the spin-orbit operator, on the other hand, must fulfill the requirements implied by the spatial symmetries of the configurations involved. Therefore, a convenient approach for the calculation of spin-orbit matrix elements in CI calculations combines the appropriate cartesian (x , y or z) space part of the spin-orbit operator with a spin part in tensorial form. The transformation from this “wrong” combination of cartesian space and tensorial

¹ The table CI does not completely eliminate the summation over determinants. Instead, this sum is avoided only for the $|ket\rangle$.

3.1. ERZEUGUNG DER SPINKOPPLUNGEN

spin part to the proper matrix elements is achieved by multiplication with the *scaled 3-j symbols* introduced by McWeeny² [20]. The Wigner-Eckart theorem [21], which is usually applied to generate matrix elements over all other M_S components, is already incorporated in the *scaled 3-j symbols*.

In the following, we will make extensive use of a relation that only holds for the spin part of the operator in its tensorial form, i.e.,

$$\left\langle S+1 \left| \sum_{k=1}^N \hat{s}_{+1}(k) \right| S \right\rangle = - \left\langle S \left| \sum_{k=1}^N \hat{s}_{-1}(k) \right| S+1 \right\rangle. \quad (4)$$

The minus sign is obtained because $(\hat{s}_{+1})^\dagger = -\hat{s}_{-1}$. Thus, spin couplings need to be generated explicitly only for \hat{s}_{+1} and \hat{s}_0 .

For convenience, we will employ second quantization for the derivation of the coupling coefficients. In the notation of second quantization, every component of our operator may be written as

$$\sum_{k=1}^N \hat{\ell}_\xi(k) \hat{s}_\zeta(k) = \sum_{i,j} h_{ij} \hat{a}_i^\dagger \hat{a}_j, \quad (5)$$

where ξ stands for one cartesian component of the space part and ζ may be 0 or +1. We will drop these subscripts now. Indices i and j run over all spin orbitals and h_{ij} is the corresponding matrix element

$$h_{ij} = \langle i(1) | \hat{\ell}(1) \hat{s}(1) | j(1) \rangle. \quad (6)$$

Separation of the molecular orbitals (MOs) i and j into spatial functions m and n and spin μ and v , respectively, yields

$$h_{m\mu,nv} = \langle m(1)\mu(1) | \hat{\ell}(1) \hat{s}(1) | n(1)v(1) \rangle \quad (7)$$

$$= \underbrace{\langle m(1) | \hat{\ell}(1) | n(1) \rangle}_{\ell_{mn}} \underbrace{\langle \mu(1) | \hat{s}(1) | v(1) \rangle}_{s_{\mu v}} \quad (8)$$

and the operator becomes

$$\begin{aligned} \hat{h} &= \sum_{m\mu,nv} h_{m\mu,nv} \hat{a}_{m\mu}^\dagger \hat{a}_{nv} \\ &= \sum_{m,n} \ell_{mn} \left(\sum_{\mu,v} s_{\mu v} \hat{a}_{m\mu}^\dagger \hat{a}_{nv} \right). \end{aligned} \quad (9)$$

The operator is now well separated into a spin-independent part (the matrix elements ℓ_{mn} which carry all system-related information) and a spin-dependent part $\sum_{\mu,v} s_{\mu v} \hat{a}_{m\mu}^\dagger \hat{a}_{nv}$, which is independent of the actual problem. Note that this separation may be equally well performed for the combination of any space and spin parts, each in an arbitrary cartesian or tensorial form.

² There is a misprint in [20]: in Table 2, the first case ($S = S_a = S_b$, $M_a = M$, $M_b = M \pm 1$) must read: $C_1 = \mp[1/2(S \pm M + 1)(S \mp M)]^{1/2}$.

3. Matrix elements over CSFs

We will follow the convention of Wetmore and Segal, denoting a CSF as linear combination of Slater determinants Δ_i by

$$|S, M_S, \omega, w\rangle = \sum_i c_i(S, M_S, \omega) \Delta_i(M_S, w), \quad (10)$$

w representing the occupation of molecular orbitals (MOs) and ω being an index for the different eigenfunctions of the \hat{S}^2 and \hat{S}_z operators with spin S and z -component M_S .

A matrix element of a one-electron spin-orbit operator over two CSFs is zero unless their respective orbital occupations differ by a single excitation. Diagonal matrix elements are zero in the basis of real orbitals because of the symmetry properties of the operator, and higher excitations cannot be coupled by a one-electron operator. If the space parts w and w' of the two CSFs differ by a single excitation $b \rightarrow a$, the matrix element with the operator (9) reads

$$\begin{aligned} &\left\langle S', \omega', w' \left| \sum_{m,n} \ell_{mn} \sum_{\mu,v} s_{\mu v} \hat{a}_{m\mu}^\dagger \hat{a}_{nv} \right| S, \omega, w \right\rangle \\ &= \ell_{ab} \left\langle S', \omega', w' \left| \sum_{\mu,v} s_{\mu v} \hat{a}_{av}^\dagger \hat{a}_{bv} \right| S, \omega, w \right\rangle \\ &=: \ell_{ab} \cdot \eta(S, S' \omega, \omega', w, w'). \end{aligned} \quad (11)$$

We see that the matrix element of the spin part over the two CSFs is just a number, labelled η , that depends on the spatial occupations w and w' , spins S and S' , and CSF indices ω and ω' . (We dropped the additional index M_S , because we have defined $M_S = S$.)

If η depends on the spatial occupation of all orbitals, the number of matrix elements will rapidly grow with the basis set size and number of electrons. However, the spin coupling is only affected by the number and the positions of the open-shell electrons. All orbitals that are either empty or doubly occupied in both configurations, w and w' , do not influence the spin coupling at all and can be removed from the occupation number vectors for this purpose. This leaves us with the singly and variably occupied orbitals. The dependence on the basis set size has completely been eliminated, as well as the dependence on the total number of electrons.

For the identification of excitation types, Wetmore and Segal introduced the so-called *excitation patterns*: the variably and singly occupied orbitals in w and w' are written as reduced occupation number vectors, where the occupation numbers may be 0, 1 or 2, and compared by a logical AND operation. This yields a binary number, which is used for the classification. In their original publications [3] they give the following examples that are repeated here for clarity:

3. METHODENENTWICKLUNG UND IMPLEMENTIERUNG

$$\begin{aligned}
 2211110 &\Rightarrow 11110 \\
 2211011 &\Rightarrow 11011 \\
 &\quad 11010 = \text{PATTERN 26} \\
 2121101 &\Rightarrow 211101 \\
 1121111 &\Rightarrow 111111 \\
 &\quad 011101 = \text{PATTERN 29}
 \end{aligned}$$

On the left, the full occupation number vectors are shown, including doubly occupied orbitals that remain unchanged. On the right, the determination of the excitation patterns from the reduced occupation number vectors can be seen. The number of possible patterns is rather small, e.g., 55 for a single excitation between two CSFs that both have ten open shells and 66 for the transition from 10 to 12 open shells.

A total of eight different types of single excitations may be found. The notation has been restricted to the orbitals involved in the excitation process:

$$\begin{array}{cccc}
 \begin{bmatrix} 1 & 0 \\ 0 & 1 \end{bmatrix} & \begin{bmatrix} 0 & 1 \\ 1 & 0 \end{bmatrix} & \begin{bmatrix} 2 & 1 \\ 1 & 2 \end{bmatrix} & \begin{bmatrix} 1 & 2 \\ 2 & 1 \end{bmatrix} \\
 \text{subcase : } & A1 & A2 & A3 & A4 \\
 \begin{bmatrix} 1 & 1 \\ 0 & 2 \end{bmatrix} & \begin{bmatrix} 1 & 1 \\ 2 & 0 \end{bmatrix} & \begin{bmatrix} 2 & 0 \\ 1 & 1 \end{bmatrix} & \begin{bmatrix} 0 & 2 \\ 1 & 1 \end{bmatrix} \\
 \text{subcase : } & B1 & B2 & B3 & B4
 \end{array}$$

The previous example, which yielded PATTERN 26, corresponds to subcase $A1$. Excitations of the types $A2$, $A3$, and $A4$ would result in exactly the same pattern. To deduce this finding, we observe that the number of open shells remains unchanged in the subcases labelled A . After performing the logical AND operation, the binary representations of their patterns are characterized by $(N - 1)$ 1's (N being the number of open shells) and two 0's. The same pattern will be obtained for all four subcases because the zeroes occur at the same places.

The excitations labelled B change the number of open shells by ± 2 . The example given for PATTERN 29 shows an excitation of type $B3$. Again, all four subcases yield the same pattern, which will have (N) 1's in the binary representation (N being the smaller of the numbers of open shells involved).

As long as we deal with a spin-free Hamiltonian, the total spin S is conserved and the spin orientation (α or β) of the excited open-shell electron does not influence the result of the spin integration. Although these statements do not hold in general for spin-dependent Hamiltonians, it is instructive to consider the case of a spin-free Hamiltonian first. Let us summarize our findings at this point: (1) Cases A and B generate different patterns. (2) For each pattern that corresponds to a single excitation, four subcases may occur. (3) The number of CSFs that can be constructed for the given numbers of open shells depends on the quantum number S . As a result,

for each pattern and quantum number S four matrices of η values have to be precomputed. The dimensions of these matrices equal the number of CSFs that can be constructed for the given number of open shells and quantum number S . To further reduce the computational expense, we notice that simple relations between these subcases exist for the spin-free Hamiltonian, such that each of the four matrices may be represented by only a single one:

$$A1 = A2^T = -1 \cdot A3^T = -1 \cdot A4,$$

$$B1 = B2 = B3^T = B4^T,$$

The matrices are related by no more than a change of sign or a transposition, denoted by the superscript T. It is therefore sufficient to calculate and store only one of them.

As outlined in detail in Appendix A, similar relations can be found for a one-electron spin-orbit Hamiltonian, too. For the \hat{s}_0 operator these are

$$A1 = A2^T = A3^T = A4,$$

$$B1 = -1 \cdot B2 = -1 \cdot B3^T = B4^T.$$

Again, by means of the same simple operations, the number of stored A and B matrices is reduced from 4 each to 1 each.

In case of the \hat{s}_{+1} operator, the relations are

$$A1 = A4,$$

$$A2 = A3,$$

$$B1 = -1 \cdot B2,$$

$$B3 = -1 \cdot B4.$$

Only two of the four A and B subcases are eliminated here.

Summarizing, we will have to compute one set of η matrices (one matrix for every valid pattern) in case of the \hat{s}_0 operator (or $S' = S$) and two sets for the \hat{s}_{+1} operator (or $S' = S + 1$).

4. Calculation of the η matrices

Wetmore and Segal proposed the generation of the η matrices by taking an existing CI code, setting all one-electron integrals to unity and all two-electron integrals to zero. We do not follow this approach, but rather calculate the η matrices directly by explicitly acting with the creation and annihilation operators on the CSFs determinant by determinant.

In principle, we could construct the CSFs for S and S' by any standard method. We have utilized here the branching-diagram functions, constructed from path-diagram functions according to Pauncz (Eq. (2.51) in

3.1. ERZEUGUNG DER SPINKOPPLUNGEN

[22]). In this way, very sparse coupling matrices are obtained. The η 's are then computed in principle as follows: for each pattern, representing a single excitation $i \rightarrow j$ and each pair of CSFs ω and ω' , the algorithm is

```

set  $\eta = 0$ 
loop a over all determinants in  $\omega$ 
    excite  $i \rightarrow j$ 
    determine the resulting determinant b
    determine the number of permutations P1
    determine the spin factor S1
    set  $\eta = \eta + c_a(S, \omega) \cdot c_b(S', \omega') \cdot (-1)^{P1} \cdot S1$ 
determine the number of permutations P2
set  $\eta = \eta \cdot (-1)^{P2} \cdot S2$ 
```

After performing the excitation, the electron is in the right orbital, but is in the wrong position in the occupation number vector. To obtain a valid Slater determinant, it must be permuted with the electrons that lie between its original and final positions. Here, doubly occupied orbitals have no influence. (This is the reason why doubly occupied orbitals, which remain unchanged, have been deleted from the reduced occupation-number vector.) Therefore, the permutation factor $P2$ is just the number of open shells in positions between orbitals i and j . The permutation factor $P1$ accounts for additional permutations that are necessary to obtain (or break) the standard ordering ($\alpha\beta$) in the doubly occupied orbitals. This is explained in more detail in Appendix A.

The spin factors $S1$ and $S2$ incorporate the spin integrals $\langle \mu | \hat{s} | \nu \rangle$ and thus involve the tensorial spin operators: $S2$ is equal to 1/2 for the \hat{s}_0 operator and to $(-1/\sqrt{2})$ for the \hat{s}_{+1} operator. The spin factor $S1$ amounts to (-1) if we evaluate the \hat{s}_0 operator and the electron excited has β spin and $(+1)$ otherwise. The same procedure may be used to generate η matrices for the spin-free Hamiltonian. In this case $S1 = S2 = 1$.

Summarizing, we have successfully derived spin-coupling matrices similar to those given by Wetmore and Segal after separating the spin-orbit operator into a spin-dependent and a spin-independent part. These matrices incorporate the spin coupling over CSFs as well as the effects of the spin operators. The classification of the excitations by patterns reduces the number of coupling matrices drastically. For the \hat{s}_0 operator, their number is the same as for the spin-free case. For the \hat{s}_{+1} operator, twice as many η -matrices must be evaluated.

The total number of coupling matrix elements for spin multiplicities up to seven is given in Table 1. In the worst case (12 open shells, triplet–quintet coupling), there are about 17 million coefficients, requiring approximately 135 megabytes of main memory. We overcome this problem by recognizing that most of the entries in the coupling arrays are zero. Therefore, we store arrays as sparse matrices. Only non-zero values are actually

Table 1
Cumulative total number of coupling coefficients for some combinations of S and S' and 9–12 open shells

S	S'	9	10	11	12
2	2	108,012		1,562,916	
3	3		596,397		9,240,879
4	4	134,822		2,367,272	
5	5		394,685		7,654,685
6	6	39,786		1,001,736	
7	7		80,381		2,285,969
1	3		563,634		8,286,822
2	4	241,179		3,845,769	
3			969,566		16,814,516
4	6	146,248		3,077,473	
5	7		355,720		8,359,870

stored for matrices with one dimension exceeding 10 (corresponding to CSFs with seven or more open shells). The arrays are constructed on the fly whenever needed. We have tested the performance impact of this treatment: in typical test cases, the generation of the coupling matrices from the stored sparse matrices takes well below 1% of the total computation time.

5. Implementation and testing

Based on the DFT/MRCI codes by Grimme and Waletzke, we have implemented the spin-dependent coupling arrays in the Spin–Orbit-Coupling Kit **SPOCK** [23]. This program computes matrix elements over CI wave functions, as well as spin–orbit coupled states either by perturbation theory or variationally by means of a spin–orbit CI. In the DFT/MRCI, extensive configuration selection is applied to drastically reduce the size of the interacting space. In a selecting CI, only a small number of all possible configurations is treated explicitly. Therefore, schemes which rely on a certain ordering of configurations cannot be used, and configuration comparison has to be done. The evaluation of a spin–orbit matrix element utilizing the η matrices requires only a few steps:

- (1) Compare the two configurations and determine whether they differ by a single excitation $b \rightarrow a$.
- (2) Generate the pattern.
- (3) Determine the subcase ($A1-A4$ or $B1-B4$).
- (4) Multiply the spatial integral by the spin-coupling array.
- (5) Multiply by the scaled 3-j symbols.

After having determined the two orbitals involved in the excitation, one needs to know the positions of these two orbitals relative to all open shells. This directly yields the pattern.

The implementation is based on the second quantization formalism and stores configurations as their differ-

3. METHODENENTWICKLUNG UND IMPLEMENTIERUNG

ence from a reference configuration, e.g., the SCF determinant. Due to this fact, steps (1) and (2) can be performed together very efficiently. Assignment of the right subcase is easily achieved by two simple comparisons: (a \leq b?) and (b doubly occupied?). These few and simple operations directly yield the spin coupling for the block of CSFs connected with the two configurations under investigation.

The multiplication with *scaled 3-j symbols* can be postponed, if dealing with matrix elements over CI wave functions. In the spin-orbit CI, this multiplication constitutes the innermost loop, the multiplication with the CI vectors.

We include here some test results to demonstrate the correctness and efficiency of the newly developed codes.

5.1. Atomic test calculations

Calculations of ground states of third row atoms have been performed with the ab initio (DFT-free) branch of DFT/MRCI and **srock**. The triple-zeta valence polarization (TZVP) [17s11p6d1f]/[6s4p3d1f] atomic basis set from the TURBOMOLE library [24] is used. Atomic orbitals are generated by the MOLCAS program [25] in a complete-active-space SCF (CASSCF) procedure that includes scalar relativistic effects. We have performed all computations in the C_i symmetry group. In C_i symmetry, all components of the spin-orbit operator are totally symmetric. This allows for thorough testing because symmetry does not help in enforcing degeneracies. Here, we list only perturbation theory results for the manganese atom and spin-orbit CI results for the arsenic atom. Results for the other atoms are of equal quality.

In the manganese atom, the CI step includes the set of 51 configurations with five electrons in the five 3d orbitals. Adding spin, there are 75 doublets, 24 quartets and 1 sextet, i.e., 2S , 2P , 2D , 2D , 2D , 2F , 2F , 2G , 2G , 2H , 2I , 4P , 4D , 4F , 4G , and 6S [26]. We have kept all but the five 3d-electrons frozen. It has to be emphasized that these calculations are not meant to be compared with experimental results but are carried out for testing the internal consistency of the formulae and the program code.

Table 2 lists all J components of all these states, computed in perturbation theory. All states come out as expected and the degeneracies of the individual J components are excellent. The deviations from perfect degeneracy are on the order of $0.02 \text{ cm}^{-1} \approx 10^{-7} \text{ a.u.}$ and resemble the deviations in the spin-free states.

In the arsenic atom, the states 4S , 2D , and 2P arising from $4p^3$ have been computed. All of their corresponding configurations have been taken as the reference space. Only the three 4p-electrons are treated explicitly. Complete single and double excitations from the references have been included in the CI step, yielding a total of 1499 CSFs for the doublet states and 682 in the

Table 2
States originating from $4s^23d^5$ occupation in the manganese atom, as computed with the new codes in perturbation theory

State	Energy	Δ
$^6S_{5/2}$	0.0	0.0000
$^4G_{5/2}$	31443.2256	0.0115
$^4G_{7/2}$	31456.3065	0.0107
$^4G_{11/2}$	31459.6818	0.0146
$^4G_{9/2}$	31464.0582	0.0123
$^4P_{5/2}$	36202.1405	0.0019
$^4P_{3/2}$	36239.4964	0.0083
$^4P_{1/2}$	36282.2951	0.0000
$^4D_{7/2}$	39196.6564	0.0224
$^4D_{1/2}$	39237.7276	0.0000
$^4D_{3/2}$	39270.5036	0.0019
$^4D_{5/2}$	39278.9995	0.0129
$^2I_{11/2}$	44783.1032	0.0084
$^2I_{13/2}$	44814.8886	0.0079
$^2D_{5/2}$	50522.3990	0.0145
$^2D_{3/2}$	50910.4211	0.0071
$^2F_{7/2}$	51867.4098	0.0064
$^2F_{5/2}$	52331.6747	0.0103
$^4F_{9/2}$	52866.8654	0.0145
$^4F_{7/2}$	52893.5350	0.0029
$^4F_{5/2}$	52954.4326	0.0068
$^4F_{3/2}$	52985.2751	0.0028
$^2H_{9/2}$	55105.2959	0.0094
$^2H_{11/2}$	55229.8639	0.0134
$^2G_{7/2}$	57007.4534	0.0263
$^2G_{9/2}$	57113.5510	0.0286
$^2F_{5/2}$	61419.4974	0.0244
$^2F_{7/2}$	61431.1287	0.0285
$^2S_{1/2}$	68052.1776	0.0000
$^2D_{3/2}$	75102.3979	0.0108
$^2D_{5/2}$	75125.7734	0.0135
$^2G_{9/2}$	82852.9409	0.0040
$^2G_{7/2}$	82862.4413	0.0048
$^2P_{3/2}$	101646.5608	0.0086
$^2P_{1/2}$	101670.1160	0.0000
$^2D_{5/2}$	109604.8237	0.0131
$^2D_{3/2}$	109623.7798	0.0038

Δ is the deviation from perfect degeneracy (all energies in cm^{-1}).

quartet case. In this basis, the Hamiltonian matrix with the conventional and the spin-orbit Hamiltonian operators has been set up and diagonalized (spin-orbit CI), see **Table 3**.

Again, we find all J components as expected with nearly perfect degeneracies. As annotated above, we

Table 3
States originating from $4p^3$ occupation in the arsenic atom, as computed with the new codes in spin-orbit CI

State	Energy	Δ
$^4S_{3/2}$	0.0000	0.0001
$^2D_{3/2}$	12700.0553	0.0026
$^2D_{5/2}$	12947.3454	0.0022
$^2P_{1/2}$	19613.6062	0.0000
$^2P_{3/2}$	19975.4884	0.0011

Δ is the deviation from perfect degeneracy (all energies in cm^{-1}).

3.1. ERZEUGUNG DER SPINKOPPLUNGEN

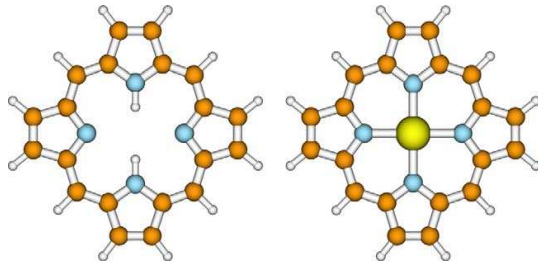


Fig. 1. Porphyrin and Zn-porphyrin as an example of a metallo-porphyrin.

do not compare our computed energies to experimental data.

Spin-free excitation energies suffer from the small reference space and the limited number of correlated electrons. In order to describe spin-orbit coupling properly, one should include excitations from the 2p orbitals, too.

5.2. Timing: Porphyrins

In order to prove the efficiency of the **SPOCK** codes, we calculated the spin-orbit matrix elements in porphy-

rin molecules containing a central metal atom. We have calculated the parent molecule without a central atom, and the metallo-porphyrins with Ga^{3+} , Mg^{2+} , and Zn^{2+} central ions, see Fig. 1.

The TZVP basis sets of the **TURBOMOLE** basis set library have been used throughout. All calculations have been performed in the D_{2h} symmetry group. We have optimized the geometries in a BH-LYP density functional calculation [27]. The succeeding CI calculations have been performed with the DFT part of the DFT/MRCI code. We have calculated the four lowest lying triplet and singlet states in every symmetry (48 states in total). The B_{2u} and B_{3u} singlet states (corresponding to the E_u states in the metallo-porphyrins) are the spectroscopically most relevant ones, constituting the $Q_{x/y}$ and Soret bands. Excitation energies for the $Q_{x/y}$ and Soret bands (singlets) and for the two lowest lying triplet states are given in Table 4.

We see that the computed energies are in very good agreement with experimental data as well as with other calculations.

Subsequently, all 576 symmetry-allowed spin-orbit matrix elements have been computed. We find that all matrix elements with the $Q_{x/y}$ and Soret states are very small (well below 1 cm^{-1}).

Table 4
Electronic excitation energies in porphyrins in comparison to experimental and CASPT2 data

Metal	Band	DFT/MRCI	CASPT2	Experiment
–	Q_x	2.01	1.63 [28]	1.98 [29]
	Q_y	2.42	2.11 [28]	2.42 [29]
	Soret	3.17/3.25	3.12/3.42 [28]	3.33 [29]
	T_1	1.85		
	T_2	2.07		
Mg^{2+}	Q_x/Q_y	2.21	1.78 [30]	2.14 [31], 2.07 [32]
	Soret	3.27	2.65 [30]	3.18 [31], 3.05 [32]
	T_1	2.06	1.55 [30]	(1.7, 1.6)
	T_2	2.14	1.79 [30]	
Zn^{2+}	Q_x/Q_y	2.24		2.21 [31]
	Soret	3.29		3.04 [31]
	T_1	2.12		
	T_2	2.16		
Ga^{3+}	Q_x/Q_y	2.29		
	Soret	3.41		
	T_1	2.10		
	T_2	2.31		

Table 5
Calculated matrix elements and timings (t) in various porphyrins

Central atom	Singlets		Triplets		$t(\text{SPOCK})$	$\langle S_1 \hat{H}_{\text{SO}} T_1 \rangle$
	#CSFs	$t(\text{MRCI})$	#CSFs	$t(\text{MRCI})$		
–	1.0×10^6	22h 16m	1.8×10^6	32h 20m	3h 34m	0.05
Mg^{2+}	1.1×10^6	25h 21m	1.8×10^6	23h 40m	5h 12m	0.50
Zn^{2+}	1.3×10^6	32h 19m	2.2×10^6	34h 05m	6h 12m	0.92
Ga^{3+}	1.0×10^6	20h 23m	1.6×10^6	24h 02m	4h 11m	0.04

The number of CSFs is per symmetry, spin-orbit matrix elements are given in cm^{-1} . The time for matrix element calculation is for all 576 matrix elements.

3. METHODENENTWICKLUNG UND IMPLEMENTIERUNG

The computation timings are on a Pentium IV Xeon (2.4 GHz) under the Linux operating system, see Table 5.

The computation time for all matrix elements takes roughly 10% of the computation time of the CI step. Therefore we conclude that, once the CI is done, computation of the spin-orbit matrix elements is not quite free, but available at very low cost.

6. Discussion

Inspection of the coupling matrices reveals that a large number of entries are zero, some matrices are even diagonal or close to diagonal. In the symmetric and unitary group approaches, these properties are identified and exploited. Presently, we do not have a systematic way for doing so, which is the main disadvantage of our procedure. We overcome this problem by storing only non-zero values. On the other hand, our approach does not suffer any penalties from a selection procedure and the size of the internal space is not restricted at all. Both of these requirements are not fulfilled by GUGA approaches, for which a large internal space may become a severe bottleneck and an individual selection procedure destroys the efficiency of the loops.

SGA approaches are able to deal with these problems and are superior to our results in the sense of exploitation of non-coupling blocks. On the other hand, our method is conceptually very simple and is the fastest and easiest way to extend the DFT/MRCI codes to include spin-orbit coupling.

Acknowledgement

We cordially thank S. Grimme and M. Waletzke for many helpful discussions. Financial support by the “Deutsche Forschungsgemeinschaft” through research project “Ma 1051/5-1” is gratefully acknowledged.

Appendix A. Relations between the subcases

For the evaluation of the relations between the subcases $A1-A4$ and $B1-B4$, one must take a detailed look at what happens to the individual electrons inside a determinant.

A.1. Unit or \hat{s}_0 spin operator

The spin of the electron that is excited from one orbital to another is conserved. The effects of the different excitation subcases on the determinants when exciting an α or β electron are as follows:

$$\begin{array}{cccc}
 & A1\alpha & A1\beta & A2\alpha & A2\beta \\
 P1 & \begin{bmatrix} \alpha & 0 \\ 0 & \alpha \end{bmatrix} & \begin{bmatrix} \beta & 0 \\ 0 & \beta \end{bmatrix} & \begin{bmatrix} 0 & \alpha \\ \alpha & 0 \end{bmatrix} & \begin{bmatrix} 0 & \beta \\ \beta & 0 \end{bmatrix} \\
 & 0 & 0 & 0 & 0 \\
 & A3\alpha & A3\beta & A4\alpha & A4\beta \\
 P1 & \begin{bmatrix} (\alpha\beta) & \beta \\ \beta & (\alpha\beta) \end{bmatrix} & \begin{bmatrix} (\alpha\beta) & \alpha \\ \alpha & (\alpha\beta) \end{bmatrix} & \begin{bmatrix} \beta & (\alpha\beta) \\ (\alpha\beta) & \beta \end{bmatrix} & \begin{bmatrix} \alpha & (\alpha\beta) \\ (\alpha\beta) & \alpha \end{bmatrix} \\
 & 1 & 1 & 1 & 1 \\
 & B1\alpha & B1\beta & B2\alpha & B2\beta \\
 P1 & \begin{bmatrix} \alpha & \beta \\ 0 & (\alpha\beta) \end{bmatrix} & \begin{bmatrix} \beta & \alpha \\ 0 & (\alpha\beta) \end{bmatrix} & \begin{bmatrix} \beta & \alpha \\ (\alpha\beta) & 0 \end{bmatrix} & \begin{bmatrix} \alpha & \beta \\ (\alpha\beta) & 0 \end{bmatrix} \\
 & 0 & 1 & 1 & 0 \\
 & B3\alpha & B3\beta & B4\alpha & B4\beta \\
 P1 & \begin{bmatrix} (\alpha\beta) & 0 \\ \beta & \alpha \end{bmatrix} & \begin{bmatrix} (\alpha\beta) & 0 \\ \alpha & \beta \end{bmatrix} & \begin{bmatrix} 0 & (\alpha\beta) \\ \alpha & \beta \end{bmatrix} & \begin{bmatrix} 0 & (\alpha\beta) \\ \beta & \alpha \end{bmatrix} \\
 & 1 & 0 & 0 & 1
 \end{array}$$

Here we see the meaning of the number of permutations $P1$. In case $A3\alpha$ for example, the α electron bypasses the β electron which resides in the same initial orbital. This results in one additional permutation, i.e., one additional change of sign.

By thorough inspection of the effects of the excitations on an individual determinant, the relations among the subcases may be obtained. Let us begin with the spin-free case (unit spin operator):

Clearly, case $A2$ is the transpose of case $A1$, and case $A4$ is the transpose of case $A3$. The effect on the open-shell spin part of a specific determinant is the same for cases $A1$ and $A4$. In both cases, an open-shell electron is annihilated at the same position i and re-inserted at the same position j , conserving its spin. The only difference is one additional permutation, resulting in a factor of (-1) . The same is true for cases $A2$ and $A3$. In the B subcases, we find again two simple transpositions, namely $B4 = B1^T$ and $B3 = B2^T$. The other relations are simply $B1 = B2$ and $B3 = B4$. This is because the effect on a determinant is the same for cases $B1\alpha$ and $B2\beta$ (and $B1\beta$ and $B2\alpha$) corresponding to no (one) additional permutation.

In case of the \hat{s}_0 operator, cases $A1$ and $A2$ (and $A3$ and $A4$) are again related by a transposition. The relation between cases $A1$ and $A4$ is more complicated: the \hat{s}_0 operator gives an additional factor of (-1) , every time it acts on a β electron. Now note that case $A1\alpha$ corresponds to case $A4\beta$ from the point of view of the effects on a determinant. For the unit-spin operator this is unimportant whereas here, we have an additional change of sign. For the \hat{s}_0 operator, we therefore have: case $A1 = A4$ and case $A2 = A3$. The minus signs appearing in the relations of the spin-free cases are can-

3.1. ERZEUGUNG DER SPINKOPPLUNGEN

celled by an additional change of sign. In the B subcases, we find in a similar way: $B4 = B1^T$, $B3 = B2^T$, and $B2 = (-1) \cdot B1$. Again, the transpositions are obvious. The additional minus sign for the transition from case $B1$ to case $B2$ is again caused by the \hat{s}_0 operator operating on β electrons. It arises in the same way as in the A cases.

A.2. \hat{s}_{+1} operator

When the \hat{s}_{+1} operator is applied during the excitation, we have to remove a β electron and re-insert it with α spin. Therefore the relations are less complicated. The effects of the individual excitation cases are:

$$\begin{array}{ccccc} & A1 & A2 & A3 & A4 \\ P1 & \begin{bmatrix} \beta & 0 \\ 0 & \alpha \end{bmatrix} & \begin{bmatrix} 0 & \beta \\ \alpha & 0 \end{bmatrix} & \begin{bmatrix} (\alpha\beta) & \beta \\ \alpha & (\alpha\beta) \end{bmatrix} & \begin{bmatrix} \beta & (\alpha\beta) \\ (\alpha\beta) & \alpha \end{bmatrix} \\ & 0 & 0 & 0 & 2 \end{array}$$

$$\begin{array}{ccccc} & B1 & B2 & B3 & B4 \\ P1 & \begin{bmatrix} \beta & \beta \\ 0 & (\alpha\beta) \end{bmatrix} & \begin{bmatrix} \beta & \beta \\ (\alpha\beta) & 0 \end{bmatrix} & \begin{bmatrix} (\alpha\beta) & 0 \\ \alpha & \alpha \end{bmatrix} & \begin{bmatrix} 0 & (\alpha\beta) \\ \alpha & \alpha \end{bmatrix} \\ & 0 & 1 & 0 & 1 \end{array}$$

Here, the obvious relations are: case $A4$ equals case $A1$, case $A3$ equals case $A2$, case $B2$ is (-1) times case $B1$ (the minus sign being caused by the additional permutation), and case $B4$ is (-1) times case $B3$.

The remaining subcases cannot be eliminated by a transposition. This is seen best by regarding the transpose of case $A1$ which does not equal case $A2$:

$$\begin{bmatrix} 0 & \alpha \\ \beta & 0 \end{bmatrix}$$

Instead, this is one of the cases that would occur for the \hat{s}_{-1} operator. The same is true for the relation of $A3-A4$, $B1-B4$ and $B2-B3$. Thus we find again that additional η matrices for the \hat{s}_{-1} operator are not required.

References

- [1] M. Sjøvoll, O. Gropen, J. Olsen, Theoret. Chim. Acta 97 (1997) 301.
- [2] T. Fleig, J. Olsen, L. Visscher, J. Chem. Phys. 119 (2003) 2963.
- [3] R.W. Wetmore, G.A. Segal, Chem. Phys. Lett. 36 (1975) 478.
- [4] G.A. Segal, R.W. Wetmore, K. Wolf, Chem. Phys. 30 (1978) 269.
- [5] R.J. Buenker, R.A. Phillips, J. Mol. Spectrosc. (Theochem) 123 (1985) 291.
- [6] B. Liu, M. Yoshomine, J. Chem. Phys. 74 (1981) 612.
- [7] R. Pauncz, The Symmetric Group in Quantum Chemistry, CRC Press, Boca Raton, FL, 1995.
- [8] R. Pauncz, The Unitary Group in Quantum Chemistry, Elsevier, Amsterdam, 1986.
- [9] B.A. Heß, Habilitation Thesis, Universität Gesamthochschule Wuppertal, 1986.
- [10] D.R. Yarkony, J. Chem. Phys. 84 (1986) 2075.
- [11] S. Yabushita, Z. Zhang, R.M. Pitzer, J. Phys. Chem. A 103 (1999) 5791.
- [12] N. Flocke, M. Barysz, J. Karowski, G.H.F. Diercksen, Int. J. Quantum Chem. 61 (1997) 1.
- [13] N. Flocke, M. Barysz, J. Karowski, G.H.F. Diercksen, Int. J. Quantum Chem. 61 (1997) 11.
- [14] N. Flocke, M. Barysz, J. Karowski, G.H.F. Diercksen, Int. J. Quantum Chem. 61 (1997) 21.
- [15] N. Flocke, Int. J. Quantum Chem. 61 (1997) 747.
- [16] S. Grimme, M. Waletzke, J. Chem. Phys. 111 (1999) 5645.
- [17] J. Tatchen, C. Marian, Chem. Phys. Lett. 313 (1999) 351.
- [18] B.A. Heß, C.M. Marian, U. Wahlgren, O. Gropen, Chem. Phys. Lett. 251 (1996) 365.
- [19] AMFI is an atomic spin-orbit integral program written by B. Schimmelpfennig, University of Stockholm, 1996.
- [20] R. McWeeny, J. Chem. Phys. 42 (1965) 1717.
- [21] E.P. Wigner, Group Theory and Its Application to Quantum Mechanics of Atomic Spectra, Academic Press, New York, 1959.
- [22] R. Pauncz, Spin Eigenfunctions, Construction and Use, Plenum Press, New York, 1979.
- [23] M. Kleinschmidt, J. Tatchen, C.C. Marian, J. Comput. Chem. 23 (2002) 824.
- [24] A. Schäfer, C. Huber, R. Ahlrichs, J. Chem. Phys. 100 (1994) 5829.
- [25] K. Andersson, M. Barysz, A. Bernhardsson, M.R.A. Blomberg, D.L. Cooper, M.P. Fülscher, C. de Graaf, B.A. Heß, G. Karlström, R. Lindh, P.-Å. Malmqvist, T. Nakajima, P. Neogrdy, J. Olsen, B.O. Roos, B. Schimmelpfennig, M. Schütz, L. Seijo, L. Serrano-Andrés, P.E.M. Siegbahn, J. Stårling, T. Thorsteinsson, V. Veryazov, P.-O. Widmark, MOLCAS Version 5.4, Lund University, Sweden, 2002.
- [26] C.E. Moore, Atomic Energy Levels, Circular of the National Bureau of Standards 467, 1958.
- [27] A.D. Becke, J. Chem. Phys. 98 (1993) 1372.
- [28] L. Serrano-Andrés, M. Merchán, M. Rubio, B.O. Roos, Chem. Phys. Lett. 295 (1998) 195.
- [29] L. Edwards, D.H. Dolphin, M. Gouterman, A.D. Adler, J. Mol. Spectrosc. 38 (1971) 16.
- [30] M. Rubio, B.O. Roos, L. Serrano-Andrés, M. Merchán, J. Chem. Phys. 110 (1999) 7202.
- [31] L. Edwards, D.H. Dolphin, M. Gouterman, J. Mol. Spectrosc. 35 (1970) 70.
- [32] G.D. Dorrough, J.R. Miller, F.M. Huennekens, J. Am. Chem. Soc. 73 (1951) 4315.

3.1.4 Erweiterung auf den Zweielektronen-Spin-Bahn-Operator

Der volle Spin-Bahn-Operator ist ein Zweielektronenoperator. Auch für diesen kann die Anwendbarkeit des Ansatzes von Wetmore und Segal gezeigt werden.

Jeder Zweielektronenoperator lässt sich im Formalismus der zweiten Quantisierung schreiben:

$$\hat{O} = \frac{1}{2} \sum_{ijkl} O_{ijkl} \hat{a}_i^\dagger \hat{a}_k^\dagger \hat{a}_l \hat{a}_j \quad (3.14)$$

mit

$$O_{ijkl} = \langle i(1)k(2) | \hat{O} | j(1)l(2) \rangle \quad (3.15)$$

Das Matrixelement des vollen Breit-Pauli-Spin-Bahn-Operators über die Spinorbitale i, j, k und l ist also:

$$H_{ijkl}^{SO} = \langle i(1)k(2) | \hat{H}_{SO} | j(1)l(2) \rangle \quad (3.16)$$

$$= C * \left\langle i(1)k(2) \left| \left(\frac{\mathbf{r}_{12}}{r_{12}^3} \times \mathbf{p}(1) \right) (\mathbf{s}(1) + 2\mathbf{s}(2)) \right| j(1)l(2) \right\rangle \quad (3.17)$$

mit $C = \frac{e^2 \hbar}{2m^2 c^2}$. Setzt man statt der Spinorbitale die räumlichen Orbitale r, s, t und u mit den Spins ρ, σ, τ und v ein, so ergibt sich:

$$\langle r(1)\rho(1)t(2)\tau(2) | H_{SO} | s(1)\sigma(1)u(2)v(2) \rangle \quad (3.18)$$

$$= C * \left\langle r(1)\rho(1)t(2)\tau(2) \left| \left(\frac{\mathbf{r}_{12}}{r_{12}^3} \times \mathbf{p}(1) \right) (\mathbf{s}(1) + 2\mathbf{s}(2)) \right| s(1)\sigma(1)u(2)v(2) \right\rangle \quad (3.19)$$

$$= C * \left\langle r(1)t(2) \left| \left(\frac{\mathbf{r}_{12}}{r_{12}^3} \times \mathbf{p}(1) \right) \right| s(1)u(2) \right\rangle \langle \rho(1)\tau(2) | (\mathbf{s}(1) + 2\mathbf{s}(2)) | \sigma(1)v(2) \rangle \quad (3.20)$$

$$= L_{rstu}^{SO} S_{\rho\sigma\tau v} \quad (3.21)$$

mit

$$L_{rstu}^{SO} = C * \left\langle rt \left| \left(\frac{\mathbf{r}_{12}}{r_{12}^3} \times \mathbf{p}(1) \right) \right| su \right\rangle \quad (3.22)$$

$$S_{\rho\sigma\tau v} = \langle \rho\tau | (\mathbf{s}(1) + 2\mathbf{s}(2)) | \sigma v \rangle \quad (3.23)$$

Hiermit lässt sich der Spin-Bahn-Operator in zweiter Quantisierung formulieren:

$$\hat{H}_{SO} = \sum_{rstu} L_{rstu}^{SO} \left(\sum_{\rho\sigma\tau v} S_{\rho\sigma\tau v} \hat{a}_{r\rho}^\dagger \hat{a}_{t\tau}^\dagger \hat{a}_{u\nu} \hat{a}_{s\sigma} \right) \quad (3.24)$$

Die Vernichter- und Erzeugeroperatoren müssen nun noch in die richtige Reihenfolge gebracht werden. Hierbei hilft die Kommutatorrelation

$$[\hat{a}_i, \hat{a}_j^\dagger \hat{a}_k] = \delta_{ij} \hat{a}_k \quad (3.25)$$

3.1. ERZEUGUNG DER SPINKOPPLUNGEN

bzw. umgeformt und mit den hier gebrauchten Indizes:

$$\hat{a}_{t\tau}^\dagger \hat{a}_{uv} \hat{a}_{s\sigma} = \hat{a}_{s\sigma} \hat{a}_{t\tau}^\dagger \hat{a}_{uv} - \delta_{st} \delta_{\sigma\tau} \hat{a}_{uv} \quad (3.26)$$

und eingesetzt:

$$\hat{H}_{SO} = \sum_{rstu} L_{rstu}^{SO} \sum_{\rho\sigma\tau\nu} S_{\rho\sigma\tau\nu} (\hat{a}_{r\rho}^\dagger \hat{a}_{s\sigma} \hat{a}_{t\tau}^\dagger \hat{a}_{uv} - \delta_{st} \delta_{\sigma\tau} \hat{a}_{r\rho}^\dagger \hat{a}_{uv}) \quad (3.27)$$

Der Spinteil des Operators lässt sich auch teilweise auflösen:

$$S_{\rho\sigma\tau\nu} = \langle \rho\tau | s(1) + 2s(2) | \sigma\nu \rangle = \delta_{\tau\nu} \langle \rho | s | \sigma \rangle + 2\delta_{\rho\sigma} \langle \tau | s | \nu \rangle \quad (3.28)$$

womit sich der gesamte Operator weiterhin ergibt zu

$$\begin{aligned} \hat{H}_{SO} &= \sum_{rstu} L_{rstu}^{SO} \sum_{\rho\sigma\tau\nu} (\delta_{\tau\nu} \langle \rho | s | \sigma \rangle + 2\delta_{\rho\sigma} \langle \tau | s | \nu \rangle) \\ &\quad \cdot (\hat{a}_{r\rho}^\dagger \hat{a}_{s\sigma} \hat{a}_{t\tau}^\dagger \hat{a}_{uv} - \delta_{st} \delta_{\sigma\tau} \hat{a}_{r\rho}^\dagger \hat{a}_{uv}) \end{aligned} \quad (3.29)$$

$$\begin{aligned} &= \sum_{rstu} L_{rstu}^{SO} \sum_{\rho\sigma\tau\nu} \delta_{\tau\nu} \langle \rho | s | \sigma \rangle \hat{a}_{r\rho}^\dagger \hat{a}_{s\sigma} \hat{a}_{t\tau}^\dagger \hat{a}_{uv} \\ &\quad + 2 \sum_{rstu} L_{rstu}^{SO} \sum_{\rho\sigma\tau\nu} \delta_{\rho\sigma} \langle \tau | s | \nu \rangle \hat{a}_{r\rho}^\dagger \hat{a}_{s\sigma} \hat{a}_{t\tau}^\dagger \hat{a}_{uv} \\ &\quad - \sum_{rstu} L_{rstu}^{SO} \sum_{\rho\sigma\tau\nu} \delta_{\tau\nu} \langle \rho | s | \sigma \rangle \delta_{st} \delta_{\sigma\tau} \hat{a}_{r\rho}^\dagger \hat{a}_{uv} \\ &\quad - 2 \sum_{rstu} L_{rstu}^{SO} \sum_{\rho\sigma\tau\nu} \delta_{\rho\sigma} \langle \tau | s | \nu \rangle \delta_{st} \delta_{\sigma\tau} \hat{a}_{r\rho}^\dagger \hat{a}_{uv} \end{aligned} \quad (3.30)$$

$$\begin{aligned} &= \sum_{rstu} L_{rstu}^{SO} \sum_{\rho\sigma} \langle \rho | s | \sigma \rangle \hat{a}_{r\rho}^\dagger \hat{a}_{s\sigma} \sum_{\tau} \hat{a}_{t\tau}^\dagger \hat{a}_{u\tau} \\ &\quad + 2 \sum_{rstu} L_{rstu}^{SO} \sum_{\rho} \hat{a}_{r\rho}^\dagger \hat{a}_{s\rho} \sum_{\tau\nu} \langle \tau | s | \nu \rangle \hat{a}_{t\tau}^\dagger \hat{a}_{uv} \\ &\quad - \sum_{rsu} L_{rsu}^{SO} \sum_{\rho\nu} \langle \rho | s | \nu \rangle \hat{a}_{r\rho}^\dagger \hat{a}_{uv} \\ &\quad - 2 \sum_{rsu} L_{rsu}^{SO} \sum_{\rho\nu} \langle \rho | s | \nu \rangle \hat{a}_{r\rho}^\dagger \hat{a}_{uv} \end{aligned} \quad (3.31)$$

Nach Einsatz der spinfreien Anregungsoperatoren $\hat{E}_{rs} = \sum_{\sigma} \hat{a}_{r\sigma}^\dagger \hat{a}_{s\sigma}$ und Zusammenfassen der letzten beiden Terme:

$$\hat{H}_{SO} = \sum_{rstu} L_{rstu}^{SO} \sum_{\rho\sigma} \langle \rho | s | \sigma \rangle \hat{a}_{r\rho}^\dagger \hat{a}_{s\sigma} \hat{E}_{tu} \quad (3.32)$$

$$+ 2 \sum_{rstu} L_{rstu}^{SO} \hat{E}_{rs} \sum_{\tau\nu} \langle \tau | s | \nu \rangle \hat{a}_{t\tau}^\dagger \hat{a}_{uv} \quad (3.33)$$

$$- 3 \sum_{rsu} L_{rsu}^{SO} \sum_{\rho\nu} \langle \rho | s | \nu \rangle \hat{a}_{r\rho}^\dagger \hat{a}_{uv} \quad (3.34)$$

Für diesen Operator ist nun zu prüfen, ob er sich mit dem Anregungsmuster-Ansatz bearbeiten lässt. Der letzte Term (3.34) ist ein Einelektronenoperator und demzufolge problemlos analog zum Einelektronen-Spin-Bahn-Operator zu behandeln.

Von den beiden Zweilektronentermen (3.32) und (3.33) sei nun exemplarisch der erste herausgegriffen, und ein Matrixelement zwischen zwei CSFs $\langle S', \omega', w' |$ und $|S, \omega, w\rangle$ (mit $M_S = S$ und $M'_S = S'$), die sich um eine Doppelanregung $b \rightarrow a$ und $d \rightarrow c$ unterscheiden, gebildet. Dabei bleibt nur dann ein nicht verschwindendes Matrixelement übrig, wenn die Vernichter, die bisher noch in einer Summe über alle Orbitale laufen, auf eines der Orbitale b oder d und gleichzeitig die Erzeuger auf eines der Orbitale a oder c treffen. So erhält man also eine Summe über vier Terme, in denen die vier möglichen Permutationen der Erzeuger und Vernichter auftreten.

$$\left\langle S', \omega', w' \left| \sum_{rstu} L_{rstu}^{SO} \sum_{\rho\sigma} \langle \rho | s | \sigma \rangle \hat{a}_{r\rho}^\dagger \hat{a}_{s\sigma} \hat{E}_{tu} \right| S, \omega, w \right\rangle \quad (3.35)$$

$$= L_{abcd}^{SO} \left\langle S', \omega', w' \left| \sum_{\rho\sigma} \langle \rho | s | \sigma \rangle \hat{a}_{a\rho}^\dagger \hat{a}_{b\sigma} \hat{E}_{cd} \right| S, \omega, w \right\rangle \quad (3.36)$$

$$+ L_{adcb}^{SO} \left\langle S', \omega', w' \left| \sum_{\rho\sigma} \langle \rho | s | \sigma \rangle \hat{a}_{a\rho}^\dagger \hat{a}_{d\sigma} \hat{E}_{cb} \right| S, \omega, w \right\rangle \quad (3.37)$$

$$+ L_{cdab}^{SO} \left\langle S', \omega', w' \left| \sum_{\rho\sigma} \langle \rho | s | \sigma \rangle \hat{a}_{c\rho}^\dagger \hat{a}_{d\sigma} \hat{E}_{ab} \right| S, \omega, w \right\rangle \quad (3.38)$$

$$+ L_{cbad}^{SO} \left\langle S', \omega', w' \left| \sum_{\rho\sigma} \langle \rho | s | \sigma \rangle \hat{a}_{c\rho}^\dagger \hat{a}_{b\sigma} \hat{E}_{ad} \right| S, \omega, w \right\rangle \quad (3.39)$$

Diese vier Terme haben jeweils den gleichen Aufbau: Ein 4-Index-Spin-Bahn-Integral wird multipliziert mit einem Matrixelement über die beiden CSFs mit einem spinfreien (\hat{E}_{cd}), und einem spinabhängigen Anregungsoperator ($\sum_{\rho\sigma} \langle \rho | s | \sigma \rangle \hat{a}_{a\rho}^\dagger \hat{a}_{b\sigma}$). Eine Trennung des Matrixelements in den physikalischen, vom konkreten Problem abhängigen Teil, und einen allgemeinen, nur von der Art der CSFs abhängigen Teil ist also schon fast gelungen. Noch hängt das verbliebene Matrixelement über die CSFs von der Problemgröße, also von der Zahl der Basisfunktionen ab.

Nach der Anwendung des ersten Anregungsoperators (\hat{E}_{cd}) ist eine Zwischenkonfiguration w'' erreicht. An dieser Stelle kann also eine Einheit als Summe über alle CSFs dieser Konfiguration eingeschoben werden, hier beispielhaft für den ersten Summanden:

$$L_{abcd}^{SO} \left\langle S', \omega', w' \left| \sum_{\rho\sigma} \langle \rho | s | \sigma \rangle \hat{a}_{a\rho}^\dagger \hat{a}_{b\sigma} \hat{E}_{cd} \right| S, \omega, w \right\rangle \quad (3.40)$$

$$= L_{abcd}^{SO} \left\langle S', \omega', w' \left| \underbrace{\sum_{\rho\sigma} \langle \rho | s | \sigma \rangle \hat{a}_{a\rho}^\dagger \hat{a}_{b\sigma}}_{=1} \sum_{\omega''} |S, \omega'', w''\rangle \langle S, \omega'', w''| \hat{E}_{cd} \right| S, \omega, w \right\rangle \quad (3.41)$$

$$= L_{abcd}^{SO} \sum_{\omega''} \left\langle S', \omega', w' \left| \sum_{\rho\sigma} \langle \rho | s | \sigma \rangle \hat{a}_{a\rho}^\dagger \hat{a}_{b\sigma} \right| S, \omega'', w'' \right\rangle \langle S, \omega'', w'' | \hat{E}_{cd} | S, \omega, w \rangle \quad (3.42)$$

Damit zerfällt das Matrixelement in eine Summe über Produkte von Matrixelementen eines spinabhängigen und eines spinfreien Einelektronenoperators. Diese einzelnen Faktoren

3.1. ERZEUGUNG DER SPINKOPPLUNGEN

sind die gleichen, wie sie schon für den spinfreien Fall, bzw. für den spinabhängigen Ein-elektronenfall abgeleitet wurden. Dieser beispielhaft herausgegriffene Teil des Spin-Bahn-Matrixelements ergibt sich also als Produkt aus einem Spin-Bahn-Integral, einem Eintrag eines spinabhängigen Kopplungsfeldes und einem Eintrag eines spinfreien Kopplungsfeldes. Analog lassen sich alle anderen Teile des gesamten Matrixelements verarbeiten.

Damit ist grundsätzlich gezeigt, dass die Behandlung der Spinkopplung über Kopp lungsmuster auch für den Fall des vollen Spin-Bahn-Operators analog zum spinfreien An satz von Wetmore und Segal möglich ist. Für eine Implementierung müssten zunächst noch alle Fälle ausgearbeitet werden. Dabei ergeben sich Vereinfachungen durch Symmetrien in den Spin-Bahn-Integralen. Da die Verwendung des vollen Spin-Bahn-Operators in SPOCK nicht angestrebt wird, wurde die Ausarbeitung jedoch abgebrochen. Aufbauend auf diese Vorarbeiten wird derzeit von Natalie Gilka im Rahmen ihrer Dissertation eine Erweiterung auf den Spin-Spin-Operator vorgenommen. Im Spin-Spin-Operator treten Produkte von Spinoperatoren auf. Sie konnte die Anwendbarkeit der Kopplungsfelder auch für diesen Fall zeigen.[33]

3.2 Spin-Bahn-Kopplung von DFT/MRCI Wellenfunktionen

Die Berechnung der Spin-Bahn-Matrixelemente über konvergierte, spinfreie DFT/MRCI-Wellenfunktionen, also der störungstheoretische Teil SPOCK.PT des SPOCK-Pakets ist in der Veröffentlichung „Spin-Orbit Coupling of DFT/MRCI Wavefunctions: Method, Test Calculations, and Application to Thiophene“ („Spin-Bahn-Kopplung von DFT/MRCI-Wellenfunktionen: Methode, Testrechnungen und Anwendung auf Thiophen“) beschrieben[34].

3.2.1 Programmtechnischer Teil

Die Implementierung basiert auf den Modulen zur Berechnung der Einteilchendichtematrix aus dem DFT/MRCI. In diesen Routinen war bereits die Kopplung von Einfachanregungen zwischen zwei CI-Wellenfunktionen unterschiedlicher Symmetrie aber gleichen Spins angelegt. Diese wurden auf die gleichzeitige Behandlung verschiedener Multiplizitäten erweitert, und zur Berechnung der Matrixelemente statt der Dichtematrix umgeschrieben. Die Programmlogik des DFT/MRCI arbeitet nach der zweiten Quantisierung, also mit Vernichter- und Erzeugeroperatoren. Die dabei intermediär auftretenden Räume mit Ein- und Zweifachlochkonfigurationen, sowie die zugehörigen Ein- und Zweifacherzeuger werden in direkter Abhängigkeit von den Referenzkonfigurationen ermittelt. Insbesondere werden die Molekülorbitale (MOs) in drei Gruppen unterteilt:

1. doppelt besetzte Orbitale, die in allen Referenzen doppelt besetzt sind,
2. interne Orbitale, die in den Referenzen variabel besetzt sind sowie,
3. externe Orbitale, die in allen Referenzen leer sind.

Die Sortierung der Orbitale richtet sich nach dieser Einteilung: jeweils in energetisch aufsteigender Reihenfolge kommen, ohne Berücksichtigung der Symmetrie, zunächst alle doppelt besetzten Orbitale, nachfolgend die internen und schließlich die externen Orbitale. Für alle Zustände gleicher Multiplizität wird bereits im ursprünglichen DFT/MRCI ein gemeinsamer Referenzraum benutzt: Konfigurationen für den CI-Raum einer Symmetrie werden nicht nur aus Referenzen dieser Symmetrie erzeugt, sondern aus Referenzen aller Symmetrien. Dies hat den Vorteil, dass bei einem Wechsel der Punktgruppe der Referenzraum gleich bleibt, und somit auch der für einen Zustand zur Verfügung stehende CI-Raum gleich bleibt.

Alle Zustände gleicher Multiplizität haben also bereits eine übereinstimmende Sortierung der Orbitale. Um auch bei der Berechnung von Matrixelementen zwischen Zuständen unterschiedlicher Multiplizität eine konsistente Orbitalsortierung zu erhalten, wurde das DFT/MRCI so abgeändert, dass beim Start einer Rechnung auch der Referenzraum anderer Multiplizitäten zusätzlich eingelesen werden kann (Parameter `$mergerefs`). Dabei werden Orbitale, die im „eigenen“ Referenzraum noch extern oder doppelt besetzt sind, im „fremden“ Referenzraum jedoch intern wären, in den internen Raum aufgenommen. Durch dieses Verfahren ist eine konsistente Orbitalsortierung in den CI-Räumen aller Spinsymmetrien gewährleistet. In typischen Rechnungen mit großen Referenzräumen sind etwa zwei bis fünf von mehreren hundert Orbitalen betroffen.

Das Programm zur Berechnung der Matrixelemente, SPOCK.PT, bearbeitet nacheinander alle auf Festplatte vorgefundenen CI-Vektoren. Hier per Eingabe eine Einschränkung

treffen zu können, erschien nicht nötig, insbesondere da die Rechenzeit für die Matrixelemente im Vergleich mit der Rechenzeit für das DFT/MRCI klein ist ($\approx 20\%$). Für jedes Paar von Spinsymmetrien werden jeweils alle Wurzeln gleichzeitig bearbeitet. Theoretisch könnte dieses Vorgehen zu Problemen mit dem zur Verfügung stehenden Hauptspeicher führen. In der Praxis kann dieser Fall jedoch nicht eintreten, da bereits im DFT/MRCI immer alle Vektoren gleichzeitig behandelt werden, und dort zweifach in den Speicher passen müssen. Erst wenn dieser potentielle Engpass im DFT/MRCI beseitigt werden sollte, wird eine entsprechende Anpassung auch im SPOCK.PT nötig werden.

Für die Berechnung der Matrixelemente werden die jeweils benötigten Spinkopplungsfelder aus der Bibliothek geladen oder, falls dort noch nicht vorhanden, neu berechnet und in die Bibliothek gespeichert. Die Spin-Bahn-Integrale werden geladen und auf die DFT/MRCI-Reihenfolge der MOs umsortiert. Dabei wird nochmals geprüft, ob alle einzelnen DFT/MRCI-Rechnungen mit gleicher MO-Sortierung durchgeführt sind. Schließlich werden alle Konfigurationen der beiden beteiligten CI-Räume im Konfigurationsvergleich gegeneinander geprüft. Sofern eine Einfachanregung angetroffen wird, werden die entsprechenden einzelnen Summanden für alle zu den beiden Konfigurationen gehörigen CSFs auf das Matrixelement aufaddiert. Da dies für alle Wurzeln der beiden Spinsymmetrien gleichzeitig geschehen kann, ist der relativ zeitaufwendige Konfigurationsvergleich nur einmal durchzuführen. Zur tiefergehenden Analyse des bearbeiteten Problems können die wichtigsten Beiträge einzelner Konfigurationspaarungen zu den Matrixelementen ausgegeben werden.

Die berechneten Spin-Bahn-Matrixelemente werden mithilfe der *scaled 3j-symbols* zusammen mit den Energien aller Zustände in eine Störungsmatrix eingetragen, die anschließend exakt diagonalisiert wird.

Die Spin-Bahn-Matrixelemente werden zusammen mit Informationen über die Anzahl der Zustände in jeder Spinsymmetrie in der Datei **SOMEs** abgespeichert. Das Speicherformat ist durch Kommentare in dieser Datei selbsterklärend. Diese Datei bildet die Schnittstelle zum Program SOC-QDTP[15], das Eigenschaften wie spinabhängige Dipolübergangsmomente oder g-Tensoren berechnet.

3.2.2 Vergleich HF- und KS-basierter MRCI-Entwicklungen

Die Anwendbarkeit des DFT/MRCI-Ansatzes, also der Einsatz von KS-Orbitalen zur Berechnung von Spin-Bahn-Matrixelementen erscheint natürlich aus theoretischer Sicht zunächst fragwürdig. Anhand von Testrechnungen an zweiatomigen Molekülen wurde im Vergleich mit Rechnungen in HF-Orbitalen diese Anwendbarkeit untersucht. Die gute Übereinstimmung der Resultate zeigt, dass der Ansatz tragfähig ist. Auch die exzellente Leistungsfähigkeit des DFT/MRCI-Ansatzes wird hier nochmals deutlich: Für qualitativ vergleichbare Ergebnisse muss im KS-Fall ein um etwa einen Faktor 20 kleinerer CI-Raum bearbeitet werden.

Pyranthion wurde bereits früher von J. Tatchen untersucht.[35] Dabei wurden die Energien mit dem DFT/MRCI ermittelt, während die Spin-Bahn-Kopplung mit dem alten BNSOC Programm[36] und *mean field* Spin-Bahn-Integralen berechnet wurde. Es diente hier nochmals als Vergleichsfall. Die wichtigsten Spin-Bahn-Matrixelemente wurden mit SPOCK nochmals gerechnet. Die Übereinstimmung ist mit einer Ausnahme sehr gut. Die in einem Fall auftretende Abweichung von $\approx 15\%$ konnte durch Unterschiede in den HF und KS MOs erklärt werden.

Spin-Orbit Coupling of DFT/MRCI Wavefunctions: Method, Test Calculations, and Application to Thiophene

MARTIN KLEINSCHMIDT, JÖRG TATCHEN, CHRISTEL M. MARIAN*

*GMD Research Center for Information Technology,
Scientific Computing and Algorithms Institute (SCAI),
Schloss Birlinghoven, 53754 St. Augustin, Germany*

*Received 7 August 2001; Accepted 20 December 2001
DOI 10.1002/jcc.10064*

Abstract: During the past decade the one-center mean-field approximation has proven to be a very appropriate framework for the accurate description of spin-orbit effects at the correlated all-electron level. Here, a new efficient code, SPOCK, is introduced that calculates spin-orbit matrix elements in the one-center mean-field approximation for multireference CI wave functions. For the first time, the computation of spin-dependent interactions within a Kohn-Sham orbital based CI (DFT/MRCI) scheme¹ is made possible. The latter approach is suitable for large scale systems with up to 100–200 valence electrons. Test calculations are performed on well-known diatomic molecules and the thiocarbonyl pyranthione. Spin-orbit matrix elements show good agreement with their Hartree-Fock orbital based counterparts but are obtained at considerably lower expense, thus demonstrating the power of the method. As an application singlet-triplet couplings in thiophene are investigated that are important for the photophysics and photochemistry. Spin-orbit matrix elements between all $\pi \rightarrow \pi^*$ excited states are found to be small. Considerably larger spin-orbit matrix elements are observed only for cases in which $\pi \rightarrow \sigma^*$ excited configurations are involved.

© 2002 Wiley Periodicals, Inc. *J Comput Chem* 23: 824–833, 2002

Key words: spin-orbit coupling; multireference configuration interaction; Kohn-Sham orbitals; program development; thiophene

Introduction

The reliable quantum chemical evaluation of spin-dependent properties for (excited) electronic states in molecular systems with 100–200 valence electrons requires the inclusion of static and dynamic electron correlation in the wave function determination, as well as an efficient treatment of spin-orbit coupling. Standard *ab initio* packages are not applicable for this purpose. The combined density functional theory/multireference configuration interaction (DFT/MRCI) method by Grimme and Waletzke has proven to yield excellent electronic spectra of organic molecules.¹ Our current approach is an extension of this method to a spin-dependent Hamiltonian.

With the new spin-orbit coupling kit (SPOCK)—described in detail in the following—spin-orbit matrix elements (SOMEs) for DFT/MRCI or conventional Hartree-Fock (HF)/MRCI wave functions can be generated. Key features of the current version are: a fast determination of spin-coupling coefficients between configuration state functions (CSFs) for spin-dependent one-electron operators; use of nonempirical atomic spin-orbit mean-field integrals; and determination of spin-orbit related properties by quasi-degenerate perturbation theory. The application of these techniques and approximations in combination with the efficient determination of

correlated wave functions and electronic energies using the DFT/MRCI approach paves the way for an economical but reliable description of spin-orbit effects in larger organic molecules.

In the first section of this article, we report briefly on the technicalities of the current program and the underlying algorithms. Test calculations show the applicability of the method to DFT/MRCI wave functions and its efficiency compared to a more traditional HF/MRCI treatment. In the last section, as a first application of the SPOCK code, an investigation of multiplet coupling in thiophene is presented.

Methods and Implementation

The Spin-Free DFT/MRCI Method

The idea behind the DFT/MRCI approach by Grimme and Waletzke¹ is to include major parts of dynamic electron correlation

*Present address: Institute of Theoretical Chemistry, Heinrich-Heine-University, Universitätsstr. 1, 40225 Düsseldorf

Correspondence to: C. M. Marian

Contract/grant sponsor: Deutsche Forschungsgemeinschaft

3.2. SPIN-BAHN-KOPPLUNG VON DFT/MRCI WELLENFUNKTIONEN

by DFT, whereas short multireference configuration interaction expansions take account of static correlation effects. To this end, the CSFs in the CI expansion are built up from Kohn-Sham (KS) orbitals. Diagonal elements of the effective DFT/MRCI Hamiltonian are constructed from the corresponding HF-based expression and a DFT specific correction term. All HF orbital energies are replaced by their KS counterparts; Coulomb and exchange integrals are modified by empirical parameters. Double counting of electron correlation is obviated by scaling off-diagonal CI matrix elements with an empirical factor that depends exponentially on the energy difference between the two CSFs. Off-diagonal CI matrix elements between two CSFs with a common spatial part but differing in their spin couplings are calculated exactly. In the effective DFT/CI Hamiltonian, all in all five empirical parameters are employed that have been fitted in extensive test calculations to experimental electronic excitation energies. In contrast to most other semiempirical approaches, the parameters depend only on the multiplicity of the desired state, the number of open shells of the CSF, and the employed density functional, but not on the specific atom or molecule. Currently, optimized parameter sets are available only for singlet and triplet multiplicities in combination with the BHLYP^{2,3} functional.

A common set of reference CSFs is used for all spatial symmetries. It can automatically be generated in a complete-active-space-like procedure. The CI expansion is kept short by extensive configuration selection. At present, the expectation value of the spin-free Hamiltonian serves as the selection criterion: all configurations with energies above a flexible threshold are discarded. In this way, even the electron correlation treatment of a molecule such as [6]-helicene (120 valence electrons) is feasible in a reasonably large AO basis set (VDZP). For details, we refer to the original publication by Grimme and Waletzke.¹ An energy based selection is well justified in a spin-free DFT/MRCI procedure because higher excitations account for dynamic correlation, which is already taken care of by the underlying DFT treatment. In a forthcoming extension of the program that includes matrix elements of the spin-orbit Hamiltonian in the CI procedure [spin-orbit configuration interaction (SOCI)], it might be meaningful to add a criterion based on the SOME of a configuration with the reference vectors. Highly energetic single excitations have proven to be important for the description of spin-polarization effects in heavy main group elements.^{4–6}

Matrix elements of the spin-free Hamiltonian are evaluated utilizing spin-coupling coefficients between CSFs as determined from the pattern-based method by Wetmore and Segal,⁷ avoiding the explicit construction of determinants. The MRCI program may be run optionally as an *ab initio* procedure, that is, a direct selecting MRCI for a HF one-particle basis. The correlation contribution of discarded CSFs is estimated by second-order Møller-Plesset perturbation theory in this case. In the present version of the HF/MRCI branch, no assignment is made between the roots in the reference space and in the CI space. This leads to meaningless MP2 corrections, if the order of the roots changes. Molecules with an odd number of electrons can presently be investigated only within the HF/MRCI scheme. A prescription for the construction of DFT/MRCI matrix elements for doublet and quartet cases has yet to be devised.

A property program for the determination of electric and magnetic dipole (transition) moments as well as rotatory strengths of circular dichroism (CD) spectra is available for both the HF/MRCI and DFT/MRCI branches.

Technically, the spin-free MRCI code and the associated property programs are linked to the TURBOMOLE package,^{8,9} and thus can take advantage of the efficiency with which the latter determines two-electron integrals and HF or KS wave functions even for large molecules. Information about basis sets and molecular orbitals is transferred via a binary file named `mos.bin`. The `tmwfn` routine generating this file is available in TURBOMOLE, versions 5.1 and higher. Computationally expensive four-index integrals are evaluated using the well-known resolution of the identity (RI) method.^{10,11} The required three-index integrals are provided by the `ritraf` module of TURBOMOLE where RI-MP2 optimized auxiliary basis sets from the TURBOMOLE library are utilized for an approximate resolution of the identity.^{11,12} To speed-up the direct evaluation of the σ vector in the iterative determination of the MRCI eigenvalues and eigenvectors by a multiroot Davidson^{13,14} procedure, four-index two-electron integrals can be precalculated if sufficient memory is available.

Spin-Orbit Mean-Field Approximation

Spin-orbit operators such as the Breit-Pauli¹⁵ or no-pair Douglas-Kroll¹⁶ operators consist of one- and two-electron terms, denoted by $\hat{\mathcal{H}}_{\text{SO}}(1)$ and $\hat{\mathcal{H}}_{\text{SO}}(2)$ here. Evaluated in a basis of molecular orbitals, up to four-index integrals will result, causing enormous requests for memory and computing times, especially for many-center systems. Therefore, even today one inevitably has to apply approximate spin-orbit Hamiltonians when dealing with larger polyatomic systems. The simplest and most frequently used of these is formally a pure one-electron operator with the nuclear charge Z replaced by an empirically parametrized effective charge Z_{eff} . A more rigorous way is to incorporate the two-electron contributions $\hat{\mathcal{H}}_{\text{SO}}(2)$ in an average way by performing a mean-field summation, comparable to HF theory, yielding an effective one-electron operator $\hat{\mathcal{H}}_{\text{SO}}^{\text{eff}}(1)$ ¹⁷:

$$\hat{\mathcal{H}}_{\text{SO}}^{\text{eff}}(1) = \hat{\mathcal{H}}_{\text{SO}}(1) + \hat{\mathcal{H}}_{\text{SO}}^{\text{mf}}(1) \quad (1)$$

A matrix representation of $\hat{\mathcal{H}}_{\text{SO}}^{\text{mf}}(1)$ in the basis of valence orbitals i, j is given by

$$\langle i | \hat{\mathcal{H}}_{\text{SO}}^{\text{mf}}(1) | j \rangle = \sum_a \gamma_a \left\{ \langle ia | \hat{\mathcal{H}}_{\text{SO}}(2) | ja \rangle - \frac{3}{2} \langle ia | \hat{\mathcal{H}}_{\text{SO}}(2) | aj \rangle - \frac{3}{2} \langle ai | \hat{\mathcal{H}}_{\text{SO}}(2) | ja \rangle \right\} \quad (2)$$

Herein, the spin densities for α and β electrons in the occupied core and valence orbitals of the mean-field are assumed to be equal. The occupation numbers γ_a range from 0 to 2.

Clearly, the number of mean-field integrals in the molecular basis is thus significantly smaller than the full set of two-electron integrals and can be kept in central memory. Furthermore, the computation of matrix elements between CI wave functions is

3. METHODENENTWICKLUNG UND IMPLEMENTIERUNG

simplified as only those CSFs contribute which are related by a single excitation.

In addition, the number of necessary raw AO integrals can be greatly reduced if all multicenter integrals are neglected. This one-center approximation is not as crude as one may assume, because both the one- and two-electron spin-orbit operators fall off like $1/r^3$ and so they act on a fairly local range only. Furthermore, multicenter contributions of $\hat{\mathcal{H}}_{SO}(1)$ and $\hat{\mathcal{H}}_{SO}(2)$ have been found to cancel to a large amount.¹⁸

For computing the spin-orbit integrals in the one-center mean-field approximation described above we use the well known AMFI program.¹⁹ It is capable of dealing with the Breit-Pauli and the no-pair Douglas-Kroll spin-orbit operators. To minimize computation time, AMFI makes use of the atomic spherical symmetry.

AMFI has been interfaced to the TURBOMOLE package using a program of our own called SOMF. It reads and translates basis set information from the `mos.bin` file and calls AMFI. The mean-field is determined in the SOMF input by specifying atomic occupation numbers and the corresponding atomic orbitals, which are obtained from restricted HF atomic ground state calculations. Finally, SOMF performs the transformation of the spin-orbit integrals from the atomic to the molecular orbital basis set.

Spin-Coupling Coefficients for a One-Electron Spin-Orbit Hamiltonian

CI calculations with the spin-free Hamiltonian are usually performed in a basis of spin-symmetry adapted CSFs. These are simultaneously eigenstates of the \hat{S}^2 and \hat{S}_z spin operators. As far as a spin-free Hamiltonian is applied, all components of a multiplet will be degenerate in energy. One is therefore free to choose any one of these components as basis functions. In the original MRCI code, the CSFs were constructed from $M_S = 0$ determinants for all multiplicities relating to an even number of electrons and from $M_S = \frac{1}{2}$ determinants otherwise. This choice becomes problematic as soon as spin-orbit coupling is included, as the example of two triplet states shows: the \hat{s}_{+1} and \hat{s}_{-1} operators cannot couple the two $M_S = 0$ states, because they yield a transition to the $M_S = 1$ or $M_S = -1$ multiplet components, respectively. The action of the $\hat{s}_0(1)$ operator on the 0-component of a triplet yields a singlet spin function:

$$\begin{aligned} \hat{s}_0(1) \frac{1}{\sqrt{2}} |\alpha(1)\beta(2) + \beta(1)\alpha(2)\rangle \\ = \frac{1}{2\sqrt{2}} |\alpha(1)\beta(2) - \beta(1)\alpha(2)\rangle \quad (3) \end{aligned}$$

Because a singlet spin function is orthogonal to a triplet, no overlap occurs and the matrix element vanishes. The same is true for the $\hat{s}_0(2)$ operator. (Note that of course the $M_S = 0$ component of the triplet is an eigenvalue to the $\hat{S}_z = \hat{s}_0 = \sum_{i=1}^N \hat{s}_0(i)$ operator.) Hence, no component of the spin-operator is able to couple the 0-components of two triplet wave functions. It was therefore necessary to rewrite the routines for generating the spin-coupling arrays in the MRCI code. Commonly, $M_S = S$ is used because in this case the CSFs comprise the minimal number of determinants.

Although with this particular choice of M_S components a matching spin-operator can be found for every symmetry-allowed combination of states, a further problem arises: the spatial symmetries of the states involved demand a certain symmetry of the spin-operator. For example, in C_{2v} symmetry, 1A_1 and 3A_2 are coupled by the z component of the spin-orbit operator. On the other hand, the singlet is computed with $M_S = 0$ in the CI and the triplet with $M_S = 1$. These spin components cannot be coupled by the $\hat{S}_z = \hat{s}_0$ operator because \hat{s}_0 retains the M_S quantum number of the states involved. The usual way out of this dilemma is to split up the calculation of the SOMEs into two steps: in the first step, the spin integration is performed for a spin-operator that matches the M_S quantum numbers of the two states involved, but not their respective spatial symmetry. In the example $\langle {}^3A_2 | \hat{\mathcal{H}}_{SO} | {}^1A_1 \rangle$, this would be the \hat{s}_+ operator. In the second step, the transition from this “wrong” spin operator to the one matching the spatial symmetry is achieved by utilizing the “scaled 3j-symbols,” introduced by McWeeny et al.^{20,21} These scaled 3j-symbols make use of the Wigner-Eckart theorem: starting from the matrix element with the wrong spin part and only one M_S component on each side, a reduced matrix element is obtained first. Multiplication with the appropriate 3j-symbols yields matrix elements over all M_S components and with the right spin operator.

The one-electron nature of the mean-field Hamiltonian leads to marked savings in the number of operations to be performed when evaluating spin-orbit matrix elements. In the notation of second quantization any of its Cartesian components ξ can be written as

$$\hat{h}(\xi) = \sum_{s,t} I_{st}(\xi) \left(\sum_{\sigma,\tau} s_{\sigma\tau}(\xi) \hat{a}_{s\sigma}^\dagger \hat{a}_{t\tau} \right) \quad (4)$$

Herein, $I_{st}(\xi)$ represents the spatial integral over the ξ component of the spin-orbit operator acting on orbitals s and t , $s_{\sigma\tau}(\xi)$ is a matrix element of the \hat{s}_ξ spin-operator over spins σ and τ ($\sigma, \tau \in \{\alpha, \beta\}$), and $\hat{a}_{s\sigma}^\dagger$ and $\hat{a}_{t\tau}$ are the creation and annihilation operators common in second quantization. Written in this form, the operator is separated into a spin-independent part (I_{st}) and a part that depends on the spin only (the expression in parentheses) but not on the physical nature of the problem studied.

The spin-coupling coefficients are the matrix elements of the latter operator over two CSFs. They are evaluated in the MRCI code according to a procedure for spin-free Hamiltonians by Wetmore and Segal.⁷ For a spin-orbit Hamiltonian, the integrals $s_{\sigma\tau}$ are the matrix elements of the \hat{s}_0 and \hat{s}_{+1} operators, whereas they are unit matrices in the spin-free case. A separate library for the \hat{s}_{-1} operator is not required because of the relation $(\hat{s}_{+1})^\dagger = -\hat{s}_{-1}$. A careful analysis shows that the method of Wetmore and Segal can easily be extended to spin-dependent operators.²² Excitation classes may be classified by “excitation patterns” in exactly the same way as in the spin-free case. However, the classification by excitation patterns cannot fully distinguish all excitation cases. For every pattern, there are four subcases, for which the coupling arrays are related by transpositions and sign changes in the spin-free case. The same is true for the \hat{s}_0 operator. On the other hand, only two of the subcases may be eliminated in this way for the \hat{s}_{+1} operator. Thus, all in all, we find three distinct coupling arrays for each pattern—one for the \hat{s}_0 and two for the \hat{s}_{+1} operator.

3.2. SPIN-BAHN-KOPPLUNG VON DFT/MRCI WELLENFUNKTIONEN

Table 1. Spin-Orbit Coupling Parameter A_{SO} (cm^{-1}), Adiabatic Excitation Energy (cm^{-1}), and CI Expansion Length of the T_1 State for Various Diatomic Molecules.

$1^3\Pi_r$	HF/MRCI			DFT/MRCI			Experiment ²⁹	
	ΔE	A_{SO}	# CSFs	ΔE	A_{SO}	# CSFs	ΔE	A_{SO}
BF	28915	23.8	79766	27831	22.3	171	29144	24.2
BCl	20281	47.4	80180	19961	46.2	418	20200	
AlF	27410	48.2	61933	27134	47.1	347	27241	47.0
AlCl	24275	63.3	82150	24202	63.9	640	24594	65.8
AlBr	22861	111.0	41694	23149	129.0	232	23779	132
CS	27421	90.0	77625	28107	88.7	316	27661	92.8
SiO	33581	70.7	86558	32590	73.5	373	33947	73.0
P ₂	27936	123.6	113000	28130	129.2	421	28197	128.9
Br ₂	11967	1157.0	96317	9963	1179.0	445	— ^a	— ^a

^aIn the Br₂ case, comparison with experiment is not reasonable: several ungerade states that exhibit strong off-diagonal coupling matrix elements are found close to the $^3\Pi_u$ state.

Admittedly, utilizing this approach is the most straightforward way of including spin-orbit interaction into the MRCI code. Nevertheless, it has several advantages: by introducing “excitation patterns,” the number of distinct spin coupling coefficients is reduced down to a level that facilitates their precomputation and storage as a program library. Storage requirements are negligible for up to 10 open shells and can easily be handled for up to 12, if only nonzero entries are stored. The method is well suited for application in an individually selecting CI: the pattern is determined during the configuration comparison step that has to be carried out anyway in a selecting CI. Summarizing, all spin coupling coefficients are already present in main memory and only a few additional operations are required to obtain the coupling array needed.

Properties

Fine-structure splittings due to spin-orbit coupling are presently calculated in the framework of quasi-degenerate perturbation theory (QDPT) by a program called SOCQDPT. It builds up and diagonalizes the spin-orbit Hamiltonian matrix in the basis of Russell-Saunders coupled states. Complex arithmetic is avoided by converting the Hermitian eigenvalue problem to a doubly sized real symmetric one.²³

Rates of spin-forbidden electric and magnetic dipole transitions can be determined perturbatively from the complex valued eigenvectors of the above mentioned spin-orbit Hamiltonian matrix and the transition moments of spin-allowed dipole processes.

As has been known for a long time, phosphorescence rates calculated by a sum-over-states treatment converge very slowly with respect to the number of states included.²⁴ In practice, this number cannot be increased beyond narrow limits due to technical reasons. Of course, in quasi-degenerate perturbation theory the same problem arises. These difficulties may be circumvented by various procedures such as a direct solution of the perturbation equations in the basis of CSFs,^{25,26} spin-orbit response theory,²⁷ or a spin-orbit configuration interaction treatment. In a SOCI, all relevant interactions are included implicitly in the variational

procedure from the beginning, the only remaining problem being the finiteness of the basis set. Future plans therefore include an implementation of routines that calculate one-electron transition density matrices for SOCI wave functions directly. Similar considerations apply to the computation of electronic g-tensor shifts of doublet state systems. The dominating contribution here usually stems from second-order terms that are actually cross terms of the spin-orbit and the orbital-Zeeman Hamiltonians.

Test of the Method

The one-center mean-field approximation was originally devised for heavy element compounds but has been shown to be applicable even to light organic molecules. The fine-structure splittings of HC₆H⁺, for example, agree up to 5% with the results obtained using the full one- and two-electron operator.¹⁸

In Table 1 spin-orbit coupling parameters for the first excited $^3\Pi$ states in some diatomic molecules are shown. These have been computed by conventional HF/MRCI on the one hand and DFT/MRCI on the other hand. Throughout, TZVP basis sets from the TURBOMOLE library are used.²⁸ No electrons are kept frozen in the CI calculations. The atomic mean field is constructed from HF atomic orbitals in both cases. Configurations are selected in the HF/MRCI calculations with respect to a threshold of $10^{-6} E_H$. In DFT/MRCI, the cutoff parameter is set to 1 E_H . Calculations are performed at the experimental geometries of the ground and $^3\Pi$ states.²⁹

Spin-orbit coupling parameters calculated with both methods agree very well. For comparison, some experimental values are also given.²⁹ The excellent agreement between theory and experiment again demonstrates the performance of the one-center mean-field approximation for light molecules. A look at the excitation energies and CI expansion lengths shows the enormous savings of computational resources within the DFT/MRCI approach: energies are obtained nearly as close to the experimental value as the results of the HF/MRCI treatment but with a CI expansion length of only

3. METHODENENTWICKLUNG UND IMPLEMENTIERUNG

Table 2. Calculation on LiBr: Analyzing the Influence of Scalar Relativistic Effects.

Correlation: scalar rel.:	DFT/MRCI no (A)	HF/MRCI no (B)	MRD-CI no (C)	MRD-CI yes (D)
$E_{\text{CI}}(^3\Pi)$	33353	37216	37189	38178
$\langle ^1\Sigma^+ \hat{\mathcal{H}}_{\text{SO}} ^3\Pi \rangle$	238	216	214	202
$\langle ^3\Pi_x \hat{\mathcal{H}}_{\text{SO}} ^3\Pi_y \rangle$	1028	1022	1005	962

Vertical excitation energy to the (repulsive) ${}^3\Pi$ T_1 state and spin-orbit matrix elements [cm^{-1}].

a few percent of that necessary for the ab initio calculations. As already mentioned, the spin-orbit coupling parameters also do not seem to be affected significantly by changing from the ab initio CI towards the DFT/MRCI based on KS orbitals.

Another benchmark calculation has been performed on the LiBr molecule (Table 2). Here, we investigate the applicability of utilizing a DFT basis for spin-orbit calculations in molecules containing heavier atoms. Unfortunately, we do not yet have the facilities to include scalar relativistic corrections in a (DFT or HF) MRCI calculation. This is because these corrections are not implemented for all-electron calculations in TURBOMOLE, and the mean-field spin-orbit integrals are not designed to be combined with the kind of core potentials that are applied in TURBOMOLE. According to our experience, the bromine atom is one of the heaviest atoms, for which neglect of scalar relativistics is not too crude an approximation. Nonetheless, in order to reveal eventual compensation of errors, we compare SPOCK results to values obtained with the older MRD-CI^{30,31} and BNSOC³² codes. This is based on the MOLECULE-SWEDEN package,³³ for which scalar relativistic corrections³⁴ are available. All in all, four calculations are carried out, all at the experimental geometry of the ground state²⁹ and applying a TZVP basis: (A) DFT/MRCI + SPOCK, (B) HF/MRCI + SPOCK, (C) MRD-CI + BNSOC, and (D) scalar relativistic MRD-CI + BNSOC.

The difference between calculations (B) and (C) is the RI-approximation utilized in the MRCI code, and these results agree very well. Inclusion of scalar relativistic corrections in calculation (D) increases the excitation energy by $\approx 1000 \text{ cm}^{-1}$. Spin-orbit matrix elements are slightly lowered (4–6%). The DFT calculation (A) yields matrix elements very close to the ones calculated in the HF basis. The large difference in the excitation energy may be explained by the repulsive nature of the excited ${}^3\Pi$ state (which is very sensitive to geometry deviations) and by the highly ionic nature of this molecule (parameterization of the DFT/MRCI method has been done with small organic molecules¹). Here, further investigations are required, but lie beyond the scope of this publication. All in all, we find good coincidence of the spin-orbit matrix elements, calculated with the different methods. This permits application of DFT orbitals in spin-orbit calculations for elements of the first four periods.

In Table 3, a few spin-orbit matrix elements for the lowest lying states of the 4H-pyran-4-thione molecule are listed to show the performance of the new code in the case of a polyatomic molecule. Here, the HF orbital based calculations were performed with the

MRD-CI and BNSOC packages to check the new code for consistency and correctness.³⁵ Actually, the HF/MRD-CI calculations include only 15,000–20,000 CSFs per space and spin symmetry, which is quite insufficient to reproduce excitation energies properly. For instance, the extrapolated MRD-CI excitation energy of the T_1 state is off by more than 2 eV for this expansion length. In the DFT/MRCI calculations again the standard energy cut-off value of 1 E_H was used, which usually suffices to keep errors in excitation energy below 0.2–0.3 eV.¹ This yields approximately 10,000–16,000 CSFs per space and spin symmetry. As is seen from Table 3, SOMEs obtained with both methods are comparable except for $\langle X^1A_1 | \hat{\mathcal{H}}_{\text{SO}} | 1^3A_2 \rangle$. A closer look at the CI expansions reveals that an $n \rightarrow \pi^*$ type excitation is by far the most important contributor to this SOME. By contrast, $\langle 1^3A_1 | \hat{\mathcal{H}}_{\text{SO}} | 1^3A_2 \rangle$ and $\langle 3^1A_1 | \hat{\mathcal{H}}_{\text{SO}} | 1^1A_2 \rangle$ are dominated by $n \rightarrow \pi$ type excitations. The amplitude of the virtual π^* HF orbital at the sulphur site is considerably lower than in the KS treatment, whereas it is almost the same for the occupied n and π orbitals. As spin-orbit coupling occurs mainly at the sulphur atom, the SOMEs obey the same trend and only the value of $\langle X^1A_1 | \hat{\mathcal{H}}_{\text{SO}} | 1^3A_2 \rangle$ changes markedly. One has to keep in mind here that the MRD-CI calculations are by no means converged and dynamical correlation is treated very poorly. Therefore, the discrepancy might disappear if the CI space could be enlarged enough. This hope, at least, is supported by the results in Table 1.

Note the large savings of computer time for the calculation of SOMEs with the new SPOCK program.

Application to Thiophene

As a first application of our new codes, we have investigated the multiplet coupling in thiophene. Photophysical properties of thiophene and its oligomers have attracted increasing attention recently.^{36–39} Ultrafast triplet formation (3 ps) was observed after two-photon absorption in thiophene with a photon energy of 3.1 eV.^{40,41} A remarkably short lifetime of the first excited singlet state (S_1) in a time-resolved pump-probe femto-second multiphoton ionization experiment was reported recently.⁴² After having pumped part of the thiophene molecules into the S_1 state, Lehr et al.⁴² observed a nearly instant appearance of photoelectrons originating from a triplet state and a complete depopulation of the S_1 within 500 fs. From these spectra the authors deduced an intersystem crossing (ISC) rate between S_1 and T_2 of the order of

Table 3. Spin-Orbit Matrix Elements (cm^{-1}) for 4H-Pyran-4-Thione.

	BNSOC HF/MRD-CI	SPOCK DFT/MRCI
$\langle T_2(1^3A_1) \hat{\mathcal{H}}_{\text{SO}} T_1(1^3A_2) \rangle$	-161.8	-164.0
$\langle T_2(1^3A_1) \hat{\mathcal{H}}_{\text{SO}} S_1(1^1A_2) \rangle$	163.5	168.6
$\langle S_0(X^1A_1) \hat{\mathcal{H}}_{\text{SO}} T_1(1^3A_2) \rangle$	-127.4	-148.2
$\langle S_3(1^1B_1) \hat{\mathcal{H}}_{\text{SO}} T_1(1^3A_2) \rangle$	-0.8	-0.6
$\langle S_4(1^1B_2) \hat{\mathcal{H}}_{\text{SO}} T_1(1^3A_2) \rangle$	0.2	0.1
• Timing (PII 400 MHz)	300 s	7 s

3.2. SPIN-BAHN-KOPPLUNG VON DFT/MRCI WELLENFUNKTIONEN

Table 4. Singlet and Triplet Excitation Energies (eV) in Thiophene, Calculated in the TZVPP+R Basis Set.

State	Dominant excitation(s)	DFT/MRCI	HF/MRCI	SAC-CI ⁴⁶	CASPT2 ⁴⁷	MRD-CI ³⁶	Experiment
1^1A_1		0.00	0.00	0.00	0.00	0.00	0.00
2^1A_1	$\pi_2 \rightarrow \pi_4^* + \pi_3 \rightarrow \pi_5^*$	5.24	7.93	5.41	5.33	6.55	$5.16^a, 5.43^b, 5.16^c$
1^1B_2	$\pi_3 \rightarrow \pi_4^*$	5.42	7.45	5.72	5.72	6.61	$5.52^a, 5.61^b, 5.99^c$
1^1A_2	$\pi_3 \rightarrow s$ Ryd.	5.72	7.56	5.70	5.93	5.78	6.0 ^a
1^1B_1	$\pi_3 \rightarrow p, d$ Ryd./ σ^*	5.88	8.62	5.87		6.41	
2^1B_1	$\pi_2 \rightarrow s$ Ryd.	6.27	7.48	6.12	6.23	6.33	
2^1A_2	$\pi_2 \rightarrow \sigma^*/p, d$ Ryd.	6.33	— ^d	6.03		6.39	
:							
3^1A_1	$\pi_3 \rightarrow \pi_5^* - \pi_2 \rightarrow \pi_4^*$	7.03	11.73	7.32	7.05	8.11	$6.76^a, 6.61^c$
:							
4^1B_2	$\pi_2 \rightarrow \pi_5^*$	7.54	9.64 ^e	7.40	7.32	8.59	
1^3B_2	$\pi_3 \rightarrow \pi_4^*$	3.39	5.19	3.94	3.75	4.45	$3.75^f, 3.8^g, 3.44^h$
1^3A_1	$\pi_2 \rightarrow \pi_4^* - \pi_3 \rightarrow \pi_5^*$	4.33	6.76	4.86	4.50	5.03	$4.62^f, 4.7^g, 4.38^{b,i}$
2^3A_1	$\pi_3 \rightarrow \pi_3^* + \pi_2 \rightarrow \pi_4^*$	5.63	8.59			6.82	
1^3A_2	$\pi_3 \rightarrow s$ Ryd.	5.64	8.21	5.75	5.88		
1^3B_1	$\pi_3 \rightarrow \sigma^*/p, d$ Ryd.	5.69	10.44 ^j	5.94	5.90		
2^3B_2	$\pi_2 \rightarrow \pi_5^*$	5.99	8.77 ^k			5.85	
2^3A_2	$\pi_2 \rightarrow \sigma^*/p, d$ Ryd.	6.11	— ^d				
2^3B_1	$\pi_2 \rightarrow s$ Ryd.	6.18	8.58		6.18		

Several Rydberg singlet states above 6.3 eV have been omitted.

^aAbsorption.³⁶

^bElectron energy loss.³⁷

^cAbsorption.⁴⁹

^dNo state of this characteristic is found among the five lowest-lying roots in A_2 symmetry.

^eA state with this characteristic is found as 3^1B_2 .

^fElectron impact.⁵⁰

^gElectron energy loss.³⁶

^hPhosphorescence.³⁸

ⁱPhotoelectron spectroscopy.³⁹

^jFound as 5^3B_1 .

^kFound as 3^3B_2 .

0.01 fs⁻¹. Because thiophene contains the element sulfur with an atomic spin-orbit splitting constant of roughly 190 cm⁻¹,⁴³ large spin-orbit coupling matrix elements between the molecular singlet and triplet states can be expected.

All our calculations were performed at the experimental geometry of the electronic ground state (S_0).⁴⁴ We employed three different basis sets: the standard TZVP and TZVPP basis sets from the TURBOMOLE library^{8,28} and a basis set, which we will call TZVPP+R, where we added 1s1p1d diffuse Gaussian Rydberg functions with origin at the center of mass and exponents of 0.011253, 0.009988, and 0.014204, respectively. These have been taken from the Rydberg basis for thiophene as given in the MOLCAS tutorial.⁴⁵ Molecular orbitals were optimized for the dominant closed shell determinant of the electronic ground state. All 26 valence electrons were correlated in the subsequent MRCI runs.

All technical details and timings given below refer to the TZVPP+R basis set. In the DFT/MRCI treatment, reference spaces comprise 179 configurations for singlets and 176 for triplets, resulting in CI expansion lengths of approximately 43,500 and 65,000 CSFs, respectively. In each symmetry, the 10 lowest electronic states were computed. In the HF/MRCI case, 187 configu-

rations for singlets and 174 for triplets were utilized. Due to the large size of the variational CI problems (1.2–2.1 million CSFs), only five roots were determined per space and spin symmetry in this case. CPU time requirements for the determination of all the above mentioned CI eigenvalues and vectors on an 800 MHz PIII processor amounted to 1 h 27' in the DFT/MRCI treatment compared to 63 h 22' for the HF/MRCI method. The evaluation of all SOMEs between DFT/MRCI wave functions by the new SPOCK takes merely 3'20" and is thus very effective. Even the handling of millions of CSFs for the HF/MRCI wave functions is considerably fast; the computation of all SOMEs requires only 13'16" of CPU time.

The HF/MRCI energies we report are the plain variational energies in the selected space. Many states exhibit a strong change in character compared to their nature in the reference space. Therefore, no MP2 correction has been applied and these energies are rather far from other results and experimental data. They are reported only for completeness.

The addition of a second polarization function (TZVPP) shows almost no effect on the DFT/MRCI results. Due to valence-Rydberg mixing, the excitation spectrum and the wave function char-

3. METHODENENTWICKLUNG UND IMPLEMENTIERUNG

acteristics are considerably affected by the inclusion of diffuse functions. On these grounds, only our TZVPP+R values are compared in Table 4 with experimental excitation energies and the results of recent quantum chemical calculations.

In accord with earlier quantum chemical investigations, we find that the two $3p_{\pi}$ electrons of sulfur are fully integrated in the aromatic ring system. To aid the analysis of the electronic structure of the excited states we have sketched the valence π orbitals in Figures 1 (b_1 symmetry) and 2 (a_2 symmetry). A virtual orbital that will play a decisive role in the interpretation of the spin-orbit results has been denominated by $\sigma^*/\text{Rydberg}$. The shapes of this orbital drawn at two different isolines are shown in Figure 3. Its valence part consists mainly of the $3p_y$ (B_2) Cartesian component of the sulfur $3p$ orbital and—with a different phase—a linear combination of the $2s$ and $2p_y$ at the neighboring carbon atoms. The diffuse charge distribution is due to some sulfur $3d$ and Rydberg d occupation.

The DFT/MRCI excitation energies computed in this work are in excellent agreement with experimental values (Table 4). In addition to excitation energies, wave function characteristics compare very well with previous SAC-CI⁴⁶ and CASPT2⁴⁷ results. Due to program restrictions, Palmer et al.³⁶ used a basis set of lower quality (DZPR) and a limited number of CSFs, yielding considerably too high excitation energies for all valence states whereas Rydberg states came out too low.

In agreement with the SAC-CI and CASPT2 treatments, we find the lowest excited triplet state (T_1) to be of B_2 symmetry resulting from a HOMO \rightarrow LUMO ($\pi_3 \rightarrow \pi_4^*$) excitation. The second and third triplet states (T_2 and T_3) are dominated by linear combinations of (HOMO-1) \rightarrow LUMO and HOMO \rightarrow (LUMO + 1) configurations (see Table 4) and exhibit A_1 symmetry. The interaction between the corresponding 1A_1 determinants is considerably stronger than for a triplet spin coupling. Furthermore, closed shell configurations, such as the double excitation ($\pi_3^2 \rightarrow \pi_4^{*2}$), contribute to the singlet coupled states. Due to this strong configuration interaction, the 1A_1 state is pushed below the HOMO \rightarrow LUMO excited 1B_2 state and becomes the S_1 , whereas the upper 3A_1 state is shifted above a series of Rydberg states.

Large spin-orbit integrals are to be expected if there is a significant probability for the electrons to be near the heaviest atom (sulfur) in both orbitals involved. However, there is no combination of π orbitals that fulfills this requirement (see Figs. 1 and 2). Spin-orbit coupling of b_1 and a_2 orbitals is symmetry allowed, but the latter exhibit a node on sulfur resulting in a small value of the spin-orbit integral. Furthermore, there is no totally symmetric component of the angular momentum as long as the molecule retains planar symmetry. As a consequence, the SOME of a $b_1 \rightarrow b_1$ excitation vanishes by symmetry. The charge distribution of Rydberg orbitals is too diffuse to give rise to a significant spin-orbit coupling. Only excitations of $\pi \rightarrow \sigma^*$ or $\sigma \rightarrow \pi^*$ character have chances to yield large spin-orbit integrals. Thus, in order to obtain substantial spin-orbit matrix elements between states, these states should differ by an excitation of the aforementioned types. This is not the case for the lowest-lying states, because they are of $\pi \rightarrow \pi^*$ character. With respect to each other they differ by an excitation of type $\pi \rightarrow \pi$ or $\pi^* \rightarrow \pi^*$ (or by a double excitation). As an example, consider the SOME between

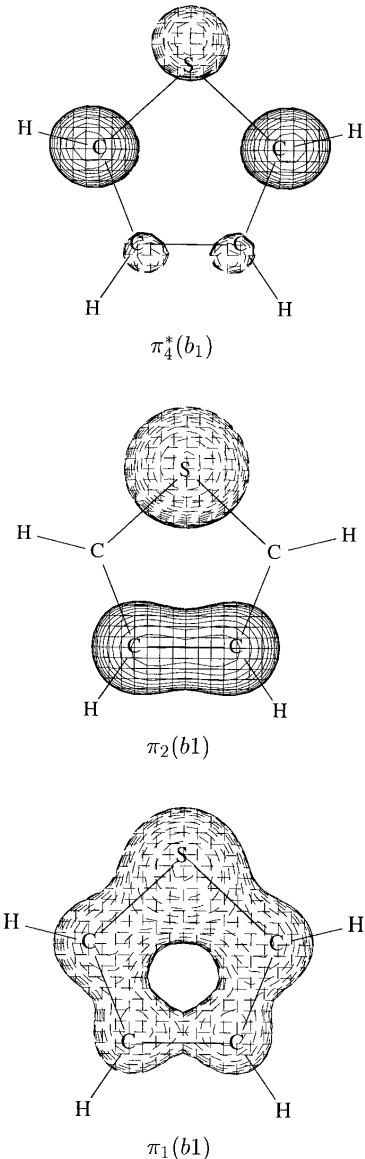


Figure 1. The valence π and π^* orbitals of b_1 -symmetry in thiophene (DFT calculation, TZVPP+R, isoline = 0.07). The Rydberg contribution is too diffuse for this choice of isolines.

the S_1 and T_1 states. S_1 is dominated by a linear combination of two configurations, $\pi_2 \rightarrow \pi_4^* + \pi_3 \rightarrow \pi_5^*$, whereas T_1 exhibits only one major configuration, $\pi_3 \rightarrow \pi_4^*$. Let us first concentrate on the SOME between the first of the two major S_1 configurations and

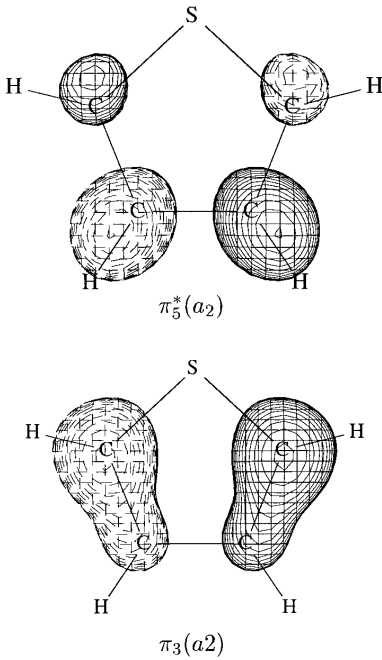


Figure 2. The valence π and π^* orbitals of a_2 -symmetry in thiophene.

the T_1 state. The configurations share a common core and π_4^* occupation, differing only in the occupation of the π_2 and π_3 orbitals. The second large S_1 configuration couples with the T_1 configuration via the $\langle \pi_5^* | \hat{\mathcal{H}}_{SO} | \pi_4^* \rangle$ integral. Both integrals, $\langle \pi_2 | \hat{\mathcal{H}}_{SO} | \pi_3 \rangle$ and $\langle \pi_5^* | \hat{\mathcal{H}}_{SO} | \pi_4^* \rangle$, have small values yielding a total $\langle S_1 | \hat{\mathcal{H}}_{SO} | T_1 \rangle$ SOMO of only 0.35 cm^{-1} . As mentioned above, the third unoccupied b_2 orbital exhibits significant contributions from the sulfur $3p_y$ atomic orbital and is the lowest-lying molecular orbital with mixed $\sigma^*/\text{Rydberg}$ character. States in which this orbital is occupied are 1^1B_1 , 2^1A_2 , 1^3B_1 , and 2^3A_2 . Among all symmetry allowed SOMEs between low-lying electronic states of thiophene, only the ones involving the $\pi \rightarrow \sigma^*/\text{Rydberg}$ excited states are considerably large (Tables 5 and 6).

The spin-orbit coupling between the S_1 and T_2 states is symmetry-forbidden as long as the molecule retains C_{2v} symmetry. We have tentatively investigated the behavior of the SOMEs between S_0 , S_1 , S_2 , T_1 , and T_2 for a situation in which the symmetry of the nuclear framework is reduced to C_s . In this case, one component of the angular momentum operator is totally symmetric, and the other two transform according to the A'' irreducible representation. An out-of-plane distortion of the sulfur atom by $0.3a_0$ yields nonzero, but small SOMEs (Table 7) that cannot explain the rapid ISC between the S_1 and T_1 or T_2 states. In principle, an indirect (higher-order) coupling via an intermediate state is also possible. The only state comprising a sizable SOME with both states is the $\pi \rightarrow \sigma^*/\text{Rydberg}$ excited 2^3A_2 state. At the

fixed ground state geometry, 2^3A_2 is located energetically at 6.1 eV according to our DFT/MRCI calculations, roughly 0.9 eV above the S_1 state and 1.8 eV above T_2 . It is questionable, however, whether this indirect coupling could lead to an ISC rate of the order of 0.01 fs^{-1} . Such a fast transition usually requires the presence of a conical intersection. On the basis of a vibrational analysis obtained from small, qualitative CASSCF calculations, Negri and Zgierski⁴⁸ argued that the equilibrium geometries of both the S_1 and S_2 states might be nonplanar. Although a conical intersection of the S_1 state potential energy hypersurface with one of the triplet surfaces has not yet been found this appears to be a realistic possibility to explain the observed fast singlet-triplet transition.

Summary and Outlook

In the present article, we propose an approach for the extension of the DFT/MRCI method to spin-orbit effects. To this end, we derived and implemented spin-coupling coefficients for a one-electron spin-orbit operator. Symmetry related spin-orbit matrix elements were generated efficiently employing scaled $3j$ -symbols.

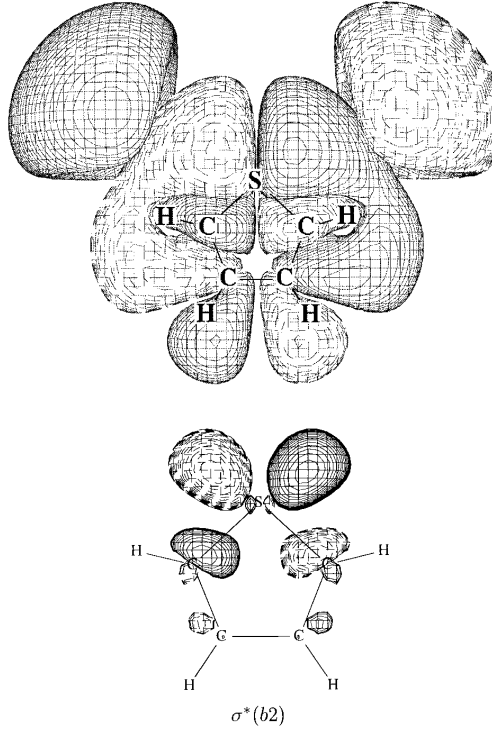


Figure 3. The lowest-lying σ^* orbital in thiophene: valence part (lower panel, isoline = 0.07) and Rydberg part (upper panel, isoline = 0.006).

3. METHODENENTWICKLUNG UND IMPLEMENTIERUNG

Table 5. Singlet-Triplet Spin-Orbit Matrix Elements of Selected States in Thiophene, Calculated in the TZVPP+R Basis with DFT/MRCI Wave Functions (cm^{-1}).

$\langle 1^3A_2 \hat{\mathcal{H}}_{\text{SO}} 1^1A_1 \rangle$	1.21	$\langle 1^3A_1 \hat{\mathcal{H}}_{\text{SO}} 1^1B_1 \rangle$	2.26
$\langle 1^3B_1 \hat{\mathcal{H}}_{\text{SO}} 1^1A_1 \rangle$	-0.07	$\langle 1^3A_2 \hat{\mathcal{H}}_{\text{SO}} 1^1B_1 \rangle$	5.63
$\langle 1^3B_1 \hat{\mathcal{H}}_{\text{SO}} 1^1A_1 \rangle$	-6.49	$\langle 1^3B_2 \hat{\mathcal{H}}_{\text{SO}} 1^1B_1 \rangle$	45.21
$\langle 2^3A_2 \hat{\mathcal{H}}_{\text{SO}} 1^1A_1 \rangle$	-94.71	$\langle 2^3A_1 \hat{\mathcal{H}}_{\text{SO}} 1^1B_1 \rangle$	-5.71
$\langle 2^3B_2 \hat{\mathcal{H}}_{\text{SO}} 1^1A_1 \rangle$	3.29	$\langle 2^3A_2 \hat{\mathcal{H}}_{\text{SO}} 1^1B_1 \rangle$	0.59
$\langle 2^3B_1 \hat{\mathcal{H}}_{\text{SO}} 1^1A_1 \rangle$	13.37	$\langle 2^3B_2 \hat{\mathcal{H}}_{\text{SO}} 1^1B_1 \rangle$	-1.83
$\langle 1^3A_2 \hat{\mathcal{H}}_{\text{SO}} 2^1A_1 \rangle$	1.23	$\langle 1^3A_1 \hat{\mathcal{H}}_{\text{SO}} 2^1B_1 \rangle$	4.54
$\langle 1^3B_2 \hat{\mathcal{H}}_{\text{SO}} 2^1A_1 \rangle$	-0.35	$\langle 1^3A_2 \hat{\mathcal{H}}_{\text{SO}} 2^1B_1 \rangle$	1.32
$\langle 1^3B_1 \hat{\mathcal{H}}_{\text{SO}} 2^1A_1 \rangle$	-3.13	$\langle 1^3B_2 \hat{\mathcal{H}}_{\text{SO}} 2^1B_1 \rangle$	7.69
$\langle 2^3A_2 \hat{\mathcal{H}}_{\text{SO}} 2^1A_1 \rangle$	44.26	$\langle 2^3A_1 \hat{\mathcal{H}}_{\text{SO}} 2^1B_1 \rangle$	0.95
$\langle 2^3B_2 \hat{\mathcal{H}}_{\text{SO}} 2^1A_1 \rangle$	-0.47	$\langle 2^3A_2 \hat{\mathcal{H}}_{\text{SO}} 2^1B_1 \rangle$	-4.37
$\langle 2^3B_1 \hat{\mathcal{H}}_{\text{SO}} 2^1A_1 \rangle$	-3.22	$\langle 2^3B_3 \hat{\mathcal{H}}_{\text{SO}} 2^1B_1 \rangle$	-0.28
$\langle 1^3A_2 \hat{\mathcal{H}}_{\text{SO}} 3^1A_1 \rangle$	-0.74	$\langle 1^3A_1 \hat{\mathcal{H}}_{\text{SO}} 1^1B_2 \rangle$	-0.57
$\langle 1^3B_2 \hat{\mathcal{H}}_{\text{SO}} 3^1A_1 \rangle$	-0.71	$\langle 1^3A_2 \hat{\mathcal{H}}_{\text{SO}} 1^1B_2 \rangle$	5.66
$\langle 1^3B_1 \hat{\mathcal{H}}_{\text{SO}} 3^1A_1 \rangle$	-6.77	$\langle 1^3B_1 \hat{\mathcal{H}}_{\text{SO}} 1^1B_2 \rangle$	38.64
$\langle 2^3A_2 \hat{\mathcal{H}}_{\text{SO}} 3^1A_1 \rangle$	-21.25	$\langle 2^3A_1 \hat{\mathcal{H}}_{\text{SO}} 1^1B_2 \rangle$	-0.05
$\langle 2^3B_2 \hat{\mathcal{H}}_{\text{SO}} 3^1A_1 \rangle$	0.32	$\langle 2^3A_2 \hat{\mathcal{H}}_{\text{SO}} 1^1B_2 \rangle$	18.25
$\langle 2^3B_1 \hat{\mathcal{H}}_{\text{SO}} 3^1A_1 \rangle$	0.27	$\langle 2^3B_1 \hat{\mathcal{H}}_{\text{SO}} 1^1B_2 \rangle$	-4.59
$\langle 1^3A_1 \hat{\mathcal{H}}_{\text{SO}} 1^1A_2 \rangle$	0.14	$\langle 1^3A_1 \hat{\mathcal{H}}_{\text{SO}} 2^1B_2 \rangle$	-0.11
$\langle 1^3B_2 \hat{\mathcal{H}}_{\text{SO}} 1^1A_2 \rangle$	-6.14	$\langle 1^3A_2 \hat{\mathcal{H}}_{\text{SO}} 2^1B_2 \rangle$	-0.87
$\langle 1^3B_1 \hat{\mathcal{H}}_{\text{SO}} 1^1A_2 \rangle$	5.90	$\langle 1^3B_1 \hat{\mathcal{H}}_{\text{SO}} 2^1B_2 \rangle$	-6.48
$\langle 2^3A_1 \hat{\mathcal{H}}_{\text{SO}} 1^1A_2 \rangle$	0.03	$\langle 2^3A_1 \hat{\mathcal{H}}_{\text{SO}} 2^1B_2 \rangle$	0.01
$\langle 2^3B_2 \hat{\mathcal{H}}_{\text{SO}} 1^1A_2 \rangle$	0.42	$\langle 2^3A_2 \hat{\mathcal{H}}_{\text{SO}} 2^1B_2 \rangle$	2.28
$\langle 2^3B_1 \hat{\mathcal{H}}_{\text{SO}} 1^1A_2 \rangle$	-1.24	$\langle 2^3B_1 \hat{\mathcal{H}}_{\text{SO}} 2^1B_2 \rangle$	1.67
$\langle 1^3A_1 \hat{\mathcal{H}}_{\text{SO}} 2^1A_2 \rangle$	38.94		
$\langle 1^3B_2 \hat{\mathcal{H}}_{\text{SO}} 2^1A_2 \rangle$	-1.92		
$\langle 1^3B_1 \hat{\mathcal{H}}_{\text{SO}} 2^1A_2 \rangle$	1.89		
$\langle 2^3A_1 \hat{\mathcal{H}}_{\text{SO}} 2^1A_2 \rangle$	7.16		
$\langle 2^3B_2 \hat{\mathcal{H}}_{\text{SO}} 2^1A_2 \rangle$	11.37		
$\langle 2^3B_1 \hat{\mathcal{H}}_{\text{SO}} 2^1A_2 \rangle$	-4.32		

Spin-orbit integrals were computed in the atomic mean-field approximation throughout. For this purpose, the existing AMFI and SOMF codes were interfaced to the TURBOMOLE package. At the present status of program development, the new spin-orbit coupling kit SPOCK is able to calculate spin-orbit matrix elements for DFT/MRCI- and optionally HF/MRCI-wave functions. Spin-dependent properties such as rates of spin-forbidden transitions can be calculated in quasi-degenerate perturbation theory.

Test calculations were performed on spin-orbit coupling parameters of ${}^3\Pi$ states for some main group diatomics. Results from DFT/MRCI wave functions agree very well with experimental values and with those from HF/MRCI calculations. The CI expansion length amounts up to 100,000 CSFs in HF/MRCI, whereas in DFT/MRCI only a few hundred CSFs have to be included in the CI space. For larger systems, pyranthione serves as a test example. Again, the numerical values from both methods for spin-orbit matrix elements of the lowest lying singlet and triplet states are comparable.

In the application to thiophene, we have demonstrated the efficiency of the new codes. When combining DFT, MRCI, spin-orbit mean-field integrals, and fast evaluation of spin-coupling coefficients, the reliable determination of excitation energies and spin-orbit matrix elements requires less than 2 h of CPU time on a standard PC. In accord with theoretical considerations, we found

Table 6. Triplet-Triplet Spin-Orbit Matrix Elements of Selected States in Thiophene, Calculated in the TZVPP+R Basis with DFT/MRCI Wave Functions (cm^{-1}).

$\langle 1^3A_2 \hat{\mathcal{H}}_{\text{SO}} 1^3A_1 \rangle$	-0.63
$\langle 1^3B_2 \hat{\mathcal{H}}_{\text{SO}} 1^3A_1 \rangle$	-0.32
$\langle 1^3B_1 \hat{\mathcal{H}}_{\text{SO}} 1^3A_1 \rangle$	-0.29
$\langle 2^3A_2 \hat{\mathcal{H}}_{\text{SO}} 1^3A_1 \rangle$	-36.85
$\langle 2^3B_2 \hat{\mathcal{H}}_{\text{SO}} 1^3A_1 \rangle$	0.15
$\langle 2^3B_1 \hat{\mathcal{H}}_{\text{SO}} 1^3A_1 \rangle$	3.23
$\langle 1^3A_2 \hat{\mathcal{H}}_{\text{SO}} 2^3A_1 \rangle$	-0.21
$\langle 1^3B_2 \hat{\mathcal{H}}_{\text{SO}} 2^3A_1 \rangle$	-0.19
$\langle 1^3B_1 \hat{\mathcal{H}}_{\text{SO}} 2^3A_1 \rangle$	6.39
$\langle 2^3A_2 \hat{\mathcal{H}}_{\text{SO}} 2^3A_1 \rangle$	-11.00
$\langle 2^3B_2 \hat{\mathcal{H}}_{\text{SO}} 2^3A_1 \rangle$	-0.09
$\langle 2^3B_1 \hat{\mathcal{H}}_{\text{SO}} 2^3A_1 \rangle$	1.46
$\langle 1^3B_2 \hat{\mathcal{H}}_{\text{SO}} 1^3A_2 \rangle$	6.62
$\langle 1^3B_1 \hat{\mathcal{H}}_{\text{SO}} 1^3A_2 \rangle$	-6.27
$\langle 2^3B_2 \hat{\mathcal{H}}_{\text{SO}} 1^3A_2 \rangle$	-0.39
$\langle 2^3B_1 \hat{\mathcal{H}}_{\text{SO}} 1^3A_2 \rangle$	0.69
$\langle 1^3B_2 \hat{\mathcal{H}}_{\text{SO}} 2^3A_2 \rangle$	2.73
$\langle 1^3B_1 \hat{\mathcal{H}}_{\text{SO}} 2^3A_2 \rangle$	0.25
$\langle 2^3B_2 \hat{\mathcal{H}}_{\text{SO}} 2^3A_2 \rangle$	6.48
$\langle 2^3B_1 \hat{\mathcal{H}}_{\text{SO}} 2^3A_2 \rangle$	-4.49
$\langle 1^3B_1 \hat{\mathcal{H}}_{\text{SO}} 1^3B_2 \rangle$	-49.85
$\langle 2^3B_1 \hat{\mathcal{H}}_{\text{SO}} 1^3B_2 \rangle$	6.45
$\langle 1^3B_1 \hat{\mathcal{H}}_{\text{SO}} 2^3B_2 \rangle$	2.62
$\langle 2^3B_1 \hat{\mathcal{H}}_{\text{SO}} 2^3B_2 \rangle$	-0.23

that the $\pi \rightarrow \pi^*$ excited singlet and triplet states do not exhibit remarkable spin-orbit matrix elements among each other or with the ground state, as long as C_{2v} symmetry is retained. Large matrix elements between low lying electronic states were found only if the $\sigma^*/\text{Rydberg}$ orbital was involved, as, for example, in the largest matrix element $\langle 2^3A_2 | \hat{\mathcal{H}}_{\text{SO}} | 1^1A_1 \rangle = 94.7 \text{ cm}^{-1}$. In our opinion, a C_s symmetric geometry of excited states and/or a conical intersection of the S_1 state with the triplet states are the most plausible explanations for the experimentally observed fast decay of the former state.

Work to include kinematic (scalar) relativistic effects and a variational treatment of spin-orbit interaction in the framework of a SOCI procedure is in progress. These features appear to be indispensable in an all-electron investigation of heavy element compounds. The effects of scalar relativistic corrections on valence electron properties are non-negligible for elements with a nuclear charge $Z \approx >20$. Furthermore, a SOCI treatment is

Table 7. Spin-Orbit Matrix Elements (Absolute Values [cm^{-1}]) of the Lowest Singlet and Triplet States in Thiophene for a C_s Symmetric Geometry (See Text), Calculated in the TZVPP+R Basis with DFT/MRCI Wave Functions.

$\langle T_1(A'') \hat{\mathcal{H}}_{\text{SO}} S_0(A') \rangle$	0.5/7.5 ^a	$\langle T_2(A') \hat{\mathcal{H}}_{\text{SO}} S_0(A') \rangle$	9.0
$\langle T_1(A'') \hat{\mathcal{H}}_{\text{SO}} S_1(A') \rangle$	0.4/1.6	$\langle T_2(A') \hat{\mathcal{H}}_{\text{SO}} S_1(A') \rangle$	1.9
$\langle T_1(A'') \hat{\mathcal{H}}_{\text{SO}} S_2(A'') \rangle$	0.4	$\langle T_2(A') \hat{\mathcal{H}}_{\text{SO}} S_2(A'') \rangle$	0.3/4.9
$\langle T_1(A'') \hat{\mathcal{H}}_{\text{SO}} T_2(A') \rangle$	0.0/2.6		

^ax-component/y-component.

expected to appreciably improve the quality of second-order properties, such as g-tensors, and phosphorescence lifetimes that are known to converge very slowly in a sum-over-states approach.

Acknowledgments

We cordially thank Stefan Grimme (Münster) and Mirko Waletzke (Bonn) for providing the source code of their DFT/MRCI program and for continuous support on implementation details. Further, we would like to thank Rainer Weinkauf (Düsseldorf) for drawing our attention to the thiophene problem and for many interesting discussions on this subject. Funding by the Deutsche Forschungsgemeinschaft (DFG) through SPP “Relativistische Effekte” and project Ma 1051/5-1 is gratefully acknowledged.

References

1. Grimme, S.; Waletzke, M. J Chem Phys 1999, 111, 5645.
2. Becke, A. D. J Chem Phys 1993, 98, 1372.
3. Lee, C.; Yang, W.; Parr, R. G. Phys Rev B 1988, 37, 785.
4. Heß, B.; Marian, C. In Computational Molecular Spectroscopy; Jensen, P., Bunker, P., Ed.; John Wiley & Sons: Sussex, 2000, pp. 169.
5. Vallet, V.; Maron, L.; Teichtel, C.; Flament, J.-P. J Chem Phys 2000, 113, 1391.
6. Buenker, R. J.; Alekseyev, A. B.; Liebermann, H.-P.; Lingott, R.; Hirsch, G. J Chem Phys 1998, 108, 3400.
7. Wetmore, R. W.; Segal, G. A. Chem Phys Lett 1975, 36, 478.
8. Ahlrichs, R.; Bär, M.; Häser, M.; Horn, H.; Kölmel, C. Chem Phys Lett 1989, 162, 165.
9. Treutler, O.; Ahlrichs, R. J Chem Phys 1995, 102, 346.
10. Vahtras, O.; Almlöf, J.; Feyereisen, M. W. Chem Phys Lett 1993, 213, 514.
11. Weigend, F.; Häser, M.; Patzelt, H.; Ahlrichs, R. Chem Phys Lett 1998, 294, 143.
12. Eichhorn, K.; Treutler, O.; Öhm, H.; Häser, M.; Ahlrichs, R. Chem Phys Lett 1995, 240, 283.
13. Davidson, E. R. J Comput Phys 1975, 17, 87.
14. Crouzeix, M.; Philippe, B.; Sadkane, M. J Sci Comput 1994, 15, 62.
15. Pauli, W. Z Phys 1927, 43, 601.
16. Samzow, R.; Heß, B. A.; Jansen, G. J Chem Phys 1992, 96, 1227.
17. Heß, B. A.; Marian, C. M.; Wahlgren, U.; Gropen, O. Chem Phys Lett 1996, 251, 365.
18. Tatchen, J.; Marian, C. M. Chem Phys Lett 1999, 313, 351.
19. AMFI is an atomic spin-orbit integral program written by B. Schimelpfennig, University of Stockholm (1996).
20. McWeeny, R. J Chem Phys 1965, 42, 1717.
21. Cooper, I. L.; Musher, J. I. J Chem Phys 1972, 57, 1333.
22. Kleinschmidt, M.; Marian, C. M. To appear.
23. Press, W. H.; Teukolsky, S. A.; Vetterling, W. T.; Flannery, B. P. Numerical Recipes in Fortran 77: the Art of Scientific Computing; Cambridge University Press: Cambridge, 1992.
24. Langhoff, S. R.; Davidson, E. R. J Chem Phys 1976, 64, 4699.
25. Heß, B. A.; Buenker, R. J.; Marian, C. M.; Peyerimhoff, S. D. Chem Phys 1982, 71, 79.
26. Havriliak, S. J.; Yarkony, D. R. J Chem Phys 1985, 83, 1168.
27. Ågren, H.; Vahtas, O.; Minaev, B. Adv Quantum Chem 1996, 27, 71.
28. Schäfer, A.; Huber, C.; Ahlrichs, R. J Chem Phys 1994, 100, 5829.
29. Huber, K. P.; Herzberg, G. Molecular Spectra and Molecular Structure, IV, Constants of Diatomic Molecules; Van Nostrand: New York, 1979.
30. Buenker, R. J.; Peyerimhoff, S. D. Theoret Chim Acta 1974, 35, 33.
31. Buenker, R. J.; Phillips, R. A. J Mol Struct THEOCHEM 1985, 123, 291.
32. BNSOC is a spin-orbit coupling program package developed at the University of Bonn, Germany, by B. A. Hess and C. M. Marian, with contributions from P. Chandra, S. Hutter, M. Kleinschmidt, F. Rakowitz, R. Samzow, B. Schimelpfennig, and J. Tatchen (1980–2000).
33. MOLECULE-SWEDE is an electronic structure program system written by J. Almlöf, C. W. Bauschlicher Jr., M. R. A. Blomberg, D. P. Chong, A. Heiberg, S. R. Langhoff, P.-Å. Malmqvist, A. P. Rendell, B. O. Roos, P. E. M. Siegbahn, and P. R. Taylor.
34. Heß, B. A. Phys Rev A 1986, 33, 3742.
35. Tatchen, J.; Waletzke, M.; Marian, C. M.; Grimme, S. Chem Phys 2001, 264, 245.
36. Palmer, M. H.; Walker, I. C.; Guest, M. F. Chem Phys 1999, 241, 275.
37. Asmis, K. R. Dissertation Nr. 1142, Université de Fribourg: Fribourg, Switzerland, 1996.
38. Becker, R. S.; de Melo, J. S.; Maçanita, A. L.; Elisei, F. J Phys Chem 1996, 100, 18683.
39. Chadwick, J. E.; Kohler, B. E. J Chem Phys 1994, 98, 3031.
40. Yang, J.; Paa, W.; Rentsch, S. Synth Met 1999, 101, 624.
41. Rentsch, S.; Yang, J. P.; Paa, W.; Birkner, E.; Schiedt, J.; Weinkauf, R. Phys Chem Chem Phys 1999, 1, 1707.
42. Lehr, L.; Weinkauf, R.; Schlag, E. W. To appear.
43. Moore, C. E. Atomic Energy Levels, NBS Circular 467; National Bureau of Standards: Washington, D.C., 1949.
44. Callomon, J. H.; Hirota, E.; Lafferty, W. J.; Maki, A. G.; Pote, C. S. Landolt-Börnstein, New Series, Group II: Atomic and Molecular Physics, Structure Data of Free Polyatomic Molecules, Vol. 7; Springer Verlag: Berlin, 1976.
45. Molcas on-line tutorial, 2000 Department of Theoretical Chemistry, Lunds Universitet: Sweden. URL: <http://www.teokem.lu.se/molcas/tutor>.
46. Wan, J.; Hada, M.; Ehara, M.; Nakatsuji, H. J Chem Phys 2001, 114, 842.
47. Serrano-Andrés, L.; Merchán, M.; Fülscher, M.; Roos, B. O. Chem Phys Lett 1993, 211, 125.
48. Negri, F.; Zgierski, Z. J Chem Phys 1994, 100, 2571.
49. Di Lonardo, G.; Galloni, G.; Trombettini, A.; Zauli, C. J Chem Soc Faraday Trans II 1972, 68, 2009.
50. Flicker, W. M.; Mosher, O. A.; Kuppermann, A. Chem Phys Lett 1976, 38, 489.

3.2.3 Berechnung von g -Tensoren mit SPOCK

In der Arbeitsgruppe Grein stieß die Entwicklung des SPOCK-Pakets auf großes Interesse. Dort werden schon seit vielen Jahren g -Tensoren kleiner Moleküle und Radikale mit den MRD-CI[37; 38] und BNSOC[36]-Programmpaketen untersucht. Die Berechnung größerer Verbindungen scheiterte oftmals an der beschränkten Anwendbarkeit des MRD-CI für diese Moleküle bzw. daran, dass für modernere CI-Programme die Spin-Bahn-Kopplung nicht implementiert war. Eine der ersten Anwendungen des SPOCK-Pakets sollten daher Berechnungen an g -Tensoren sein. Zunächst sollte jedoch die Anwendbarkeit des neuen Ansatzes auf diese Fragestellung überprüft werden.

In der Veröffentlichung „Efficient calculation of electron paramagnetic resonance g -tensors by multireference configuration interaction sum-over-state expansions, using the atomic mean-field spin-orbit method“ („Effiziente Berechnung von Electron Paramagnetic Resonance g -Tensoren mit Multireferenz-Konfigurationswechselwirkungs-Zustandssummen-Entwicklungen mit der atomaren *mean-field* Methode“) werden mit SPOCK.PT berechnete Spin-Bahn-Matrixelemente zur Berechnung von g -Tensoren verwendet. Es wurden Rechnungen an zwei- bis vieratomigen Molekülen durchgeführt, zu denen Vergleichswerte aus der Literatur vorliegen. Der Schwerpunkt liegt auf einem Test der neuen Methode und der Überprüfung der Korrektheit bei dieser Anwendung. Da mit dem *ab-initio*-Zweig gearbeitet wurde, konnte hier insbesondere auch die Implementierung einem Praxistest ohne eventuellen Einfluß der DFT-Terme unterzogen werden.

Die paramagnetische Elektronenspinresonanz (ESR) oder Electron Paramagnetic Resonance (EPR) ist eine spektroskopische Methode, bei der die Anregung des Spins eines ungepaarten Elektrons durch Mikrowellenstrahlung gemessen wird. Die Aufspaltung der Feinstrukturniveaus wird dabei durch den Zeeman-Effekt in einem starken Magnetfeld erreicht.

In einem Molekül spielt dabei die relative Orientierung des Magnetfelds zum Molekül eine Rolle. Die Spin-Bahn-Kopplung bewirkt eine Kopplung des Spins an den Orbitaldrehimpuls, so dass in verschiedenen Raumrichtungen unterschiedliche Aufspaltungen gemessen werden können. Ist der g -Faktor für ein Atom noch ein Skalar, so wird er hierdurch für ein Molekül zur tensoriellen Größe.

Die störungstheoretische Berechnung der g -Tensoren erfordert den Einbezug der Spin-Bahn-Kopplung. In Zusammenarbeit mit Fritz Grein, der über langjährige Erfahrung mit g -Tensoren verfügt, haben wir die Eignung von SPOCK.PT für die Berechnung von g -Tensoren untersucht.

Als Einschränkung bei der Berechnung der g -Tensoren muss genannt werden, dass derzeit für Dupletts ausschließlich der *ab-initio*-Zweig genutzt werden kann. Diese Einschränkung liegt jedoch nicht im SPOCK-Paket begründet, sondern im zugrundeliegenden MRCI-Paket. Sobald Parameter für die Berechnung von Dupletts im DFT/MRCI vorliegen, können ohne Änderungen an SPOCK auch Spin-Bahn-Matrixelemente und daraus g -Tensoren mit dem DFT-Zweig gerechnet werden.

In dieser Arbeit wurden g -Tensoren für 16 Hauptgruppenradikale und drei Übergangsmetallverbindungen störungstheoretisch berechnet. Da es sich bei den betrachteten Molekülen um Dupletts handelt, kommt der *ab-initio* Zweig von DFT/MRCI und SPOCK.PT zum Einsatz.

Soweit ein Vergleich möglich ist, sind die Ergebnisse von vergleichbarer Qualität wie die früheren Arbeiten von Grein et. al., bei denen das MRD-CI von Buenker und Peyerim-

3.2. SPIN-BAHN-KOPPLUNG VON DFT/MRCI WELLENFUNKTIONEN

hoff sowie das ältere BNSOC Paket mit explizitem Zweielektronen-Spin-Bahn-Operator eingesetzt wurde. Die Verwendung der wesentlich kostengünstigeren atomaren *mean-field*-Integrale führt nicht zu wesentlichen Genauigkeitsverlusten. Die Übereinstimmung mit experimentellen Daten ist gut.

Der *ab-initio*-Zweig des SPOCK.PT wird in der Arbeitsgruppe Grein weiterhin zur Berechnung von *g*-Tensoren genutzt. In der Veröffentlichung „Geometries, electronic *g*-tensor elements, hyperfine coupling constants, and vertical excitation energies for small gallium arsenide doublet radicals, Ga_xAs_y ($x + y = 3, 5$)“[39] werden *g*-Tensoren kleiner Gallium-Arsenid-Cluster mit drei und fünf Atomen behandelt. Die berechneten *g*-Tensoren unterscheiden sich für verschiedene Geometrien deutlich, so dass eine Unterscheidbarkeit im Experiment vorhergesagt wird.

In einer weiteren Veröffentlichung werden die Isomerpaares HCO/COH, HCS/CSH, HSiO/SiOH und HSiS/SiSH untersucht.[40]

Diese Arbeiten zu *g*-Tensoren sind die einzigen Veröffentlichungen, die ausschließlich mit dem *ab-initio*-Zweig der MRCI und SPOCK-Programme gerechnet wurden.

3. METHODENENTWICKLUNG UND IMPLEMENTIERUNG

JOURNAL OF CHEMICAL PHYSICS

VOLUME 118, NUMBER 21

1 JUNE 2003

Efficient calculation of electron paramagnetic resonance *g*-tensors by multireference configuration interaction sum-over-state expansions, using the atomic mean-field spin-orbit method

Scott Brownridge and Friedrich Grein^{a)}

Department of Chemistry, University of New Brunswick, Fredericton, New Brunswick E3B 6E2, Canada

Jörg Tatchen, Martin Kleinschmidt, and Christel M. Marian^{b)}

Institute of Theoretical Chemistry, University of Duesseldorf, Universitaetsstr. 1,
D-40225 Duesseldorf, Germany

(Received 3 February 2003; accepted 3 March 2003)

Using the multireference configuration interaction method due to Grimme and Waletzke, combined with the atomic mean-field approximations for the efficient calculation of spin-orbit matrix elements, the *g*-tensors in second-order perturbation theory have been calculated for the main group radicals CO⁺, CN, BO, BS, MgF, AlO, O₂, HCO, H₂O⁺, NO₂, CO₂⁻, NF₂, NO₂⁻, O₃⁻, ClO₂, and H₂CO⁺, and for the transition metal compounds ZnH, ZnF, and TiF₃, using explicit sum-over-state expansions for up to 20 excited states. In most cases, a valence triple-zeta basis set with polarization functions has been employed. It is shown that the addition of diffuse functions to this basis set does not improve the *g*-tensor results, and in several instances leads to slower convergence of the sum-over-state expansion. The calculated *g*-tensors are in good agreement with experimental values, and with our previous multireference configuration interaction results available for 9 of the 19 radicals. Our results are shown to be equivalent to, or better than, values obtained by other theoretical methods. Examples of radicals for which *g*-tensor calculations presented problems in the past are AlO and TiF₃. For AlO, we obtain $\Delta g_{\perp} = -1530$ ppm (parts per million), compared with an experimental value of -1900 ppm in Ne matrix. Using the SVP (valence double-zeta plus polarization) basis set, Δg_{\perp} of TiF₃ is calculated to be -115.3 ppt (parts per thousand), compared with experimental values of -111.9 and -123.7 ppt. © 2003 American Institute of Physics.

[DOI: 10.1063/1.1569243]

I. INTRODUCTION

Starting in 1992, a major effort was undertaken at the University of New Brunswick to develop programs and perform theoretical *ab initio* studies on the electron paramagnetic resonance (EPR) *g*-tensor. At that time, to our knowledge, only one *ab initio* paper on *g*-tensors, by Moores and McWeeney on CN and NO₂,¹ had been published, to which we will refer later. On the other hand, extensive theoretical developments had been performed on hyperfine coupling constants (see review article by Engels, Eriksson, and Lunell²).

For *g*-tensor calculations, the spin-Zeeman (SZ) term H_{SZ}, the one- and two-electron gauge corrections (GC) H_{GC(1)} and H_{GC(2)}, and the relativistic mass correction (RMC) term H_{RMC} contribute in first-order perturbation, whereas the spin-orbit (SO) operator H_{SO} and the orbital Zeeman (OZ) operator H_{OZ} contribute in second order.³

Initially, computer programs were developed for *g*-tensor calculations based on ROHF wave functions. In particular, new programs had to be written for the two-electron gauge correction terms.⁴

In the first papers, results for NO₂, CO₂⁻, C₃H₅,

H₂CO⁺, NF₃⁺,⁵ NO, O₂,⁶ NO₂, CO⁺, H₂O⁺,⁷ and hydrides of Li, Be, B⁸ were given and discussed. Basis set and gauge dependencies were studied extensively. Following work by Luzanov *et al.*,⁹ the coordinate origin was always placed at the electronic charge centroid.

It soon became obvious that correlated wave functions were needed in order to obtain reliable *g*-tensor values. For example, while Moores and McWeeney,¹ using self-consistent field (SCF) methods with an STO-4G basis set, calculated $-10\,275$ ppm for Δg_{yy} of NO₂ (we use the notation $g = g_e + \Delta g$), a much larger and polarized basis set gave an restricted open Hartree-Fock (ROHF) value of -6660 ppm,⁷ compared to an experimental result of $-11\,300$ ppm.

For the calculation of first-order terms, which are usually small, the ROHF process was retained, but the second-order contributions were evaluated by methods based on multireference configuration interaction (MRCI) wave functions, using the “MRD-CI” programs developed by Buenker, Peyerimhoff, and co-workers.¹⁰ In second-order Rayleigh-Schrödinger perturbation theory, a sum over states (SOS) has to be calculated, each term having the simple form $\langle\langle SO\rangle\langle L\rangle/\Delta E$, where $\langle SO\rangle$ and $\langle L\rangle$ are the spin-orbit and angular momentum matrix elements between the ground state and the respective excited state, and ΔE is the energy difference between these states.

In exploratory MRD-CI work on MgF,¹¹ NO₂, H₂O⁺,

^{a)}Electronic mail: fritz@unb.ca

^{b)}Electronic mail: christel.marian@uni-duesseldorf.de

3.2. SPIN-BAHN-KOPPLUNG VON DFT/MRCI WELLENFUNKTIONEN

and CO^+ ,¹² several SOS situations arose: (i) The major contribution to Δg may come from one term (one excited state) in the SOS, e.g., Δg_{yy} of NO_2 , where 1^2B_1 gives $-10\ 195$ ppm and all higher roots only contribute about 60 ppm;¹² (ii) several excited states make sizeable contributions, such that in the end a large $|\Delta g|$ remains, e.g., Δg_{xx} of NO_2 , where 13^2B_2 states contribute 3900 ppm, the largest individual term being 2300 ppm (absolute); (iii) again, many excited states make large contributions, but the sum over states is almost zero, e.g., Δg_{zz} for NO_2 , for which 15^2A_2 states contribute a total of -128 ppm, although the largest individual term is 1405 ppm; (iv) finally, it may also happen that all individual terms in the SOS are small, resulting in a near-zero total contribution. Obviously, case (i) is ideal, and case (iii) is bad. The situation is especially difficult if the SOS consists of two similarly large terms of opposite sign, as in the case of AlO ,^{13,14} H_2CO^+ ,¹⁵ and other radicals.

Fortunately, the SOS usually shows rapid convergence, and in most cases the calculation of nine excited states of a particular species (like 2^2B_1 states for C_{2v} symmetry) is sufficient, in the sense that the last few roots make small and diminishing contributions to Δg . In addition, only excited states of valence type are important, since diffuse states show small $\langle L \rangle$ matrix elements, or have only “weak magnetic coupling” with the ground state (GS).

In order to extend the g -tensor calculations based on multireference CI wave functions, with explicit second-order term-by-term evaluations, to larger systems, the need arose to use MRCI programs applicable to larger systems. Fortunately, such programs including evaluation of the $\langle L \rangle$ matrix elements were developed earlier by Grimme and Waletzke,¹⁶ and were made available to us. These programs are based on the TURBOMOLE package,¹⁷ using the resolution of the identity (RI) approximation.¹⁸ Spin-orbit matrix elements for MRCI wave functions are generated with the spin-orbit coupling kit (Spock), described in detail in Ref. 19. Key features of this program are a fast determination of spin-coupling coefficients between configuration state functions (CSF) for spin-dependent one-electron operators and the use of nonempirical atomic spin-orbit mean-field integrals. The one-center mean-field approximation due to Hess, Marian *et al.*,²⁰ treats the two-electron part of the spin-orbit operator by an effective one-electron interaction, thereby leading to time savings without compromising the results in any serious manner.^{21,22} Exploiting spherical symmetry in the atomic mean-field integral (AMFI) program by Schimmelpfennig²³ drastically reduces computational expenses. Herein, the molecular mean field is replaced by a sum of atomic mean-field integrals. The atomic mean-field approximation has recently found its way into various fields of application,^{24–26} in particular g -tensor calculations by other groups, e.g., Refs. 27 and 28.

In the following, the new methods (MRCI, AMFI, and Spock) will be applied to the calculation of g -tensors for a standard set of radicals. The standard set contains systems for which g -tensor results, both experimental and theoretical, are available in the literature, such that the new results can be judged against previous theoretical values obtained by us and by other groups, and compared with experimental results.

TABLE I. Optimized geometries [MP2/6-311+G(2df)].

Radical	Symmetry	Ground state	Bond distances (\AA) and angles ($^\circ$)
CO^+	$C_{\infty v}$	$X^2\Sigma^+$	$\text{C}-\text{O} 1.091$
CN	$C_{\infty v}$	$X^2\Sigma^+$	$\text{C}-\text{N} 1.125$
BO	$C_{\infty v}$	$X^2\Sigma^+$	$\text{B}-\text{O} 1.210$
BS	$C_{\infty v}$	$X^2\Sigma^+$	$\text{B}-\text{S} 1.610$
MgF	$C_{\infty v}$	$X^2\Sigma^+$	$\text{Mg}-\text{F} 1.804$
AlO	$C_{\infty v}$	$X^2\Sigma^+$	$\text{Al}-\text{O} 1.621$
ZnH	$C_{\infty v}$	$X^2\Sigma^+$	$\text{Zn}-\text{H} 1.572^a$
ZnF	$C_{\infty v}$	$X^2\Sigma^+$	$\text{Zn}-\text{F} 1.770$
O_2	$D_{\infty h}$	$X^3\Sigma_g^-$	$\text{O}-\text{O} 1.221$
HCO	C_s	X^2A'	$\text{H}-\text{C} 1.122, \text{C}-\text{O} 1.183,$ $\text{H}-\text{C}-\text{O} 124.27^a$
H_2O^+	C_{2v}	X^2B_1	$\text{H}-\text{O} 0.997, \text{H}-\text{O}-\text{H} 109.17^a$
NO_2	C_{2v}	X^2A_1	$\text{N}-\text{O} 1.199, \text{O}-\text{N}-\text{O} 134.28$
CO_2^-	C_{2v}	X^2A_1	$\text{C}-\text{O} 1.233, \text{O}-\text{C}-\text{O} 137.60$
NF_2	C_{2v}	X^2B_1	$\text{N}-\text{F} 1.340, \text{F}-\text{N}-\text{F} 103.57$
NO_2^-	C_{2v}	X^2B_1	$\text{N}-\text{O} 1.364, \text{O}-\text{N}-\text{O} 113.66$
O_3^-	C_{2v}	X^2B_1	$\text{O}-\text{O} 1.321, \text{O}-\text{O}-\text{O} 114.74$
ClO_2	C_{2v}	X^2B_1	$\text{Cl}-\text{O} 1.481, \text{O}-\text{Cl}-\text{O} 117.92$
H_2CO^+	C_{2v}	X^2B_2	$\text{H}-\text{C} 1.112, \text{C}-\text{O} 1.195,$ $\text{H}-\text{C}-\text{O} 118.76^a$
TiF_3	D_{3h}	$X^2A'_1$	$\text{Ti}-\text{F} 1.783, \text{F}-\text{Ti}-\text{F} 120.0$

^aMP2/6-311++G(*d,p*).

About half of the radicals in our standard set are new, in the sense that there are no prior MRCI calculations on their g -tensors. They include three transition metal compounds. The hope is that approximations introduced into these new methods (such as the RI and mean-field approximations) do not, or not significantly, influence the quality of the results.

II. METHODS

Geometry optimizations were carried out with the GAUSSIAN 98 suite of programs²⁹ at the MP2/6-311+G(2df) level [MP2/6-311++G(*d,p*) for ZnH , HCO , H_2O^+ , and H_2CO^+]. The resulting optimized geometries are given in Table I. The theoretical evaluation of g -tensors using perturbation theory is described in detail in Refs. 11, 12, 30, and 31. The total Δg for a given molecule is comprised of first- and second-order terms. In this paper, only second-order g -tensor components were calculated. The first-order contributions to the total Δg are usually quite small in relation to the second order Δg values.

In general, the nine lowest excited states of each required symmetry species were calculated and used in the SOS. In two cases, the 9-root expansions had not converged, and additional 20-root calculations were performed. The reference configurations, in the order of 100, were obtained by running a series of preliminary CI calculations, and consist of those configurations that have $c^2 > 0.003$. For the final CI, a configuration selection threshold of 5 μh (or smaller as stated in the text) was taken, resulting in about 100 000–500 000 CSF's to be used for matrix diagonalization. To the CI energies, the sum of the second-order Møller–Plesset (MP2) energies of the neglected configurations is added, and a Langhoff–Davidson correction,³² to account for triply and higher-excited configurations, is applied. Please note that in the new MRCI programs, an energy extrapolation, as done in

3. METHODENENTWICKLUNG UND IMPLEMENTIERUNG

9554 J. Chem. Phys., Vol. 118, No. 21, 1 June 2003

Brownridge *et al.*

the MRD-CI package, is not performed. Rather than a fraction (λ), the total sum of the energies of the neglected configurations is added to the CI energies.

Routinely, the TZVPP basis set by Schäfer *et al.*³³ was used. In order to study the effect of diffuse functions on the g -tensor, additional TZVPP+diffuse function (DF) calculations were performed. The diffuse functions were taken from the aug-cc-pVDZ basis set,^{34–36} and are $1s1p1d$ functions for first- and second-row atoms. The corresponding RI basis sets were adjusted for the diffuse functions. For transition metal compounds, however, diffuse functions were not added.

III. RESULTS

The second-order g -tensor results obtained with the new methods are given in Table II. Two separate columns show values for the TZVPP and TZVPP+DF basis sets. Comparison is made with experimental results, as well as theoretical ones obtained previously by us and by other authors. For inclusion in Table II, we have selected publications that deal with a large number of radicals, such as the DFT papers by Schreckenbach and Ziegler (SZ) from 1997³⁷ (separate column), and by Kaupp *et al.* (KRM) from 2002²⁷ (under “Other”). In the latter work, which is an extension of a previous paper (Malkina *et al.*, 2000)³⁸ having essentially the same authorship, the AMFI method is employed as mentioned before. Of the various density functionals used in the KRM paper, we selected results for the B3PW91 and BHPW91 hybrid functionals, which are stated to be the most satisfactory ones for transition metal complexes, and to give results for main group radicals similar to those obtained with the other functionals. Furthermore, in Table II we included a column for the coupled perturbed Hartree–Fock and Kohn–Sham theory results of Neese,³⁹ specifically for the BP86 functional. Neese stated that the results using hybrid functionals (e.g., B3LYP) showed slight or no improvement over those using the generalized gradient approximation (GGA, e.g., BP86) for radicals made of light atoms, but he also noted that the hybrid functionals failed completely for AlO and H₂CO⁺.³⁹ According to Neese and KRM, the hybrid functionals (e.g., B3LYP, B3PW91) gave slightly better results for transition metal complexes, but were still in significant disagreement with experimental Δg values.^{27,39} Also included in Table II is a separate column for the results obtained by Jayatilaka, using a generalized Hartree–Fock (GHF) method.⁴⁰

Theoretical g -tensor results obtained by other authors are listed in the last two columns of Table II under “Other,” or are given in the text. In particular, van Lenthe *et al.* (LWA) developed a relativistic density functional method within the zero-order regular approximation (ZORA) approach, and performed calculations on NO₂, HCO, and TiF₃;⁴¹ Belanzoni *et al.* (BLB) carried out ZORA calculations on AlO, BO, BS and 19 small metal compounds (e.g., ZnH, ZnF, HgCN, CdAg).⁴² Also mentioned will be results by Quiney and Belanzoni (QB), who did Dirac–Hartree–Fock (DHF) calculations on 19 diatomic hydrides, fluorides, oxides and sulfides, including BO, BS, MgF, ZnH, and ZnF;⁴³ and by Vahtras *et al.*, who developed *ab initio* re-

sponse theory methods for ROHF and MCSCF wave functions.^{28,44} Lushington recently reported small closed-form CI expansion g -tensor results for H₂O⁺, MgF, NO₂, CO⁺, and H₂CO⁺.⁴⁵

A. Diatomic radicals

For all diatomic radicals, the contributions of 1 $^2\Pi$ and 2 $^2\Pi$ to Δg_{\perp} are given in Table III for the TZVPP basis set.

1. CO⁺, CN, BO, BS

All these radicals have nine valence electrons (VE) and a $^2\Sigma^{+}$ ground-state (GS) with an electronic configuration of $\pi^4\sigma^1$. The perpendicular component, Δg_{\perp} , arises from the coupling of the GS with the manifold of $^2\Pi$ excited states. In all cases, the major contributions to Δg_{\perp} come from 1 $^2\Pi$ and 2 $^2\Pi$, both being negative, as shown in Table III. For all four radicals, $\Delta g_{\perp}(2 ^2\Pi)$ is larger in magnitude than $\Delta g_{\perp}(1 ^2\Pi)$.

For CO⁺ and CN, Δg_{\perp} is calculated to be slightly less negative than the experimental value, whereas most other theoretical Δg_{\perp} 's, including Lushington's (−2537 ppm)⁴⁵ and our own MRD-CI value for CO⁺, are more negative.

For BO, the new Δg_{\perp} is close to our previous MRD-CI value.¹³ It is seen from Table II that the new and all previously calculated Δg_{\perp} 's are much more negative than the experimental result of −1100 ppm.

For BS, Δg_{\perp} is calculated to be close to the experimental result and to that obtained by QB (−7500 ppm),⁴³ but much less negative than the density functional theory (DFT) values from SZ and Neese.

There are no systematic differences between Δg_{\perp} values calculated with the two basis sets. Diffuse functions added to a valence triple-zeta basis set with polarization functions obviously have no strong influence on the results obtained for these diatomic radicals.

The parallel component has, for all four radicals, second-order contributions of less than 1 ppm. In first-order, our previous calculations gave −174 ppm for Δg_{\parallel} of CO⁺,¹³ and −99 ppm for that of BO,¹³ agreeing quite well with results listed in other theoretical studies. For all four radicals, the experimental values of Δg_{\parallel} are much more negative (−700 to −1400 ppm), probably due to matrix effects.

2. MgF

This radical also has 9 VE's and a $^2\Sigma^{+}$ GS. It distinguishes itself from the previously discussed radicals in that the contribution to Δg_{\perp} from 2 $^2\Pi$ is almost zero, whereas it was the dominant contribution for the earlier ones (Table III). The calculated Δg_{\perp} 's are −2020/−1885 ppm, close to our former MRD-CI value of −1809 ppm,¹³ and similar to some of the other theoretical results. QB obtained a Δg_{\perp} of −1400 ppm.⁴³ All but Lushington's (−1151 ppm)⁴⁵ and Jayatilaka's (−1314 ppm)⁴⁰ results are more negative than the experimental value of −1300 ppm.

The parallel component in second-order is zero, and was calculated to be −54 ppm in our earlier study.¹³

3.2. SPIN-BAHN-KOPPLUNG VON DFT/MRCI WELLENFUNKTIONEN

TABLE II. New MRCI g -tensor results (second-order only) and comparison to experimental and other theoretical results. All results in ppm unless otherwise noted.

Radical	Δg	Expt. ^a	TZVPP ^b	TZVPP + DF ^b	Grein ^c MRD-CI	SZ ^d DFT-GIAO	Neese ^e BP86	Jayatilaka ^f GHF	Other	Other
CO ⁺	Δg_{\parallel}	-1200, -1400	0	0	-174	-138	-165	-42	-88 ^g	-96 ^h
	Δg_{\perp}	-2400, -3000	-2015	-2225	-2609	-3129	-2622	-2798	-2512	-2426
CN	Δg_{\parallel}	-700	0	0	...	-137	-145	-63
	Δg_{\perp}	-2000	-1715	-1650	...	-2514	-2033	-1983
BO	Δg_{\parallel}	-800	0	0	-99	-72	-92	...	-100 ⁱ	-100 ^j
	Δg_{\perp}	-1100	-1735	-1635	-1899	-2298	-1924	...	-1400	-2500
BS	Δg_{\parallel}	-700, -800	0	0	-114	-83	-128	...	-100 ⁱ	-500 ^j
	Δg_{\perp}	-8100, -7900	-7740	-7120	-8449	-9974	-9928	20	-7500	-12400
MgF	Δg_{\parallel}	-300	0	0	-54	-60	-88	17 ^g	16 ^h	...
	Δg_{\perp}	-1300	-2020	-1885	-1809	-2178	-2433	-1314	-1573	-1740
AlO	Δg_{\parallel}	-800, -900	0	0	-114	-142	-153	-300 ^j
	Δg_{\perp}	-1900, -2600	-1530	-2175	-2284	-222	-2920	800
ZnH	Δg_{\parallel}	-2000, -3300	0	-2100 ⁱ	-400 ^j
	Δg_{\perp}	-17100, -18200	-14490	-1800	-24900
ZnF	Δg_{\parallel}	0	0	-400 ⁱ	-300 ^j
	Δg_{\perp}	-6000	-7015	-43700	-6800
O ₂	Δg_{\parallel}	-294, -380	0	0	...	0	0	...
	Δg_{\perp}	2850, 2519	2900	2875	3100 ^k	3100 ^k	3100 ^k	2912 ^l
HCO	Δg_{xx}	0	-85	-20	...	-270	-307	-183	-184 ^g	-176 ^h
	Δg_{yy}	-7500	-7885	-7870	...	-9468	-7891	-6859	-7659	-7778
H ₂ O ⁺	Δg_{zz}	1500	2175	1875	2749	2183	2073	2320	2303	...
	Δg_{xx}	200	15	15	-249	103	-185	-229	-174 ^g	-175 ^h
NO ₂	Δg_{yy}	18800	16025	15710	15733	13824	11475	12704	11983	11676
	Δg_{zz}	4800	4210	4170	4105	5126	4412	3306	3721	3827
NO ₂ ⁻	Δg_{xx}	3900	3400	3600	3571	4158	3281	3368	4286 ^g	3888 ^h
	Δg_{yy}	-11300	-11830	-11790	-10296	-13717	-11270	-11008	-12328	-11918
CO ₂ ⁻	Δg_{zz}	-300	-440	-605	-537	-760	-706	-623	-725	-628
	Δg_{xx}	700, 880	655	560 ^m	...	1522	490	805
NF ₂	Δg_{yy}	-4800, -5070	-5080	-4530	...	-7210	-5151	-4767
	Δg_{zz}	-500, -710	-1110	-340	...	-803	-969	-571
NO ₂ ²⁻	Δg_{xx}	-100	-470	-90	...	-738	-636	-447	-758 ^g	-644 ^h
	Δg_{yy}	6200	5985	6370	7619	6970	5649	6258	6547	...
O ₃ ⁻	Δg_{zz}	2800	3220	3690	4678	4264	2892	3564	3955	...
	Δg_{xx}	600, 1500	-105	100 ⁿ	...	-472
O ₃ ⁻	Δg_{yy}	5500, 7600	6255	6680	9082	9082	9082	9082	9082	9082
	Δg_{zz}	4800, 4700	3705	2700	4319	4319	4319	4319	4319	4319
ClO ₂	Δg_{xx}	200, 1300	-150	20	-475	-554	-476	-597
	Δg_{yy}	14700, 16400	15915	16890	16673	19380	15323	17933
H ₂ CO ⁺	Δg_{zz}	9700, 10000	10385	10360	10121	10542	8736	10945
	Δg_{xx}	-100, 1300 ^p	-351	-40	...	-455	-512	...	30 ^q	...
TiF ₃ ^s	Δg_{yy}	13400, 16000	17790	14435	12292	14569	13690	13690	13690	13690
	Δg_{zz}	10200, 6500	11740	9620	10606	11416	11416	11416	11416	11416
TiF ₃ ^s	Δg_{xx}	4600	5840	5835	5510	6231	5507	5472	6252	...
	Δg_{yy}	-800	240	200	-50	-1220	-678	927	-326	...
TiF ₃ ^s	Δg_{zz}	200	300	485	1296	76	18	2976	4219 ^r	...
	Δg_{\parallel}	-11.1, -3.7	-0.9 ^t	-1.7 ^u	-0.9	...	-1.4 ^g	0.5 ^v
	Δg_{\perp}	-111.9, -123.7	-115.3	-42.8	-30.7	-71.4	-71.4	-97.5

^aExperimental values cited from Refs. 37, 38, 40, 44, 49, and 50.

^bThis work.

^cMRD-CI results from Refs. 12–15 and 51.

^dResults from Ref. 37.

^eResults from Ref. 39.

^fResults from Ref. 40.

^gBHPW91 results by KRM from Ref. 27.

^hB3PW91 results by KRM from Ref. 27.

ⁱDHF results by QB from Ref. 43.

^jZORA results by BLB from Ref. 42.

^kDFT (BP86) results from Ref. 48.

^lMCSCF results by Vahtras *et al.* from Ref. 44.

^mResults for 20 roots. With 9 roots, $\Delta g_{xx} = -1070$, $\Delta g_{yy} = -4615$, $\Delta g_{zz} = -385$ ppm.

ⁿResults for 20 roots. With 9 roots, $\Delta g_{xx} = 70$, $\Delta g_{yy} = 6535$, $\Delta g_{zz} = 1335$ ppm.

^oClO₂ in Ne matrix (Ref. 53).

^pClO₂ in a KClO₄ host crystal (Ref. 54).

^qMCSCF results by Vahtras *et al.* from Ref. 28.

^rClosed-form CI results by Lushington from Ref. 45.

^sResults in ppt. $\Delta g_{\parallel} = \Delta g_{zz}$, Δg_{\perp} = average of Δg_{xx} and Δg_{yy} .

^tSVP basis set; first-order included, see text.

^uValues calculated by LWA (Ref. 41) using the DFT-GIAO programs of SZ (Ref. 37).

^vDFT results from Ref. 57.

3. METHODENENTWICKLUNG UND IMPLEMENTIERUNG

9556 J. Chem. Phys., Vol. 118, No. 21, 1 June 2003

Brownridge *et al.*

TABLE III. Second-order contributions of $1^2\Pi$ and $2^2\Pi$ to Δg_{\perp} (ppm) for diatomic molecules having a $X^2\Sigma^+$ ground state, and of $1^3\Pi_g$ and $2^3\Pi_g$ for O_2 with a $X^3\Sigma_g^-$ ground state. TZVPP basis set.

Radical	Δg_{\perp} ($1^2\Pi/1^3\Pi_g$)	Δg_{\perp} ($2^2\Pi/2^3\Pi_g$)	Δg_{\perp} (total)
CO ⁺	-526	-1778	-2015
CN	-328	-1420	-1715
BO	-590	-1217	-1735
BS	-2887	-5101	-7740
MgF	-1994	-6	-2020
AlO	2342	-3696	-1530
ZnH	-15626	-271	-14490
ZnF	-1022	-6948	-7015
O ₂	2802	-433	2900

3. AlO

In the past, the g -tensor calculation of AlO presented many difficulties. The first calculation was done by SZ,³⁷ who obtained $\Delta g_{\perp} = -222$ ppm, compared to an experimental value of -1900 ppm (in Ne matrix). In a systematic study done by this group, it became necessary to use natural orbitals (NO) in order to arrive at a reasonable result for Δg_{\perp} (-2284 ppm).¹⁴ CI wave functions based on MO's gave -3375 ppm. The improvements due to using NO's were explained by a configuration change around R_e , requiring the wave function to have two-configuration character. The Δg_{\perp} of AlO is difficult to calculate since the contributions from $1^2\Pi$ and $2^2\Pi$ are of similar magnitude, but have opposite sign, as shown in Table III. In all previously discussed cases of diatomic molecules with 9 VE's, the signs of the contributions from $1^2\Pi$ and $2^2\Pi$ were the same (or $2^2\Pi$ gave a near-zero contribution for MgF). Also, Δg_{\perp} depends strongly on the bond distance since the potential curves for $X^2\Sigma^+$ and $1^2\Pi$ cross at $R \approx 1.85$ Å (the equilibrium distance is 1.618 Å), causing ΔE to approach zero and Δg_{\perp} to approach infinity as one gets nearer to the crossing point. These technical difficulties can possibly be avoided by computing the g -factor in the basis of vibronic states. A similar technique has been applied previously to the computation of Λ doubling in the vicinity of potential curve crossings.⁴⁶

To further complicate matters, the observed Δg_{\perp} also depends strongly on the matrix used, with experimental values ranging from -1900 for a Ne matrix to -5000 ppm for a Kr matrix.⁴⁷ From the known rotational coupling constant, using Curl's equation, a gas-phase value for Δg_{\perp} of about -1450 ppm has been derived by us.¹⁴

The newly calculated Δg_{\perp} of -1530 ppm without DF's, and -2175 ppm with, are among the best values obtained so far by theoretical methods.

The parallel component has again a very small contribution in second-order perturbation. Its first-order contribution was previously calculated by us to be -114 ppm, in good agreement with other theoretical results (but quite different from the experimental value of -800 ppm).

4. ZnH and ZnF

The valence electrons are $4s$ and $3d$ on Zn, $1s$ on H, and $2s$ and $2p$ on F, to give a total of 13 VE's for ZnH, and 19 for ZnF. For both radicals, only the TZVPP basis set was used.

Our results for Δg_{\perp} , given in Table II, are in good agreement with experimental values of $-17\,100$ (in Ar matrix)⁴⁹ and $-18\,200$ (in Ne matrix)⁵⁰ ppm for ZnH, and -6000 ppm for ZnF. QB obtained -1800 for ZnH, and $-43\,700$ for ZnF, whereas the ZORA results of BLB are $-24\,900$ and -6800 ppm for ZnH and ZnF, respectively.

Table III shows that the dominant contribution to Δg_{\perp} is due to $1^2\Pi$ for ZnH, and to $2^2\Pi$ for ZnF. For ZnF, the contributions to Δg_{\perp} are similar to those of CO⁺, CN, BO, and BS, in that Δg_{\perp} ($2^2\Pi$) is larger in magnitude than Δg_{\perp} ($1^2\Pi$), and both components are negative. The Δg_{\perp} of ZnH, like MgF, is dominated by the interaction of the ground state with $1^2\Pi$.

The second-order contributions to Δg_{\parallel} are zero in both cases. First-order ROHF calculations give $\Delta g_{\parallel} = -110$ ppm for ZnH, and -130 ppm for ZnF, both values being very small. While the experimental Δg_{\parallel} is zero for ZnF, in agreement with our result, it is -2000 ppm (in Ar matrix; -3300 ppm in Ne matrix) for ZnH. Interestingly, QB obtained -2100 ppm for Δg_{\parallel} of ZnH.

5. O₂

As an example of a triplet molecule, the Δg components of O₂ were calculated. For both basis sets, the Δg_{\perp} results are nearly identical, lying close to the higher of the two experimental values given in Table II (2850 ppm). The only other theoretical values are by Patchkovskii and Ziegler (3100 ppm)⁴⁸ and Vahtras *et al.* (2912 ppm).⁴⁴ For Δg_{\parallel} we obtain an ROHF result of -277 ppm.⁶

6. General trends for diatomic radicals

According to Table III, for CO⁺, CN, BO, and BS, both $1^2\Pi$ and $2^2\Pi$ make negative contributions to Δg_{\perp} . The first $2^2\Pi$ results from a $\pi \rightarrow \sigma$ excitation, of DOMO \rightarrow SOMO type, whereas the second one results from $\sigma \rightarrow \pi^*$ (SOMO \rightarrow virtual MO). According to well-established rules,⁴⁹ DOMO \rightarrow SOMO excited states should contribute positively to Δg_{\perp} , opposite to the findings for the above four radicals, and SOMO \rightarrow virtual MO excited states should contribute negatively, in agreement with our results. On the other hand, for AlO the rules are followed for both $1^2\Pi$ and $2^2\Pi$. This situation is discussed in more detail in Ref. 14. There it is shown that BN⁻ and BP⁻ behave like BO and BS, whereas AlN⁻, AIS, and AlP⁻ behave like AlO. It might also be mentioned that SiO⁺, discussed in Ref. 13, has a positive and a negative contribution to Δg_{\perp} from $1^2\Pi$ and $2^2\Pi$, respectively, similar to AlO.

For MgF, as well as BeF,¹⁴ the lowest $2^2\Pi$ state is due to $\sigma \rightarrow \pi^*$, and contributes negatively, as expected. As both σ and π^* are localized on Mg or Be, such contribution is large. In contrast, $2^2\Pi$, from $\pi \rightarrow \sigma$, contributes little since π is localized on F.

For ZnH, the lowest $2^2\Pi$ state (at 4.29 eV) results from the $\sigma \rightarrow \pi^*$ excitation. As the σ MO is localized mainly, and the π^* MO exclusively on Zn, both $\langle L \rangle$ (-0.81 a.u.) and $\langle SO \rangle$ (162 cm⁻¹) are large, leading to a sizeable negative

3.2. SPIN-BAHN-KOPPLUNG VON DFT/MRCI WELLENFUNKTIONEN

Δg_{\perp} contribution from $1^2\Pi$. All other $^2\Pi$ states lie much higher in energy, including the $\pi \rightarrow \sigma$ state (about 10 eV), and practically do not contribute to Δg_{\perp} .

The situation for ZnF is quite different. Here, $1^2\Pi$, from $\pi \rightarrow \sigma$, and $2^2\Pi$, from $\sigma \rightarrow \pi^*$, do mix, and therefore, have similar energies (5.06 and 5.98 eV, respectively). The π MO is localized mainly on F, but σ and π^* reside on Zn. Therefore, $\langle L \rangle$ and $\langle SO \rangle$ are small for $1^2\Pi$ (-0.25 a.u., 40 cm^{-1}), but much larger for $2^2\Pi$ (-0.63 a.u., 130 cm^{-1}). As the numbers show, both make a negative contribution to Δg_{\perp} , although according to the previously stated rules, $1^2\Pi$ should lead to a positive Δg_{\perp} . Since Zn has a closed d -shell, the Δg results for both ZnH and ZnF are typical of corresponding main group radicals rather than transition metal compounds.

To conclude, O_2 has a $\sigma_g^2 \pi_g^2$ occupation, and only one valence $^3\Pi_g$ state, resulting from $\sigma_g \rightarrow \pi_g$, is of relevance.⁴⁴ It makes, as expected, a positive contribution to Δg_{\perp} .

B. Polyatomic radicals

In Table IV, the three most important contributions to the components of Δg are given for the polyatomic radicals studied here. The contributions to Δg are governed by the selection rules of the angular momentum operator. For HCO, in C_s symmetry (with the molecule in the xy -plane), Δg_{xx} and Δg_{yy} result from coupling of X^2A' with $^2A''$ states, and Δg_{zz} from coupling with $^2A'$ states. For C_{2v} molecules (in the yz -plane), the three components of Δg (in the order x , y , z) arise from coupling with 2B_2 , 2B_1 , and 2A_2 excited states if the GS is 2A_1 (NO_2 , CO_2^-), from coupling with 2A_2 , 2A_1 , and 2B_2 states if the GS is 2B_1 (H_2O^+ , NF_2 , NO_2^- , O_3^- , ClO_2), and from coupling with 2A_1 , 2A_2 , and 2B_1 states if the GS is 2B_2 (H_2CO^+).

1. HCO

With the atoms placed in the xy -plane, the x and y components of Δg mix, and a matrix diagonalization is required. According to Table IV, the (undiagonalized) xx component has large contributions from $4^2A''$, $6^2A''$, and $3^2A''$ for TZVPP, and from $6^2A''$, $7^2A''$, and $1^2A''$ for TZVPP + DF, with a near cancellation between the first two terms in the latter case. The yy component is dominated by $1^2A''$ for both basis sets, due to its low energy, and $\langle L \rangle$ as well as $\langle SO \rangle$ being relatively large. After diagonalization, Δg_{xx} ($-85/-20$ ppm) and Δg_{yy} ($-7885/-7870$ ppm) (Table II) are close to the experimental values of 0 and -7500 ppm, respectively. Other theoretical results, given in Table II, range from -176 to -307 ppm for Δg_{xx} , and from -6859 to -9468 ppm for Δg_{yy} . The out-of-plane component, Δg_{zz} (2175 ppm from TZVPP) is closer to the experimental value than other theoretical results. Contributions to Δg_{zz} arise mainly from $6^2A'$, $4^2A'$, and $2^2A'$ (TZVPP), all being positive.

Spin-unrestricted GGA values by LWA are -300 for Δg_{xx} , -9700 for Δg_{yy} , and 2700 for Δg_{zz} .⁴¹

2. H_2O^+

This radical has a 2B_1 GS in C_{2v} symmetry. The total Δg_{xx} is small, and all individual terms in the SOS are also

small. Δg_{yy} is mainly due to 1^2A_1 (16 186 versus 16 025 ppm for all 9 roots, using TZVPP), whereas Δg_{zz} is dominated by coupling with 1^2B_2 (4470 versus 4210 ppm in total). Including first-order contributions, Δg_{xx} was calculated to be -249 ppm, Δg_{yy} was 15 733 ppm, and Δg_{zz} was 4105 ppm in our earlier work.¹²

Referring to the general discussion given in the Introduction, this radical is the easiest we ever encountered, since all three components of Δg are either close to zero or have only one large contribution in the SOS. Despite the simple Δg structure and the predominance of low-lying excited states in the CI expansions, the results for Δg_{yy} (listed in Table II) that were obtained by other theoreticians are much lower (11 475–13 824 ppm), well below the experimental value of 18 800 ppm. In addition to the (poor) BP86 result given in Table II, Neese reports a Δg_{yy} value of 17 683 ppm using the local density approximation, and a very large ZORA value of 46 527 ppm.³⁹ MVS stated that Kohn–Sham based methods may have difficulty with radicals such as H_2O^+ , for which the HOMO and SOMO are nearly degenerate.³⁸ Lushington's closed-form CI results of -302 , $17\,300$, and 5133 ppm for the respective x , y , and z components⁴⁵ are in good agreement with experiment.

3. NO_2

As mentioned in the Introduction, NO_2 has been our test molecule in the development of the g -tensor methods, and the first ROHF⁵ as well as MRD-CI¹² calculations were done on this radical. Results obtained with the new methods are similar to our previous ones, and close to the experimental values. The major contributions to Δg_{xx} are 1^2B_2 , 3^2B_2 , and 5^2B_2 (in both basis sets), whereas Δg_{yy} derives almost exclusively from coupling with 1^2B_1 . Most other theoretical results are similar to the ones obtained here, and to the experimental values.

Not listed in Table II are spin-unrestricted GGA ZORA results by LWA of 4200, $-13\,800$, and -800 ppm for the x , y , and z components, respectively;⁴¹ and the closed-form CI results by Lushington of 3785, $-10\,071$, and -333 ppm, respectively.⁴⁵

4. CO_2^-

Like NO_2 , CO_2^- is a 17 VE radical. The Δg_{xx} component has sizeable contributions from 1^2B_2 , 2^2B_2 , and 5^2B_2 without DF's, but only from 1^2B_2 and 2^2B_2 with DF's in a 9-root calculation. Due to a large positive contribution of 5^2B_2 without DF's, Δg_{xx} is positive (655 ppm), close to the experimental values of 700 and 880 ppm, but differs drastically from the negative value of -1070 ppm obtained in the 9-root calculation with DF's. All other theoretical results for this component are positive. We, therefore, concluded that with diffuse functions the root corresponding to 5^2B_2 was missed, and should occur beyond 9^2B_2 . In a 20-root recalculation of the 2^2B_2 manifold for the basis set including diffuse functions, the equivalent to root 5^2B_2 without DF's was found as root 13. The latter root has $\langle L \rangle$, $\langle SO \rangle$, and ΔE values similar to its 5^2B_2 counterpart, and Δg_{xx} (20-root) becomes

3. METHODENENTWICKLUNG UND IMPLEMENTIERUNG

TABLE IV. Dominant second-order contributions from various excited states to Δg (ppm) for nonlinear molecules, in order of decreasing magnitude.

Radical	Component	Δg (a) ^a	Δg (b) ^a	Δg (c) ^a	Δg (total) ^a
$\text{HCO}(X^2A')$	$\Delta g_{xx}(^2A'')$ ^b	(4) -667 (6) -771	(6) 277 (7) 642	(3) 123 (1) -385	-620 -550
	$\Delta g_{yy}(^2A'')$ ^b	(1) -7652 (1) -7621	(2) 199 (2) 180	(4) -44 (6) -53	-7350 -7345
	$\Delta g_{zz}(^2A')$	(6) 1159 (6) 1109	(4) 542 (3) 461	(2) 466 (8) 459	2175 1875
$\text{H}_2\text{O}^+(X^2B_1)$	$\Delta g_{xx}(^2A_2)$	(1) 176 (1) 166	(2) -92 (2) -86	(4) -75 (4) -80	15 15
	$\Delta g_{yy}(^2A_1)$	(1) 16 186 (1) 15 853	(2) -154 (2) -148	(4) 38 (5) 22	16 025 15 710
	$\Delta g_{zz}(^2B_2)$	(1) 4470 (1) 4421	(2) -224 (2) -220	(9) 30 (9) 15	4210 4170
$\text{NO}_2(X^2A_1)$	$\Delta g_{xx}(^2B_2)$	(5) 2371 (5) 2407	(3) 763 (1) 651	(1) 760 (3) 346	3400 3600
	$\Delta g_{yy}(^2B_1)$	(1) -11 929 (1) -11 869	(2) 165 (2) 179	(4) 93 (4) -84	-11 830 -11 790
	$\Delta g_{zz}(^2A_2)$	(5) 1569 (3) -307	(4) -786 (1) -224	(6) -766 (8) -194	-440 -605
$\text{CO}_2^-(X^2A_1)^c$	$\Delta g_{xx}(^2B_2)$	(5) 1847 (2) -696 (13) 1068	(2) -540 (1) -292 (2) -652	(1) -349 (9) -89 (12) 375	655 -1070 560
	$\Delta g_{yy}(^2B_1)$	(1) -5280 (2) -3996 (2) -3657	(3) 199 (1) -671 (1) -815	(7) 58 (6) 195 (5) -207	-5080 -4615 -4530
	$\Delta g_{zz}(^2A_2)$	(8) -526 (1) -320 (1) -321	(1) -396 (9) -23 (20) 51	(4) 154 (6) -20 (12) -45	-1110 -385 -340
$\text{NF}_2(X^2B_1)$	$\Delta g_{xx}(^2A_2)$	(4) -2119 (8) -370	(5) 1627 (4) 224	(3) 655 (7) -144	-470 -90
	$\Delta g_{yy}(^2A_1)$	(1) 6332 (1) 6457	(6) -452 (3) -222	(2) 367 (9) 222	5985 6370
	$\Delta g_{zz}(^2B_2)$	(2) 1719 (5) 3112	(3) 1661 (2) 343	(5) 164 (3) 218	3220 3690
$\text{NO}_2^-(X^2B_1)^c$	$\Delta g_{xx}(^2A_2)$	(4) -436	(7) 338	(3) 286	-105
	$\Delta g_{yy}(^2A_1)$	(1) 230 (2) 278	(3) -155 (3) -199	(7) -53 (12) 196	70 100
	$\Delta g_{zz}(^2B_2)$	(1) 7129 (3) 6278 (3) 6903	(3) -521 (5) -736 (5) -557	(2) -306 (6) 543 (1) 302	6255 6535 6680
$\text{O}_3^-(X^2B_1)$	$\Delta g_{xx}(^2A_2)$	(2) -1299	(3) 980	(5) 135	-150
	$\Delta g_{yy}(^2A_1)$	(2) 160 (1) 15 495 (1) 16 113	(3) -130 (3) 540 (8) 675	(7) 47 (9) -453 (2) 277	20 15 915 16 890
	$\Delta g_{zz}(^2B_2)$	(1) 5523 (1) 5896	(4) 2400 (6) 4465	(3) 1730 (2) -172	10 385 10 360
$\text{ClO}_2(X^2B_1)$	$\Delta g_{xx}(^2A_2)$	(9) -409 (6) 319	(8) -266 (7) -252	(5) 252 (3) -146	-350 -40
	$\Delta g_{yy}(^2A_1)$	(1) 18 887 (1) 17 660	(2) -4276 (2) -6681	(3) 3026 (4) 2956	17 790 14 435
	$\Delta g_{zz}(^2B_2)$	(4) 9880 (4) 9403	(1) 4295 (2) -4256	(2) -3654 (1) 3666	11 740 9620
$\text{H}_2\text{CO}^+(X^2B_2)$	$\Delta g_{xx}(^2A_1)$	(1) 5541 (1) 5507	(4) 307 (4) 201	(3) -170 (3) -158	5840 5835
	$\Delta g_{yy}(^2A_2)$	(1) 1528 (1) 1467	(2) -1224 (2) -1216	(5) -51 (5) -47	240 200
	$\Delta g_{zz}(^2B_1)$	(1) 3718 (1) 3861	(2) -3412 (2) -3364	(3) -189 (3) -197	300 485
$\text{TiF}_3(X^2A_1)^d$	$\Delta g_{xx}(^2B_1)$	(1) -112 819	(7) 903	(3) -544	-112 560
	$\Delta g_{yy}(^2A_2)$	(1) -116 140	(8) -1671	(5) 1089	-116 910
	$\Delta g_{zz}(^2B_2)$	(6) -167	(2) 123	(7) -44	-90

^aRoot numbers in parentheses. First line=TZVPP, second line=TZVPP+DF basis set.

^b Δg_{xx} and Δg_{yy} before diagonalization.

^cThird line=TZVPP+DF basis set, 20 roots.

^dSVP basis set. TiF_3 has D_{3h} symmetry, with a $^2A'_1$ ground state; here, C_{2v} notation is used.

3.2. SPIN-BAHN-KOPPLUNG VON DFT/MRCI WELLENFUNKTIONEN

560 ppm, close to 655 ppm obtained without DF's. In Table IV, the 20-root results are given in the third row of each Δg_{ii} .

The Δg_{yy} component is dominated by 1^2B_1 (as for NO_3^-) without, but by 2^2B_1 with DF's. In the latter case, the 1^2B_1 state is mainly of diffuse character, as indicated by small $\langle L \rangle$ and $\langle SO \rangle$ contributions. A 20-root calculation hardly changes the 9-root result (Table IV).

Similar to the x -component, Δg_{zz} has several negative contributions above ± 100 ppm without DF's, but only one with DF's. The total Δg_{zz} is -1100 without, -385 ppm with DF's in a 9-root calculation, and -340 ppm in a 20-root calculation. The experimental results (-500 , -710 ppm) lie in between.

Theoretical literature values as reported in Table II range from 490 to 1522 ppm for Δg_{xx} , -4767 to -7210 ppm for Δg_{yy} , and from -571 to -969 ppm for Δg_{zz} .

5. NF_2

This radical has 19 VE's and a 2^2B_1 GS. The SOS for Δg_{xx} consists of positive and negative terms, resulting in a small total value, whereas Δg_{yy} is dominated by 1^2A_1 . For Δg_{zz} , however, the SOS has its largest contribution from 5^2B_2 when diffuse functions are used and from 2^2B_2 and 3^2B_2 without diffuse functions. Contrary to the case of H_2O^+ (also having a X^2B_1 GS), there is no contribution from 1^2B_2 . Such a shift in the leading excited states is probably caused by the fluorines introducing new low-lying and more diffuse excited states which are of little significance to Δg .

The small Δg_{xx} component has an experimental value of -100 ppm, being less negative than the calculated ones (except TZVPP+DF) that range from -447 to -758 ppm.

Our results for Δg_{yy} , 5985/6370 ppm, lie below and above the experimental value of 6200 ppm. Other theoretical results listed in Table II range from 5649 to 7619 ppm. Both of our calculated Δg_{zz} values lie above the experimental counterpart. Most of the DFT results are even higher. Only Jayatilaka's GHF result (2892 ppm)⁴⁰ is close to the experimental value of 2800 ppm.

6. NO_2^{2-}

This dianion is isoelectronic with NF_2 , and also has a 2^2B_1 GS. NO_2^{2-} is unstable with respect to the loss of an electron. The EPR spectra of NO_2^{2-} were obtained by irradiation of KNO_3 -doped KN_3 crystals.⁵¹

As before, the contributions to Δg_{xx} (from 2^2A_2 excited states) are small. Δg_{yy} is dominated by 1^2A_1 without diffuse functions and by 3^2A_1 with DF's, but $\Delta g_{yy}(\text{tot})$ is nearly the same for both basis sets. The 9-root results for Δg_{zz} (total) depend very much on the basis set: 3705 ppm without DF's versus 1335 ppm with (the experimental values are 4700–4800 ppm). The large difference can be explained by DF's introducing diffuse and low-lying excited states which are not contributing to Δg_{zz} , thereby pushing the needed valence states to higher roots or spreading them over diffuse states.

As for CO_2^- , the MRCI calculations with diffuse functions were redone for 20 roots. The results, given in the third line of Table IV, show little change for the xx and yy components, but Δg_{zz} moves from 1335 to 2700 ppm, closer to the non-DF result of 3705 ppm. Without diffuse functions, 1^2B_2 and 3^2B_2 make large positive contributions. With diffuse functions, and 9 roots, 1^2B_2 moves to 4^2B_2 , but 3^2B_2 has no equivalent. With 20 roots, 1^2B_2 corresponds to 9^2B_2 , which, however, is of mixed character, and 3^2B_2 corresponds to 19^2B_2 , the highest root we ever found to make a significant contribution to Δg . The essential ingredients, $\langle SO \rangle$, $\langle L \rangle$, and ΔE , have similar values for 3^2B_2 without, and 19^2B_2 with DF's.

The calculated Δg_{yy} , in both basis sets, compares well with experimental results. For Δg_{zz} , the TZVPP value is closer to the experimental one. For the small Δg_{xx} component, experimental values are much larger than the calculated ones, as has also been seen for the small component in other radicals.

SZ obtained a much larger Δg_{yy} , which lies well beyond the experimental results, and a Δg_{zz} which is close to the experimental value.³⁷ Their optimized geometry is very similar to ours.

7. O_3^-

This radical is also isoelectronic with NF_2 and NO_2^{2-} , and again has a 2^2B_1 ground state. Δg_{xx} is close to zero due to near cancellation of two large terms in the non-DF case, or small terms only in the DF case. Δg_{yy} is dominated by 1^2A_1 . Contrary to NO_2^{2-} , diffuse functions do not lead to any difficulties regarding missing 2^2B_2 states for O_3^- . With or without DF's, Δg_{zz} is about 10 400 ppm, although with DF's the major contributions come from 1^2B_2 and 6^2B_2 , whereas without DF's they are mainly due to 1^2B_2 , 3^2B_2 , and 4^2B_2 . O_3^- is obviously not as diffuse an anion as NO_2^{2-} , and the use of diffuse functions actually improves the convergence of the 2^2B_2 series.

The new results for Δg_{yy} and Δg_{zz} are in good agreement with the experimental and our MRD-CI⁵² as well as other theoretical results. Lacking first-order contributions, the new Δg_{xx} values are close to zero. Our previous MRD-CI value for Δg_{xx} is about -500 ppm, in line with other theoretical results, whereas both experimental numbers are positive.

8. ClO_2

Again, ClO_2 is a 19 VE radical, with a X^2B_1 GS. As for O_3^- , Δg_{xx} is composed of small terms only (see Table IV). The dominating contribution to Δg_{yy} from 1^2A_1 is similar in both basis sets. Large contributions also come from 2^2A_1 and 3^2A_1 (2^2A_1 and 4^2A_1 with DF's), which are of opposite sign and nearly cancel each other without DF's, but differ by about 3700 ppm with DF's, resulting in Δg_{yy} (tot) values that differ by 3355 ppm. For Δg_{zz} , the largest term derives from 4^2B_2 , but smaller terms due to 1^2B_2 and 2^2B_2 have opposite sign, nearly canceling each other. The difference between the 1^2B_2 and 2^2B_2 contribution is $\sim +600$ ppm without DF's and -600 ppm with DF's, giving

3. METHODENENTWICKLUNG UND IMPLEMENTIERUNG

Δg_{zz} (tot)'s of 11 740 and 9620 ppm, respectively. Our results for Δg_{zz} , as well as those of SZ and Neese, are close to the experimental Ne matrix value of 10 200 ppm,⁵³ which differs significantly from the result in a KClO_4 host crystal (6500 ppm).⁵⁴

The MCSCF response theory AMFI results of Vahtras *et al.*²⁸ are in good agreement with experimental values for Δg_{xx} (30 ppm) and Δg_{yy} (13 690 ppm), but Δg_{zz} (17 690 ppm) is poor; their results are virtually identical to those obtained in a full spin-orbit calculation (210, 13 730, and 17 800 ppm, respectively).²⁸

9. H_2CO^+

The ground state of H_2CO^+ is X^2B_2 . The Δg results with or without DF's are similar. The Δg_{xx} component is dominated by 1^2A_1 , whereas Δg_{yy} has large contributions from 1^2A_2 and 2^2A_2 , of opposite sign, resulting in a small Δg_{yy} of about 200 ppm. A similar situation is encountered for Δg_{zz} , where 1^2B_1 and 2^2B_1 nearly cancel, resulting in $\Delta g_{zz}=300/485$ ppm. When including the first-order contributions of about -300 ppm for each component, as calculated in our previous work,¹⁵ the total Δg 's are now about 5550, -50, and 0 ppm for the three components, respectively. While the first two agree with our previous results,¹⁵ Δg_{zz} was then calculated to be 1296 ppm. In second order, the positive contribution from 1^2B_1 was somewhat larger, and the negative one smaller in magnitude such that the sum of the two terms (1530 ppm) was more than three times the sum we obtained here. While we find no big changes in the individual ΔE , $\langle \text{SO} \rangle$ and $\langle L \rangle$ values, the required expressions ($\langle \text{SO} \rangle \langle L \rangle / \Delta E$) just happen to develop in opposite ways.

Although the new Δg_{zz} of about 0 ppm is closer to the experimental (matrix) value of 200 ppm than the formerly obtained 1296 ppm, in the previous paper¹⁵ we suggested that the gas phase (rather than matrix) Δg 's should be about 5500, 100, and 1100 ppm, respectively, based on an estimate of matrix effects given in the experimental paper.⁵⁵ Therefore, Δg_{zz} of 1296 ppm is closer to the estimated gas phase Δg_{zz} than our new value. Most likely, the final word on this problem has not yet been spoken.

For the large Δg_{xx} component other theoretical results, listed in Table II, are similar to ours. For Δg_{yy} , SZ and Neese are in reasonably good agreement with the experimental value of -800 ppm, whereas Jayatilaka's result is positive and relatively large. For Δg_{zz} , SZ and Neese obtained results close to zero, but Jayatilaka's value is very large. Not listed in Table II are the closed-form CI results of Lushington, which gave reasonable values for Δg_{xx} (6252 ppm) and Δg_{yy} (-326 ppm), but a poor result for Δg_{zz} (4219 ppm).⁴⁵

10. TiF_3

TiF_3 has D_{3h} symmetry with a $2^2A'_1$ GS; Δg_{xx} and Δg_{yy} result from coupling with $2^2E''$ excited states. Our Δg calculations were done in C_{2v} symmetry (X^2A_1), such that the degenerate Δg_{xx} and Δg_{yy} (Δg_{\perp}) derive from coupling of X^2A_1 with 2^2A_2 and 2^2B_1 states, respectively, and Δg_{zz} (Δg_{\parallel}) from coupling with 2^2B_2 states. For checking the accuracy of our calculations, we evaluated Δg_{\perp} for both 2^2A_2 and 2^2B_1

states. Due to the independent selection of reference configurations and extrapolation for 2^2A_2 and 2^2B_1 states, slightly different values were obtained for Δg_{xx} and Δg_{yy} , as shown in Table IV (the degenerate components of Δg will always be called Δg_{xx} and Δg_{yy} , and the nondegenerate one Δg_{zz} , corresponding to the D_{3h} notation).

The calculations were performed with Schäfer *et al.* SVP basis set,⁵⁶ having valence double-zeta plus polarization character, at a configuration selection threshold of 1 μh (before always 5 μh), for nine roots of each irreducible representation. Only the $4s$ and $3d$ electrons of Ti, and the $2p$ electrons of F, were left open for excitations, resulting in 19 VE's.

The 2^2B_1 , 2^2B_2 , and 2^2A_2 states in C_{2v} symmetry also include D_{3h} states that are not coupling to the GS, such as A'_2 , A''_1 , A''_2 , and E' , which, however, are characterized by a low $\langle L \rangle$ (ideally zero) and, therefore, should make no, or insignificant, contributions to the total Δg .

The $2^2B_1/2^2A_2$ degeneracy can be verified for most roots (see Table IV). Root 1 makes by far the largest contribution, with -112.8 and -116.1 ppt (parts per thousand) for 1^2B_1 and 1^2A_2 , respectively. The corresponding ΔE , $\langle \text{SO} \rangle$ and $\langle L \rangle$ are 0.644 eV, -98.5 cm^{-1} and 1.447 a.u. for 1^2B_2 , and 0.624 eV, -98.3 cm^{-1} , and 1.446 a.u. for 1^2A_2 , are indeed in excellent agreement with each other, supporting the high level of CI calculations. Adding contributions from the other 8 roots leads to $\Delta g_{xx} = -112.6$ ppt for 2^2B_1 , and $\Delta g_{yy} = -116.9$ ppt for 2^2A_2 , for an average of -114.7 ppt.

For the parallel component Δg_{zz} , all roots of 2^2B_2 have small contributions, none larger than 170 ppm. The SOS gives -90 ppm. Since the experimental Δg_{\parallel} is -11.1 or -3.7 ppt, and other calculated values are in the order of -1 ppt, we decided to investigate the contributions due to first-order perturbation theory. First-order values calculated for main group systems are usually small, in the order of -100 to -200 ppm, however they may be much larger for transition metals. Using the GSTEPS package^{5,7} which is based on ROHF wave functions, we obtained in first-order $\Delta g_{xx} = \Delta g_{yy} = -0.6$ ppt and $\Delta g_{zz} = -0.8$ ppt. Adding the ROHF first-order contributions to the new MRCI second-order results gives final calculated values of -115.3 ppt for the in-plane, and -0.9 ppt for the out-of-plane components of Δg . The latter value is in good agreement with results obtained by other researchers.

It is interesting to note that most of the DFT results for the perpendicular component are close to our ROHF value (-55.5 ppt for first- and second-order perturbation), such as the B3PW91 result by KRM (-48.8 ppt),²⁷ the value of -42.8 ppt by LWA⁴¹ using the DFT-GIAO programs of SZ,³⁷ or the B3LYP result of -46.1 ppt by Neese (better than the BP86 value of -30.7 ppt given in Table II).³⁹ The best literature values are those by Belanzoni *et al.*,⁵⁷ with $\Delta g_{\perp} = -97.5$ ppt and $\Delta g_{\parallel} = 0.5$ ppt.

IV. DISCUSSION

For most radicals, calculations were performed with two basis sets, one being TZVPP (SVP for TiF_3), the other TZVPP with added diffuse functions. In general, diffuse

3.2. SPIN-BAHN-KOPPLUNG VON DFT/MRCI WELLENFUNKTIONEN

functions give rise to additional excited states of diffuse character, which do not contribute much to Δg , but may slow the rate of the SOS convergence. For diatomic radicals, differences in Δg only show for AlO, where TZVPP+DF results are closer to our previous MRD-CI value. Since, however, Δg_{\perp} of AlO is a highly sensitive property, as outlined earlier, and since the MRD-CI results were obtained with natural orbitals, the good agreement may be fortuitous, and a conclusion about which basis set is better should not be drawn for this case. For ZnH and ZnF, only the TZVPP basis set was used.

Problems encountered in the initial 9-root calculations for Δg_{xx} of CO_2^- and Δg_{zz} of NO_2^- were addressed by allowing for 20 roots in the TZVPP+DF basis set. Hereby, Δg_{xx} of CO_2^- moves from -1070 to +560 ppm, close to 655 ppm obtained with TZVPP, and Δg_{xx} of NO_2^- changes from 1335 to 2700 ppm: Closer to, but still well below, the TZVPP result of 3705 ppm.

We now like to compare the new results with those previously obtained by Grein and co-workers, available for nine of the 19 radicals studied here. Both methods employ multi-reference wave functions, with the new method using approximations in the treatment of two-electron integrals and in the evaluation of spin-orbit matrix elements.

A look at Table III reveals significant differences only for Δg_{zz} of H_2CO^+ , where the new results of about 300–400 ppm are compared with about 1300 ppm obtained earlier. As mentioned in the previous section, we believe that the MRD-CI result is closer to the experimental *gas-phase* value, although this hypothesis needs confirmation.

Besides this drastic case, there are several instances of 10%–20% differences, like Δg_{\perp} (CO^+) being about -2100 ppm with the new, and about -2600 ppm with the old method. Unfortunately, at this time we cannot say which results are better, as most experimental values show deviations of this magnitude. It is hoped that more definitive gas-phase values will become available in the future, allowing for refinements in the theoretical treatment.

Finally, the new results presented here may be compared with other theoretical results. Such comparison has been made in the previous section for individual radicals. Comparison with density functional results is often difficult due to the strong dependence of such results on the particular functional used, which reduces the predictive value of the method. For a particular approach, some functionals give results in good agreement with ours, but other functionals lead to quite different values.

A comparison with other correlated *ab initio* results can only be made for ClO_2 and O_2 . For ClO_2 , the MCSCF response function method leads to values for Δg_{xx} and Δg_{yy} which are similar to ours, but shows a large deviation from the experimental and from our result for Δg_{zz} . It is not clear what causes such error. For O_2 , the agreement is good.

A comparison with noncorrelated *ab initio* results can be made for the molecules examined by Jayatilaka, using a general Hartree-Fock method (see Table II). Overall, the results agree well with experiment, but Δg_{yy} and Δg_{zz} for both H_2CO^+ and H_2O^+ are, as Jayatilaka states, “qualitatively wrong.”⁴⁰

V. SUMMARY AND CONCLUSIONS

In this work, g -tensors were calculated for 16 main group radicals and three transition metal compounds, using explicit term-by-term calculations in second-order perturbation theory. In the sum-over-states expression, wave functions and energies were determined by means of the efficient MRCI method, due to Grimme and Waletzke. For the evaluation of spin-orbit matrix elements, we used the new Spock code that employs an effective one-electron spin-orbit operator and thus avoids the explicit treatment of the expensive two-electron terms of the spin-orbit operator.

The results obtained are of similar quality (as far as comparison is possible) as those obtained by us earlier using the MRD-CI method of Peyerimhoff and Buenker, in connection with an explicit calculation of the two-electron part of the spin-orbit operator. Agreement with experimental values is good. For all radicals except ZnH, ZnF, and TiF_3 , we performed calculations for two basis sets: One without, and one with diffuse functions. In two instances, inferior results obtained with diffuse functions in a 9-root CI treatment could be traced to missing valence states. Such problems have been dealt with by performing 20-root calculations.

Comparison with theoretical literature values, mostly obtained with density-functional methods, was made; our results are generally similar or superior. A problem with DFT methods is the large variation of the calculated Δg results, depending on the functional used.

The new MRCI methods tested here have been applied to gallium arsenide clusters Ga_mAs_n ($m+n=3, 5$), and to other group 13/15 clusters. Publications on such work are forthcoming. We are confident that with these new methods g -tensors for systems with 40 to 50 valence electrons can be reliably calculated.

ACKNOWLEDGMENTS

The authors are much indebted to the U.S. Air Force Office of Scientific Research (AFOSR) in Arlington, VA, and Major Daniel K. Johnstone, for a research grant to S.B. and F.G. which made this work possible. We also like to thank Dr. Shashi Karna for his help, encouragement, and discussions. Financial support by NSERC (Canada) is gratefully acknowledged. J.T. and M.K. received financial support from the Deutsche Forschungsgemeinschaft via project Ma 1051/5-1. Many thanks to Professor Stefan Grimme, at the University of Muenster, for making his MRCI package available to us, and to Dr. Pablo Bruna for helpful discussions and valuable suggestions on improving the manuscript.

¹W. H. Moores and R. McWeeney, Proc. R. Soc. London, Ser. A **332**, 365 (1973).

²B. Engels, L. A. Eriksson, and S. Lunell, Adv. Quantum Chem. **27**, 298 (1996).

³J. E. Harriman, *Theoretical Foundations of Electron Spin Resonance* (Academic, New York, 1978).

⁴G. H. Lushington, Ph.D. thesis, University of New Brunswick, Fredericton, NB, Canada, 1996.

⁵G. H. Lushington, P. Bündgen, and F. Grein, Int. J. Quantum Chem. **55**, 377 (1995).

⁶P. Bündgen, G. H. Lushington, and F. Grein, Int. J. Quantum Chem., Quantum Chem. Symp. **29**, 283 (1995).

⁷G. H. Lushington and F. Grein, Theor. Chim. Acta **93**, 259 (1996).

3. METHODENENTWICKLUNG UND IMPLEMENTIERUNG

- ⁸G. H. Lushington, P. J. Bruna, and F. Grein, *Z. Phys. D: At., Mol. Clusters* **36**, 301 (1996).
- ⁹A. V. Luzanov, E. N. Babich, and V. V. Ivanov, *J. Mol. Struct.: THEOCHEM* **311**, 211 (1994).
- ¹⁰R. J. Buenker and S. D. Peyerimhoff, *Theor. Chim. Acta* **35**, 33 (1974); **39**, 217 (1975); R. J. Buenker, S. D. Peyerimhoff, and W. Butscher, *Mol. Phys.* **35**, 771 (1978); R. J. Buenker, in *Current Aspects of Quantum Chemistry, Studies in Physical and Theoretical Chemistry*, edited by R. Carbo (Elsevier, Amsterdam, 1982), Vol. 21, p. 17; C. M. Marian, Ph.D. thesis, Bonn, Germany, 1981; B. A. Hess, Ph.D. thesis, Bonn, Germany, 1981; P. Chandra and R. J. Buenker, *J. Chem. Phys.* **79**, 358 (1983).
- ¹¹G. H. Lushington and F. Grein, *Int. J. Quantum Chem.* **60**, 1679 (1996).
- ¹²G. H. Lushington and F. Grein, *J. Chem. Phys.* **106**, 3292 (1997).
- ¹³P. J. Bruna and F. Grein, *Int. J. Quantum Chem.* **77**, 324 (2000).
- ¹⁴P. J. Bruna and F. Grein, *J. Phys. Chem. A* **105**, 3328 (2001).
- ¹⁵P. J. Bruna, G. H. Lushington, and F. Grein, *J. Mol. Struct.: THEOCHEM* **527**, 139 (2000).
- ¹⁶S. Grimme and M. Waletzke, *J. Chem. Phys.* **111**, 5645 (1999); S. Grimme and M. Waletzke, *Phys. Chem. Chem. Phys.* **2**, 2075 (2000).
- ¹⁷R. Ahlrichs, M. Bär, M. Häser, H. Horn, and C. Kölmel, *Chem. Phys. Lett.* **162**, 165 (1989).
- ¹⁸O. Vahtras, J. Almlöf, and M. W. Feyereisen, *Chem. Phys. Lett.* **213**, 514 (1993); F. Weigend and M. Häser, *Theor. Chem. Acc.* **97**, 331 (1997); F. Weigend, M. Häser, H. Patzelt, and R. Ahlrichs, *Chem. Phys. Lett.* **294**, 143 (1998).
- ¹⁹M. Kleinschmidt, J. Tatchen, and C. M. Marian, *J. Comput. Chem.* **23**, 824 (2002).
- ²⁰B. A. Hess, C. M. Marian, U. Wahlgren, and O. Gropen, *Chem. Phys. Lett.* **251**, 365 (1996).
- ²¹D. Danovich, C. M. Marian, T. Neuheuser, S. D. Peyerimhoff, and S. Shaik, *J. Phys. Chem. A* **102**, 5923 (1998).
- ²²J. Tatchen and C. M. Marian, *Chem. Phys. Lett.* **313**, 351 (1999).
- ²³B. Schimmelpfennig, AMFI: An atomic spin-orbit mean-field integral program, University of Stockholm, Sweden, 1996.
- ²⁴O. L. Malkina, B. Schimmelpfennig, M. Kaupp, B. A. Hess, P. Chandra, U. Wahlgren, and V. G. Malkin, *Chem. Phys. Lett.* **296**, 93 (1998).
- ²⁵O. Christiansen, J. Gauss, and B. Schimmelpfennig, *Phys. Chem. Chem. Phys.* **2**, 965 (2000).
- ²⁶K. Ruud, B. Schimmelpfennig, and H. Ågren, *Chem. Phys. Lett.* **310**, 215 (1999).
- ²⁷M. Kaupp, R. Reviakine, O. L. Malkina, A. Arbuznikov, B. Schimmelpfennig, and V. G. Malkin, *J. Comput. Chem.* **23**, 794 (2002).
- ²⁸P. Vahtras, M. Engström, and B. Schimmelpfennig, *Chem. Phys. Lett.* **351**, 424 (2002).
- ²⁹M. J. Frisch, G. W. Trucks, H. B. Schlegel *et al.* GAUSSIAN 98, Revision A.9, Gaussian, Inc., Pittsburgh, PA, 1998.
- ³⁰P. J. Bruna, G. H. Lushington, and F. Grein, *Chem. Phys.* **225**, 1 (1997).
- ³¹P. J. Bruna and F. Grein, *J. Phys. Chem. A* **102**, 3141 (1998).
- ³²S. R. Langhoff and E. R. Davidson, *Int. J. Quantum Chem.* **8**, 61 (1974).
- ³³A. Schäfer, C. Huber, and R. Ahlrichs, *J. Chem. Phys.* **100**, 5829 (1994).
- ³⁴T. H. Dunning, Jr., *J. Chem. Phys.* **90**, 1007 (1989).
- ³⁵D. E. Woon and T. H. Dunning, Jr., *J. Chem. Phys.* **98**, 1358 (1993).
- ³⁶R. A. Kendall, T. H. Dunning, Jr., and R. J. Harrison, *J. Chem. Phys.* **96**, 6796 (1992).
- ³⁷G. Schreckenbach and T. Ziegler, *J. Phys. Chem. A* **101**, 3388 (1997).
- ³⁸O. L. Malkina, J. Vaara, B. Schimmelpfennig, M. Munzarová, V. G. Malkin, and M. Kaupp, *J. Am. Chem. Soc.* **122**, 9206 (2000).
- ³⁹F. Neese, *J. Chem. Phys.* **115**, 11080 (2001).
- ⁴⁰D. Jayatilaka, *J. Chem. Phys.* **108**, 7587 (1998).
- ⁴¹E. van Lenthe, P. E. S. Wormer, and A. van der Avoird, *J. Chem. Phys.* **107**, 2488 (1997).
- ⁴²P. Belanzoni, E. van Lenthe, and E. J. Baerends, *J. Chem. Phys.* **114**, 4421 (2001).
- ⁴³H. M. Quiney and P. Belanzoni, *Chem. Phys. Lett.* **353**, 253 (2002).
- ⁴⁴O. Vahras, B. Minaev, and H. Ågren, *Chem. Phys. Lett.* **281**, 186 (1997).
- ⁴⁵G. H. Lushington, *J. Phys. Chem. A* **104**, 2969 (2000).
- ⁴⁶C. M. Marian, *Ber. Bunsenges. Phys. Chem.* **99**, 254 (1995).
- ⁴⁷L. B. Knight and W. Weltner, Jr., *J. Chem. Phys.* **55**, 5066 (1971).
- ⁴⁸S. Patchkovskii and T. Ziegler, *J. Phys. Chem. A* **105**, 5490 (2001).
- ⁴⁹W. Weltner, Jr., *Magnetic Atoms and Molecules* (Van Nostrand Reinhold, New York, 1983).
- ⁵⁰A. J. McKinley, E. Karakyriacos, L. B. Knight, Jr., R. Babb, and A. Williams, *J. Phys. Chem. A* **104**, 3528 (2000).
- ⁵¹A. Reuveni, R. Poupko, and Z. Luz, *J. Magn. Reson.* **18**, 358 (1975).
- ⁵²P. J. Bruna and F. Grein, *J. Chem. Phys.* **109**, 9439 (1998).
- ⁵³C. A. McDowell, P. Raghunathan, and J. C. Tait, *J. Chem. Phys.* **59**, 5858 (1973).
- ⁵⁴W. Gordy, *Theory and Application of Electron Spin Resonance Spectroscopy* (Wiley, New York, 1978).
- ⁵⁵L. B. Knight and J. Steadman, *J. Chem. Phys.* **80**, 1018 (1984).
- ⁵⁶A. Schäfer, H. Horn, and R. Ahlrichs, *J. Chem. Phys.* **97**, 2571 (1992).
- ⁵⁷P. Belanzoni, E. J. Baerends, S. van Asselt, and P. B. Langewen, *J. Phys. Chem.* **99**, 13094 (1995).

3.3 Spin-Bahn CI

Die Arbeit „SPOCK.CI: A Multi-Reference Spin-Orbit Configuration Interaction Method for Large Molecules“ („SPOCK.CI: Eine Multireferenz-Spin-Bahn-Wechselwirkungsmethode für große Moleküle“) behandelt Spin-Bahn-Konfigurationswechselwirkung, also die gleichzeitige variationelle Behandlung von Spin-Bahn-Wechselwirkung und nichtrelativistischem elektronischem Hamilton-Operator. Sie gliedert sich in einen programmtechnischen Teil, der Aspekte der Implementierung des Spin-Bahn-CI und der daran angeschlossenen Module zur Berechnung von Eigenschaften¹ beschreibt, sowie einen Anwendungsteil.

Ein Spin-Bahn-CI hat gegenüber der störungstheoretischen Behandlung der Spin-Bahn-Kopplung Vorteile bei sehr schweren Elementen, sowie bei der Berechnung von Eigenschaften. Bei der störungstheoretischen Behandlung sind die Wellenfunktionen der spinfreien Zustände eingefroren, das heißt sie können nicht auf den Einfluss des Spin-Bahn-Operators reagieren. Eine Relaxation der Wellenfunktion ist jedoch in Verbindungen mit schweren Elementen unabdingbar, wie am Beispiel des PbH oder TlH gezeigt wurde[41; 42]. Anstelle des Spin-Bahn-CI könnte zwar auch eine sehr große Störungsrechnung, also eine mit sehr vielen störenden Zuständen treten, jedoch ist der Aufwand dafür groß und die Konvergenz fraglich.

Auch bei der Berechnung von Eigenschaften mit ungestörten Wellenfunktionen ist die Konvergenz mit der Zahl der störenden Zustände oft schlecht und vor allem schlecht abschätzbar. Hier bietet das Spin-Bahn-CI die Möglichkeit, die Zustandssumme zu vermeiden.

3.3.1 Programmtechnischer Teil

Die Implementierung des Spin-Bahn-CI umfasst mehrere Teile:

- Den Aufbau der Startvektoren
- Die Berechnung des Produkts der Testvektoren mit der Hamiltonmatrix
- Die Diagonalisierung

3.3.1.1 Aufbau der Startvektoren

Für den Aufbau eines Startvektors werden die spinfreien CI-Vektoren aller Zustände aus dem DFT/MRCI mit den Koeffizienten des entsprechenden in SPOCK.PT erhaltenen störungstheoretischen Eigenvektors multipliziert. Der dabei entstehende komplexwertige Vektor umfasst bereits alle beteiligten Multiplizitäten und Symmetrien. Ein Start mit ungestörten Zuständen ist auch möglich. Dazu werden die spinfreien DFT/MRCI-Zustände mit entsprechend vielen Nullen auf die vollständige Dimension gebracht. Ein vollständiger Neustart mit Einheitsvektoren als Startvektoren ist nicht vorgesehen.

3.3.1.2 Berechnung des Matrix-Vektor-Produkts

Zur Multiplikation der Testvektoren mit der Spin-Bahn-CI-Matrix werden der spinfreie Hamiltonoperator und der Spin-Bahn-Operator nacheinander angewendet. Zunächst wirkt

¹Diese wurden von Jörg Tatchen im Rahmen seiner Dissertation geschrieben.

der spinfreie Operator auf die Blöcke gleichen Spins und gleicher Multiplizität. Die Routinen aus dem DFT/MRCI konnten hierzu weitgehend unverändert übernommen werden. Der einzige Unterschied zum DFT/MRCI ist die gleichzeitige Anwesenheit aller Multiplett-komponenten sowie die Komplexwertigkeit der Vektorkoeffizienten.

Bei der Anwendung des Spin-Bahn-Operators wurde von den Routinen zur Matrixelementberechnung des SPOCK.PT ausgegangen. Auch hier sind die Änderungen dann nur noch gering. Zusätzlich zu den Spin-Bahn-Integralen und den Spinkopplungskoeffizienten müssen auch die Matrizen mit den *scaled-3j-symbols*, sowie die Ergebnisvektoren bis in die innerste Schleife weitergereicht werden. Dort wird dann, statt zum Spin-Bahn-Matrixelement aufzusummen, der jeweils errechnete Eintrag der Hamiltonmatrix mit den Vektoren multipliziert und auf den Ergebnisvektor addiert. An dieser Stelle ist groÙe Sorgfalt vonnöten, da viele Quellen für Vorzeichenwechsel korrekt berücksichtigt werden müssen. Neben den Spin-Bahn-Integralen selbst, die im Gegensatz zu den Coulombintegrale antisymmetrisch sind, treten weitere Vorzeichenwechsel auf: aus der Berücksichtigung der Unterfälle der Spinkopplung, durch die komplexe Arithmetik (evtl. Faktor $i^2 = -1$), aus den *scaled-3j-symbols*, sowie aus implementierungstechnischen Details, da das „obere“ und „untere“ Dreieck der Matrix mit den gleichen Routinen behandelt werden.

3.3.1.3 Diagonalisierung der komplexen Matrix

Eine vollständige, exakte Diagonalisierung der CI Matrix ist nur etwa bis zu einer GröÙenordnung von etwa 10^3 bis 10^4 möglich. Für größere Matrizen scheitert dies sowohl an der Rechenzeit als auch am Speicherbedarf für die Matrix bzw. die Eigenvektoren. Da die zu behandelnden Matrizen in der Quantenchemie deutlich größer sind — im vorliegenden Programm wird eine GröÙenordnung von 10^5 bis 10^7 angestrebt — müssen Näherungsmethoden angewandt werden.

Die Mathematik kennt eine Vielzahl von Methoden zur genäherten Berechnung von Eigenwerten und Eigenvektoren groÙer Matrizen, eine umfassende Übersicht findet sich in [43]. Einer der erfolgreichsten und für quantenchemische Probleme am besten geeigneten Algorithmen ist der Davidson–Algorithmus[44]. Er wurde in seiner ursprünglichen Form vom Quantenchemiker E. R. Davidson für CI–Rechnungen entwickelt. Seitdem hat er nicht nur in der theoretischen Chemie weite Verbreitung gefunden. Wichtige Erweiterungen aus quantenchemischer Sicht sind das *root-homing*[45], also die Möglichkeit, für eine bestimmte einzelne Wurzel direkt zu lösen, sowie das *multi-root*-Verfahren[46; 47]. Letzteres bietet die Möglichkeit, mehrere Zustände an einem Ende des Spektrums gleichzeitig zu finden.

Der Davidson–Algorithmus ist ein Projektions–Methode. Dabei wird die große zu diagonalisierende Matrix A auf einen Unterraum K mit Dimension k projiziert. Aus den Testvektoren \mathbf{b}_i ergibt sich die Projektionsmatrix zu:

$$\tilde{A}_{ij} = (\mathbf{b}_i, H\mathbf{b}_j) \quad (3.43)$$

Kennt man einen genäherten Eigenvektor \mathbf{b}_i der Matrix H , so erfüllt er nicht die Eigenwertgleichung, sondern es bleibt ein Restvektor $\mathbf{r} \neq 0$ bestehen:

$$(H - e_i) \mathbf{b}_i = \mathbf{r}, \quad (3.44)$$

Setzt man nun

$$\tilde{\mathbf{b}}_i = \mathbf{b}_i - (H - e_i)^{-1} \mathbf{r}, \quad (3.45)$$

so ist $\tilde{\mathbf{b}}_i$ Eigenvektor von H . Zwar ist es ebenso schwierig, die Inverse zu H bzw. zu $(H - e_i)$ zu berechnen wie die Eigenwerte zu H , jedoch ergibt sich hier eine Möglichkeit, eine Näherung einzuführen.

Die in der Quantenchemie vorkommenden Matrizen sind diagonal dominant: Auf und in der Nähe der Diagonalen stehen die größten Zahlen. Ersetzt man nun bei der Invertierung die Matrix H durch ihre Diagonale D_H , also $(H - e_i)^{-1}$ durch $(D_H - e_i)^{-1}$, so bleibt lediglich die (triviale) Invertierung einer Diagonalmatrix übrig, man erhält aber auch nur einen genäherten Korrekturvektor. Dennoch ist diese Näherung recht gut, und in typischen Fällen werden etwa acht bis zwölf Iterationen bis zur Konvergenz benötigt.

3.3.2 Orthogonalitätsprobleme

Voraussetzung für die Anwendbarkeit des Davidson-Algorithmus ist eine reelle symmetrische oder komplexe hermitische Matrix. Bei der Diagonalisierung einer komplexwertigen Matrix kann diese durch eine doppelt so große reelle Matrix ersetzt werden. Dieser Ansatz war vom SPDIAG des BNSOC bekannt[48] und wurde auch zunächst in SPOCK.CI implementiert. Der Vorteil dieses Vorgehens liegt darin, dass komplexe Arithmetik in der Implementierung vermieden wird. Dieser Vorteil ist bei genauer Betrachtung keiner, denn bei allen Operationen, außer der Orthogonalisierung, wird genau die gleiche Anzahl an Rechenschritten ausgeführt. Die vermeintliche Einsparung bei der Orthogonalisierung entpuppt sich jedoch als Fehler, der in Fällen mit entarteten Eigenwerten zu nicht-orthogonalen Eigenvektoren führen kann. Diese Problematik ist im Anhang der Veröffentlichung zum SPOCK.CI ausführlich erläutert.

Da sich das Phänomen erst zeigt, wenn mit den CI-Vektoren Eigenschaften berechnet werden, und auf die erhaltenen Energiewerte keinen Einfluss hat, wurde es im SPDIAG nicht entdeckt, denn mit diesem Programm wurden nie Eigenschaften mit den erhaltenen Spin-Bahn-CI-Vektoren berechnet.

Zur Behebung dieses Fehlers wäre es eigentlich ausreichend, die Orthogonalisierung entsprechend anzupassen. Der Rest der Davidson-Implementierung müsste nicht geändert werden. Das im SPOCK.CI ursprünglich verwendete Davidson-Unterprogramm war dem DFT/MRCI Programm entnommen und für das Spin-Bahn-CI modifiziert worden. Auch die im DFT/MRCI verwendete Version war schon aus einem anderen Programm abgeleitet worden und der Programmcode trug viele Altlasten mit sich. Für SPOCK.CI wurde daher eine komplett neue Implementierung des Davidson-Algorithmus vorgenommen. Der Code ist dabei allgemein gehalten, und es kann aus dem gleichen Quelltext wahlweise eine reelle, oder eine komplexe Version kompiliert werden. Dem Algorithmus kann per Parameter mitgeteilt werden, wie viel Arbeitsspeicher er für die Vektoren verwenden darf. Die Mindestanforderung sind hierbei zwei komplette SOCI-Vektoren. Steht ausreichend Speicher zur Verfügung, so werden alle Vektoren im Multi-Root-Verfahren gleichzeitig behandelt. Reicht der Speicher dafür nicht aus, so werden die einzelnen Schritte des Algorithmus' in jeder Iteration mehrfach jeweils mit einem Teil der Vektoren durchgeführt.

3.3.3 Testrechnungen und Anwendungen

Die grundsätzliche Funktionsfähigkeit des Spin-Bahn-CI Programms wurde anhand von Testrechnungen an Metallatomen der 3. Periode verifiziert. Hierbei wurde weniger Wert auf gute Übereinstimmung mit experimentellen Daten gelegt, als vielmehr darauf geachtet,

dass die Reihenfolge und Entartungen der einzelnen Feinstruktur niveaus korrekt reproduziert werden. Dies ist ein exzellerter Test für die gesamte Programmlogik. Alle Integrale und Spinkopplungen müssen korrekt verarbeitet werden, um korrekte Ergebnisse zu produzieren. Die Rechnungen am Arsenatom wurden im Artikel über Spinkopplungskoeffizienten publiziert.[28] Sie zeigen eine, im Rahmen der Konvergenz, perfekte Entartung der einzelnen Niveaus. Rechnungen an Übergangsmetallatomen mit anderen Multiplizitäten zeigten ebenso gute Resultate, sodass von einer technischen Funktionsfähigkeit des Programms ausgegangen werden konnte.

An weiteren Testrechnungen am Dithiosuccinimid und am Pyranthion wurden wesentliche Eigenschaften des neuen Programms einer Prüfung unterzogen. Die Rechnungen zum Porphyrin, die ebenfalls in der Arbeit über SPOCK.CI veröffentlicht sind, werden bei den Anwendungen im Kapitel 4.5 besprochen.

3.3.3.1 Dithiosuccinimid

Das Dithiosuccinimid wurde in einer eigenständigen Publikation[49] eingehend untersucht (siehe Abschnitt 4.3). In der Veröffentlichung zu SPOCK.CI diente es als Testfall, um die Konvergenz des Spin-Bahn-CI mit der störungstheoretischen Behandlung zu vergleichen. Während die Ergebnisse mit Spin-Bahn-CI sich für die drei Rechnungen in unterschiedlich großen CI-Räumen nur wenig unterscheiden, ist das störungstheoretische Ergebnis in der kleinsten durchgeföhrten Rechnung noch weit von der Konvergenz entfernt. Es nähert sich in den größeren Räumen zwar den Ergebnissen des Spin-Bahn-CI an, erreicht dieses jedoch auch in der umfangreichsten Rechnung nicht vollständig. Hier zeigt sich also sehr schön die Überlegenheit des variationellen Ansatzes zur Berechnungen von Eigenschaften auch in leichten Molekülen.

3.3.3.2 Pyranthion

Auch für SPOCK.CI wurde nochmals das Pyranthion als Testbeispiel gewählt. An diesem Molekül wurde der Einfluss des Konvergenzkriteriums im Spin-Bahn-CI auf die Ergebnisse untersucht. Da das Spin-Bahn-CI mit den konvergierten spinfreien Vektoren startet, die darüber hinaus auch bereits störungstheoretisch miteinander gekoppelt wurden, sind die im SOCI zu erwartenden Änderungen der Energie gering. Das Konvergenzkriterium des Spin-Bahn-CI basiert jedoch ausschließlich auf Energieänderung. Ein zu grob gewähltes Konvergenzkriterium könnte hier also dazu führen, dass das Spin-Bahn-CI abbricht, bevor die Vektoren ausreichend relaxieren konnten. In den Ergebnissen zeigt sich, dass die Auswirkungen gering sind, ein Konvergenzkriterium von $5 * 10^{-7} E_h$ erscheint ausreichend.

Der Vergleich einer kleinen und einer großen Störungstheorie-Rechnung am Pyranthion mit den entsprechenden SOCI-Ergebnissen zeigt auch hier die deutliche Überlegenheit des Spin-Bahn-CI-Ansatzes. Auch wenn die Spin-Bahn-CI-Rechnung mit nur 8 LS Zuständen (1 Zustand pro Spinsymmetrie) noch nicht vollständig konvergiert ist, so ist sie doch wesentlich näher am Ergebnis für 48 LS-Zustände als die störungstheoretische Rechnung.

3.3. SPIN-BAHN CI

THE JOURNAL OF CHEMICAL PHYSICS 124, 124101 (2006)

SPOCK.CI: A multireference spin-orbit configuration interaction method for large molecules

Martin Kleinschmidt, Jörg Tatchen, and Christel M. Marian^{a)}
*Institute of Theoretical and Computational Chemistry, Heinrich Heine University, Universitätsstrasse 1,
D-40225 Düsseldorf, Germany*

(Received 22 November 2005; accepted 17 January 2006; published online 22 March 2006)

We present SPOCK.CI, a selecting direct multireference spin-orbit configuration interaction (MRSOCl) program based on configuration state functions. It constitutes an extension of the spin-free density functional theory/multireference configuration interaction (DFT/MRCI) code by Grimme and Waletzke [J. Chem. Phys. **111**, 5645 (1999)] and includes spin-orbit interaction on the same footing with electron correlation. Key features of SPOCK.CI are a fast determination of coupling coefficients between configuration state functions, the use of a nonempirical effective one-electron spin-orbit atomic mean-field Hamiltonian, the application of a resolution-of-the-identity approximation to computationally expensive spin-free four-index integrals, and the use of an efficient multiroot Davidson diagonalization scheme for the complex Hamiltonian matrix. SPOCK.CI can be run either in *ab initio* mode or as semiempirical procedure combined with density functional theory (DFT/MRSOCl). The application of these techniques and approximations makes it possible to compute spin-dependent properties of large molecules in ground and electronically excited states efficiently and with high confidence. Second-order properties such as phosphorescence rates are known to converge very slowly when evaluated perturbationally by sum-over-state approaches. We have investigated the performance of SPOCK.CI on these properties in three case studies on 4*H*-pyran-4-thione, dithiosuccinimide, and free-base porphin. In particular, we have studied the dependence of the computed phosphorescence lifetimes on various technical parameters of the MRSOCl wave function such as the size of the configuration space, selection of single excitations, diagonalization thresholds, etc. The results are compared to the outcome of extensive quasidegenerate perturbation theory (QDPT) calculations as well as experiment. In all three cases, the MRSOCl approach is found to be superior to the QDPT expansion and yields results in very good agreement with experimental findings. For molecules up to the size of free-base porphin, MRSOCl calculations can easily be run on a single-processor personal computer. Total CPU times for the evaluation of the electronic excitation spectrum and the phosphorescence lifetime of this molecule are below 40 h. © 2006 American Institute of Physics. [DOI: [10.1063/1.2173246](https://doi.org/10.1063/1.2173246)]

I. INTRODUCTION

Spin-orbit coupling (SOC) is a relativistic effect. In the four-component Dirac equation of a single electron moving in the central field of a nucleus, the coupling between electronic spin and angular momenta is accomplished automatically. The spectrum of the Dirac Hamiltonian consists of electronic solutions with positive energy and a negative energy continuum of positronic states. Because the operator is not bounded from below, special precautions (such as elimination of highly oscillating functions and kinetic balance conditions) have to be taken in the variational determination of the electronic solutions.¹ The resulting four-component one-electron wave functions (bispinors) are eigenfunctions of the total angular momentum $\hat{\mathbf{j}}^2 = (\hat{\ell} + \hat{\mathbf{s}})^2$, but not of the orbital ($\hat{\ell}^2$) and spin ($\hat{\mathbf{s}}^2$) angular momentum operators separately. As a consequence, radial and angular distributions of

the electron density in $j=\ell+1/2$ and $j=\ell-1/2$ bispinors differ. This effect is frequently called spin polarization of the electron density.

While a fully relativistic many-electron Hamiltonian has not been devised so far, the most stringent way of incorporating SOC in a many-electron equation is a four-component ansatz employing the Dirac-Coulomb-Breit Hamiltonian. In this case, bispinors are obtained from the corresponding mean-field equations, i.e., the Dirac-Coulomb-Breit-Fock equations or the more frequently employed Dirac-Coulomb-Fock equations. Similar to the one-electron case, the many-particle wave function is not an eigenfunction of the total spin $\hat{\mathbf{S}}^2$ operator. The coupling of spin and spatial electronic degrees of freedom thus undermines the familiar concept of a spin multiplicity from nonrelativistic theories. Nevertheless, it can be useful to introduce an approximate total spin quantum number S when SOC is small (*LS*-coupling regime). In light elements, the probability of a radiative transition between two electronic states with different spin multiplicities (phosphorescence) is typically several orders of magnitude smaller than the corresponding transition (fluorescence) be-

^{a)}Electronic mail: christel.marian@uni-duesseldorf.de; URL: <http://www.theochem.uni-duesseldorf.de>

3. METHODENENTWICKLUNG UND IMPLEMENTIERUNG

124101-2 Kleinschmidt, Tatchen, and Marian

J. Chem. Phys. 124, 124101 (2006)

tween states of equal S . The same is true for nonradiative transitions where the “spin-forbidden” intersystem crossing is opposed to “spin-allowed” internal conversion. In heavy element compounds, on the other hand, $j-j$ coupling prevails. Here, a discrimination between spin-allowed and spin-forbidden processes is meaningless. Concerning the total energy of a many-electron system, SOC leads to a splitting of nonrelativistic spin-multiplet degeneracies even in the absence of an external field. This zero-field splitting is also dubbed fine-structure splitting. The latter denomination is justified in the LS -coupling regime where the energy separation between fine-structure levels is considerably smaller than the energy gap between two different electronic states but loses its literal meaning in heavy element compounds where term energies and zero-field splittings are of the same order of magnitude. In either case, a reliable theoretical determination of electronic excitation energies and transition moments requires us to go beyond a mean-field theory because of differential electron correlation effects. Unfortunately, a four-component treatment of electronically excited states that takes electron correlation into account is technically feasible only for atoms and small molecules at the present stage.

For the treatment of SOC effects in typical organic molecules of the size we are striving for (e.g., porphyrin) it appears more advisable to separate spin-independent (scalar) and spin-dependent (magnetic) parts of the Hamiltonian in the first step and to use only the scalar part to construct a set of molecular orbitals. Spin-orbit coupling is introduced then at a later stage either as a perturbation of the LS -coupled correlated wave function or in a variational procedure on the same footing with electron correlation. In a four-component approach, an exact separation of the spin-free and spin-dependent terms of the Dirac-Coulomb-Breit Operator is possible, in principle, albeit not unambiguous.² This separation at the four-component level reduces the computational costs of the calculations only marginally, because the atomic orbital (AO) basis set requirement for the small-component wave function continues to be huge because of kinetic balance. For calculations on large molecules a more passable approach appears to be a reduction of the number of components to 2 combined with a decoupling of the scalar and magnetic parts of the Hamiltonian. Various approximate schemes have been devised for this purpose (for reviews on this topic see, for example, Refs. 3 and 4). Several of these Hamiltonians (including the familiar Breit-Pauli spin-orbit Hamiltonian) are not bounded from below and can strictly not be employed beyond first-order perturbation theory. Nevertheless, for molecules composed of light elements a variational collapse is not observed as long as contracted atomic orbital basis sets for the inner shells are employed in the calculations. This kind of regularization closely resembles the procedure in the optimization of the positive-energy solutions of Dirac(-Fock)-type equations.

The spin-orbit coupling kit (SPOCK) developed in this laboratory contains modules that determine spin-orbit interactions of multireference configuration interaction (MRCI) wave functions either in a perturbational or variational manner.^{5,6} In a previous publication,⁷ the perturbation theory

branch SPOCK.PT was described in some detail. Key features of SPOCK.PT are a fast determination of coupling coefficients between eigenfunctions of the \hat{S}^2 operator [configuration state functions (CSFs)] for spin-dependent one-electron operators⁸ and the use of a nonempirical effective one-electron spin-orbit mean-field Hamiltonian.^{9,10} The application of these techniques and approximations in combination with the generation of correlated wave functions via the combined density functional theory/multireference configuration interaction (DFT/MRCI) method by Grimme and Waletzke¹¹ makes it possible to compute spin-orbit coupling matrix elements (SOCMEs) in organic molecules efficiently and with high confidence.

In many cases, a perturbational treatment of SOC is computationally less demanding than a variational approach because spin and spatial symmetries of the zeroth-order wave functions can be exploited separately. Furthermore, perturbation theory is advantageous if intersystem crossing (ISC) rates of light molecules are to be determined because ISC probabilities depend directly on the SOCMEs between two states of different multiplicities. Obtaining this information from a variational spin-orbit calculation would require a subsequent diabatization of the states under consideration. A disadvantage of Rayleigh-Schrödinger perturbation theory is the slow convergence of perturbation expansions for second-order properties, such as phosphorescence rates or electronic g factors.^{12,13} An explicit summation over unperturbed states can be avoided in response theory or variational perturbation theory. The application of response theory to second-order spin-dependent properties has been presented in combination with various spin-orbit-free methods, e.g., multiconfiguration self-consistent field (MCSCF),^{13,14} DFT,^{15,16} and coupled-cluster singles and doubles (CCSD).¹⁷ While dynamic electron correlation is included only to a minor extent in typical MCSCF calculations, DFT and CCSD lack static correlation contributions. In particular, for electronically excited states both types of electron correlation are important. It is therefore desirable to have a more general electronic structure method at hand for the evaluation of second-order spin-dependent properties of electronically excited states. One possibility is to use a MRCI ansatz for electron correlation. The disadvantage of this method is, of course, that it is not size extensive. We shall see later how this problem can be alleviated without resorting to extremely expensive methods such as multireference coupled-cluster approaches. Variational perturbation theory of MRCI wave functions was used frequently in the 1980s for the computation of phosphorescence rates of small molecules.^{18,19}

Alternatively, SOC can be treated variationally. In the SPOCK.CI module, described in more detail in Sec. II, spin-orbit mixed wave functions are generated in an uncontracted multireference spin-orbit configuration interaction (MR-SOCI) treatment. In this context, “uncontracted” means that the coefficients of all CSFs are allowed to vary freely. This full variational freedom has the advantage that spin-orbit interaction is treated on the same footing with electron correlation. Other MR-SOCI codes such as the older conventional SPDIAG (Ref. 20) program, the selecting direct spin-orbit configuration interaction MRD-CI (Ref. 21) and EPCISO (Ref.

22) packages, the direct DGCI (Ref. 23) program exploiting the unitary group approach, as well as the string-based direct generalized active space CI (GASCI) programs^{24,25} have typically been applied to smaller heavy element compounds.

In this work, we present a new multireference spin-orbit configuration interaction program package that is capable of treating second-order spin-dependent properties in large organic molecules. Systematic tests of the program and its features have been undertaken for two smaller organic molecules, dithiosuccinimide and 4*H*-pyran-4-thione. In particular, we compare phosphorescence rates obtained from extensive perturbation expansions and by variational inclusion of SOC. To further explore the capabilities and timing requirements of our new code, we have investigated the phosphorescence in free-base porphin.

II. METHODS

A. General procedure

In principle, the MRCI program by Grimme and Waletzke and the corresponding MRSOCl, presented in this work, can be run as an *ab initio* MRCI or as the semiempirical DFT/MRCI procedure. In most cases we use the faster DFT/MRCI branch. For systems with an odd number of electrons, however, presently the *ab initio* MRCI has to be used because DFT/MRCI parameters are available only for singlet and triplet states.

Our spin-orbit CI calculations are carried out in several steps.

- (1) Separate spin-orbit-free *ab initio* MRCI or DFT/MRCI calculations for multiple roots in different spin and space symmetries are performed, yielding *LS*-coupled MRCI wave functions.
- (2) In the basis of these *LS*-coupled MRCI wave functions—augmented by appropriate spin factors to take account of different M_S quantum numbers—(spin-free plus spin-orbit) Hamiltonian matrix is set up. Diagonalization of this Hamiltonian matrix yields not only starting vectors for the iterative diagonalization of the final MRSOCl matrix but has a value in itself as this procedure corresponds to quasidegenerate perturbation theory (QDPT).
- (3) The MRSOCl calculation is carried out in the full configuration basis of the preceding MRCI calculations.

In the latter step, the spin-free and spin-orbit operators act simultaneously on the configurational wave functions. This allows for full flexibility of the coefficients and a response of the electronic structure to the effects of the spin-orbit operator (spin polarization). The intermediate QDPT calculation is merely used as a favorable conditioner for the multiroot Davidson diagonalization of the full MRSOCl matrix. The MRSOCl is therefore to be compared with a “one-step” (or uncontracted) spin-orbit CI in the sense of Vallet *et al.*²² although it is technically carried out in several steps. The “two-step” procedure of Vallet *et al.* and the *LS*-contracted CI of Buenker *et al.*²¹ are equivalent to our QDPT solution.

B. Spin-orbit-free calculations

1. The DFT/MRCI method

The DFT/MRCI method by Grimme and Waletzke¹¹ was shown to yield excellent electronic spectra of large organic molecules at reasonable computational expense. The idea behind this approach is to include major parts of dynamic electron correlation by density functional theory whereas short MRCI expansions take account of static correlation effects. In this way, severe size-extensivity problems can be avoided even for systems with many valence electrons. The CSFs in the MRCI expansion are built up from Kohn-Sham (KS) orbitals of a closed-shell reference state. Diagonal elements of the effective DFT/MRCI Hamiltonian are constructed from the corresponding Hartree-Fock-based expression and a DFT-specific correction term. In the effective DFT/MRCI Hamiltonian, five empirical parameters are employed that depend only on the multiplicity of the desired state, the number of open shells of a configuration, and the type of density functional employed, but not on the specific atom or molecule. Currently, optimized parameter sets for the effective DFT/MRCI Hamiltonian are available in combination with the BH-LYP (Ref. 26 and 27) functional. To avoid double counting of dynamic correlation, the MRCI expansion is kept short by extensive configuration selection. For details concerning the integration of DFT information into the MRCI procedure, we refer to the original publication by Grimme and Waletzke.¹¹ Some other technical details of the MRCI program need to be mentioned here, however, because they are of significance for the subsequent spin-orbit calculations.

A strong feature of the MRCI code is its focus on second-quantization formalism and, in close connection with this, the separation of the molecular orbital (MO) space into frozen (doubly occupied in all configurations), internal (occupied at least in some reference configurations), and external (empty in all references) MOs. To make full use of second quantization in spin-orbit calculations, an identical internal/external separation of the MO space is required for all spin multiplicities and irreducible representations of the molecular point group. Within a given multiplicity, this condition is fulfilled automatically by the original MRCI program because excitations with respect to the reference functions are not limited by spatial symmetry constraints. In this way, a common set of reference CSFs can be employed for all states of a given spin multiplicity. A further advantage of this procedure is that the CI space will not change when changing from one point group to another. The initial set of reference configurations can be generated in a complete-active-space-type procedure and is then iteratively improved. To ensure a consistent classification of MOs into internal/external spaces also for different spin multiplicities, some extensions had to be made to the original MRCI code. After separate and independent reference space calculations for each spin multiplicity, the resulting MO classifications are compared. MOs that had been classified as external orbitals in the first iteration are moved to the internal space if they appear in the reference wave function of another spin

3. METHODENENTWICKLUNG UND IMPLEMENTIERUNG

124101-4 Kleinschmidt, Tatchen, and Marian

J. Chem. Phys. 124, 124101 (2006)

multiplicity. With this reordered set of MOs the final spin-orbit-free MRCI wave functions are generated.

Technically, the MRCI and SPOCK codes and the associated property programs are interfaced to the TURBOMOLE package.²⁸ They can thus take advantage of the efficiency with which the latter determines two-electron integrals and KS wave functions even for large molecules. Computationally expensive four-index integrals are evaluated using the well-known resolution-of-the-identity (RI) approximation.²⁹ The latter approximation is also known as density fitting. In addition to the TURBOMOLE links, interfaces of the MRCI and SPOCK codes to the MOLCAS suite of programs³⁰ have been implemented. This enables the use of CASSCF or RASSCF MO bases in *ab initio* MRCI calculations instead of Hartree-Fock-based MOs. Moreover, scalar relativistic corrections may be included that are not provided by the current TURBOMOLE versions.

2. Singles selection

Spin-orbit coupling is dominated by single excitations. This is not only true for heavy elements but has also been shown to hold for lighter elements,^{31,32} facilitating the use of a one-electron mean-field approximation which we make use of. An example, where high-lying single excitations play an important role, is the zero-field splitting of the thallium atom in its electronic ground state.³³ Spin polarization of the 6p orbital toward 6p_{1/2} and 6p_{3/2} spinors is described by single excitations to energetically high-lying *p* orbitals. According to Brillouin's theorem, the contribution of these configurations to the spin-orbit free energy is insignificant, but they have a large influence on the zero-field splitting in spin-orbit calculations.

The configuration selection procedure in the original DFT/MRCI code had been devised to account for contributions to electron correlation only. Here, we have to distinguish between the DFT/MRCI and the conventional *ab initio* MRCI branches. In the *ab initio* branch, a second-order Møller-Plesset perturbation theory estimate for the energy contribution of every configuration determines whether it is included in the CI space or not. In this procedure, single excitations with respect to the Hartree-Fock configuration are likely to be discarded, because they contribute only indirectly to the correlation energy of the electronic ground state. In the DFT/MRCI, on the other hand, configurations are selected solely on an orbital energy gap criterion. As a result, all configurations with orbital excitation energies above this gap are neglected, whereas all configurations below are selected, no matter whether they are single or double excitations. Thus, in both cases, single excitations important for SOC may be missing: the energetically high ones in the DFT/MRCI case and single excitations of all kinds in the *ab initio* branch.

To include these configurations in the calculation, the MRCI configuration selector has been modified. In the current version of the program, it is possible to add single excitations to the CI space based on symmetry criteria: configurations can be included if they couple to any reference function via (a) the spin-orbit operator or (b) the electric

dipole operator. As a further option, single excitations may be limited to the internal MO space. Selection of all single excitations is also possible, of course.

C. Spin-orbit configuration interaction

The SOCI matrix is usually much larger than the Hamiltonian matrix in spin-orbit-free CI calculations, because the blocking of the matrix by spin and symmetry is destroyed in general. Despite rigorous configuration selection, it is therefore not possible to store the matrix in core memory. For efficiency considerations, it is also not advisable to store the matrix on a disk. A way out is the use of a direct CI procedure, first introduced by Roos and Siegbahn.³⁴ Here, the Hamiltonian matrix is constructed on the fly, whenever it is needed. In the following, we will describe the ingredients necessary for building up the SOCI Hamiltonian matrix in our program.

1. Integrals

The spin-orbit mean-field (SOMF) Hamiltonian utilized in this work is derived from the one- and two-electron Breit-Pauli Hamiltonians,

$$\hat{\mathcal{H}}_{\text{SO}}^{\text{BP}} = \hat{h}_{\text{SO}}^{\text{BP}}(1) + \hat{\mathcal{H}}_{\text{SO}}^{\text{BP}}(1,2). \quad (1)$$

Here, $\hat{h}_{\text{SO}}^{\text{BP}}(1)$ represents the one-electron part and $\hat{\mathcal{H}}_{\text{SO}}^{\text{BP}}(1,2)$ is a sum of two-electron spin-same-orbit and spin-other-orbit terms.

$$\hat{h}_{\text{SO}}^{\text{BP}}(1) = \frac{e^2}{2m_e^2 c^2} \sum_i \left(-\nabla_i \left(\sum_I \frac{Z_I}{\hat{r}_{il}} \right) \times \hat{\mathbf{p}}_i \right) \cdot \hat{\mathbf{s}}_i, \quad (2)$$

$$\begin{aligned} \hat{\mathcal{H}}_{\text{SO}}^{\text{BP}}(1,2) = & \frac{e^2}{2m_e^2 c^2} \left\{ \sum_i \sum_{j \neq i} \left(\nabla_i \left(\frac{1}{\hat{r}_{ij}} \right) \times \hat{\mathbf{p}}_i \right) \cdot \hat{\mathbf{s}}_i \right. \\ & + \sum_i \sum_{j \neq i} \left(\nabla_j \left(\frac{1}{\hat{r}_{ij}} \right) \times \hat{\mathbf{p}}_j \right) \cdot \hat{\mathbf{s}}_i \\ & \left. + \sum_j \sum_{i \neq j} \left(\nabla_i \left(\frac{1}{\hat{r}_{ji}} \right) \times \hat{\mathbf{p}}_i \right) \cdot \hat{\mathbf{s}}_j \right\}. \end{aligned} \quad (3)$$

I labels nuclei, *i* and *j* label electrons, Z_I is the charge of nucleus *I*, e and m_e are the charge and the mass of an electron, respectively, and c is the speed of light. Alternatively, a quasirelativistic no-pair spin-orbit Hamiltonian^{35,36} can be employed. These operators have a structure similar to the Breit-Pauli spin-orbit terms in Eqs. (2) and (3). In contrast to the latter, the no-pair operators are bounded from below, however, and can therefore be used in unconstrained variational calculations on heavy element compounds. For consistency reasons, they should be applied only in combination with the corresponding scalar relativistic spin-free Hamiltonian.

To arrive at an effective one-electron operator, the screening by other electrons is incorporated in a Fock-type manner.⁹ A matrix element (ME) of the resulting SOMF Hamiltonian is given by

3.3. SPIN-BAHN CI

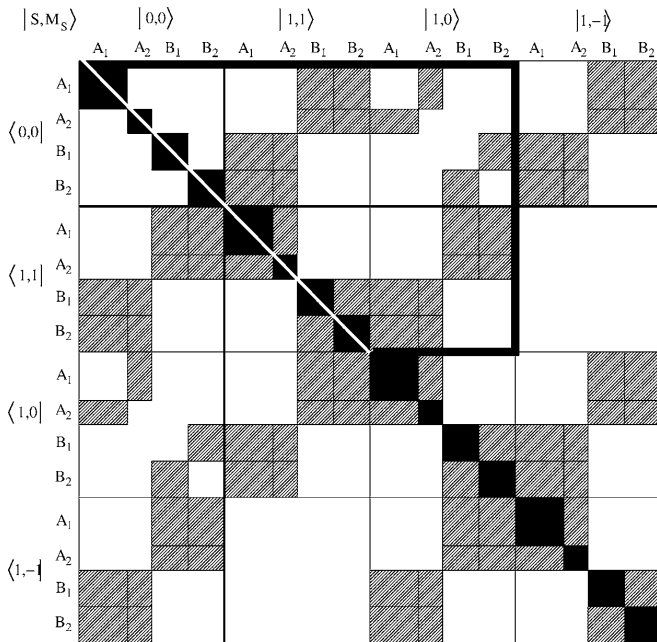


FIG. 1. Block structure of the MRSOCl matrix (C_{2v} symmetry).

$$\begin{aligned} \langle i(1) | \hat{\mathcal{H}}_{SO}^{\text{mf}} | j(1) \rangle &= \langle i(1) | \hat{\mathcal{H}}_{SO}^{\text{BP}}(1) | j(1) \rangle \\ &\quad + \frac{1}{2} \sum_k n_k \{ 2 \langle i(1) k(2) | \hat{\mathcal{H}}_{SO}^{\text{BP}}(1,2) | j(1) k(2) \rangle \\ &\quad - 3 \langle k(1) i(2) | \hat{\mathcal{H}}_{SO}^{\text{BP}}(1,2) | j(1) k(2) \rangle \\ &\quad - 3 \langle i(1) k(2) | \hat{\mathcal{H}}_{SO}^{\text{BP}}(1,2) | k(1) j(2) \rangle \}. \end{aligned} \quad (4)$$

As an additional approximation, all multicenter spin-orbit integrals are neglected. In this way, the molecular mean field reduces to a sum of atomic mean fields where the summation index k runs over all spatial atomic orbitals and n_k is their average occupation number. Mean-field orbitals are generated automatically for each atom from a restricted (open-shell) Hartree-Fock atomic ground state calculation. The atomic mean-field integral program AMFI (Ref. 10) makes use of spherical symmetry; spin-orbit integral evaluation is thus extremely fast. After multiplication with the appropriate Wigner-Eckart coefficients, the Cartesian atomic spin-orbit integrals are finally transformed to the MO basis set.

In the SPOCK.CI module, spin-orbit integrals and one-electron integrals of the spin-free Hamiltonian are kept in the main memory. The same applies to the three-index RI integrals from which the four-index Coulomb and exchange integrals are constructed on the fly. If storage requirements for the CI vectors allow, computationally expensive four-index integrals may be precomputed.

2. Hamiltonian matrix elements

The SPOCK.CI works in a basis of CSFs. As described in Sec. II B, the $M_S=S$ functions are selected in separate (DFT)/MRCI calculations for all desired spin and space symmetries

and are then merged. Matrix elements for the other M_S components are subsequently generated by means of the Wigner-Eckart theorem.

In a basis of Slater determinants, the spin-orbit interaction of two functions with a one-electron operator is either zero (if no matching single excitation can be found) or equal to the spatial spin-orbit integral of the single excitation multiplied by a plain spin factor. Despite the simplicity of this approach, we refrain from working in a basis of Slater determinants because we want to exploit the block structure of the Hamiltonian matrix due to spin symmetry as far as possible. (An example for this blocking in a singlet/triplet case in C_{2v} spatial symmetry is shown in Fig. 1.) Furthermore, the coupling of multiplicities can be restricted to $\Delta S=0, \pm 1$. The price one has to pay for this convenience is a considerably more involved calculation of one-electron interactions in a basis of eigenfunctions of the $\hat{\mathbf{S}}^2$ operator (i.e., CSFs). CSFs are linear combinations of Slater determinants. When acting with a spin-dependent one-particle excitation operator on a CSF $|S, \omega, \mathbf{n}\rangle$ [see Eq. (5)], the result will again be a linear combination of Slater determinants but, in general, not an eigenfunction of the $\hat{\mathbf{S}}^2$ operator. The overlap of this linear combination with a CSF $\langle S', \omega', \mathbf{n}' |$ is called a spin-coupling coefficient.

$$\begin{aligned} \langle S', \omega', \mathbf{n}' | \sum_{m,n} \ell_{mn} \sum_{\mu,\nu} s_{\mu\nu} \hat{a}_{m\mu}^\dagger \hat{a}_{n\nu} | S, \omega, \mathbf{n} \rangle \\ = \ell_{ab} \langle S', \omega', \mathbf{n}' | \sum_{\mu,\nu} s_{\mu\nu} \hat{a}_{a\mu}^\dagger \hat{a}_{b\nu} | S, \omega, \mathbf{n} \rangle \\ =: \ell_{ab} \cdot \eta(S, S', \omega, \omega', \mathbf{n}, \mathbf{n}'). \end{aligned} \quad (5)$$

Here, \mathbf{n} represents an orbital occupation, ω labels the CSFs, ℓ_{ab} is a spin-orbit integral, and η is a spin-coupling coeffi-

3. METHODENENTWICKLUNG UND IMPLEMENTIERUNG

124101-6 Kleinschmidt, Tatchen, and Marian

J. Chem. Phys. 124, 124101 (2006)

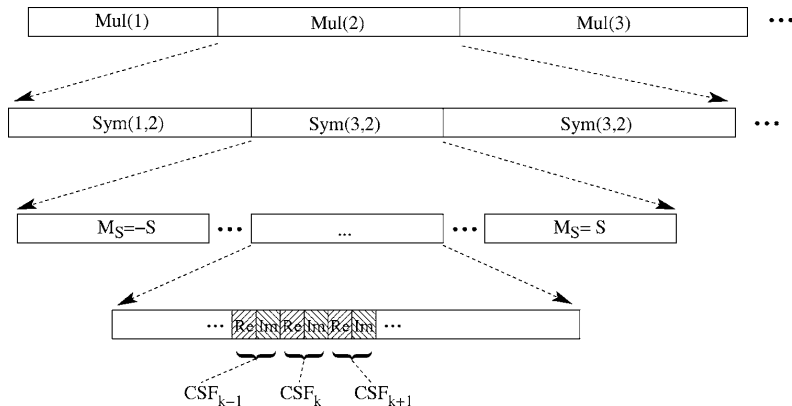


FIG. 2. Organization of the eigenvectors in the SPOCK.CI module.

cient. As seen from Eq. (5), η depends on the multiplicities of the states involved, the orbital occupations of the configurations, and the particular CSF pair, but not on the spin-orbit coupling integral.

Various ways of handling these coefficients have been developed in the last decades. In the original DFT/MRCI program, an older but relatively simple approach by Wetmore and Segal had been implemented. The basic idea was to reduce the number of potential coupling coefficients by dealing with reduced occupation number vectors only, to organize the remaining couplings by so-called excitation patterns, and then to precompute and store all coupling coefficients. This approach is, of course, less elegant than, e.g., the symmetric or unitary group approaches, but it has the advantage of simplicity, efficiency, and straightforward implementation in a selecting CI code.

We extended the approach by Wetmore and Segal to spin-dependent one-electron operators⁸ and implemented it in our spin-orbit CI program. For each pattern that corresponds to a single excitation four subcases may occur. When permutational symmetry and transposition relations are exploited, the number of independent subcases reduces to 1 in case of the \hat{s}_0 operator, i.e., only one spin-coupling coefficient needs to be stored per pattern. For the \hat{s}_{+1} operator, two nonequivalent subcases remain. Finally, no additional spin-coupling coefficients need to be stored for the \hat{s}_{-1} operator because they can be obtained from those of \hat{s}_{+1} by Hermitian conjugation. For further details see Ref. 8. Because of this extensive use of symmetry relations, storage of all non-equivalent coupling coefficients for a spin-orbit CI calculation with singlet and triplet CSFs with up to ten open shells requires only 21 Mbytes of memory.

This procedure yields MEs over the $M_S=S$ components of the CSFs. MEs for all other M_S quantum numbers are obtained by application of the *scaled 3j*-symbol approach of McWeeny.^{37,38}

3. Matrix-vector multiplication and organization of eigenvectors

In Fig. 1, we exemplify a typical SOCI matrix in C_{2v} symmetry with singlet and triplet states. With the spin-free operator, MEs occur only in the black-colored blocks on the

diagonal. No coupling of different symmetries or \hat{S}^2 eigenfunctions takes place. Furthermore, all M_S components of the triplet are degenerate, so that only one of them needs to be computed explicitly. Taking into account Hermiticity, it is thus sufficient to evaluate the upper black triangular blocks enframed by the thick black-and-white lines in Fig. 1, and each is calculated separately. When switching on spin-orbit coupling in the SOCI, symmetry selection rules are exploited. Coupling of different multiplicities is restricted to a maximum of $\Delta S=\pm 1$ and $\Delta M_S=\pm 1$. In C_{2v} symmetry, MEs of the spin-orbit operator emerge only in the hatched blocks in Fig. 1. The block structure of the matrix is destroyed, in general, by the spin-orbit operator; all symmetries and spin components have to be treated simultaneously. Nevertheless, the matrix retains some structure and sparsity. Some blocks are zero by symmetry, while others are related by Hermiticity or may be obtained by application of the *scaled 3j* symbols. Therefore again, only the blocks inside the enframed area need to be calculated explicitly.³⁹ The resulting block structure of the matrix predefines the algorithm for the matrix-vector multiplication in the Davidson diagonalization. The organization of the CSFs inside a SOCI vector (Fig. 2) and the order, in which the different blocks in the Hamiltonian matrix are processed, are closely related but not identical, as will be seen below.

The ordering of CSFs in the MRSOCl vectors (Fig. 2) is as follows: The outermost loop runs over different roots of the secular equation. For a given state, the first block contains CSFs with the smallest S quantum number (e.g., singlets), then $S+1$, and so on. Within each of these blocks of given multiplicity, segments of different spatial symmetries are arranged, maintaining the standard ordering of TURBOMOLE. These segments are further subdivided into arrays with different M_S quantum numbers, with $M_S=-S$ coming first, $M_S=-S+1$ next, etc. At the innermost level, individual CSF coefficients are stored. Each of those segments with defined total spin, M_S quantum number, and spatial symmetry reflects one spin-orbit-free CI space, with the difference that the coefficients are complex numbers instead of real ones.

To avoid repeated configuration comparisons for different M_S components of the same configuration and to enable

3.3. SPIN-BAHN CI

the use of the Wigner-Eckart theorem in the ME evaluation, the loops over CSFs and M_S quantum numbers are reversed in the matrix-vector multiplication. Furthermore, if memory requirements allow the storage of multiple CI vectors c and $\sigma = Hc$ vectors, the reevaluation of Hamiltonian MEs for different roots in the same iteration of the multiroot Davidson procedure can be avoided. The blocks to be incorporated and computed in every iteration are as follows.

- (1) For each multiplicity and spatial irreducible representation, one triangular matrix (upper left corner in the example shown in Fig. 1) has to be evaluated for $M_S=S$ with the conventional spin-free one- and two-electron operators. These MEs are real valued. Diagonal blocks for other M_S quantum numbers are identical and can simply be replicated.
- (2) For point group C_{2v} or higher, $\hat{\mathcal{H}}_{SO}$ does not couple configurations of the same spatial symmetry. (In the example shown in Fig. 1, therefore, diagonal spin-orbit blocks do not occur.) In lower point groups, however, SOCMEs may also contribute to diagonal blocks. The complex-valued MEs are evaluated once for $M_S=S$ functions employing integrals over the appropriate Cartesian x, y , or z components of $\hat{\mathcal{H}}_{SO}$ combined with \hat{s}_0 spin MEs. Blocks for all pairs of M_S quantum numbers can be obtained by multiplication with scaled $3j$ symbols.
- (3) Off-diagonal blocks connecting CSFs of different spin and/or space symmetries (hatched areas in the upper left corner in Fig. 1) are only computed if a matching spin-orbit operator may be found. The complex-valued SOCMEs are evaluated in a similar fashion as described above. In contrast to the diagonal blocks, also \hat{s}_{+1} or \hat{s}_{-1} may be involved, depending on ΔS . Again, blocks for all pairs of M_S quantum numbers are obtained by multiplication with scaled $3j$ symbols.

4. Davidson diagonalization

In contrast to the spin-free case, the Hamiltonian matrix and the CI coefficients are complex valued. As the spin-orbit Hamiltonian mixes different multiplicities and spatial symmetries and lifts the degeneracy of the multiplet levels, the dimension of a MRSOCl is much larger than for a spin-orbit-free MRCI and easily reaches 10^7 terms. Diagonalization of these large matrices requires the use of an approximate algorithm. The Davidson algorithm is an iterative scheme capable of computing eigenvalues and eigenvectors for a few energetically low-lying states. It has been devised originally by Davidson⁴⁰ for configuration interaction procedures and has been widely used in quantum chemistry ever since, although most of the times for problems dealing with real numbers only.

Usually we are interested not only in the ground state but also in excited state wave functions for calculating transition properties. To this end, we use a multiroot extension of the Davidson algorithm,⁴¹ capable of extracting several low-lying roots simultaneously. Alternatively, a root-homing approach could be employed that is based on an eigenvector-

following algorithm.⁴² Earlier experience with the SPDIAG spin-orbit CI program^{20,43} reveals the superiority of the multiroot Davidson method over the root-homing procedure in case of near degeneracies. According to our experience, the convergence of the root-homing procedure is slow if roots change order. However, in the course of this calculation good approximations for other roots are built up. Instead of starting over again for each root, it is advantageous to use this information on approximate eigenvectors. In many cases it is therefore faster to compute all desired roots simultaneously. Only in cases where a particular, very high-lying root is to be computed and lower roots are of no interest at all, the root-homing may become favorable.

To determine the eigenvalues of a complex, Hermitian matrix C with real part A and imaginary part iB

$$C = (A + iB), \quad (6)$$

the conventional (real) Davidson algorithm has to be extended. Either the Davidson scheme has to be reformulated using complex algebra or alternatively a double-sized, real symmetric matrix

$$R = \begin{pmatrix} A & -B \\ B & A \end{pmatrix} \quad (7)$$

can be diagonalized. It can easily be shown⁴⁴ that C and R have identical eigenvalues, but each eigenvalue (artificially) occurs twice for R . This allows us, in principle, to use existing and well-tested conventional Davidson diagonalization implementations for real matrices.

However, great care has to be taken when using the eigenvectors of the real algorithm for the computation of properties. In cases with truly degenerate eigenvalues, eigenvectors of the real matrix may mix in a way that orthogonality of the complex vectors is not guaranteed (see the Appendix for details), although orthogonality in the real scalar product is ensured by the algorithm. Eigenvalues (and therefore energies) are not affected. However, problems arise in calculation of transition density matrices. To avoid these complications, we implemented a completely new complex version of the multiroot Davidson algorithm in our spin-orbit CI code. A further advantage of the complex algorithm over the real one is the reduced disk storage requirement. Although the number of double words needed to store a single complex or real MRSOCl vector is exactly identical, the total disk space requirement is four times as large in the real Davidson scheme because twice as many c and $\sigma = Hc$ vectors must be stored due to the double degeneracy of all eigenvalues.

Memory requirements for the c and σ vectors may easily become significant. Nevertheless, calculations of this type can be performed on a personal computer. In the largest single-processor test case so far, the MRSOCl expansion length amounts to approximately 20×10^6 CSFs and four roots are determined simultaneously. A parallelized version of the program that can handle larger CI spaces is currently under development.

3. METHODENENTWICKLUNG UND IMPLEMENTIERUNG

124101-8 Kleinschmidt, Tatchen, and Marian

J. Chem. Phys. 124, 124101 (2006)

5. Properties

Probabilities and rates of spin-forbidden radiative transitions are obtained from the spin-free electric dipole operator MEs and the eigenvectors of the spin-dependent Hamiltonian matrix in QDPT or MRSOCl.

To enable the formulation of a working equation for the transition density matrices, $\rho^{[BA]}$, we cast the MRSOCl wave function $|A\rangle$ as linear combination of CSFs:

$$|A\rangle = \sum_{S=S_{\min}}^{S_{\max}} \sum_{M_S=-S}^S \sum_{\{\Gamma\}} \sum_{\{\mathbf{n}\}} \sum_{\omega(\mathbf{n})} a_{S,M_S,\Gamma,\mathbf{n},\omega(\mathbf{n})} \times |S,M_S,\Gamma,\mathbf{n},\omega(\mathbf{n})\rangle. \quad (8)$$

The linear combination runs over all possible spin quantum numbers S and M_S , all irreducible representations Γ (IRREP, only with respect to the spatial part), all occupation number vectors \mathbf{n} (configurations), and all associated CSF indices $\omega(\mathbf{n})$. The set of possible configurations $\{\mathbf{n}\}$ actually depends on both S and Γ . For brevity, this dependence is not indicated in Eq. (8).

MEs of spin-independent one-electron operators between MRSOCl wave functions are computed via reduced one-particle density matrices (1-RDMs) and transition density matrices (1-RTDMs) in the basis of MOs. Adopting a notation for $|B\rangle$ similar to Eq. (8), the elements $\rho_{ji}^{[BA]}$ of the 1-RTDMs are given by MEs of the spin-free one-electron excitation operator $\hat{E}_{ij} = \sum_{\sigma} \hat{a}_{i\sigma}^\dagger \hat{a}_{j\sigma}$:

$$\begin{aligned} \rho_{ji}^{[BA]} &= \langle A | \hat{E}_{ij} | B \rangle \\ &= \sum_{S=S_{\min}}^{S_{\max}} \sum_{\{\Gamma\}} \sum_{\{\mathbf{n}\}} \sum_{\omega(\mathbf{n})} \eta(S, \mathbf{n}, \omega(\mathbf{n}), \mathbf{n}', \omega'(\mathbf{n}')) \\ &\quad \times \sum_{\{\Gamma'\}} \sum_{\{\mathbf{n}'\}} \sum_{\omega'(\mathbf{n}')} \times \sum_{M_S=-S}^S a_{S,M_S,\Gamma,\mathbf{n},\omega(\mathbf{n})}^* b_{S,M_S,\Gamma',\mathbf{n}',\omega'(\mathbf{n}')}. \end{aligned} \quad (9)$$

In this expression, we have exploited the fact that the operators \hat{E}_{ij} preserve the spin and hence only terms with $S'=S$ and $M'_{S'}=M_S$ contribute. Moreover, the $\langle S, M_S, \mathbf{n}, \omega | \hat{E}_{ij} | S, M_S, \mathbf{n}', \omega' \rangle$ have been replaced by the (spin-free) η coefficients of Wetmore and Segal.⁴⁵ Compared to the standard formalism of 1-RTDMs for spin-orbit-free MRCI wave functions, Eq. (9) contains summations over the spin quantum numbers S and M_S in addition to summations over the irreducible representations Γ and Γ' . Furthermore, it should be noted that the 1-RTDMs are complex valued for the MRSOCl case. With respect to computational expense, the calculation of a 1-RTDM in the MRSOCl case is thus considerably more demanding than in the MRCI case.

For any spin-independent one-electron operator \hat{F} , the ME between two MRSOCl wave functions $|A\rangle$ and $|B\rangle$ may be obtained from the 1-RTDM $\rho^{[BA]}$ and the matrix of one-electron integrals $f_{ij}=[i|\hat{f}|j]$ by the trace operation

$$\langle A | \hat{F} | B \rangle = \text{tr}\{\mathbf{f} \rho^{[BA]}\} = \sum_{i,j} f_{ij} \rho_{ji}^{[BA]}. \quad (10)$$

Our implementation for the computation of molecular properties at the MRSOCl level basically consists of two parts which both are derived from spin-orbit-free precursors available in the MRCI package of Grimme and Waletzke.

- (1) The DMAT extension module for the SPOCK.CI program builds up the 1-R(T)DMs according to Eq. (9) and writes them to a disk. To avoid unnecessary repetition of the time consuming configuration comparison, the summation over M_S was positioned as the innermost loop, i.e., inside the configuration comparison routines [as already indicated in Eq. (9)]. Further efficiency is gained by building up several 1-R(T)DMs simultaneously.
- (2) The program SOPROPER first provides the one-electron integrals f_{ij} . It consists of integral routines for the following operators: identity (\hat{I}), overlap integrals S_{ij} , electric dipole in length form ($\hat{\mathbf{r}}$), electric quadrupole (\hat{Q}), angular momentum ($\hat{\ell}$), and linear momentum ($\hat{\mathbf{p}}$). The latter two types of integrals are usually employed for the calculation of magnetic dipole transition moments ($\hat{\ell}$) and electric dipole transition moments in velocity form ($\hat{\mathbf{p}}$). After reading the 1-R(T)DMs from the disk, SOPROPER then calculates the final MEs by performing the trace operation according to Eq. (10).

In spin-allowed transitions, the length and velocity forms of the electric dipole transition operator give identical results (save for the incompleteness of the wave function representation). This is not true for spin-forbidden radiative transitions. In the spin-orbit coupling case, the linear momentum $\hat{\mathbf{p}}$ alone is not sufficient for the calculation of electric dipole transition probabilities. Instead of using $\Sigma_i \hat{\mathbf{p}}_i$, the appropriate transition dipole operator in the velocity form in Breit-Pauli theory is given by^{46,47}

$$\hat{\Pi} = \sum_i \left(\hat{\mathbf{p}}_i + \frac{e^2 \hbar}{2m^2 c^2} \hat{\mathbf{s}}_i \times \nabla_i \left\{ \sum_{\alpha} \frac{Z_{\alpha}}{\hat{r}_{i\alpha}} - \sum_{j \neq i} \frac{1}{\hat{r}_{ij}} \right\} \right), \quad (11)$$

where α denotes the nuclei and i and j the electrons. Similar considerations apply to the no-pair operator. $\hat{\Pi}$ can be expressed by the commutator $[\hat{\mathcal{H}}^{(0)} + \hat{\mathcal{H}}_{SO}, \hat{\mathbf{r}}] = (i\hbar/m)\hat{\Pi}$. Thus in contrast to $\hat{\mathbf{p}}, e\hat{\mathbf{r}}$ is a correct dipole transition operator for the evaluation of radiative spin-forbidden transition moments.

Phosphorescence rates ($k_{p,\xi}$) and lifetimes ($\tau_{p,\xi}$) for individual sublevels of the lowest triplet state are given by the usual expression for spontaneous emission, applied to the spin-orbit coupled system:

$$k_{p,\xi} = \frac{1}{\tau_{p,\xi}} = \frac{4e^2}{3c^3 \hbar^4} (E_{T_1} - E_{S_0})^3 |\mu_{el}(T_{1,\xi} \rightarrow S_0)|^2. \quad (12)$$

Here, spin-orbit coupled states are labeled by letters S and T in contrast to S and T for the Russel-Saunders (LS)-coupled pure multiplet states. If there is no pronounced fine-structure splitting and the experiment is not conducted at temperatures

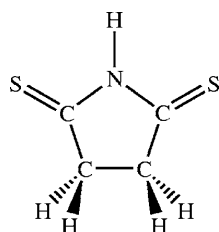


FIG. 3. Chemical structure of dithiosuccinimide.

close to 0 K, the triplet sublevels will be almost equally populated at thermal equilibrium. Under these circumstances, one can only observe the average of the individual phosphorescence rates which is termed the high-temperature limit of the phosphorescence rate $\bar{k}_{p,\text{high}}$:

$$\bar{k}_p = \frac{1}{\bar{\tau}_p} = \frac{1}{3}(k_{p,x} + k_{p,y} + k_{p,z}). \quad (13)$$

III. APPLICATIONS

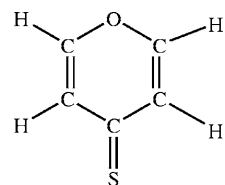
A. Technical details

All calculations were performed employing the valence triple zeta basis set with polarization functions (d, p) from the TURBOMOLE library.^{48,49} The equilibrium geometries of the electronic ground states were determined for a restricted closed-shell KS determinant. For dithiosuccinimide and free-base porphin, we optimized the geometries of the low-lying singlet and triplet states by means of a time-dependent DFT (TDDFT) gradient.⁵⁰ In the case of pyranthion, the minimum geometry of the lowest-lying triplet state was determined by unrestricted density functional theory (UDFT). All (U)DFT/TDDFT calculations were carried out utilizing by the TURBOMOLE quantum chemistry program package.²⁸ In the MRCI runs, all valence electrons were correlated. For the RI approximation of the expensive four-index integrals of the two-electron Coulomb operator, RI-MP2-optimized auxiliary basis sets from the TURBOMOLE library^{51,52} were employed.

B. Test cases

A detailed understanding of the properties of triplet states in larger organic molecules belongs to the basic knowledge in photochemistry and photophysics.^{53,54} In particular, when heteroatoms such as oxygen, sulfur, or chlorine are present in the molecule, singlet-triplet ISC becomes more and more competitive with other decay processes following the primary electronic excitation. The lowest triplet state (T_1) serves as an energy sink for the absorbed radiation that triggers photochemical reactions.

Beside intermolecular solvent induced relaxation and nonradiative $T_1 \sim S_0$ ISC, phosphorescence is one of the most important decay channels to the ground state. Large phosphorescence quantum yields (ϕ_p) have been observed for several thioketones.^{55–59} Two of these compounds, dithiosuccinimide (Fig. 3) and 4*H*-pyran-4-thione (Fig. 4), will serve as test cases here.

FIG. 4. Chemical structure of 4*H*-pyran-4-thione.

1. Dithiosuccinimide

Intense phosphorescence of high quantum yield was observed experimentally in a glassy matrix at 77 K and assigned to the emission from and ($n \rightarrow \pi^*$) excited T_1 state by Meskers *et al.*⁵⁸ QDPT calculations on the phosphorescence lifetime of dithiosuccinimide were performed earlier in this laboratory by Tatchen *et al.*⁶⁰ Further information concerning technical details of the MRCI calculations, the resulting electronic spectrum, and the optimized nuclear geometries are available in that publication.

Phosphorescence lifetimes computed at the MRSOCl level are presented together with QDPT results in Table I. At the optimized geometry of the T_1 state, the chromophore exhibits C_2 symmetry, but deviations from planarity (C_{2v} symmetry) are small.⁶⁰ As expected for C_{2v} symmetry selection rules, major contributions to the $S_0 \leftarrow T_1$ transition are due to the z and y fine-structure levels of the T_1 state, whereas the emission from the x sublevel is negligible.⁶⁰ The MRSOCl results are almost converged already for the smallest CI space (14 676 configurations) that was generated from 4 LS states (one state per spin and space symmetry: S_0, S_1, T_1, T_2). Only the transition moment of the weakly interacting $T_{1,x}$ fine-structure level changes when the interaction space is increased to 50 481 configurations (32 LS states) and no further change is observed when proceeding to 68 143 configurations (64 LS states). Not surprisingly, this is not the case for the QDPT approach. The $T_{1,z}$ sublevel interacts with singlet states of approximate B_2 spatial symmetry, the most important being the $S_3(\pi \rightarrow \pi^*)$ state due to its large dipole transition moment and relatively small energy separation. As the S_3 state is not included in the shortest perturbation expansion, the computed transition rate $T_{1,z}$ is much too small. In the MRSOCl space, on the other hand, the leading configurations of the S_3 state are contained as single excitations in the MRCI expansion of the S_1 state. Since the coefficients of all configurations (CSFs to be precise) are allowed to vary freely in the MRSOCl secular equation, the singlet ($\pi \rightarrow \pi^*$) excitations gain weight in the $T_{1,z}$ eigenvector, yielding a large electric dipole transition moment to the S_0 state. The improvement of the computed transition moment with the length of the perturbation expansion is less dramatic for $T_{1,y}$ because this fine-structure level exhibits a strong direct interaction with the electronic ground state. The longest QDPT expansion (64 LS) state appears nearly converged. In the limit of a full QDPT expansion, the results have to be identical to the MRSOCl results, of course.

The computed high-temperature phosphorescence lifetime of approximately 0.5 ms for the T_1 state is in good agreement with experiment. Meskers *et al.*⁵⁸ determined a

3. METHODENENTWICKLUNG UND IMPLEMENTIERUNG

TABLE I. Convergence of T_1 phosphorescence lifetimes of dithiosuccinimide with expansion lengths.

4 LS states		QDPT		MRSOCl	
level		$\mu (ea_0)$	τ (ms)	$\mu (ea_0)$	τ (ms)
$T_{1,x}$		2.49×10^{-5}	115 308	1.66×10^{-4}	2596
$T_{1,y}$		3.35×10^{-3}	6.40	7.83×10^{-3}	1.17
$T_{1,z}$		6.65×10^{-3}	1.62	1.90×10^{-2}	0.198
High- T average			3.88		0.51
32 LS states		QDPT ^a		MRSOCl	
level		$\mu (ea_0)$	τ (ms)	$\mu (ea_0)$	τ (ms)
$T_{1,x}$		8.74×10^{-5}	9670	1.60×10^{-4}	2904
$T_{1,y}$		7.16×10^{-3}	1.45	7.96×10^{-3}	1.16
$T_{1,z}$		1.63×10^{-2}	0.28	1.90×10^{-2}	0.204
High- T average			0.70		0.52
64 LS states		QDPT ^a		MRSOCl	
level		$\mu (ea_0)$	τ (ms)	$\mu (ea_0)$	τ (ms)
$T_{1,x}$		1.20×10^{-4}	5130	1.52×10^{-4}	3224
$T_{1,y}$		7.30×10^{-3}	1.40	7.94×10^{-3}	1.18
$T_{1,z}$		1.90×10^{-2}	0.21	1.90×10^{-2}	0.205
High- T average			0.54		0.52

^aReference 60.

total (radiative and nonradiative) T_1 lifetime of 0.1 ms for dithiosuccinimide. They report the luminescence quantum yield to be 0.5 ± 0.2 from which an experimental radiative lifetime of approximately 0.2 ms can be deduced.

2. 4H-pyran-4-thione

As for dithiosuccinimide, we carried out extensive tests on the dependence of phosphorescence lifetimes of 4H-pyran-4-thione with QDPT and MRSOCl expansion lengths. In addition, we investigated the sensitivity of the electric dipole transition moments of the spin-forbidden radiative T_1 decay with respect to the precision of the MRSOCl vector in the Davidson diagonalization procedure. By default, a MRSOCl vector is considered converged if the energy difference between two successive Davidson iterations is less than $5 \times 10^{-6} E_h \approx 1 \text{ cm}^{-1}$. As fine-structure splittings in the T_1 state of organic molecules are often of the same order of magnitude as the convergence threshold, we tightened this threshold in a series of calculations. Furthermore, we studied the influence of single excitations on the phosphorescence. It is well known that in *ab initio* single and double excitation calculations single excitations contribute only indirectly to the correlation energy of the electronic ground state and their coefficients are therefore small. The electric dipole operator, on the other hand, is a pure one-electron operator that couples only single excitations. The same is true for the mean-field spin-orbit operator employed in this work. It is thus expected that the inclusion of single excitations in the CI space (not based on a correlation energy selection criterion) might affect these one-electron properties.

QDPT calculations on the T_1 phosphorescence lifetime

of 4H-pyran-4-thione had been carried out in our laboratory earlier.⁶¹ However, at that time SPOCK.PT had not been finished and SOCMEs had to be evaluated with a precursor program for much shorter MRCI wave functions. On these grounds we have reinvestigated the performance of QDPT employing DFT/MRCI wave functions as zeroth-order states. The T_1 state has an ($n \rightarrow \pi^*$) electronic structure (1^3A_2) which lets us expect that phosphorescence emission is efficient. According to our earlier investigation,⁶¹ it exhibits a planar minimum geometry.

Under C_{2v} symmetry constraints, the minimum number of LS states required to span the MRSOCl space amounts to 8, i.e., one state per multiplicity and spatial symmetry. However, if the calculations are carried out for the same nuclear geometry without exploiting symmetry, the number of LS states can formally be reduced to 2, i.e., the S_0 and T_1 states. Astoundingly, even in this minimal case the MRSOCl transition moments are almost identical to the ones obtained from the largest calculations (see Table II). This result is particularly encouraging with regard to second-order spin-orbit properties of larger molecules for which the calculation of many LS states may be cumbersome. With respect to the vector convergence threshold, a value of $5 \times 10^{-7} E_h$ appears to be sufficient here.

In the case of 4H-pyran-4-thione, the additional inclusion of single excitations is not necessary. We carried out test calculations where all single excitations within the internal space were selected automatically. Likewise, MRSOCl calculations were performed with CI spaces that contained all external single excitations in addition to the energy selected configurations. Transition moments (not shown here) remain essentially unchanged. This might be different for MRSOCl

TABLE II. Sensitivity of the $T_1 \rightarrow S_0$ transition moments μ (ea_0) of 4H-pyran-4-thione with respect to the MRSOCl vector convergence threshold vct (E_h) in the Davidson diagonalization procedure.

	μ			
	vct=5×10 ⁻⁶	vct=5×10 ⁻⁷	vct=5×10 ⁻⁸	vct=5×10 ⁻⁹
2 LS states ^a				
$T_{1,x}$	2.53×10 ⁻³	2.39×10 ⁻³	2.39×10 ⁻³	2.38×10 ⁻³
$T_{1,y}$	1.07×10 ⁻³	1.09×10 ⁻³	1.08×10 ⁻³	1.08×10 ⁻³
$T_{1,z}$	3.81×10 ⁻²	3.84×10 ⁻²	3.84×10 ⁻²	3.84×10 ⁻²
4 LS states ^a				
$T_{1,x}$	2.32×10 ⁻³	2.39×10 ⁻³	2.40×10 ⁻³	2.40×10 ⁻³
$T_{1,y}$	1.09×10 ⁻³	1.09×10 ⁻³	1.09×10 ⁻³	1.09×10 ⁻³
$T_{1,z}$	3.33×10 ⁻²	3.85×10 ⁻²	3.87×10 ⁻²	3.87×10 ⁻²
8 LS states ^b				
$T_{1,x}$	2.31×10 ⁻³	2.41×10 ⁻³	2.42×10 ⁻³	2.42×10 ⁻³
$T_{1,y}$	1.05×10 ⁻³	1.07×10 ⁻³	1.07×10 ⁻³	1.07×10 ⁻³
$T_{1,z}$	3.30×10 ⁻²	3.83×10 ⁻²	3.86×10 ⁻²	3.86×10 ⁻²
48 LS states ^b				
$T_{1,x}$	2.44×10 ⁻³	2.43×10 ⁻³	2.45×10 ⁻³	2.45×10 ⁻³
$T_{1,y}$	1.08×10 ⁻³	1.08×10 ⁻³	1.08×10 ⁻³	1.08×10 ⁻³
$T_{1,z}$	3.84×10 ⁻²	3.83×10 ⁻²	3.83×10 ⁻²	3.83×10 ⁻²

^aNo symmetry exploited in calculations.

^b C_{2v} symmetry exploited in calculations.

treatments of heavy element compounds where spin-orbit relaxation of the electron density is a well-known phenomenon.^{21–23}

A comparison of QDPT versus MRSOCl (Table III) shows that the phosphorescence lifetime of the $T_{1,z}$ level is converged when 48 LS states are employed in the perturbation expansion. As the $S_0 \leftarrow T_{1,z}$ emission is by far the fastest radiative decay channel of T_1 , the high-temperature lifetimes determined with the QDPT and MRSOCl approaches are nearly equal, despite the fact that the lifetimes of the individual $T_{1,x}$ and $T_{1,y}$ levels differ by a factor of roughly 2. The $S_0 \leftarrow T_{1,z}$ phosphorescence mainly borrows its intensity from two sources: (1) the significant direct spin-orbit coupling of the initial and final states ($\langle S_0 | \hat{H}_{SO} | T_{1z} \rangle = 150.1 \text{ cm}^{-1}$, $\Delta E = 14\ 506 \text{ cm}^{-1}$) weighted by a considerable dipole moment difference ($\Delta\mu = 1.81 ea_0$) between these states and (2) the

large spin-orbit contribution of the $S_2(\pi \rightarrow \pi^*)$ state to the $T_{1,z}$ wave function ($\langle S_0 | \hat{H}_{SO} | T_{1z} \rangle = 118.8 \text{ cm}^{-1}$, $\Delta E = -14\ 002 \text{ cm}^{-1}$) that is to be multiplied by the strong $S_0 \leftarrow S_2$ transition moment ($\langle S_0 | \mu | S_2 \rangle = -2.28 ea_0$). The contribution of the direct term is also present in the QDPT calculations based on eight zeroth-order states, whereas the second term is missing in this expansion. A similar analysis of the $S_0 \leftarrow T_{1,x}$ and $S_0 \leftarrow T_{1,y}$ emission reveals that the contribution of low-lying electronic states is small. The most prominent individual contribution to the $S_0 \leftarrow T_{1,x}$ transition stems from the 2^1B_1 state (not contained in the eight LS state basis) that is related to the S_0 and T_1 states by ($\sigma \rightarrow \pi^*$) and ($\sigma \rightarrow n$) single excitations, respectively. In case of the $T_{1,y}$ emission, no dominant contribution can be singled out. This level interacts with singlet states of B_2 symmetry. The ($n \rightarrow \sigma^*$) excited 3^1B_2 and 5^1B_2 states, exhibit medium-sized SOCMEs with T_1 but their amplitudes enter $\langle S_0 | \mu | T_{1,y} \rangle$ with different phases and thus cancel partially.

Experimentally, decay rates of the T_1 state of 4H-pyran-4-thione were determined in *n*-pentane matrices at temperatures between 1 and 77 K and in solution at room temperature. In the low-temperature regime, Taherian and Maki were able to observe emission from the $T_{1,x}$ and $T_{1,y}$ sublevels with lifetimes of $\tau_x = 2.3 \text{ ms}$ and $\tau_y = 3.7 \text{ ms}$.³⁵ Emission from the T_z sublevel starts at temperatures between 10 and 20 K. Assuming a Boltzmann distribution of the fine-structure level populations and a triplet quantum yield of 1, a lifetime of $\tau_z = 21 \mu\text{s}$ was deduced then by these authors from the known values for τ_x and τ_y , the fine-structure splitting in trap site B ($\sim 24 \text{ cm}^{-1}$), and the high-temperature value of $\bar{\tau} = 85 \mu\text{s}$ measured at 77 K. Unfortunately, Taherian and Maki did not determine phosphorescence quantum yields. Due to the experimental conditions, the decay rates are free from self-quenching of the T_1 state, but they contain contributions from phosphorescence as well as the ISC $T_1 \rightsquigarrow S_0$. Pure phosphorescence lifetimes were deduced by Szymanski *et al.* from T_1 lifetime measurements at room temperature for various concentrations of 4H-pyran-4-thione in 3-methylpentane (3-MP) and perfluoro-1,3-dimethylcyclohexane (PF-1,3-DMCH).⁵⁷ Self-quenching rates were eliminated by extrapolating observed decay rates to infinite dilution. By means of measured quantum yields

TABLE III. Convergence of T_1 phosphorescence lifetimes of pyranthione with expansion lengths.

	QDPT			MRSOCl		
	ΔE (cm ⁻¹)	μ (ea_0)	τ (ms)	ΔE (cm ⁻¹)	μ (ea_0)	τ (ms)
8 LS states						
$T_{1,x}$	14 652.31	1.69×10^{-6}	5×10^8	14 653.53	2.31×10^{-3}	29
$T_{1,y}$	14 652.31	2.81×10^{-5}	2×10^5	14 653.54	1.05×10^{-3}	142
$T_{1,z}$	14 674.93	1.89×10^{-2}	0.437	14 674.85	3.30×10^{-2}	0.143
High- T average			1.311			0.426
48 LS states						
$T_{1,x}$	14 489.13	1.63×10^{-3}	61	14 490.03	2.45×10^{-3}	27
$T_{1,y}$	14 489.20	0.73×10^{-3}	302	14 490.04	1.08×10^{-3}	140
$T_{1,z}$	14 508.78	3.81×10^{-2}	0.111	14 509.48	3.84×10^{-2}	0.110
High- T average			0.332			0.328

3. METHODENENTWICKLUNG UND IMPLEMENTIERUNG

124101-12 Kleinschmidt, Tatchen, and Marian

J. Chem. Phys. **124**, 124101 (2006)

and several assumptions concerning interconversion rates, they estimated phosphorescence lifetimes of $\bar{\tau}_p=90\ \mu\text{s}$ in PF-1,3-DMCH and $\bar{\tau}_p=137\ \mu\text{s}$. Given the uncertainties these assumptions entail, we find very good agreement between our computed high-temperature lifetime of T_1 and the experimental values. The triplet lifetimes of the individual $T_{1,x}$ and $T_{1,y}$ sublevels measured in the low-temperature regime⁵⁵ are significantly shorter than the calculated phosphorescence lifetimes. At the present state of knowledge we attribute this difference to nonradiative relaxation via efficient $T_1 \rightsquigarrow S_0$ ISC.

C. Application to free-base porphyrin

Porphyrin derivatives are frequently used as triplet sensitizers. Triplet sensitizers exhibit a high triplet quantum yield and a sufficiently long T_1 lifetime to undergo spin-exchange reactions with other molecules. Only 5% of the photoexcited free-base porphyrin molecules decay by fluorescence after excitation of the optically bright Soret band and internal conversion to S_1 .⁶² The triplet quantum yield is found to be nearly 90%. It is generally assumed that the efficient triplet population is due to $S_1 \rightsquigarrow T_1$ ISC, but the mechanism is not known in detail.

Despite the high triplet quantum yield, no phosphorescence was observed for free-base porphyrin in *n*-octane or Ne matrices at 4.2 K.^{63,64} Under these conditions, most of the triplet population decays nonradiatively to the ground state by $T_1 \rightsquigarrow S_0$ ISC. The phosphorescence quantum yield was predicted to be of the order of 10^{-4} .^{65,66} Extremely weak phosphorescence with 0-0 transition at 794 nm (1.56 eV) was observed for free-base porphyrin in a mixture of benzene and octane by Tsvirko *et al.*⁶⁶ These authors determined the probability for a radiative $S_0 \leftarrow T_1$ transition to be $0.0078\ \text{s}^{-1}$ at 77 K, corresponding to a natural phosphorescence lifetime of $\bar{\tau}_p=128\ \text{s}$. A similar value ($\bar{\tau}_p=80\ \text{s}$) was reported by Gouterman and Khalil⁶⁵ for free-base porphyrin in glassy matrices of an ethyl ether/isopentane/ethanol/ethyl iodide (EPA/EtI) admixture. Furthermore, these authors were able to resolve the 0-0 transition $S_0 \leftarrow T_1$ at 785 nm (1.58 eV). A considerably longer lifetime was concluded from the dynamics of microwave-induced fluorescence transients by van Dorp *et al.*⁶³ in *n*-octane. $T_{1,x}$ was found to be the only active level.⁶⁷ van Dorp *et al.* estimated its radiative decay rate to be of the order of $2 \times 10^{-3}\ \text{s}^{-1}$. In Xe matrices at 4 K, fluorescence is completely quenched. Radziszewski *et al.*⁶⁴ identified the origins of phosphorescence emissions at two different matrix environments to be located at $12\ 677\ \text{cm}^{-1}$ (site A, 1.57 eV) and $12\ 588\ \text{cm}^{-1}$ (site B, 1.56 eV), respectively. These spectra show a nice vibrational progression based on a totally symmetric (a_g) $1614\ \text{cm}^{-1}$ mode.

Theoretical phosphorescence lifetimes of the 1^3B_{2u} state were reported by Loboda *et al.*⁶⁸ and Minaev and Ågren.⁶⁹ They applied time-dependent quadratic response theory utilizing the B3-LYP density functional. The results appear to be rather sensitive to the AO basis set. Loboda *et al.*⁶⁸ obtain a phosphorescence lifetime of $\tau_{p,x}=385\ \text{s}$ for the $T_{1,x}$ level⁷⁰ employing a cc-pVTZ basis. The contributions of the other triplet levels to the radiative decay are small. The high-

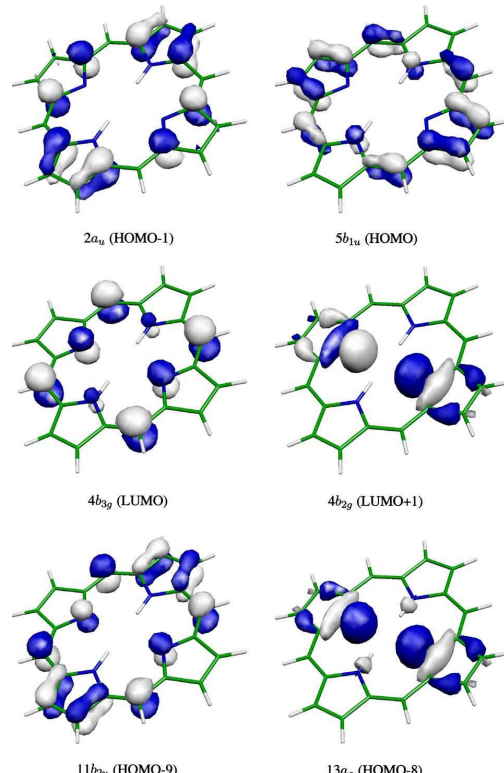


FIG. 5. (Color online) Orbitals of porphyrin at the T_1 geometry.

temperature limit of $\bar{\tau}_p=1128\ \text{s}$ is thus determined almost solely by the $T_{1,x} \rightarrow S_0$ transition. Minaev and Ågren⁶⁹ find similar values when using the very small 3-21G basis ($\tau_x=540\ \text{s}$, $\bar{\tau}_p=1619\ \text{s}$) whereas the better 6-31G** basis yields a ten times longer phosphorescence lifetime ($\tau_x=5128\ \text{s}$, $\bar{\tau}_p=15\ 381\ \text{s}$). Except for the 6-31G** result, the calculated phosphorescence lifetimes agree well with the experimental estimate by van Dorp *et al.*,⁶³ but are considerably longer than the high-temperature phosphorescence lifetimes determined by Tsvirko *et al.*⁶⁶ and Gouterman and Khalil.⁶⁵ Moreover, it has to be noted that Minaev and Ågren carried out the response calculations at the ground state equilibrium geometry. Strictly speaking, their calculated electronic transition rates thus do not correspond to true Einstein probabilities for spontaneous phosphorescence emission as the latter have to be evaluated at the T_1 minimum geometry where the vertical S_0-T_1 energy gap ΔE is smaller than at the S_0 geometry. Because ΔE enters expression (12) to the third power, the actual choice of the nuclear geometry might have a significant influence on the computed emission probability and thus on the phosphorescence lifetime.

We optimized the geometries of the porphyrin molecule in its S_0, S_1 , and T_1 electronic states in C_1 symmetry by means of (TD)DFT employing the B3-LYP density functional.^{27,71} In agreement with conventions, the x axis is chosen to pass through the N-H bonds of free-base porphyrin

TABLE IV. Excitation energies (eV) of singlet and triplet states in porphyrin at different nuclear geometries.

Method AO basis Reference Geometry	DFT/MRCI			TDDFT/B-P		TDDFT/B3-LYP		CASPT2
	TZVP		SVP+diff.	cc-PVTZ	6-31G**	ANO-S		
	<i>T</i> ₁	<i>S</i> ₁	<i>S</i> ₀	73	68	69	74	
<i>S</i> ₀ (1 ¹ <i>A</i> _g)	0.23	0.05	0.00	0.00	0.00	0.00	0.00	
<i>S</i> ₁ (1 ¹ <i>B</i> _{3u})	2.13	<u>1.94</u>	1.94	2.13	2.25	2.27	1.63	
<i>S</i> ₂ (1 ¹ <i>B</i> _{2u})	2.52	2.39	2.37	2.25	2.35	2.44	2.11	
<i>S</i> ₃ (2 ¹ <i>B</i> _{3u})	3.32	3.06	3.09	2.94	3.32	3.33	3.08	
<i>S</i> ₄ (1 ¹ <i>B</i> _{1g})	3.15	3.08	3.15	2.90	
<i>S</i> ₅ (2 ¹ <i>A</i> _g)	3.14	3.14	3.16	2.94	
<i>S</i> ₆ (2 ¹ <i>B</i> _{2u})	3.33	3.16	3.16	2.96	3.39	3.41	3.12	
:								
<i>S</i> ₁₉ (1 ¹ <i>B</i> _{1u})	4.18	4.28	4.26	3.28	3.82	3.85	...	
<i>T</i> ₁ (1 ³ <i>B</i> _{2u})	<u>1.68</u>	1.81	1.79	1.58	1.51	1.46	1.52	
<i>T</i> ₂ (1 ³ <i>B</i> _{3u})	2.24	2.01	2.02	1.74	1.70	1.81	1.85	
<i>T</i> ₃ (2 ³ <i>B</i> _{2u})	2.59	2.10	2.08	1.97	2.01	...	1.98	
<i>T</i> ₄ (2 ³ <i>B</i> _{3u})	2.47	2.32	2.26	1.99	2.15	...	1.88	
<i>T</i> ₅ (1 ³ <i>B</i> _{1g})	3.23	2.85	2.91	2.56	2.68	
<i>T</i> ₆ (3 ³ <i>B</i> _{3u})	3.32	2.94	2.98	2.63	
<i>T</i> ₇ (1 ³ <i>A</i> _g)	3.19	3.16	3.17	2.63	3.25	

and the *z* axis is perpendicular to the molecular plane. Although the starting geometry was artificially distorted by displacing some atoms, these states exhibit *D*_{2h} symmetry after optimization. The two highest occupied MOs, *2a*_u(HOMO-1) and *5b*_{1u} (HOMO) (see Fig. 5, upper panel), are very close in energy so that their energetic order may swap even for small nuclear distortions. A similar observation is made for the two lowest unoccupied MOs, *4b*_{3g} (LUMO) and *4b*_{2g}(LUMO+1) (Ref. 72) (see Fig. 5, middle). Not surprisingly, the electronic structures of low-lying excited singlet and triplet states are of strong multiconfigurational character.

The nuclear distortions in the *T*₁ state with respect to the electronic ground state equilibrium structure follow the trends expected from the MO picture. At the *S*₀ geometry, the *T*₁ state (1³*B*_{2u}) is dominated by the HOMO→LUMO excitation with a smaller contribution from the HOMO-1→LUMO+1 excitation. As the HOMO is a nonbonding π orbital, the nodal structure of the LUMO primarily determines the geometry shifts on the *T*₁ hypersurface. The latter π orbital is partially bonding and partially antibonding within the pyrrol moieties. Furthermore, it exhibits negative interference between the pyrrol amplitudes and the neighboring carbon *p*_z orbitals of the methine bridges. When the geometry is relaxed, the preponderance of the leading electronic configuration is strengthened and reinforces the geometric effect. In the *T*₁ state, the central C₃-C'₃ bonds of the pyrrol rings are elongated by about 3 pm, whereas the C₂-C₃ and C'₂-C'₃ bonds shrink by the same amount. Due to the antibonding interaction in the LUMO, the bonds connecting the C₂/C'₂ centers of the pyrrol rings with the methine bridges become longer, too. As a result, the perimeter of the porphyrin ring is larger in *T*₁ compared to *S*₀.

Because of the larger exchange interaction between the *5b*_{1u} and *4b*_{3g} orbitals compared to the *5b*_{1u} and *4b*_{2g} pair,

the order of the singlet states is reversed with respect to the triplets. Furthermore, their electronic structures are dominated by two configurations with nearly equal weights. In the *S*₁ state, the bond length changes expected for the HOMO→LUMO+1 and HOMO-1→LUMO excitations nearly cancel. The only remarkable geometric distortion in the *S*₁ state is a variation of the bond angles in the porphin ring, leading to an increase of the distance between the two azine nitrogens by 0.04 pm.

DFT/MRCI calculations were performed for four singlet and four triplet states in each irreducible representation (64 states in total). Energies of low-lying singlet and triplet states are listed in Table IV relative to the ground state minimum. Additionally, the first singlet (*n*→π*) state is included because states of this type play an important role in explaining the observed phosphorescence rates. For comparison, we also included theoretically determined excitation energies from other studies that comprise triplet states.^{68,69,73,74}

DFT/MRCI calculations on several ¹*B*_{2u} and ¹*B*_{3u} have been carried out earlier by Parusel and Grimme using a smaller (SVP) AO basis set.⁷⁵ The excitation energies are nearly unaffected when extending the AO basis set to TZVP quality. For these ¹*B*_{2u} and ¹*B*_{3u} states, the differences between their SVP and our TZVP results amount to at most 0.02 eV. Compared to experiment, we find excellent agreement. In vapor spectra, Edwards *et al.*⁷⁶ measured an excitation energy of 1.98 eV (627.5 nm) for the 0-0 transition of the *Q*_x band (*S*₀→*S*₁) which may be compared to our adiabatic excitation energy of 1.94 eV. (Note the almost negligible effect of the geometry relaxation in the *S*₁ state on the calculated excitation spectrum.) Also our computed vertical *S*₂ excitation energy (2.37 eV) agrees favorably with the experimentally determined origin transition of the *Q*_y band (*S*₀→*S*₂) at 2.42 eV (511.5 nm).⁷⁶ In the wavelength range

3. METHODENENTWICKLUNG UND IMPLEMENTIERUNG

TABLE V. Dipole transition moments, phosphorescence rates, and lifetimes in free-base porphin computed at the S_0 and T_1 geometries by means of quasi-degenerate perturbation theory and spin-orbit configuration interaction procedures. $\tau(T_1)$ denotes the averaged lifetime of the T_1 sublevels in the high-temperature limit.

	$\langle T_{1,z} x S_0\rangle$ (ea_0)	$\langle T_{1,x} z S_0\rangle$ (ea_0)	k_z (s^{-1})	k_x (s^{-1})	$\tau(T_{1,z})$ (s)	$\tau(T_{1,x})$ (s)	$\tau(T_1)$ (s)
QDPT(S_0), 16 states	6.6×10^{-6}	68.2×10^{-6}	2.7×10^{-4}	0.0289	3 720	34.6	103
QDPT(S_0), 64 states	4.4×10^{-6}	62.4×10^{-6}	1.2×10^{-4}	0.0237	8 470	42.1	126
SOCI(S_0)	2.2×10^{-6}	53.0×10^{-6}	3.0×10^{-5}	0.0175	33 235	57.3	171
QDPT(T_1), 16 states	4.2×10^{-6}	68.7×10^{-6}	5.6×10^{-5}	0.0151	17 700	66.2	198
QDPT(T_1), 64 states	3.0×10^{-6}	68.4×10^{-6}	2.9×10^{-5}	0.0150	34 624	66.7	200
SOCI(T_1)	0.5×10^{-6}	91.8×10^{-6}	8.1×10^{-7}	0.275	1 200 000	36.4	109

of the Soret band ($\lambda_{\text{max}}=372.5$ nm,⁷⁶ corresponding to 3.33 eV), we actually find four strong vertical transitions in our calculations, $1^1A_g \rightarrow 2^1B_{3u}$ (3.09 eV), $1^1A_g \rightarrow 2^1B_{3u}$ (3.16 eV), $1^1A_g \rightarrow 3^1B_{3u}$ (3.53 eV), and $1^1A_g \rightarrow 3^1B_{3u}$ (3.54 eV). Our computed adiabatic excitation energy of the T_1 state (1.68 eV) is slightly higher than the 0-0 transition of the phosphorescence band (1.56–1.58 eV),^{64–66} but it should be kept in mind that the latter values were determined in matrices.

With the exception of the S_1 state, the TDDFT calculations employing the purely local B-P density functional⁷³ place all electronic states at lower excitation energies. In particular, the position of the ($n \rightarrow \pi^*$) excited 1^1B_{1u} state differs from its location in our calculated spectrum by nearly 1 eV. Presumably, this deviation can be attributed to the wrong asymptotic behavior of the B-P functional. When the B3-LYP functional with 20% Hartree-Fock exchange is used instead in the TDDFT calculations,^{68,69} the agreement is rather good, except for S_1 where the TDDFT excitation energy is higher than our DFT/MRCI value by about 0.3 eV and for T_1 and T_2 which are underestimated by approximately the same amount with respect to our results. Finally, the CASPT2 calculations with 16 active electrons in 14 active orbitals⁷⁴ yield S_1 , S_2 , T_1 , and T_2 excitation energies that are lower than ours by 0.2–0.3 eV, whereas excellent agreement is found for the higher 2^1B_{3u} and 2^1B_{2u} states.

SOCMEs of triplet and singlet states with excitation energies below 4 eV, evaluated at the T_1 minimum geometry, are extremely small, none of them exceeding 0.1 cm^{-1} (see Table V). A similar observation was made in a previous study⁸ for SOCMEs computed at the ground state equilibrium geometry. The only SOCMEs of considerable magnitude are found with the states of ($n \rightarrow \pi^*$) character. In our calculations, the lowest-lying *ungerade* singlet ($n \rightarrow \pi^*$) state, 1^1B_{1u} , comes as S_{19} at 4.18 eV, 2.50 eV above T_1 . This 1^1B_{1u} state is dominated by the $11b_{2u}$ (HOMO-9) $\rightarrow 4b_{3g}$ (LUMO) excitation. Herein $11b_{2u}$ is a lone-pair (n) orbital centered at the nitrogen atoms in the two dehydropyrrrol rings (Fig. 5, lower panel). The SOCME of this state with the T_1 state amounts to 20.88 cm^{-1} (18.13 cm^{-1} at S_0 geometry). In *gerade* symmetry, we observe large SOCMEs between S_0 and 3^1B_{2g} as well as 3^1B_{3g} . These triplet ($n \rightarrow \pi^*$) states originate from excitations of a lone-pair electron in the $13a_g$ orbital (HOMO-8, Fig. 5, lower panel) to LUMO and LUMO+1, respectively. For the MRSOCl calculation, the configuration space has been built up for a single state per

irreducible representation and multiplicity (16 states in total). As the energy gap selection criterion of the DFT/MRCI is based on the reference state with highest energy within a given multiplicity, this choice leads to a much smaller configuration space than for the above-mentioned DFT/MRCI calculations including 32 states in each multiplicity (see Table VI). Because the spin-orbit operator cannot couple *gerade* and *ungerade* symmetries, two separate MRSOCl calculations were performed. The dimension of the two MRSOCl matrices amounts to 8.8×10^6 in both cases. A tight convergence criterion of $5 \times 10^{-9} E_h$ was applied. In *gerade* symmetry, only the ground state root was computed, converging after the fifth iteration. In *ungerade* symmetry, the three roots corresponding to the T_1 state have reached convergence after ten iterations. For the calculation of transition MEs, the MR-SOCl vectors were merged subsequently.

For a better comparison with experiment, on one hand, and the theoretical results by Loboda *et al.*⁶⁸ and Minaev and Ågren,⁶⁹ on the other hand, we evaluated phosphorescence lifetimes both at the T_1 and S_0 minimum geometries. Since the transition from the $T_{1,y}$ level is symmetry forbidden in D_{2h} , only results for the $T_{1,x}$ and $T_{1,z}$ levels are shown in Table V. As a general trend we find that the dipole transition moments connecting the $T_{1,x}$ sublevel of T_1 with the electronic ground state are at least an order of magnitude larger than those of $T_{1,z}$. The largest single contribution to $\langle T_{1,x}|z|S_0\rangle$ comes from the above-mentioned $1^1B_{1u}(n \rightarrow \pi^*)$ state. Its coefficient in the spin-orbit perturbed wave function of the $T_{1,x}$ level amounts to 0.001 035. A similar value (0.001 012) is found for the projection of the $T_{1,x}$ MRSOCl vector on the unperturbed S_{19} wave function. The perturbational contribution of this state to the phosphorescence rate can be estimated by multiplying its coefficient in the spin-orbit perturbed wave function with the spin-free dipole transition moment to the ground state (0.1909), yielding $198 \times 10^{-6} ea_0$. Its effect is partially canceled by the contributions of higher-lying 1^1B_{1u} states as well as 3^1B_{2g} and 3^1B_{3g} states.

A clear trend concerning the size of the transition MEs cannot be made out when comparing corresponding numbers at the S_0 and T_1 geometries. While the transition moment relating the $T_{1,z}$ level with S_0 decreases upon geometry relaxation in the excited state, the MEs coupling $T_{1,x}$ and S_0 remain almost constant when evaluated at the QDPT level and nearly double at the MRSOCl level. The decrease of the vertical excitation energy from 1.79 eV at the S_0 geometry to

TABLE VI. Timings for different stages of the calculations on free-base porphyrin (D_{2h} symmetry) measured on a single Intel Xeon 2.4 GHz processor.

	Dim (1 vector)	CPU time (h)
MRCI (singlets, 4 states/IRREP)	1.1×10^6	26.5
MRCI (triplets, 4 states/IRREP)	1.9×10^6	35.5
1-RTDMs (32 singlets+32 triplets)		2.5
576 SOCMEs over 64 states		5.5
Total (perturbation theory)		≈ 70
MRCI (singlets, 1 state/IRREP)	0.4×10^6	1.0
MRCI (triplets, 1 state/IRREP)	0.6×10^6	7.5
MRSOCl (4 roots)	8.8×10^6	25.0
1-RTDMs (4 MRSOCl vectors)		4.8
Total (linear variation)		≈ 39

1.45 eV at the T_1 geometry generally leads to an increase of the T_1 phosphorescence lifetime. In the MRSOCl calculations, this effect is surpassed, however, by the strong increase of the dipole transition ME that enters Eq. (12) quadratically. The phosphorescence lifetime of the T_1 state of free-base porphyrin, determined as the high-temperature limit in our MRSOCl calculations, is in excellent agreement with the experimentally determined natural phosphorescence lifetimes of $\bar{\tau}_p=128$ s (Ref. 66) and $\bar{\tau}_p=80$ s.⁶⁵ Our phosphorescence lifetime computed from a perturbation expansion in the basis of 64 electronic states is somewhat longer, but still in the right ballpark, whereas the lifetimes resulting from TDDFT response calculations^{68,69} are two orders of magnitude larger. The TDDFT response results appear to agree better with the experimental estimate by van Dorp *et al.*⁶³ predicting a lifetime of about 500 s for the $T_{1,x}$ level. It should be kept in mind, however, that the latter authors did not observe phosphorescence at all but estimated the phosphorescence lifetime indirectly from the dynamics of microwave-induced fluorescence signals.

Computer resources required for carrying out spin-orbit calculations on a molecule as large as porphyrin using the DFT/MR(SO)CI branch of the SPOCK package are moderate. All calculations could be performed on a single-processor personal computer (PC) with 2 Gbytes memory. Timings for the various steps of the perturbational and variational calculations are collected in Table VI. The smaller dimension and shorter CPU times for the second set of spin-orbit-free DFT/MRCI runs is a consequence of the fact that a smaller number of LS states are sufficient to reach convergence in the MRSOCl approach compared to QDPT. Starting the Davidson procedure in the MRSOCl calculations with converged spin-orbit-free MRCI vectors accelerates the diagonalization process significantly so that the actual timing for the MRSOCl step (four roots) is kept low.

IV. SUMMARY AND CONCLUSIONS

In this paper, we have presented a new multireference spin-orbit coupling configuration interaction program, SPOCK.CI. In principle, it can be run as an *ab initio* MRSOCl or as an extension of semiempirical DFT/MRCI procedure including spin coupling between singlet and triplet

states. Extensive test calculations have been performed for three typical organic compounds, dithiosuccinimide, 4*H*-pyran-4-thione, and free-base porphyrin, utilizing the faster DFT/MRSOCl branch. In all three test cases, computed excitation energies and phosphorescence lifetimes of the T_1 states are in very good agreement with experimental results.

DFT/MRSOCl calculations carried out with various CI expansion lengths show that it is sufficient to merge the configuration spaces built up in spin-orbit-free DFT/MRCI calculations for a single root per space and spin symmetry, at least for typical organic compounds. The computed dipole transition moments for the $S_0 \leftarrow T_1$ emission are almost identical to the ones obtained from the largest calculations. This result is particularly encouraging with regard to second-order spin-orbit properties of larger molecules for which the calculation of many LS states may be cumbersome but is required for reaching a comparable convergence at the level of quasidegenerate perturbation theory. For the test cases studied, the additional inclusion of single excitations showed only a minor influence on the computed phosphorescence lifetimes. However, the results were found to be sensitive to the vector convergence threshold of the iterative Davidson diagonalization. The proper resolution of the near-degenerate triplet sublevels requires tight convergence criteria. The necessary convergence threshold is related to the fine-structure splitting in the T_1 state which is often well below 1 cm⁻¹ in light organic compounds.

With regard to timing, SPOCK.CI benefits from the application of various efficient techniques and approximations. We would like to mention here the implementation of a second-quantization formalism, the expansion of the wave functions in CSFs and fast algorithms for determining their spin-coupling coefficients, the extensive exertion of the Wigner-theorem, the use of effective one-electron spin-orbit integrals, the resolution-of-the-identity approximation for spin-independent four-index integrals, application of a multiroot Davidson diagonalization scheme, and, last not least, the very efficient DFT/MRCI ansatz. Many of these features were inherited from the original MRCI code by Grimme and Waletzke;¹¹ others were adapted by us to complex algebra and extended to include spin-orbit interactions. For the extremely fast generation of atomic spin-orbit mean-field integrals, the AMFI module by Schimmelpfennig¹⁰ has been made part of the SPOCK package. The variational determination of phosphorescence rates employing SPOCK.CI may be even faster than a sum-over-states or a QDPT approach because the number of roots that have to be determined in the Davidson procedure is significantly smaller.

Problems may arise in the current single-processor version of the program due to the large dimensions of the MRSOCl vectors. In particular, if properties of higher triplet states are to be investigated, memory requirements for the simultaneous storage of the c and σ vectors of all roots may become significant. A parallelized version of the SPOCK.CI program that can handle these cases is currently under development. A further obvious desideratum is the availability of scalar relativistic integrals for the treatment of large heavy element compounds. Presently, scalar relativity can be taken

3. METHODENENTWICKLUNG UND IMPLEMENTIERUNG

124101-16 Kleinschmidt, Tatchen, and Marian

J. Chem. Phys. 124, 124101 (2006)

into account only in the *ab initio* branch of SPOCK.CI through its interface to the MOLCAS program. *Ab initio* MRSOCl calculations, on the other hand, are feasible only for small to medium-sized molecules because of the slow convergence of the correlation energy with configuration space size and because of size-extensivity problems. An implementation of scalar relativistic no-pair integral routines into the TURBOMOLE package that could remedy this is underway.

ACKNOWLEDGMENTS

We are grateful to Mirko Waletzke and Stefan Grimme (University of Münster, Germany) for providing us with the spin-orbit-free DFT/MRCI code and many helpful discussions. Furthermore, we would like to thank Bernd Schimelpfennig (Forschungszentrum Karlsruhe, Germany) for the AMFI integral routines. This work was supported by Deutsche Forschungsgemeinschaft through Grant Nos. Ma 1051/5-1,3 and SFB663/C1.

APPENDIX: PROBLEMS IN A REAL DAVIDSON ALGORITHM

It can be shown⁴⁴ that the eigenvalues of a complex Hermitian matrix C ,

$$C = (A + iB), \quad (\text{A1})$$

with real part A and imaginary part iB are equal to the eigenvalues of a (double-sized) real symmetric matrix R ,⁷⁷

$$R = \begin{pmatrix} A & -B \\ B & A \end{pmatrix}. \quad (\text{A2})$$

In the real secular equation all eigenvalues experience an artificial double degeneracy but are otherwise identical to the ones of the complex matrix. Concomitantly, two (double-sized) real eigenvectors,

$$\begin{pmatrix} v \\ w \end{pmatrix} \text{ and } \begin{pmatrix} -w \\ v \end{pmatrix}, \quad (\text{A3})$$

are obtained instead of one complex eigenvector $(v + iw)$ of matrix C . The second half of the real vectors is to be interpreted as the imaginary part, and the second vector is nothing but the first one multiplied by the phase factor i . Due to their degeneracy usually only one of these two eigenvectors is required for evaluating properties.

Operations occurring in the course of the Davidson algorithm are multiplications of vectors with a real scalar, additions of vectors, the matrix-vector multiplication, and, in the orthogonalization step, scalar products of vectors. All of these steps yield identical results no matter whether we use a complex or double-sized real algorithm, exemplified here for the matrix-vector multiplication,

$$(A + iB)(v + iw) = Av - Bw + i(Aw + Bv), \quad (\text{A4})$$

$$\begin{pmatrix} A & -B \\ B & A \end{pmatrix} \begin{pmatrix} v \\ w \end{pmatrix} = \begin{pmatrix} Av - Bw \\ Aw + Bv \end{pmatrix}, \quad (\text{A5})$$

except for the scalar product. While the norm is conserved and expectation values (and therefore energies) are not af-

fected, this does not necessarily apply to off-diagonal MEs. The scalar product of two complex eigenvectors $(v + iw)$ and $(x + iy)$ yields

$$(v + iw)^{\dagger} \cdot (x + iy) = v^T x + w^T y + i(-w^T x + v^T y). \quad (\text{A6})$$

For these vectors to be orthogonal (as required in the complex secular equation), the real and imaginary parts have to vanish separately. The scalar product of the corresponding vectors in real space gives

$$\begin{pmatrix} v \\ w \end{pmatrix}^T \cdot \begin{pmatrix} x \\ y \end{pmatrix} = v^T x + w^T y. \quad (\text{A7})$$

In order to restore the imaginary part of the complex-valued ME in Eq. (A6), one needs to compute a second scalar product between the pairs of degenerate eigenvectors in real space, e.g.,

$$\begin{pmatrix} -w \\ v \end{pmatrix}^T \cdot \begin{pmatrix} x \\ y \end{pmatrix} = -w^T x + v^T y. \quad (\text{A8})$$

The orthogonalization of the real vectors in the real Davidson algorithm ensures that the right-hand sides of Eqs. (A7) and (A8) are zero and, therefore, also the complex scalar product equals zero and orthogonality is guaranteed.

On the other hand, the scalar product of the two artificially degenerate real vectors (A3) does not vanish when they are interpreted as members of the complex vector space:

$$(v + iw)^* (-w + iv) = i(v^2 + w^2) = i. \quad (\text{A9})$$

Their nonorthogonality in the complex sense does not constitute a problem as long as no true degeneracy of eigenvalues occurs (not counting the artificial degeneracy), because one may freely choose any one of these two vectors, $(v + iw)$ or $(-w + iv)$, for the computation of properties. In cases with true (e.g., twofold) degeneracy of eigenvalues, with corresponding eigenvectors $(v + iw)$ and $(s + it)$, the four vectors occurring in the real Davidson algorithm would ideally follow the form of Eq. (A3):

$$\begin{pmatrix} v \\ w \end{pmatrix} \text{ and } \begin{pmatrix} -w \\ v \end{pmatrix} \text{ and } \begin{pmatrix} s \\ t \end{pmatrix} \text{ and } \begin{pmatrix} -t \\ s \end{pmatrix}. \quad (\text{A10})$$

In this case, it is not straightforward to deduce which two of these vectors to choose for the evaluation of properties, in particular, because the order in which they appear is random. In the complex sense, the first two vectors are not orthogonal among each other, but are orthogonal to the second group of two eigenvectors, which, in turn, are not orthogonal to each other. Moreover, linear combinations may occur, e.g., the two rightmost vectors may undergo a linear combination:

$$\begin{pmatrix} v \\ w \end{pmatrix} \text{ and } \begin{pmatrix} s \\ t \end{pmatrix} \text{ and } \begin{pmatrix} -w - t \\ +v + s \end{pmatrix} \text{ and } \begin{pmatrix} -w + t \\ +v - s \end{pmatrix} \quad (\text{A11})$$

(normalization has been left out here). Orthogonality in the real sense is ensured by the algorithm; but in complex vector space now the first vector is neither orthogonal to the third nor to the fourth vector. By further mixing of the vectors, orthogonality may be totally destroyed, leading to unphysical results in a subsequent property calculation. It should be noted that this problem is not of theoretical nature but was

encountered by us in actual calculations on linear molecules.

In conclusion, this means that the substitution of the complex Hamiltonian matrix in a SOCI calculation by a real symmetric one is only applicable if the vectors are not used in subsequent property calculations. Otherwise, either a complex Davidson algorithm must be employed, or at least, the orthogonalization step in the real Davidson scheme has to be modified.

- ¹I. P. Grant and H. M. Quiney, *Relativistic Self-Consistent Fields* (Elsevier, Amsterdam, 2002), vol. 1, p. 107.
- ²K. G. Dyall, J. Chem. Phys. **100**, 2118 (1994).
- ³B. Heß and C. Marian, in *Computational Molecular Spectroscopy*, edited by P. Jensen and P. Bunker (Wiley, Sussex, 2000), pp. 169–219.
- ⁴*Relativistic Electronic Structure Theory*, edited by P. Schwerdtfeger (Elsevier, Amsterdam, 2002), Vol. 1.
- ⁵M. Kleinschmidt, Ph.D. thesis, Heinrich Heine University Düsseldorf, 2005.
- ⁶J. E. Tatchen, Ph.D. thesis, Heinrich Heine University Düsseldorf, 2005.
- ⁷M. Kleinschmidt, J. Tatchen, and C. M. Marian, J. Comput. Chem. **23**, 824 (2002).
- ⁸M. Kleinschmidt and C. M. Marian, Chem. Phys. **311**, 71 (2005).
- ⁹B. A. Heß, C. M. Marian, U. Wahlgren, and O. Gropen, Chem. Phys. Lett. **251**, 365 (1996).
- ¹⁰B. Schimelpfennig, AMPI, an atomic spin-orbit integral program, University of Stockholm, 1996.
- ¹¹S. Grimme and M. Waletzke, J. Chem. Phys. **111**, 5645 (1999).
- ¹²S. R. Langhoff and C. W. Kern, in *Modern Theoretical Chemistry*, edited by H. F. Schaefer III (Plenum, New York, 1977), Vol. 4, pp. 381–437.
- ¹³H. Ågren, O. Vahtras, and B. Minaev, Adv. Quantum Chem. **27**, 71 (1996).
- ¹⁴O. Vahtras, H. Ågren, P. Jørgensen, H. J. A. Jensen, T. Helgaker, and J. Olsen, J. Chem. Phys. **97**, 9178 (1992).
- ¹⁵I. Tunell, Z. Rinkevicius, O. Vahtras, P. Salek, T. Helgaker, and H. Ågren, J. Chem. Phys. **119**, 11024 (2003).
- ¹⁶F. Neese, J. Chem. Phys. **115**, 11080 (2001).
- ¹⁷O. Christiansen and J. Gaus, J. Chem. Phys. **116**, 6674 (2002).
- ¹⁸B. A. Heß, R. J. Buerker, C. M. Marian, and S. D. Peyerimhoff, Chem. Phys. **71**, 79 (1982).
- ¹⁹D. R. Yarkony, J. Chem. Phys. **84**, 2075 (1986).
- ²⁰S. J. Hutter, Ph.D. thesis, University of Bonn, 1994.
- ²¹R. J. Buerker, A. B. Alekseyev, H.-P. Liebermann, R. Lingott, and G. Hirsch, J. Chem. Phys. **108**, 3400 (1998).
- ²²V. Vallet, L. Maron, C. Teichteil, and J.-P. Flament, J. Chem. Phys. **113**, 1391 (2000).
- ²³S. Yabushita, Z. Zhang, and R. M. Pitzer, J. Phys. Chem. A **103**, 5791 (1999).
- ²⁴M. Sjovoll, O. Gropen, and J. Olsen, Theor. Chem. Acc. **97**, 301 (1997).
- ²⁵T. Fleig, J. Olsen, and C. M. Marian, J. Chem. Phys. **114**, 4775 (2001).
- ²⁶A. D. Becke, J. Chem. Phys. **98**, 1372 (1993).
- ²⁷C. Lee, W. Yang, and R. G. Parr, Phys. Rev. B **37**, 785 (1988).
- ²⁸R. Ahlrichs, M. Bär, H.-P. Baron *et al.*, TURBOMOLE, Version 5.6, Universität Karlsruhe, 2002.
- ²⁹O. Vahtras, J. Almof, and M. W. Feyereisen, Chem. Phys. Lett. **213**, 514 (1993).
- ³⁰K. Andersson, M. Barysz, A. Bernhardsson *et al.*, MOLCAS, Lund's University.
- ³¹J. Tatchen and C. M. Marian, Chem. Phys. Lett. **313**, 351 (1999).
- ³²D. Danovich, C. M. Marian, T. Neuheuser, S. D. Peyerimhoff, and S. Shaik, J. Phys. Chem. A **102**, 5923 (1998).
- ³³F. Rakowitz and C. M. Marian, Chem. Phys. Lett. **257**, 105 (1996).
- ³⁴B. O. Roos and P. E. M. Siegbahn, in *Modern Theoretical Chemistry*, edited by H. F. Schaefer III (Plenum, New York, 1977), Vol. 3, pp. 277–318.
- ³⁵R. Samzow and B. A. Heß, Chem. Phys. Lett. **184**, 491 (1991).
- ³⁶R. Samzow, B. A. Heß, and G. Jansen, J. Chem. Phys. **96**, 1227 (1992).
- ³⁷R. McWeeny, J. Chem. Phys. **42**, 1717 (1965).
- ³⁸Note a typo in Table 2 of Ref. 37. The first case ($S=S_a=S_b$, $M_a=M$, $M_b=M \pm 1$) should read $C_1=\mp[1/2(S\pm M+1)(S\mp M)]^{1/2}$.
- ³⁹In the actual implementation always $M_S=S$ wave functions are employed, irrespective of the irreducible representation of the spatial part. Before multiplying the spatial integrals with the spin factor, the latter is converted to a matrix element of the appropriate Cartesian spin operator by means of the scaled $3j$ -symbol approach (Ref. 37).
- ⁴⁰E. R. Davidson, J. Comput. Phys. **17**, 87 (1975).
- ⁴¹M. Crouzeix, B. Philippe, and M. Sadkane, J. Sci. Comput. **15**, 62 (1994).
- ⁴²W. Butscher and W. Kammer, J. Comput. Phys. **20**, 313 (1976).
- ⁴³M. Kleinschmidt, Diploma thesis, University of Bonn, 1999, www.thch.uni-bonn.de/tcl/
- ⁴⁴W. H. Press, S. A. Teukolsky, W. T. Vetterling, and B. P. Flannery, *Numerical Recipes in Fortran 77: The Art of Scientific Computing* (Cambridge University Press, Cambridge, 1992).
- ⁴⁵R. W. Wetmore and G. A. Segal, Chem. Phys. Lett. **36**, 478 (1975).
- ⁴⁶L. L. Lohr, Jr., J. Chem. Phys. **45**, 1362 (1966).
- ⁴⁷L. Goodman and B. J. Laurenzi, Adv. Quantum Chem. **4**, 153 (1968).
- ⁴⁸R. Ahlrichs, M. Bär, M. Häser, H. Horn, and C. Kölmel, Chem. Phys. Lett. **162**, 165 (1989).
- ⁴⁹A. Schäfer, C. Huber, and R. Ahlrichs, J. Chem. Phys. **100**, 5829 (1994).
- ⁵⁰F. Furche and R. Ahlrichs, J. Chem. Phys. **117**, 7433 (2002).
- ⁵¹F. Weigend, M. Häser, H. Patzelt, and R. Ahlrichs, Chem. Phys. Lett. **294**, 143 (1998).
- ⁵²K. Eichhorn, O. Treutler, H. Öhm, M. Häser, and R. Ahlrichs, Chem. Phys. Lett. **240**, 283 (1995).
- ⁵³N. J. Turro, *Modern Molecular Photochemistry* (University Science Books, Sausalito, CA, 1991).
- ⁵⁴M. Klessinger and J. Michl, *Excited States and Photochemistry of Organic Molecules* (VCH, Weinheim, 1995).
- ⁵⁵M. R. Taherian and A. H. Maki, Chem. Phys. Lett. **96**, 541 (1983).
- ⁵⁶A. Safarzadeh-Amiri, R. E. Verall, and R. P. Steer, Can. J. Chem. **61**, 894 (1983).
- ⁵⁷M. Szymanski, R. P. Steer, and A. Maciejewski, Chem. Phys. Lett. **135**, 243 (1987).
- ⁵⁸S. C. J. Meskers, T. Poloński, and H. M. Dekkers, J. Phys. Chem. **99**, 1134 (1995).
- ⁵⁹A. Maciejewski and R. P. Steer, Chem. Rev. (Washington, D.C.) **93**, 67 (1993).
- ⁶⁰J. Tatchen, M. Kleinschmidt, C. M. Marian, M. Parac, and S. Grimme, Z. Phys. Chem. **217**, 205 (2003).
- ⁶¹J. Tatchen, M. Waletzke, C. M. Marian, and S. Grimme, Chem. Phys. **264**, 245 (2001).
- ⁶²A. T. Gradyushko and M. P. Tsvirko, Opt. Spectrosc. **31**, 291 (1971).
- ⁶³W. G. van Dorp, W. H. Schoemaker, M. Soma, and J. H. van der Waals, Mol. Phys. **30**, 1701 (1975).
- ⁶⁴J. G. Radziszewski, J. Waluk, M. Nepraš, and J. Michl, J. Phys. Chem. **95**, 1963 (1991).
- ⁶⁵M. Gouterman and G.-E. Khalil, J. Mol. Spectrosc. **53**, 88 (1974).
- ⁶⁶M. P. Tsvirko, K. N. Solovev, A. T. Gradyushko, and S. S. Dvornikov, Opt. Spectrosc. **38**, 400 (1975).
- ⁶⁷The x axis passes through the N–H bonds of free-base porphin and the z axis is perpendicular to the molecular plane.
- ⁶⁸O. Loboda, I. Tunnell, B. Minaev, and H. Ågren, Chem. Phys. **312**, 299 (2005).
- ⁶⁹B. Minaev and H. Ågren, Chem. Phys. **315**, 215 (2005).
- ⁷⁰In the original publication, this sublevel is denoted $^3B_{2u}^*$ because the x and z axes had been interchanged.
- ⁷¹P. J. Stephens, F. J. Devlin, C. F. Chabalowski, and M. J. Frisch, J. Phys. Chem. **98**, 11623 (1994).
- ⁷²In metalloporphyrins of D_{4h} symmetry, the latter two orbitals even form a degenerate pair (e_g).
- ⁷³D. Sundholm, Phys. Chem. Chem. Phys. **2**, 2275 (2000).
- ⁷⁴A. Serrano-Andrés, M. Merchan, M. Rubio, and B. O. Roos, Chem. Phys. Lett. **295**, 195 (1998).
- ⁷⁵A. Paruseł and S. Grimme, J. Porphyr. Phthalocyanines **5**, 1 (2001).
- ⁷⁶L. Edwards, D. H. Dolphin, M. Gouterman, and A. D. Adler, J. Mol. Spectrosc. **38**, 16 (1971).
- ⁷⁷For C being Hermitian, the matrix A has to be symmetric while B has to be skew symmetric. From this it easily follows that R is symmetric.

3. METHODENENTWICKLUNG UND IMPLEMENTIERUNG

4

Anwendungen

Der DFT-Zweig des SPOCK-Pakets wurde inzwischen in einer Reihe unterschiedlicher Moleküle angewendet. Im Laufe der Anwendungen fand eine stetige Fortentwicklung des SPOCK-Programms statt. Immer wieder wurde die Notwendigkeit von Detailverbesserungen oder neuen Funktionen aufgedeckt und diese implementiert.

4.1 Thiophen

Als erste Anwendung der störungstheoretischen Teils von SPOCK, SPOCK.PT, wurde das Thiophenmolekül gewählt. Als moderat großes organisches Molekül lässt es noch eine Behandlung mit dem *ab-initio* Zweig zu.

Das Thiophen wurde in der Arbeitsgruppe Weinkauf spektroskopiert. Aus den Beobachtungen nach Anregung des S_1 -Zustands wurde auf ein sehr schnelles ISC in den T_2 Zustand, sowie von dort einen ebenfalls sehr schnellen Zerfall in den T_1 Zustand geschlossen. Diese experimentellen Befunde sollten mit einer quantenchemischen Untersuchung durchleuchtet werden. Im Rahmen dieser ersten Untersuchung konnte keine zufriedenstellende Erklärung für das Verhalten des Thiophens gefunden werden: An der Geometrie des Grundzustands sind alle berechneten Matrixelemente zwischen den beteiligten Zuständen so klein, dass die schnelle Relaxation in den Triplettzustand nicht erklärt werden konnte. Auch ein künstlicher Symmetriebruch durch ein Kippen des Schwefels aus der Molekülebene brachte keinen weiteren Aufschluss. Die Ergebnisse sind in der Veröffentlichung zum SPOCK.PT in größerer Breite diskutiert.

Eine tiefergehende Untersuchung des Thiophens wurde in der Diplomarbeit von Susanne Salzmann mit SPOCK.PT und SPOCK.CI durchgeführt.[50] Dabei wurden auch Geometrien der angeregten Zustände optimiert sowie Geometrieverzerrungen berücksichtigt. In den meisten betrachteten Minimumgeometrien angeregter Zustände (bei S_1 , S_2 , T_1 und T_2) ist das Molekül nicht mehr planar. In S_3 und T_3 wurde darüberhinaus eine starke Aufweitung einer C-S-Bindung gefunden. S_3 ist das globale Minimum der Singulett-Potentialfläche. (Die Nomenklatur der Zustände folgt hier ihrer Reihenfolge im vertikalen Spektrum.) Vom S_1 ausgehend wurde ein Pfad minimaler Energie zum Minimum des S_3 Zustands ermittelt, der nur eine minimale Barriere aufweist, und in dessen Verlauf es zu mehreren Überschneidungen mit Triplettzuständen kommt.

4.2 Uracil

In der Arbeit „Electronic excitation and singlet-triplet coupling in uracil tautomers and uracil-water complexes“ („Elektronische Anregung und Singulett-Triplett-Kopplung in Uracil-Tautomeren und Uracil-Wasser-Komplexen“) wurden Singulett- und Tripletspektren von Uracil-Tautomeren untersucht. Die stabilste Kernanordnung entspricht der Diketoform des Uracils. Die elektronischen Grundzustände der anderen Tautomere liegen energetisch etwa 0.5-1 eV höher. Die Rechnungen liefern in Übereinstimmung mit früheren theoretischen und experimentellen Studien große Oszillatorstärken für $\pi \rightarrow \pi^*$ Anregungen. Für Rydberg- und $n \rightarrow \pi^*$ Zustände sind die Dipolübergangswahrscheinlichkeiten zum bzw. vom elektronischen Grundzustand klein. Der tiefstliegende Zustand entspricht einer ${}^3(\pi \rightarrow \pi^*)$ Anregung, gefolgt von einem $n \rightarrow \pi^*$ Triplett. Im Singulettspektrum der Diketoform ist die Reihenfolge der Zustände umgekehrt. Die Ergebnisse dieser theoretischen Studie zeigen, dass der erste dunkle ${}^1(n \rightarrow \pi^*) S_1$ und der ${}^1(\pi \rightarrow \pi^*) S_2$ Zustand, in den Anregung beobachtet wird, an der S_2 -Geometrie energetisch nahe beieinander liegen. Der Energieunterschied dieser beiden Zustände wird durch eine polare Umgebung und durch die Bildung von Wasserstoffbrücken weiter abgesenkt. Diese Nähe von dunklen und absorbierenden Zuständen ist ein möglicher Grund für das diffuse Spektrum der Absorptionsbanden im Uracil. Die Rechnungen weisen auch darauf hin, dass ein dissoziativer A'' Zustand, in dem ein σ_{NH}^* Orbital besetzt wird, eine entscheidende Rolle spielen könnte.

Spin-Bahn-*mean-field*-Rechnungen mit SPOCK.PT ergeben vernachlässigbare Kopplungen (kleiner 0.3 cm^{-1}) zwischen Singulets und Triplets gleicher Symmetrie. Im Gegensatz dazu sind die Kopplungsmatrixelemente zwischen den elektronischen A' und A'' Zuständen groß (etwa 20 bis 40 cm^{-1}). Aus den Spin-Bahn-Matrixelementen, Dipolübergangsmomenten und Anregungsenergien die sich an der T_1 -Geometrie ergeben, wurde die Phosphoreszenzlebensdauer störungstheoretisch unter Einbezug von je 17 Singulett- und Tripletzuständen zu $\tau_P^0 \approx 7.5 \text{ s}$ berechnet. ISC-Raten zwischen S_2 und T_1 werden als sehr klein vorhergesagt. Daher kann der T_1 -Zustand nicht direkt über die intensive $S_0 \rightarrow S_2$ -Anregung besetzt werden. Stattdessen kann T_1 indirekt über eine interne Konversion (IC) von S_2 nach S_1 und anschließendes ISC nach T_1 oder über ISC von S_2 nach T_2 und IC zwischen den Triplets erreicht werden.

Im Gegensatz dazu weist T_2 ein starkes Spin-Bahn-Matrixelement mit dem Grundzustand auf und ihre Dipolmomente unterscheiden sich beträchtlich. Weiterhin lehrt ihm der energetisch nahe liegende S_2 Zustand Intensität und ermöglicht eine effektive Besetzung von T_2 über ISC nach Absorption. Für T_2 ergeben die Rechnungen demzufolge auch eine wesentlich kürzere Phosphoreszenzlebensdauer von $\tau_P^0 \approx 1 \text{ ms}$. Die berechneten Phosphoreszenzlebensdauern stützen die Annahme, dass die in 2-Methyl-Tetrahydrofuran nach $S_0 \rightarrow S_2$ ${}^1(\pi \rightarrow \pi^*)$ Anregung gemessene Phosphoreszenz aus dem ${}^3(\pi \rightarrow \pi^*) T_1$ Zustand stammt.

Electronic excitation and singlet-triplet coupling in uracil tautomers and uracil-water complexes

A quantum chemical investigation

C.M. Marian^a, F. Schneider, M. Kleinschmidt, and J. Tatchen

Institute of Theoretical Chemistry, Heinrich-Heine-University, Universitätsstr. 1, 40225 Düsseldorf, Germany

Received 18 February 2002 / Received in final form 5 June 2002

Published online 13 September 2002 – © EDP Sciences, Società Italiana di Fisica, Springer-Verlag 2002

Abstract. Electronic spectra of uracil in its diketo (lactam) form and five enol (lactim) tautomeric forms have been investigated by means of combined density functional and configuration interaction methods. We have simulated the effects of hydrogen bonding with a protic solvent by recomputing the spectrum of uracil in the presence of two, four, or six water molecules. Geometries of the electronic ground state and several low-lying excited states have been optimized. Spin-orbit coupling has been determined for correlated wavefunctions employing a non-empirical spin-orbit mean-field approach. In accord with experiment, we find the diketo tautomer to be the most stable one. The calculations confirm that the first absorption band arises from the $^1(\pi \rightarrow \pi^*) S_0 \rightarrow S_2$ excitation. The experimentally observed vibrational structure in this band originates from a breathing mode of the six ring. Complexation with water molecules is seen to cause a significant blue shift of $n \rightarrow \pi^*$ excitations while leaving $\pi \rightarrow \pi^*$ excitations nearly uninfluenced. Computed radiative lifetimes are presented for the experimentally known weak phosphorescence from the $\pi \rightarrow \pi^*$ excited T_1 state. Among the uracil lactim tautomers, one is particularly interesting from a spectroscopic point of view. In this tautomer, the $\pi \rightarrow \pi^*$ excitation gives rise to the S_1 state.

PACS. 31. Electronic structure of atoms and molecules: theory – 33. Molecular properties and interaction with photons – 33.50.-j Fluorescence and phosphorescence; radiationless transitions, quenching (intersystem crossing, internal conversion)

1 Introduction

The pyrimidine bases uracil and thymine exhibit broad absorption bands in the ultra violet, both in the gas phase and in solution [1–7]. The first band with an onset at approximately 4.5 eV in vapor spectra has been assigned to a $\pi \rightarrow \pi^*$ transition [2,7]. This assignment is supported by recent *ab initio* quantum chemical studies [8,9]. They have shown that the $\pi \rightarrow \pi^*$ excited S_2 states of uracil and thymine are the lowest singlet states connected with the S_0 ground state by a considerable dipole transition probability. The computed oscillator strength for the $n \rightarrow \pi^*$ transition ($S_0 \rightarrow S_1$) is about three orders of magnitude smaller. In the first system, some vibrational structure was resolved (uracil $\approx 790 \text{ cm}^{-1}$; thymine $\approx 740 \text{ cm}^{-1}$ at low temperatures (77 K) in 2-methyltetrahydrofuran (2-MTHF)) [3]. At room temperature or in methanol-ethanol, no vibrational structure could be made out. Further, Becker and Kogan report weak fluorescence or phosphorescence, the appearance of which depends strongly on the solvent.

The reason for the diffuseness of the absorption spectra of thymine and uracil is not yet clear. Brady *et al.* attribute the spectral broadening either to mixing with a lower-lying electronic state or to a large geometry change between the ground and excited electronic states [7]. Candidates for an extensive intensity borrowing from the S_2 state of uracil could be highly excited vibronic levels of S_0 , S_1 , or some triplet state. High quality *ab initio* investigations predict S_1 to have a vertical excitation energy of about 4.5 eV [9], just at the onset of the observed broad band. So far, the energetic location of the triplet states has not been determined with high confidence and knowledge about electronic singlet-triplet coupling strengths in uracil is completely missing. Considering geometric effects, certainly a change of bond lengths and angles is to be expected upon a $\pi \rightarrow \pi^*$ excitation. It is not known, however, how strongly the molecular geometry influences the electronic spectrum.

Due to hydrogen migration, several tautomeric forms of uracil can be thought of (*cf.* Fig. 1). It is generally agreed that the diketo (lactam) form (A) is the most stable one in the electronic ground state and no other tautomer has ever been identified in solution or in the gas phase [3].

^a e-mail: Christel.Marian@uni-duesseldorf.de

4. ANWENDUNGEN

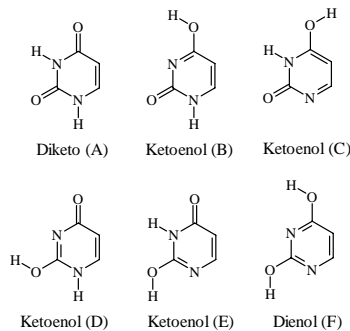


Fig. 1. Six tautomeric forms of uracil.

The situation is less clear for the excited electronic states, however. Ito and coworkers reported two band systems with well-resolved vibrational structures in fluorescence excitation and dispersed fluorescence spectra in a supersonic jet [5, 6]. They assigned the two band systems with 0^0 transition wavenumbers of $35\,288\text{ cm}^{-1}$ (4.38 eV, system I) and $30\,917\text{ cm}^{-1}$ (3.83 eV, system II) to $n \rightarrow \pi^*$ transitions in the diketo and a keto-enol tautomer, respectively. If the observation of a keto-enol tautomer of uracil or thymine were confirmed, this had large implications with respect to mutations in RNA or DNA replication. Brady *et al.* were able to reproduce system I [7]. They could show, however, that the carrier of this sharp fluorescence spectrum was not uracil but an impurity with higher mass produced in the oven. The origin of system II remained unclear.

The aim of the present quantum chemical study is to find an answer to some of these open questions. For all six tautomers shown in Figure 1, we have determined the ground state geometry and the electronic spectrum as well as properties of the low-lying singlet and triplet states including their spin-orbit interaction. We have studied the effects of singlet and triplet $\pi \rightarrow \pi^*$ and $n \rightarrow \pi^*$ excitations on the geometry of the diketo tautomeric form. The geometry relaxation after $\pi \rightarrow \sigma^*$ excitations has been estimated by calculating the electronic spectrum at the optimized geometry of the corresponding triplet state, T₄. Further, we have investigated the influence of hydrogen bonding on the molecular structure and the electronic spectrum by computing several uracil water complexes.

2 Methods

The reliable quantum chemical evaluation of the electronic spectrum and the spin-orbit coupling between electronic states requires the inclusion of static and dynamic electron correlation in the wavefunction determination as well as an efficient treatment of spin-orbit coupling. Standard *ab initio* packages are not applicable for this purpose, if the number of correlated electrons is large.

The combined density functional theory/multi-reference configuration interaction (DFT/MRCI) method by

Grimme and Waletzke has proven to yield excellent electronic spectra of organic molecules [10]. We have used this method for the determination of pure singlet and triplet electronic states of uracil in various tautomeric forms. The idea behind this approach is to include major parts of dynamic electron correlation by density functional theory whereas short MRCI expansions take account of static correlation effects. To this end, the configuration state functions (CSFs) in the MRCI expansion are built up from Kohn-Sham (KS) orbitals. Diagonal elements of the effective DFT/MRCI Hamiltonian are constructed from the corresponding Hartree-Fock based expression and a DFT specific correction term. In the effective DFT/MRCI Hamiltonian, all in all five empirical parameters are employed. These parameters depend only on the multiplicity of the desired state, the number of open shells of a configuration, and the employed density functional, but not on the specific atom or molecule. Currently, optimized parameter sets are available only for singlet and triplet multiplicities in combination with the BH-LYP [11, 12] functional. A common set of reference CSFs is used for all spatial symmetries. The initial set can be generated automatically in a complete active space (CAS)-like procedure and is then iteratively improved. The MRCI expansion is kept short by extensive configuration selection. For further details, we refer to the original publication by Grimme and Waletzke [10].

Technically, the MRCI code and the associated property programs are linked to the Turbomole package [13, 14]. They can thus take advantage of the efficiency with which the latter determines two-electron integrals and KS wavefunctions even for large molecules. Computationally expensive four-index integrals are evaluated using the well-known resolution of the identity (RI) method employing the RI-MP2 optimized auxiliary basis sets from the Turbomole library [15–17].

Geometry optimizations at the (U)DFT level were performed utilizing analytical gradients and approximate Hessians as generated by the rdgrad and relax modules of the Turbomole package. Unfortunately, these methods cannot be applied to open-shell singlet states. Moreover, analytical DFT/MRCI gradients are not yet available. To enable the geometry optimization of the S₁ and S₂ states at the correlated level, gradients were constructed numerically by finite difference techniques and the minima were located by a conjugate gradient search [18]. The current first program version works sequentially (one energy point at a time) and includes drivers for the dscf and ridft modules of Turbomole and for a DFT/MRCI calculation. An improved parallelized version will be available soon.

Spin-orbit matrix elements for DFT/MRCI wavefunctions have been generated with the recently presented spin-orbit coupling kit (Spock) [19]. Key features of this program are a fast determination of spin-coupling coefficients between CSFs for spin-dependent one-electron operators and the use of non-empirical atomic spin-orbit mean-field integrals. The spin-orbit mean-field Hamiltonian utilized in this work is an effective one-electron operator derived from the Breit-Pauli Hamiltonian; herein,

4.2. URACIL

screening by other electrons is incorporated in a Fock-like manner [20]. As an additional approximation, all multi-center spin-orbit integrals are neglected. In this way, the molecular mean field reduces to a sum of atomic mean fields.

The spin-orbit mean-field approach as such was shown to yield matrix elements in excellent agreement with those of the full one- and two-electron spin-orbit Hamiltonian [20]. Even for light molecules, the errors are usually well below 1% [21,22]. For light, conjugated molecules such as uracil, the one-center approximation is the most critical one in the hierarchy of approximations for the treatment of spin-orbit coupling. It was originally developed for the treatment of spin-orbit coupling in heavy metal compounds [20]. Multi-center spin-orbit integrals were found to contribute approximately 5% to the spin-orbit splitting in the ground state of the π -conjugated molecules HC_6H^+ , NC_5H^+ , and NC_4N^+ , composed of first-row elements only [21]. Errors of this size appear acceptable, as a full spin-orbit treatment is presently out of reach for molecules of the size of uracil. Moreover, there are little alternatives to this procedure. A neglect of multi-center two-electron integrals only, while keeping all generic one-electron terms, leads to larger deviations because the one- and two-electron multi-center terms tend to cancel systematically. Pseudopotential approaches that are technically also feasible meet the very same difficulties as the mean-field approach whereas parameterized effective charge spin-orbit Hamiltonians are generally too crude.

Spock is interfaced to the Turbomole package by the program S0mf [19]. Herein, mean-field orbitals are generated automatically for each atom from a restricted (open-shell) Hartree-Fock atomic ground state calculation and the atomic mean-field integral program Amfi [23] is called. Amfi makes use of spherical symmetry; spin-orbit integral evaluation is thus extremely fast. Finally, S0mf performs the transformation of the spin-orbit integrals from the atomic to the molecular orbital (MO) basis set. The application of these techniques and approximations in combination with the generation of correlated wavefunctions *via* the DFT/MRCI approach makes it possible to compute spin-orbit coupling in organic molecules efficiently and with high confidence.

3 Technical details

Geometry optimizations of the six local minima (A) - (F) on the electronic ground state surface were performed for a restricted closed shell KS determinant. Herein, all atoms were constrained to lie in a common plane, thus imposing C_s symmetry. In all cases, the BH-LYP density functional was employed [11,12]. In addition, we have optimized the geometries of three low-lying triplet states by means of an unrestricted open-shell density functional theory procedure. It has to be noted in this context that the order of the triplet states is reversed with respect to the singlet states: T_1 has the same electronic structure as S_2 whereas T_2 closely resembles S_1 . Starting from the DFT optimized

structures, the geometries of the three lowest-lying singlets (S_0 , S_1 , and S_2) as well as the two lowest-lying triplets (T_1 and T_2) were refined at the DFT/MRCI level.

We tested three different basis sets: the standard TZVP and TZVPP basis sets from the Turbomole library [13,24] and a basis set, which we will call TZVPP+Ryd, where we added $3s$, $3p$, and $1d$ primitive diffuse Gaussians with origin at a dummy center and exponents of 0.05, 0.02, 0.008 (s and p Rydberg) and 0.015 (d Rydberg). The position of this dummy center was allowed to adjust in the geometry optimizations. It coincides approximately with the molecular center of mass. A numerical grid, usually employed for the cesium atom, was chosen for the quadrature of the exchange correlation at the dummy center. It turned out that the addition of a second polarization function (TZVPP) had almost no effect on the DFT/MRCI results. Further, excitation energies of the low-lying states were not altered upon augmentation of the basis set by Rydberg functions. On these grounds, we performed all geometry optimizations utilizing the TZVP basis. Further, the relative energetic location of the low-lying states of conformers (A) - (F) and the spin-orbit coupling between singlet and triplet states were determined in this basis. On the other hand, excitation energies and wavefunction characteristics of higher-lying electronic states are considerably affected by the inclusion of diffuse functions due to valence-Rydberg mixing. For the diketo tautomer (A), a vertical spectrum was calculated both in the TZVP and the TZVPP+Ryd bases.

A common set of molecular KS orbitals, optimized for the dominant closed shell determinant of the electronic ground state, was employed as a one-particle basis for the subsequent MRCI runs. In the latter step, all 42 valence electrons of uracil were correlated. In the TZVP basis, the MRCI space was spanned by energy-selected single and double excitations from approximately 70 reference CSFs. In each irreducible representation, eigenvalues and eigenvectors of six singlet and triplet states were determined. The reference space of the MRCI calculations in the TZVPP+Rydberg basis comprised approximately 130 CSFs for twelve roots in either spin and space symmetry.

The structure of the uracil-water complexes was determined without symmetry constraints. As it was not meant to explore a great part of the multi-minima potential energy hypersurface, we optimized just a single local minimum in each case, starting from a decently guessed nuclear arrangement. A TZVP basis was used throughout and all valence electrons on uracil and the water molecules were correlated. In the MRCI calculations, we computed the six lowest singlet and triplet states of each complex.

4 Results and discussion

4.1 The diketo form of uracil

4.1.1 The electronic ground state

The calculated equilibrium geometry of uracil in its diketo form is shown in Figure 2. Bond lengths in the six ring

4. ANWENDUNGEN

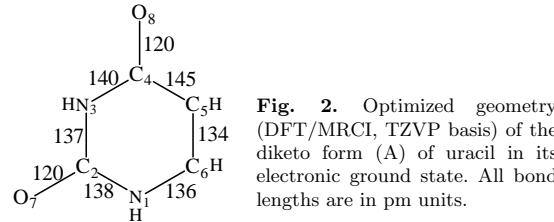


Fig. 2. Optimized geometry (DFT/MRCI, TZVP basis) of the diketo form (A) of uracil in its electronic ground state. All bond lengths are in pm units.

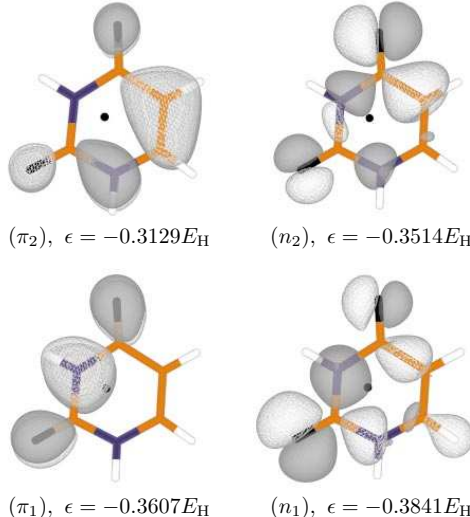


Fig. 3. The highest occupied n and π MOs. (Diketo form (A), S_0 geometry, TZVPP+Ryd basis, isoline = 0.020) The black dot in the six ring indicates the origin of the Rydberg basis.

agree excellently with experimental X-ray structural parameters [25]. Carbonyl bonds are slightly shorter than in the crystal structure (120 pm (both C–O groups, this work) vs. 121.5 pm (C₂–O₇) and 124.5 pm (C₄–O₈) [25]). We attribute parts of these differences to pairing effects in the solid state. Uracil crystals are built up from hydrogen bonded dimers in which the carbonyl oxygen O₈ is bonded to the N₃H group of the partner molecule thus leading to an elongation of the C₄–O₈ carbonyl bond. A trend in this direction is also seen in the uracil water complexes (see below) where the C–O bond distances are larger by 2–3 pm than in the isolated molecule.

Valence MOs that are important for an understanding of the spectrum are plotted in Figures 3 and 4. The highest occupied molecular orbital (HOMO, π_2) is a π -type orbital. It has a C₅–C₆ bonding character and is non-bonding elsewhere. The second highest MO (HOMO-1, n_2) is an in-plane orbital with large amplitudes for the O₈ carbonyl oxygen lone pair and the C₄–C₅ σ bond. The other oxygen lone pair, at O₇, dominates the n_1 orbital (HOMO-3). Finally, the third highest occupied MO (HOMO-2, π_1) has major contributions from the p_z orbitals on N₃ and both oxygen atoms. The lowest unoccu-



Fig. 4. The lowest unoccupied π^* MOs (other information as in Fig. 3).

pied MO (LUMO, π_3^*) exhibits a node between C₅ and C₆ whereas it is π bonding with respect to C₄–C₅. Further, it shows some C₄–O₈ anti-bonding characteristics. Several Rydberg orbitals are located in the energy gap between π_3^* and π_4^* , the next valence type MO. Like π_1 , π_4^* is nearly C_{2v} symmetric with the second vertical reflection plane running through N₃ and C₆.

4.1.2 Vertical absorption spectrum and characterization of excited states

Vertical singlet and triplet spectra of uracil were computed both in the TZVP and TZVPP+Ryd basis sets. As the results in Tables 1 and 2 suggest, the low-lying states (S_1 , S_2 , T_1 , T_2 , and T_3) are hardly influenced by the addition of further polarization functions and diffuse Gaussians. The first Rydberg excitations are found at 5.73 eV (triplet) and 5.83 eV (singlet). Energies and wavefunction characteristics of all states above 5.7 eV can therefore be trusted only if computed in basis sets augmented by Rydberg functions.

The first excited singlet state (S_1) is dominated by a single excitation from the second highest occupied MO (n_2 , HOMO-1) to the lowest unoccupied MO (π_3^* , LUMO). The singlet-coupled $\pi_2 \rightarrow \pi_3^*$ (HOMO-LUMO) excitation yields the second excited singlet S_2 . S_3 is of ${}^1A''$ symmetry. Its electronic structure corresponds to the promotion of an electron from the HOMO to the lowest a' orbital, which has Rydberg character at the ground state equilibrium geometry. Higher-lying singlets are considerably mixed. Dominant excitations occur into the valence π_3^* and π_4^* orbitals or into a variety of Rydberg orbitals that are globally labeled by R in Table 1.

As expected for ketones, $n \rightarrow \pi^*$ excitations are found to have negligible oscillator strengths for a dipole transition from the S_0 state. On the other hand, we obtain significant absorption probabilities for valence $\pi \rightarrow \pi^*$ excitations, in agreement with earlier theoretical treatments [8,9,27]. All strong transitions found in our calculated spectrum of uracil correspond to experimentally observed bands [1–4]. It has to be noted, however, that in polar solvents band maxima may shift considerably with respect to vapor spectra.

The first broad band in the vapor spectrum with a maximum at about 244 nm (5.08 eV) [2] is clearly due to

4.2. URACIL

Table 1. Vertical singlet excitation energies ΔE [eV] and dipole transition oscillator strengths $f(r)$ of uracil in its diketo form.

State	HF/MRCI; RPA [8]		CASPT2 [9]		DFT/MRCI, present work			absorption maximum	
	DZVP+Ryd		TZVP+Ryd	TZVP	TZVPP+Ryd				
	ΔE_{MRCI}	ΔE_{RPA}	ΔE	$f(r)$	ΔE	$f(r)$	dominant excitation(s)		
S ₀	1 ¹ A'	0.00	0.00	0.00	0.00	0.00			
S ₁	1 ¹ A''	5.48	6.04	4.54	0.00	4.61	4.61	0.0002 $n_2 \rightarrow \pi_3^*$	
S ₂	2 ¹ A'	6.28	6.29	5.00	0.19	5.48	5.44	0.2626 $\pi_2 \rightarrow \pi_3^*$	
S ₃	2 ¹ A''					5.83	0.0055	$\pi_2 \rightarrow R$	
S ₄	3 ¹ A''	7.15	7.32	6.00	0.00	(6.05)	5.95	0.0000 $n_2 \rightarrow \pi_4^*, n_1 \rightarrow \{\pi_3^*, \pi_4^*\}$	
S ₅	3 ¹ A'			5.81	0.08	(6.14)	6.15	0.0501 $\pi_1 \rightarrow \pi_3^*$	
S ₆	4 ¹ A'			6.46	0.29	(6.79)	6.53	0.1565 $\pi_2 \rightarrow \{\pi_4^*, R\}, n_2 \rightarrow R$	
S ₇	4 ¹ A''			6.37	0.00	(6.65)	6.57	0.0000 $n_1 \rightarrow \pi_3^*, n_2 \rightarrow \pi_4^*$	
S ₈	5 ¹ A'					(7.56)	6.65	0.0815 $n_2 \rightarrow R, \pi_2 \rightarrow \{R, \pi_4^*\}$	
S ₉	5 ¹ A''						6.71	0.0050 $\pi_2 \rightarrow R$	
S ₁₀	6 ¹ A''						6.76	0.0105 $\pi_2 \rightarrow R$	
S ₁₁	7 ¹ A''		6.95	0.00	(7.05)		6.85	0.0000 $n_2 \rightarrow \{\pi_4^*, R\}$	
S ₁₂	6 ¹ A'						7.07	0.0108 $\pi_2 \rightarrow R$	
S ₁₃	8 ¹ A''						7.09	0.0012 $\pi_1 \rightarrow R$	
S ₁₄	7 ¹ A'						7.17	0.0543 $n_2 \rightarrow R$	
S ₁₅	8 ¹ A'						7.29	0.0246 $n_1 \rightarrow R, n_2 \rightarrow R$	
S ₁₆	9 ¹ A'		7.01	0.76	(7.66)		7.39	0.5071 $\pi_1 \rightarrow \{\pi_4^*, R\}, n_2 \rightarrow R$	
								6.97 ^e	

^a weak perpendicular transition in orthorhombic crystals of 1-methyluracil [26]; ^b vapor spectrum [2], (shoulder);

^c in trimethyl phosphate [2]; ^d in water [1]; ^e in water [4]; ^f in 2-methyltetrahydrofuran and ethanol/methanol [3].

Table 2. Vertical triplet excitation energies ΔE [eV] and dipole transition oscillator strengths $f(r)$ of uracil in its diketo form.

State	HF/MRCI [8]		DFT/MRCI, present work			absorption maximum	
	DZVP+Ryd		TZVP	TZVPP+Ryd			
	ΔE	ΔE	ΔE	$f(r)$	dominant excitation(s)		
T ₁	1 ¹ A'	4.00	3.68	3.68	$\pi_2 \rightarrow \pi_3^*$		
T ₂	1 ¹ A''	5.30	4.40	4.39	$n_2 \rightarrow \pi_3^*$		
T ₃	2 ¹ A'	6.15	5.10	5.08	0.0061 $\pi_1 \rightarrow \pi_3^*, \pi_2 \rightarrow \pi_4^*$		
T ₄	2 ¹ A''	6.94		5.73	0.0005 $\pi_2 \rightarrow R$		
T ₅	3 ¹ A'	7.28	(5.85)	5.74	0.0139 $\pi_2 \rightarrow \pi_4^*, \pi_1 \rightarrow \{\pi_3^*, \pi_4^*\}$		
T ₆	3 ¹ A''		(5.87)	5.76	0.0000 $n_2 \rightarrow \pi_4^*, n_1 \rightarrow \{\pi_3^*, \pi_4^*\}$		
T ₇	4 ¹ A'		(6.39)	6.25	0.0155 $\pi_1 \rightarrow \{\pi_4^*, R, \pi_3^*\}, \pi_2 \rightarrow \pi_4^*$		
T ₈	4 ¹ A''		(6.59)	6.50	0.0000 $n_1 \rightarrow \{\pi_3^*, \pi_4^*\}$		
T ₉	5 ¹ A'			6.55	0.0000 $n_2 \rightarrow R$		
T ₁₀	5 ¹ A''			6.63	0.0003 $\pi_2 \rightarrow R$		
T ₁₁	6 ¹ A''			6.67	0.0000 $\pi_2 \rightarrow R$		
T ₁₂	7 ¹ A''		(6.91)	6.73	0.0000 $n_1 \rightarrow \{\pi_4^*, R, \pi_3^*\}, n_2 \rightarrow \pi_3^*$		
T ₁₃	6 ¹ A'			6.98	0.0021 $\pi_2 \rightarrow R$		
T ₁₄	8 ¹ A''			7.01	0.0000 $\pi_1 \rightarrow R$		
T ₁₅	7 ¹ A'			7.09	0.0000 $n_2 \rightarrow R$		
T ₁₆	8 ¹ A'			7.19	0.0000 $n_1 \rightarrow R, n_2 \rightarrow R$		
T ₁₇	9 ¹ A'		(7.41)	7.38	0.0911 $\pi_0 \rightarrow \pi_3^*$		

4. ANWENDUNGEN

the $S_0 \rightarrow S_2$ transition. Our best calculation (DFT/MRCI geometry, TZVPP+Ryd basis) poses the S_2 vertically at 5.44 eV. The band maximum experiences solvent shifts toward lower energies by up to 0.33 eV (compare Tab. 1). These trends are easily explained by the higher dipole moment of the S_2 state (5.59 D in the TZVPP+Ryd basis) compared to the ground state dipole moment (4.51 D) and the concomitant larger electrostatic interaction with the solvent. We attribute the shoulder at 205 nm (6.05 eV) [2] in the vapor spectrum to the weaker $S_0 \rightarrow S_5$ transition. In accord with the smaller dipole moment of the upper state (2.48 D), this band experiences a blue shift in polar solvents. For the next higher band system, measured at 187 nm (6.63 eV) [2] in the gas phase, a blue shift is reported in water. In this case, we find nearly equal dipole moments in the upper (S_6 4.06 D) and lower (S_0 4.51 D) states. However, the S_6 MRCI wavefunction has considerably large coefficients for $n_2 \rightarrow R$ excitations that are disadvantaged by hydrogen bonding (see below). The transition for which we find the largest dipole oscillator strength is $S_0 \rightarrow S_{16}$ at 7.39 eV. We believe that this excitation corresponds to the strong band at 177 nm (6.97 eV) reported by Callis for uracil in water [4]. A similar assignment was made by Lorentzon *et al.* [9]. As shown in Table 1, we find a valence-Rydberg mixed character for the S_{16} state. The most prominent valence configuration represents an excitation from the π_1 orbital to the virtual π_4^* orbital (see Figs. 3 and 4). Both orbitals are nearly symmetric with respect to an approximate vertical reflection plane and a two-fold rotation axis through N_3 and C_6 . As already discussed by Lorentzon *et al.* [9], the large transition moment stems from a charge transfer from N_3 to the carbonyl groups.

The order of states is different in the triplet manifold where the $\pi_2 \rightarrow \pi_3^*$ excited state corresponds to T_1 and the triplet-coupled $n_2 \rightarrow \pi_3^*$ excitation to T_2 (Tab. 2). The third triplet state T_3 is a mixture of HOMO \rightarrow LUMO+1 and HOMO-2 \rightarrow LUMO excited configurations. It is located energetically well below a closely spaced group of triplets containing among others the first Rydberg state (T_4) in the triplet spectrum.

Most of our findings are in good agreement with experimental gas phase spectra and the results of previous CASPT2 calculations [2,9]. The largest deviation is found for the $S_0 \rightarrow S_2$ transition. If the band maximum is identified with the vertical excitation energy, our calculated value is too high by 0.35 eV. Our computed $S_0 \rightarrow S_5$ and $S_0 \rightarrow S_6$ vertical excitation energies, on the other hand, agree very well with experimental observations. Both correspond primarily to $\pi \rightarrow \pi^*$ excitations, *i.e.*, $\pi_1 \rightarrow \pi_3^*$ and $\pi_2 \rightarrow \pi_4^*$, respectively. It remains unclear at this point, why the first $\pi_2 \rightarrow \pi_3^*$ excitation ($S_0 \rightarrow S_2$) behaves differently. The energetic location of the Rydberg states was not determined at the CASPT2 level nor did the authors investigate the triplet states of uracil. Differences between the computed CASPT2 and DFT/MRCI excitation energies are found to be somewhat smaller for $n \rightarrow \pi^*$ states than for $\pi \rightarrow \pi^*$ states. The general good agreement between the computed DFT/MRCI spec-

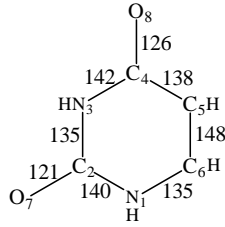


Fig. 5. Optimized geometry (DFT/MRCI, TZVP basis) of the second excited singlet state of uracil.

trum and experiment found in this work are in accord with the results of Grimme and Waletzke [10]. In a series of DFT/MRCI calculations on 37 vertical transitions in mostly organic molecules, these authors obtained a root mean square deviation from experimental data of 0.15 eV, the largest error being -0.35 eV for an $n \rightarrow \pi^*$ transition in thioformaldehyde. Unscaled excitation energies from Hartree-Fock based MRCI and random phase approximation (RPA) calculations by Petke *et al.* [8] are considerably too high.

4.1.3 Geometries of excited states and vibrational fine structure

The observation of at least three vibrational quanta (spaced by $\approx 790 \text{ cm}^{-1}$) superimposed on the broad, otherwise featureless first band suggests a considerable change of geometry in the upper state [3]. A harmonic vibrational analysis of the S_0 equilibrium structure (at the DFT level) exhibits two modes in the desired energy range. Mode 11 at 798 cm^{-1} is an out-of-plane vibration of C_2 (the center of the N,N-C-O trihedron). Mode 12 at 802 cm^{-1} corresponds to an in-plane breathing vibration of the six ring. The computed frequency of mode 11 is in excellent agreement with a measured IR band for a C-O out-of-plane vibration at 806 cm^{-1} [28]. The intensity of mode 12 (4 km/mol) is probably too low for an experimental observation in the infrared.

Optimization of the S_2 state geometry without symmetry constraints at the DFT/MRCI level did not show any tendency for an S_2 minimum structure with a pyramidal N,N-C-O group. The most obvious change with respect to the S_0 molecular geometry is the breaking of the double bond between C_5 and C_6 (compare Figs. 2 and 5) and the shortening of the single bond between C_4 and C_5 . These trends are consistent with the nuclear distortions in mode 12. Indeed, the central CH group (C_5 and the H linked to it) is the group with the largest displacement vector. From these results we conclude that the vibrational structure observed by Becker and Kogan in the first band system is due to a symmetric breathing mode of the six ring. This assignment is also consistent with a moderate change of the vibrational spacing for N,N-dimethyluracil (DMU) ($\approx 770 \text{ cm}^{-1}$) and a larger red shift for thymine, *i.e.*, 5-methyluracil with the methyl group replacing the hydrogen at C_5 . Due to geometry relaxation, the energy of the S_2 state drops by approximately 0.5 eV yielding an adiabatic excitation of 4.99 eV in the TZVP

4.2. URACIL

Table 3. Relative energies ΔE [eV] of uracil in the diketo tautomeric form at various molecular geometries (DFT/MRCI, TZVP basis). The nomenclature S₀, S₁, S₂, T₁, T₂, and T₄ follows the order of states at the ground state equilibrium geometry.

State	S ₀ geometry	S ₁ geometry $n \rightarrow \pi^*$	S ₂ geometry $\pi \rightarrow \pi^*$	T ₁ geometry $\pi \rightarrow \pi^*$	T ₂ geometry $n \rightarrow \pi^*$	T ₄ geometry ^a $\pi \rightarrow \sigma^*$
S ₀ , 1 ¹ A'	0.00	0.59	0.63	0.47	0.52	5.84
S ₁ , 1 ¹ A''	4.61	3.96	4.30	4.41	3.96	4.11
S ₂ , 2 ¹ A'	5.48	5.21	4.99	5.10	5.23	5.88
T ₁ , 1 ³ A'	3.68	3.51	3.29	3.20	3.52	6.09
T ₂ , 1 ³ A''	4.40	3.84	4.22	4.32	3.83	4.97
T ₃ , 2 ³ A'	5.10	4.72	4.99	5.04	4.73	6.52

^a optimized at the UDFT level.

Table 4. Dipole moments μ [D] of uracil in the diketo tautomeric form at the ground state geometry and at the equilibrium geometry of the respective state (DFT/MRCI, TZVP basis).

State	S ₀ geometry	equilibrium geometry
S ₀ , 1 ¹ A'	4.58	4.58
S ₁ , 1 ¹ A''	2.54	2.98
S ₂ , 2 ¹ A'	5.85	5.11
T ₁ , 1 ³ A'	3.89	3.75
T ₂ , 1 ³ A''	2.67	3.02

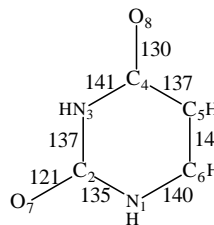


Fig. 6. Optimized geometry (DFT/MRCI, TZVP basis) of the first excited singlet state of uracil.

basis. Emission from the S₂ state is predicted to occur at 4.36 eV because the molecule retains the S₂ geometry for a short period of time also in the S₀ state (see Tab. 3).

Weak fluorescence was observed at 300 nm (4.13 eV) for uracil and DMU in a hydroxylic solvent (ethanol-methanol) and attributed to an $n \rightarrow \pi^*$ transition [3]. In 2-MTHF, only DMU shows fluorescence whereas uracil phosphorescences. The $n_2 \rightarrow \pi_3^*$ excitation leads to a considerable lengthening of the C₄-O₈ carbonyl bond and the formation of a double bond between C₄ and C₅ (Fig. 6). An adiabatic excitation energy of 3.95 eV (compared to 4.61 eV in absorption and 3.36 eV in emission) is obtained for S₁.

The S₁ state exhibits a much smaller dipole moment than the S₀ ground state (Tab. 3), and will experience a blue shift in polar media whereas S₂ is lowered. Moreover, hydrogen bonding is supposed to favor electronic states with doubly occupied n_1 and n_2 orbitals because these orbitals exhibit considerable lone-pair character at the carbonyl oxygens (Fig. 3). In a polar protic solvent, hydrogen bonding will therefore enforce the blue shift of

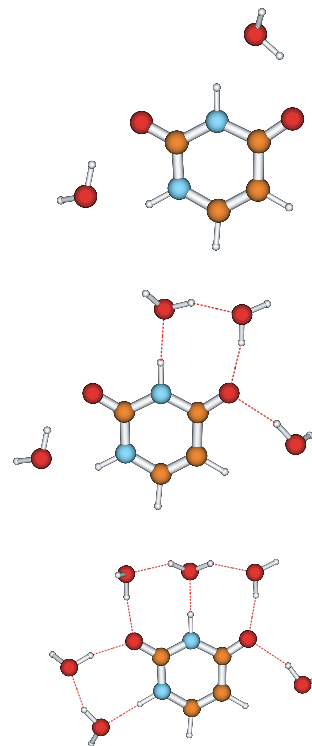


Fig. 7. Optimized geometries (DFT, TZVP basis) of uracil-water complexes.

the S₁ excitation energy, thus reducing the energy gap between S₁ and S₂ further. These assumptions are verified by the trends found for various uracil water complexes sketched in Figure 7. Interestingly, we find the largest effects for uracil-4H₂O, probably due to the asymmetric arrangement of the water molecules. (In the starting geometry, each water molecule was bonded to a single N or O atom. The asymmetric arrangement is caused by collaborative reinforcement of the hydrogen bonds.) As shown

4. ANWENDUNGEN

Table 5. Excitation energies ΔE [eV] of low-lying electronic states in isolated uracil molecules compared with uracil-water complexes. All geometries were optimized at the DFT level.

State	DFT/MRCI, TZVP basis			
	uracil	uracil-2H ₂ O	uracil-4H ₂ O	uracil-6H ₂ O
S ₁ ¹ (n ₂ → π ₃ [*])	4.68	4.91	5.13	5.07
S ₂ ¹ (π ₂ → π ₃ [*])	5.55	5.44	5.33	5.43
T ₁ ³ (π ₂ → π ₃ [*])	3.77	3.78	3.77	3.83
T ₂ ³ (n ₂ → π ₃ [*])	4.45	4.70	4.94	4.87
T ₃ ³ (π ₁ → π ₃ , π ₂ → π ₄ [*])	5.16	5.14	5.13	5.12

in Table 5, the $n \rightarrow \pi^*$ excited states (S₁ and T₂) are significantly raised in energy in hydrogen bonded complexes with respect to the ground state and $\pi \rightarrow \pi^*$ excitations. Oscillator strengths for a dipole transition to the electronic ground state remain nearly constant upon complexation with water molecules. In conclusion, energy considerations argue for S₁ as the origin of the 300 nm fluorescence. The computed oscillator strength of the vertical transition amounts to merely 4×10^{-5} at this point on the potential hypersurface, however [3].

Surprising results are obtained if one optimizes the geometry of another A'' open shell configuration (T₄ and S₃ in the vertical spectrum) where a hole has been created in π_2 and a particle in the lowest unoccupied a' symmetric orbital. As mentioned before, this orbital has predominantly Rydberg character at the S₀ equilibrium geometry. When the geometry of the triplet state is relaxed, the a' orbital gains more and more valence character and eventually turns into a σ_{NH}^* antibonding orbital. As a consequence, uracil loses the hydrogen atom linked to N₁. (In nucleic acids, this particular photochemical bond cleavage will not occur as uracil is linked to the RNA backbone at the N₁ position.) At large N₁-H distances, the lowest electronic state is a singlet of ${}^1A''$ symmetry. In addition to the dominant $\pi_2 \rightarrow \sigma_{\text{NH}}^*$ configuration, the wavefunction has large coefficients for double excitations, the most important being $\sigma_{\text{NH}}\pi_2 \rightarrow \sigma_{\text{NH}}^*$. At the T₄ optimized geometry (with an N-H distance of roughly 400 pm), ${}^1A''$ is located ≈4.1 eV above the diketo minimum on the S₀ potential energy hypersurface and only marginally above the ${}^1A''$ ($n_2 \rightarrow \pi_3^*$) S₁ minimum. The corresponding triplet state is higher in energy (at ≈5.0 eV). Both A'' states are located significantly below the first ${}^1A'$ state (≈5.8 eV) that correlates with the the diketo (A) ground state configuration. These results are noteworthy, because they suggest the existence of a flat potential well on the singlet hypersurface close to the dissociation continuum. Further, they imply that various intersections of potential energy hypersurfaces occur in the energy regime of the $\pi_2 \rightarrow \pi_3^*$ absorption. At present, we do not have a computer code for a systematic search of potential hypersurface crossings. Without having properly located the seam or point of intersection between ${}^1(\pi_2 \rightarrow \sigma^*)$ and the other singlet states, all discussion about predissociation or a fast relaxation to the electronic ground state being the cause for the diffuseness of the absorption spectrum must remain speculative, of course. Nevertheless, our results strongly

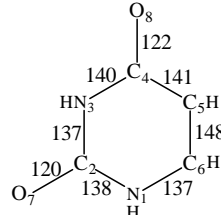


Fig. 8. Optimized geometry (DFT/MRCI, TZVP basis) of the first excited triplet state of uracil.

point towards a participation of the ${}^1(\pi_2 \rightarrow \sigma_{\text{NH}}^*)$ excited state in the depletion of the ${}^1(\pi_2 \rightarrow \pi_3^*)$ population¹.

4.1.4 Spin-orbit coupling and phosphorescence

A broad phosphorescence band with maximum at 450 nm (2.76 eV) was observed by Becker and Kogan [3] at 77 K for uracil in 2-MTHF, a polar aprotic solvent. It is quenched upon N,N-dimethyl substitution or in a hydroxylic solvent. In the latter cases, fluorescence is found instead. The triplet state lifetime was not determined for the uracil molecule. A rough estimate can be obtained from measurements of the corresponding transition in thymine, however. For thymine, Becker and Kogan observe a total triplet lifetime of $\tau_P^{\text{obs}} = 75$ ms at 77 K in 2-MTHF from which they derive a phosphorescence lifetime of $\tau_P^0 \approx 0.7$ s [3]. This weak phosphorescence was assigned as ${}^3(\pi \leftarrow \pi^*)$ transition by these scientists.

From an energetic point of view, this assignment is in good agreement with our calculations: at the T₁ equilibrium geometry (sketched in Fig. 8), the computed vertical deexcitation energy of the isolated molecule amounts to ≈2.73 eV (see Tab. 3). Adiabatically, T₁ is located about 3.20 eV above S₀. For phosphorescence in an organic molecule to be large, two scenarios can be thought of [30,31]:

1. the triplet state interacts strongly via spin-orbit coupling with an excited singlet state that in turn has a large dipole transition moment to the singlet ground state;
2. the triplet state has a large spin-orbit matrix element with the singlet ground state and the (static) dipole moments differ considerably between the two.

¹ After submission of this work we became aware of an article discussing the role of singlet $\pi\sigma^*$ states in photochemical hydrogen detachment and hydrogen transfer reactions [29].

4.2. URACIL

Table 6. Spin-orbit matrix elements (absolute values) [cm^{-1}] of the lowest singlet and triplet states in the diketo (A) form of uracil, calculated at the T_1 geometry. The component of the spin-orbit Hamiltonian is indicated in parentheses.

$\langle T_1(A') \mathcal{H}_{\text{SO}} S_0(A') \rangle$	0.008(z)
$\langle T_1(A') \mathcal{H}_{\text{SO}} S_1(A'') \rangle$	0.510(x)/33.523(y)
$\langle T_1(A') \mathcal{H}_{\text{SO}} S_2(A') \rangle$	0.024(z)
$\langle T_2(A'') \mathcal{H}_{\text{SO}} S_0(A') \rangle$	9.157(x)/42.805(y)
$\langle T_2(A'') \mathcal{H}_{\text{SO}} S_1(A'') \rangle$	0.215(z)
$\langle T_2(A'') \mathcal{H}_{\text{SO}} S_2(A') \rangle$	2.936(x)/23.370(y)
$\langle T_2(A'') \mathcal{H}_{\text{SO}} T_1(A') \rangle$	0.402(x)/30.874(y)
$\langle T_3(A') \mathcal{H}_{\text{SO}} S_0(A') \rangle$	0.001(z)
$\langle T_3(A') \mathcal{H}_{\text{SO}} S_1(A'') \rangle$	2.870(x)/31.610(y)
$\langle T_3(A') \mathcal{H}_{\text{SO}} S_2(A') \rangle$	0.019(z)
$\langle T_3(A') \mathcal{H}_{\text{SO}} T_1(A') \rangle$	0.020(z)
$\langle T_3(A') \mathcal{H}_{\text{SO}} T_2(A'') \rangle$	2.616(x)/32.428(y)

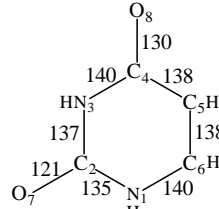


Fig. 9. Optimized geometry (DFT/MRCI, TZVP basis) of the second excited triplet state of uracil.



Fig. 10. Relative DFT/MRCI energies (TZVP basis) of low-lying electronic states for various tautomers of uracil: diketo (A), ketoenol (B)-(E), dienol (F) (*cf.* Fig. 1). Solid lines denote states of A' symmetry, dashed lines A'' states. For each tautomer, singlets are shown to the left, triplets to the right.

Neither condition is fulfilled by the T_1 state of uracil. In Table 6, spin-orbit matrix elements between the low-lying electronic states of uracil are listed. Spin-orbit interaction is very weak between T_1 and A' symmetric singlets, *i.e.*, $\pi \rightarrow \pi^*$ excitations that have high probabilities for a dipole transition to the ground state. This applies equally to matrix elements with energetically higher A' states, not shown in the table. The direct spin-orbit interaction between T_1 and S_0 is negligibly small, too. On the other hand, significant spin-orbit interaction with the A'' states ($n \rightarrow \pi^*$) is found, the latter having only marginal radiative transition probabilities to S_0 . Employing spin-orbit matrix elements, dipole transition moments, and excitation energies as computed at the T_1 geometry, we calculate the high-temperature limit for the T_1 phosphorescence lifetime to be $\tau_P^0 \approx 7.5$ s. These results are in agreement with qualitative considerations about phosphorescence rates of ${}^3(\pi \rightarrow \pi^*)$ states in organic molecules [32]. Further, rates for inter-system crossing (ISC) between S_2 and T_1 are predicted to be very small. T_1 will therefore not be populated directly *via* the strong $S_0 \rightarrow S_2$ absorption. Indirectly, T_1 may be reached from the S_2 state either by internal conversion (IC) from S_2 to S_1 and subsequent ISC to T_1 or by ISC between S_2 and T_2 and IC within the triplet moiety.

The T_2 state, by contrast, exhibits an important direct spin-orbit coupling matrix element with the S_0 electronic ground state (Tab. 6) and their dipole moments differ considerably (Tab. 3). Moreover, its spin-orbit interaction with the close-lying S_2 state lends intensity to the phosphorescence and enables the effective population of T_2 *via* ISC after absorption. Accordingly, our calculations predict a much smaller radiative lifetime for T_2 ($\tau_P^0 \approx 1$ ms). On the other hand, the large spin-orbit coupling between T_2 and the lower-lying T_1 and S_0 states will lead to a rapid non-radiative decay of the T_2 state, if vibrational overlap is sufficient. At the T_2 optimized geom-

try (Fig. 9), the energy gap between T_2 and S_0 amounts to approximately 3.3 eV which is still quite a lot, whereas the energy difference between T_2 and T_1 is only 0.3 eV. All of these facts support the assumption that the radiative and non-radiative depletion of the T_2 is fast.

4.2 Other tautomeric forms of uracil

4.2.1 Relative stabilities of ground and excited states

Relative energies of the electronic ground states and low-lying excited states of the six tautomeric forms (A-F) of uracil are sketched in Figure 10. In accord with experiment, the diketo form (A) is found to represent the global minimum on the ground state potential energy surface. Next in energetic order come the ketoenol forms (B) and (E) and the dienol tautomer (F). They are predicted to have very similar ground state energies in the gas phase, approximately 0.5 eV above the diketo minimum. Estimating solvent effects on the basis of dipole moment differences (Tab. 7), it can be assumed that tautomer (B) is stabilized relative to the diketo form by a polar solvent whereas (E) and (F) will be destabilized. The ketoenol forms (C) and (D) are those with the largest dipole moments and least favorable energies in vacuo. Similar trends have been obtained earlier by AM1 calculations [33,34].

The first excited triplet state ($\pi \rightarrow \pi^*$ in all tautomers) follows roughly the energetic trend of the electronic ground state, with the exception of the dienol form (F) where T_1 is considerably blue shifted. No such

4. ANWENDUNGEN

Table 7. Relative DFT/MRCI energies, dipole moments (TZVP basis) and oscillator strengths of uracil in various tautomeric forms: diketo (A), keto-enol (B)–(E), dienol (F). Ground state geometries were optimized at the DFT level. For structure codes, see Figure 1.

tautomer	$1^1A'(S_0)$			$1^1A''(n \rightarrow \pi^*)$			$2^1A'(\pi \rightarrow \pi^*)$		
	ΔE [eV]	μ [D]	ΔE [eV]	μ [D]	$f(r)$	ΔE [eV]	μ [D]	$f(r)$	
diketo	(A)	0.00	4.53	4.68	2.53	0.2×10^{-3}	5.55	5.88	0.277
keto-enol	(B)	0.54	4.98	5.62	1.10	1.2×10^{-3}	5.34	3.68	0.110
keto-enol	(C)	0.95	7.33	5.49	4.25	3.6×10^{-3}	5.55	2.55	0.179
keto-enol	(D)	0.83	6.47	5.17	2.11	0.7×10^{-4}	6.43	5.14	0.095
keto-enol	(E)	0.47	3.23	5.36	2.26	0.3×10^{-3}	5.55	3.04	0.223
dienol	(F)	0.52	1.35	5.82	1.96	9.9×10^{-3}	5.85	0.82	0.113

trends can be made out for the other low-lying excited electronic states. Even their relative order varies from tautomer to tautomer. Oscillator strengths are found to be very small for all $n_2 \rightarrow \pi_3^*$ excitations. The observation of strong fluorescence from an $n \rightarrow \pi^*$ excited state in a keto-enol tautomeric form of uracil, as reported by Ito and coworkers [5,6], appears thus extremely improbable. In contrast, the $\pi \rightarrow \pi^*$ excited $2^1A'$ state is connected to S_0 by a reasonable dipole transition probability in all tautomers.

4.2.2 The keto-enol tautomer (B)

Among all non-diketo tautomers, keto-enol (B) is the most interesting one: besides (A) and the higher lying form (D), it is the only tautomer that can occur in nucleic acids. Furthermore, the order of the $n \rightarrow \pi^*$ and $\pi \rightarrow \pi^*$ excited singlet states is reversed compared to their order in the diketo form, *i.e.*, $2^1A'$ represents the S_1 state in tautomer (B). This fact shows that the $2^1A'(\pi \rightarrow \pi^*)$ and $1^1A''(n \rightarrow \pi^*)$ potential energy surfaces must intersect somewhere. A geometry optimization of the T_1 state in the keto-enol form (B) leads to the lowest point on the $2^1A'$ hypersurface detected so far, merely 4.99 eV above the diketo ground state or 4.45 eV above the local minimum of form (B). The calculated oscillator strength for a dipole transition from $S_0 \rightarrow S_1$ should be sufficient for an experimental observation in absorption.

Whether it will be possible to observe fluorescence from this state will critically depend on the solvent. We predict the S_1 and T_2 states of tautomer (B) to be nearly degenerate in the gas phase. The electronic spin-orbit coupling matrix element between these states is not very large (see Tab. 8), but appears to be sufficient for a rapid inter-system crossing between states with nearly zero energy gap. In a polar solvent, S_1 should drop significantly below T_2 because of its higher dipole moment (3.68 D (S_1) *vs.* 0.27 D (T_2)) precluding a non-radiative spin-forbidden transition from S_1 to T_2 . Complexation with water molecules in the gas phase ought to have a similar effect on the energy gap between S_1 to T_2 . Spin-orbit coupling to the lower-lying T_1 state is not efficient either because of a nearly vanishing electronic interaction matrix element and small vibrational overlap. In a po-

Table 8. Spin-orbit matrix elements (absolute values) [cm^{-1}] of the lowest singlet and triplet states in the keto-enol (B) forms of uracil at the ground state equilibrium geometry. The component of the spin-orbit Hamiltonian is indicated in parentheses. Note that the order of singlet states is reversed with respect to tautomer (A).

$\langle T_1(A') \mathcal{H}_{\text{SO}} S_0(A') \rangle$	0.04(z)
$\langle T_1(A') \mathcal{H}_{\text{SO}} S_2(A'') \rangle$	8.15(x)/16.08(y)
$\langle T_1(A') \mathcal{H}_{\text{SO}} S_1(A') \rangle$	0.00(z)
$\langle T_2(A'') \mathcal{H}_{\text{SO}} S_0(A') \rangle$	4.69(x)/1.60(y)
$\langle T_2(A'') \mathcal{H}_{\text{SO}} S_2(A'') \rangle$	2.82(z)
$\langle T_2(A'') \mathcal{H}_{\text{SO}} S_1(A') \rangle$	5.04(x)/1.00(y)
$\langle T_2(A'') \mathcal{H}_{\text{SO}} T_1(A') \rangle$	2.08(x)/0.27(y)
$\langle T_3(A') \mathcal{H}_{\text{SO}} S_0(A') \rangle$	0.00(z)
$\langle T_3(A') \mathcal{H}_{\text{SO}} S_2(A'') \rangle$	8.39(x)/1.44(y)
$\langle T_3(A') \mathcal{H}_{\text{SO}} S_1(A') \rangle$	0.01(z)
$\langle T_3(A') \mathcal{H}_{\text{SO}} T_1(A') \rangle$	0.01(z)
$\langle T_3(A') \mathcal{H}_{\text{SO}} T_2(A'') \rangle$	4.50(x)/2.57(y)

lar surrounding or in hydrogen-bonded complexes, the $S_1(\pi \rightarrow \pi^*)$ state might therefore show fluorescence in the keto-enol tautomeric form (B), if the latter can be synthesized.

5 Conclusions

In this work, we have investigated the singlet and triplet spectra of several uracil tautomers by quantum chemical methods. The most stable nuclear arrangement corresponds to the diketo form of uracil, the electronic ground state of other tautomers being approximately 0.5–1 eV higher in energy. Our calculations yield large oscillator strengths for $\pi \rightarrow \pi^*$ excitations, in agreement with earlier theoretical and experimental studies. Rydberg and $n \rightarrow \pi^*$ states exhibit very small probabilities for a dipole transition from or to the electronic ground state. The lowest lying excited state corresponds to a $3(\pi \rightarrow \pi^*)$ excitation, followed by a triplet coupled $n \rightarrow \pi^*$ state. The order of states is reversed in the singlet spectrum of the diketo form. The results of the present theoretical investigation show that the first dark $1(n \rightarrow \pi^*)$ S_1 and the $1(\pi \rightarrow \pi^*)$

4.2. URACIL

S_2 state, into which absorption is observed, are close in energy at the S_2 equilibrium geometry. The energy gap between these states is even diminished in a polar surrounding and due to hydrogen bonding. The proximity of dark and absorbing states may be one reason for the difuseness of the uracil absorption bands. Our calculations indicate that also a dissociative A'' state in which a σ_{NH}^* antibonding orbital is occupied might play a decisive role.

The vibrational structure in the first broad band with a spacing of $\approx 790 \text{ cm}^{-1}$ has been identified to stem from a breathing vibration of the uracil six ring. A carbonyl out-of-plane vibrational mode exhibits nearly the same frequency. The question whether the latter mode leads to vibronic interaction between the S_1 and S_2 state can presently not be answered with high confidence and must remain speculation for the time being.

Spin-orbit mean-field calculations yield large coupling matrix elements between A' and A'' electronic states. By contrast, the interaction between singlets and triplets of the same spatial symmetry is negligible. Calculated phosphorescence lifetimes support the assumption that the phosphorescence, measured in 2-methyl-tetrahydrofuran after $S_0 \rightarrow S_2 \overset{1}{\pi} (\pi \rightarrow \pi^*)$ absorption, stems from the ${}^3(\pi \rightarrow \pi^*) T_1$ state.

Funding by the Deutsche Forschungsgemeinschaft (DFG) through project Ma 1051/5-1 is gratefully acknowledged. It is a pleasure to thank Stefan Grimme (Münster) and Mirko Waletzke for making their DFT/MRCI code available to us. Thanks are also due to Rainer Weinkauf (Düsseldorf) for valuable discussions and to Marcus Gastreich (FhG-SCAI, St. Augustin) for technical assistance with the molecular orbital plots.

References

- D.R. Voet, W.B. Gratzer, R.A. Cox, P. Doty, *Biopolymers* **1**, 193 (1963)
- L.B. Clark, G.G. Peschel, I. Tinoco Jr, *J. Phys. Chem.* **69**, 3615 (1965)
- R. Becker, G. Kogan, *Photochem. Photobiol.* **31**, 5 (1980)
- P.R. Callis, *Annu. Rev. Phys. Chem.* **34**, 329 (1983)
- M. Fujii, T. Tamura, N. Mikami, M. Ito, *Phys. Chem. Lett.* **126**, 583 (1986)
- Y. Tsuchiya, T. Tamura, M. Fujii, M. Ito, *J. Phys. Chem.* **92**, 1760 (1988)
- B.B. Brady, L.A. Peteanu, D.H. Levy, *Chem. Phys. Lett.* **147**, 538 (1988)
- J.D. Petke, G.M. Maggiora, R.E. Christoffersen, *J. Phys. Chem.* **96**, 6992 (1992)
- J. Lorentzon, M.P. Fülscher, B.O. Roos, *J. Am. Chem. Soc.* **117**, 9265 (1995)
- S. Grimme, M. Waletzke, *J. Chem. Phys.* **111**, 5645 (1999)
- A.D. Becke, *J. Chem. Phys.* **98**, 1372 (1993)
- C. Lee, W. Yang, R.G. Parr, *Phys. Rev. B* **37**, 785 (1988)
- R. Ahlrichs, M. Bär, M. Häser, H. Horn, C. Kölmel, *Chem. Phys. Lett.* **162**, 165 (1989)
- O. Treutler, R. Ahlrichs, *J. Chem. Phys.* **102**, 346 (1995)
- O. Vahtras, J. Almlöf, M.W. Feyereisen, *Chem. Phys. Lett.* **213**, 514 (1993)
- F. Weigend, M. Häser, H. Patzelt, R. Ahlrichs, *Chem. Phys. Lett.* **294**, 143 (1998)
- K. Eichhorn, O. Treutler, H. Öhm, M. Häser, R. Ahlrichs, *Chem. Phys. Lett.* **240**, 283 (1995)
- F Schneider, *Entwicklung eines Treibers zur numerischen Bestimmung von Minima auf CI-Potenzialflächen und Anwendung auf angeregte Elektronenzustände des Uracil-Moleküls*, diploma thesis, University of Bonn available through: <http://www.theochem.uni-duesseldorf.de> (2002)
- M. Kleinschmidt, J. Tatchen, C.M. Marian, *J. Comp. Chem.* **23**, 824 (2002)
- B.A. Heß, C.M. Marian, U. Wahlgren, O. Gropen, *Chem. Phys. Lett.* **251**, 365 (1996)
- J. Tatchen, C.M. Marian, *Chem. Phys. Lett.* **313**, 351 (1999)
- D. Danovich, C.M. Marian, T. Neuheuser, S.D. Peyerimhoff, S. Shaik, *J. Phys. Chem. A* **102**, 5923 (1998)
- Amfi is an atomic spin-orbit integral program written by B. Schimmelpfennig, University of Stockholm, 1996
- A. Schäfer, C. Huber, R. Ahlrichs, *J. Chem. Phys.* **100**, 5829 (1994)
- R.F. Steward, L.H. Jensen, *Acta Chrystallogr.* **23**, 1102 (1967)
- W.A. Eaton, T.P. Lewis, *J. Chem. Phys.* **53**, 2164 (1970)
- A. Broo, A. Holmén, *J. Phys. Chem.* **101**, 3589 (1997)
- M. Szczesniak, M.J. Novak, H. Rostkowska, K. Szczesniak, *J. Am. Chem. Soc.* **105**, 5969 (1983)
- A.L. Sobolewski, W. Domcke, C. Dedonder-Lardeux, C. Jouvet, *Phys. Chem. Chem. Phys.* **4**, 1093 (2002)
- C.M. Marian, Spin-orbit coupling in molecules, in *Reviews In Computational Chemistry*, edited by K. Lipkowitz, D. Boyd (Wiley-VCH, Weinheim, 2001), Vol. 17, pp. 99–204
- J. Tatchen, M. Waletzke, C.M. Marian, S. Grimme, *Chem. Phys.* **264**, 245 (2001)
- N.J. Turro, *Modern Molecular Photochemistry* (University Science Books, Sausalito, CA, 1991)
- U. Norinder, *J. Mol. Struct. (Theochem)* **151**, 259 (1987)
- A.R. Katritzky, M. Karelson, *J. Am. Chem. Soc.* **113**, 1561 (1991)

4.3 Dithiosuccinimid

In der Arbeit „Quantum Chemical Investigation of Spin-Forbidden Transitions in Dithiosuccinimide“ („Quantenchemische Untersuchung spinverbotener Übergänge in Dithiosuccinimid“) wurden das elektronische Anregungsspektrum des Dithiosuccinimids sowie die auftretenden Spin-Bahn-Kopplungseffekte untersucht. Die Ergebnisse stehen in sehr guter Übereinstimmung mit Experimenten von Meskers *et. al.*[51], und bieten darüber hinaus Erklärungen für bisher rätselhafte Details der beobachteten Spektren.

Aufgrund der zwei Thiocaobonylgruppen zeigt Dithiosuccinimid ein dichtes Spektrum tiefliegender Valenzzustände. Die ersten beiden angeregten Singulettzustände S_1 (1B_1) und S_2 (1A_2) haben $n \rightarrow \pi^*$ -Charakter und sind lediglich 0.2 eV getrennt. Hier bestätigen sich die Ergebnisse von Meskers *et. al.*, die die Symmetrieeigenschaften dieser Zustände aus polarisierten Phosphoreszenzanregungsspektren bestimmt haben. Die Übergangswahrscheinlichkeiten in den elektronischen Grundzustand sind gering, wie es für $n \rightarrow \pi^*$ angeregte Zustände zu erwarten ist. Die beiden starken Absorptionsbanden bei 3.96 und 4.96 eV [51] sind dominiert von Einfachanregungen aus hochliegenden besetzten π -Orbitalen ins tiefstliegende π^* Orbital. Die zugeordneten Zustände sind 1B_2 (S_3) und 1A_1 . Eine Vielzahl weiterer, dunkler Singulets liegt unterhalb dieser beiden stark absorbierenden Zustände. Bemerkenswert ist, dass einer dieser Zwischenzustände einer Doppelanregung aus den beiden höchsten besetzten nichtbindenden Orbitalen in zwei π^* -Orbitale entspricht. Drei Triplettzustände finden sich in unmittelbarer Nachbarschaft zu S_1 und S_2 : zwei $n \rightarrow \pi^*$ Zustände (T_1 und T_2), sowie die $\pi \rightarrow \pi^*$ Triplettanregung (T_3).

Der elektronische Grundzustand und die tiefliegenden $\pi \rightarrow \pi^*$ angeregten Zustände sind C_{2v} -symmetrisch. In den letzteren ist die C–S-Bindung gegenüber dem Grundzustand deutlich aufgeweitet. Diese Geometrierelaxation beträgt etwa 0.3 eV. Im Gegensatz zu den $\pi \rightarrow \pi^*$ Anregungen zeigen die ersten beiden $n \rightarrow \pi^*$ Zustände C_2 -Symmetrie mit einem symmetrisch verdrillten Ring, wobei interessanterweise der SC(NH)CS-Chromophor seine Planarität nachzu beibehält. Die adiabatischen Anregungsenergien der $\pi \rightarrow \pi^*$ Zustände weichen um lediglich 0.1 eV von der vertikalen ab. Dies zeigt, dass die Energiehyperflächen flach und die geometrischen Verzerrungen klein sind.

Große Spin–Bahn–Matrixelemente treten zwischen $n \rightarrow \pi^*$ auf der einen Seite und dem elektronischen Grundzustand oder $\pi \rightarrow \pi^*$ Zuständen auf der anderen Seite auf. Der Absolutwert des Matrixelements zwischen T_1 und T_2 hängt stark vom Scherenwinkel $2\alpha = 180^\circ - 2\phi$ zwischen den beiden C=S-Gruppen ab, ihr Verhältnis ist proportional zu $\tan(\phi)$. Betrachtet man die nichtbindenden Orbitale n_1 und n_2 als Linearkombinationen reiner Schwefel- p_y und p_z -Orbitale, so lässt sich dieser Befund leicht erklären (Definition der Winkel und Achsen finden sich in der Veröffentlichung).

Die Phosphoreszenz aus T_1 erhält ihre Intensität hauptsächlich aus zwei Quellen. Die z -Komponente zeigt starke Wechselwirkung mit dem S_3 Zustand, der seinerseits einen starken dipolerlaubten Übergang in den elektronischen Grundzustand hat. Die y -Komponente koppelt direkt über $\hat{\mathcal{H}}_{SO}$ mit S_0 . Neben der Spin-Bahn-Kopplung bestimmt der Unterschied in den Dipolmomenten von T_1 und S_0 die Kopplungsstärke. Die Emission aus der x -Komponente ist unerheblich. Eine störungstheoretische Rechnung mit einer Zustandssumme über 64 Singulett- und Triplettzustände ergibt eine Hochtemperatur-Phosphoreszenzlebensdauer von 0.5 ms für T_1 in qualitativer Übereinstimmung mit der experimentellen Gesamtlebensdauer (strahlend und strahlungslos) von 0.1 ms und der Lumineszenz-Quantenausbeute von 0.5 ± 0.2 , aus der eine experimentelle strahlende Lebensdauer von

4.3. DITHIOSUCCINIMID

0.2 ms geschlossen wird. Die großen Spin-Bahn-Matrixelemente mit S_3 führen zu erheblichen Dipolübergangsmatrixelementen zwischen S_0 und T_2 . Während strahlungslose Prozesse die Emission effizient löschen, wird ein spinverbotener Übergang von S_0 nach T_2 mit einer Wahrscheinlichkeit vergleichbar derer der spinerlaubten $S_0 \rightarrow S_1$ Absorption vorhergesagt. Die y -polarisierte Bande Nummer 3 im Phosphoreszenzanregungsspektrum[51] wird diesem spinverbotenen Übergang zugeordnet. Auf diese Weise löst sich das Rätsel um den Intensitätsunterschied zum Absorptionsspektrum.

Bei den späteren Spin-Bahn-CI-Rechnungen zeigte sich, dass die störungstheoretischen Rechnungen in dieser Publikation noch nicht vollständig konvergiert waren.[52] Die Unterschiede sind aber insbesondere in den kurzlebigen Zuständen so gering, dass sich keine Änderung der wesentlichen Aussagen ergibt.

4. ANWENDUNGEN

Z. Phys. Chem. **217** (2003) 205–230
© by Oldenbourg Wissenschaftsverlag, München

Quantum Chemical Investigation of Spin-Forbidden Transitions in Dithiosuccinimide

By Jörg Tatchen¹, Martin Kleinschmidt¹, Christel M. Marian^{1,*},
Maja Parac², and Stefan Grimme²

¹ Institute of Theoretical Chemistry, Heinrich-Heine-Universität, Universitätsstr. 1,
D-40225 Düsseldorf, Germany

² Institute of Organic Chemistry, Westfälische Wilhelms-Universität, Correnstr. 40,
D-48149 Münster, Germany

*Dedicated to Prof. Dr. Sigrid Doris Peyerimhoff on the occasion
of her 65th birthday*

(Received August 12, 2002; accepted August 22, 2002)

***Spin-Orbit Coupling / Multi-Reference Configuration Interaction /
Ab Initio Methods / Electronic Spectrum / Phosphorescence /
Inter-System Crossing / Thiocarbonyls***

The vertical and adiabatic electronic spectra of dithiosuccinimide have been investigated by means of multi-reference Møller-Plesset perturbation theory and combined density functional/multi-reference configuration interaction methods. Geometries of the electronic ground state and several low-lying excited states have been optimised at the level of time-dependent density functional theory. We have determined spin-orbit coupling for correlated wavefunctions utilising a non-empirical spin-orbit mean-field approach.

Because of the two thiocarbonyl groups present in the molecule, dithiosuccinimide exhibits a dense spectrum of low-lying valence states. The first two excited singlet states (S_1 and S_2) originate from $n \rightarrow \pi^*$ excitations. Nearby, three triplet states are located, two $n \rightarrow \pi^*$ states (T_1 and T_2), and a $\pi \rightarrow \pi^*$ triplet excitation (T_3). The experimentally observed strong absorption band with maximum at 3.96 eV arises from the $\pi \rightarrow \pi^*$ excited 1B_2 (S_3) state.

Computed radiative lifetimes are presented for the experimentally known phosphorescence from the $n \rightarrow \pi^*$ excited T_1 state. Further, we find nearly equal probabilities for the spin-forbidden $S_0 \rightarrow T_2$ and the spin-allowed $S_0 \rightarrow S_1$ transitions in absorption. On these grounds, we assign band number 3 in the spectra measured by Meskers *et al.* [J. Phys. Chem. **99** (1995) 1134] to this spin-forbidden transition.

* Corresponding author. E-mail: Christel.Marian@uni-duesseldorf.de

1. Introduction

Thiocarbonyl compounds have been subject of spectroscopic research for a long time [1]. Their $n \rightarrow \pi^*$ and $\pi \rightarrow \pi^*$ excited states are found at considerably lower energies than in the parent carbonyl compounds. Therefore, these states often tend to relax by photophysical rather than photochemical processes even in solution. In addition, spin-orbit coupling is much more pronounced in sulphur containing systems. Spin-forbidden transitions in thiocarbonyl compounds are thus more easily accessible to experimental investigation.

Only recently, Moule and Lim provided a rationale behind the remarkable diversity in gas-phase luminescence properties of small, highly symmetric (C_{2v}) thiocarbonyl systems such as thioformaldehyde, thiophosgene, thiocyclobutanone, and thiocyclopentanone [2]. They correlate the presence or absence of detectable luminescence to the extent of non-planarity in the excited state. This governs the Franck–Condon factors and hence the rate of the competing radiationless transition if the responsible electronic coupling is not absent for other (symmetry) reasons.

The medium-sized dithiosuccinimide molecule is highly (C_{2v}) symmetric (*cf.* Fig. 1), too. However, the two coupled C=S groups in the chromophore entail a larger number of excited states in the low energy regime, compared to simple thiocarbonyls. Intense phosphorescence of high quantum yield has been found experimentally in a glassy matrix at 77 K by Meskers *et al.* [3]. From magnetic circular dichroism and polarised phosphorescence excitation spectra, the same authors were able to assign the lowest singlet and triplet $n \rightarrow \pi^*$ states and determine the polarization and intensity source of the phosphorescence. An X-ray crystal structure aided by semi-empirical molecular geometry optimization was reported by Ratajczak-Sitarz *et al.* [4]. Earlier work comprises absorption spectra that were interpreted by semiempirical CNDO/S calculations [5, 6]. To our knowledge, no *ab initio* electronic structure calculation has been performed for this system until now.

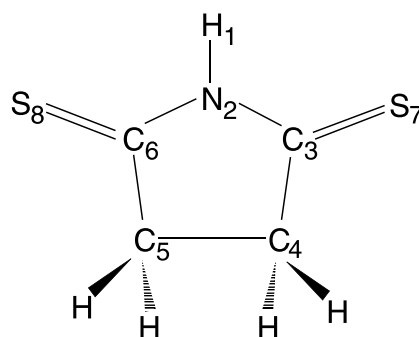


Fig. 1. The dithiosuccinimide molecule.

In this paper, we present a quantum chemical investigation of the photo-physics of the dithiosuccinimide molecule which focusses on spin-forbidden transitions. Computed vertical electronic excitation spectra are reported, including triplet states of low energy that have not been characterised in experiment. In addition, geometries of the lowest excited states have been optimised to examine the adiabatic order of states. From the calculated spin-orbit coupling matrix elements, we are able to give a detailed picture of triplet state population and depopulation mechanisms such as singlet-triplet absorption and inter-system crossing. A theoretical value for the radiative lifetime of the lowest triplet state is given.

2. Methods

Rates of photophysical processes in molecular systems depend, of course, on the magnitude of the underlying coupling (spin-orbit coupling in our case), but also on the energetic location and/or details of the potential energy surfaces of the involved (excited) electronic states. From the quantum chemist's point of view, description of both these factors represents a difficult task: For excited electronic states, static and dynamic electron correlation have to be taken into account in the wave function determination. Evaluation of spin-orbit coupling matrix elements in a non parametrised manner is bottlenecked by the complexity of the two-electron term of the spin-orbit Hamiltonian. Therefore, if the system under consideration is not a small molecule, standard *ab initio* packages can hardly be used and one has to think how the computational efforts may be reduced.

A very efficient and accurate way to compute spin-free electronic spectra of organic molecules is the combined density functional theory/multi-reference configuration interaction (DFT/MRCI) approach [7]. The principal idea is to include major parts of dynamic electron correlation by density functional theory whereas static correlation effects are taken into account by short MRCI expansions. The configuration state function (CSF) basis of this MRCI expansion is built up from Kohn-Sham (KS) orbitals. The effective DFT/MRCI Hamiltonian matrix is constructed from the exact (*ab initio*) expressions and DFT specific corrections. All in all, five global parameters are introduced, depending only on the multiplicity of the considered state, the number of open shells of the respective configuration, and the employed density functional, but **not** on the specific atom or molecule. Currently, optimised parameter sets are available only for singlet and triplet multiplicities in combination with the BH-LYP [8, 9] functional. A common set of reference CSFs is used for all spatial symmetries. The initial set can be generated in a complete active space (CAS)-like procedure and is then iteratively improved. The MRCI expansion is kept short by extensive configuration selection. For further details, we refer to the original publication [7].

Technically, the MRCI code and the associated property programmes are linked to the TURBOMOLE package [10, 11]. They can thus take advantage of the efficiency with which the latter reduces the computational expense for the two-electron integrals and the determination of the KS wavefunction. Four-index integrals are handled using the well-known resolution of the identity (RI) method [12, 13]. Throughout, we employ the RI-MP2 optimised sets from the TURBOMOLE library as auxiliary basis sets [14, 15].

For comparison, we also computed the electronic spectrum by means of multi-reference Møller–Plesset theory. For this purpose, we used the PARALLEL RI-MR programme [16]. Here, the zeroth-order reference consists of a (restricted) CI wave function in a Hartree–Fock (HF) one-particle basis. The programme allows for configuration selection on the basis of the MR-MP2 energy contribution of a CSF to any of the states of interest. The advantage of this method is that the number of selected CSFs that enter the laborious iterative determination of the first-order perturbed wavefunction is extremely reduced. Therefore, even excited states of large systems such as C₆₀ can be investigated by this pure *ab initio* treatment. For further details we refer to Ref. [16].

The geometries of the low-lying singlet and triplet excited states were optimised employing an analytical time-dependent density functional theory (TD-DFT) gradient [17]. The computations were carried out with the `escf` module of TURBOMOLE Version 5.5 [17–19].

Spin-orbit coupling matrix elements in the basis of the DFT/MRCI wavefunctions are computed using the recently developed spin-orbit coupling kit SPOCK [20]. Key features of this programme are: Firstly, spin-coupling coefficients between CSFs for spin-dependent one-electron operators are determined fastly by means of a pattern technique which is an extension of the work of Wetmore *et al.* [21] to spin-dependent one-electron operators [20, 22]. Secondly, the (one-center) spin-orbit mean-field Hamiltonian is applied, which is a non-empirical effective one-electron operator [23]. Herein, the expensive two-electron terms of the full Breit–Pauli Hamiltonian are treated in a Fock-like manner. Even for light molecules for which these terms result in a screening of the one-electron terms of up to 50%, the errors introduced by this approximation are usually well below 1% [24, 25]. Additional computational savings are achieved in the one-center approximation where the molecular mean field reduces to a sum of atomic contributions. Originally devised for heavy-metal compounds [23], this atomic mean-field approximation could be thought of as the more critical one for organic, especially conjugated systems, constituted from light atoms only. For the first-order spin-orbit splitting in the ground state of the systems HC₆H⁺, NC₅H⁺, and NC₄N⁺, it was found that the one-center approximation causes an error of only approximately 5% [25]. Errors of this size appear quite acceptable in view of the enormous requirements of resources for a full spin-orbit treatment even of medium-sized molecules. Moreover, this approach has the ad-

vantage of being controllable at each step in the hierarchy of approximations.

SPOCK is interfaced to the TURBOMOLE package by the program SOMF [20]. Herein, mean-field orbitals in the employed basis set are generated automatically for each atom from a restricted (open-shell) Hartree–Fock atomic ground state calculation. Afterwards, these are transferred to the atomic mean-field integral program AMFI [26], together with the atomic orbital (AO) basis set data. AMFI makes use of the spherical atomic symmetry; spin-orbit integral evaluation is thus extremely fast. Finally, SOMF performs the transformation of the spin-orbit integrals from the AO to the molecular orbital (MO) basis set.

Spin-orbit coupled wave functions, fine-structure splittings, and dipole transition probabilities of spin-forbidden transitions are determined at the level of quasi-degenerate perturbation theory (QDPT) in the basis of the LS coupled CI states [27].

The application of these techniques and approximations in combination with the generation of correlated wavefunctions via the DFT/MRCI approach makes it possible to compute spin-orbit coupling in organic molecules efficiently and with high confidence.

Vibrational frequencies and normal modes for the ground state KS determinant were computed with the `aoforce` module of the TURBOMOLE programme package [10, 11]. Information about the vibrational structure of the phosphorescence band was obtained with the HOTFCHT programme of Berger *et al.* which is based on a time-independent approach [28]. Franck–Condon factors for electronic transitions are calculated in the harmonic approximation. We employed the closed-shell KS determinant vibrational frequencies and normal modes for both ground and excited states. We are thus able to detect contributions to the Franck–Condon activity from displacements in the excited state.

3. Technical details

For all geometry optimisations at the density functional level of theory we chose the BH-LYP functional [8, 9]. TZVP basis sets from the TURBOMOLE library are applied throughout, unless mentioned otherwise [29]. The geometry of the electronic ground state of the dithiosuccinimide molecule was optimised applying the restricted Kohn–Sham density functional theory algorithm of the TURBOMOLE package [10, 11]. From X-ray data, the ground state geometry of dithiosuccinimide is known to exhibit approximately C_{2v} symmetry in the solid state [4]; the observed small distortions may be explained by site-site interactions in the crystal. Geometry optimisation of the isolated molecule without symmetry constraints revealed an almost C_{2v} symmetric structure distorted slightly towards C_2 by a small torsion of the $-\text{H}_2\text{C}=\text{CH}_2-$ group with respect

to the chromophore. When C_{2v} constraints are imposed, an almost isoenergetic structure is obtained. Therefore, in order to facilitate comparison with other work, only the C_{2v} constrained ground state structure will be considered further.

Excited states of (thio)carbonyl compounds are known to exhibit a pyramidal structure at the (thio)carbonyl carbon atom in many cases. To account for this, for each state under consideration TD-DFT optimisations in the lower symmetries C_2 and C_s were run.

At the optimised geometries, single-point DFT/MRCI calculations were carried out. The one-particle basis consisted of the KS orbitals of the recomputed closed-shell ground state determinant at the respective geometry. 1s electrons at carbon and nitrogen centers and 1s, 2s, and 2p electrons at sulfur centers were treated as frozen core; thus all the valence electrons were correlated. In the case of C_{2v} symmetry, four roots of singlet and triplet multiplicity were determined in each irreducible representation. In the case of the lower point groups C_2 and C_s this corresponds to eight roots. The reference space approximately comprised 130 CSFs in total for all states of one multiplicity. The dimension of the actual MRCI space per spatial and spin symmetry including energy-selected single and double excitations out of the reference space was approximately 17 000 CSFs in C_{2v} and 36 000 CSFs in the lower point groups. Additionally, for the ground state geometry a DFT/MRCI calculation was performed utilizing the TZVPP basis sets from the TURBOMOLE library [29], augmented by 3s, 3p, and 1d primitive diffuse Gaussians located at the molecular center of mass. Exponents were chosen as 0.05, 0.02, 0.008 (*s* and *p* Rydberg) and 0.015 (*d* Rydberg). This basis set will be called TZVPP+Ryd in the following. The MRCI problem in this basis blows up to 190 reference CSFs and 160 000 selected CSFs.

The one-particle basis for the complementary MR-MP2 calculations was comprised by a closed-shell HF determinant. Four singlet and three triplet states were computed in each spatial symmetry. The reference space contained all in all 665 configurations in the singlet case and 444 configurations in the triplet case. Using a selection threshold of $0.1\mu E_H$, a total of 6.5×10^6 (4.4×10^6) configurations were incorporated into the truncated singlet (triplet) first-order interaction space.

Spectral shifts due to electrostatic interactions in polar solvents were estimated employing the conductor-like screening model (COSMO) of solvation which is implemented in the TURBOMOLE package [30]. A dielectric constant of $\epsilon = 32.60$ corresponding to methanol at room temperature was chosen. Of course, hydrogen bonding cannot be taken into account properly this way. The COSMO module provides gradients but, unfortunately, is unable to handle open shell cases at present. Therefore, the geometric relaxation in solution could be computed only for the ground state. Spectral shifts for the excited states are taken from DFT/MRCI calculations in the one-particle basis of COSMO optimised KS orbitals.

4. Results and discussion

4.1 Electronic structure and spectrum

4.1.1 The electronic ground state

The calculated structural parameters for the electronic ground state in C_{2v} symmetry are listed in Table 1. Our structure agrees with the experimental data from X-ray crystallography [4] up to 1 pm in bond lengths and 2 degrees in bond angles. For example, the average bond length in the two thiocarbonyl groups in the crystal amounts to 163 pm which is exactly the same value as in our optimised structure. For the C–N bond distance we obtain 136 pm, compared to 137 pm from experiment. The largest difference in bond angle of 2 degrees is found for C–N–C with 117 degrees (this work) and 114.7 degrees (experiment). This overall good agreement may be regarded as a confirmation that dimer formation in the crystal package due to N–H \cdots S hydrogen bonding has little effect on the molecular skeleton. Similar conclusions could already be drawn from semiempirical calculations [4], but their calculated C=S bond lengths for the isolated molecule are generally smaller than the X-ray data by 4–7 pm.

For the subsequent discussion of electronic structure, the five-membered ring is chosen to lie in the yz plane which is consistent with Ref. [3]. Valence molecular orbitals that are important for an understanding of the electronic spectrum are depicted in Figs. 2 and 3. As the dithiosuccinimide chromophore contains two coupled C=S moieties, two linear combinations of sulphur lone-

Table 1. Selected structural parameters for the optimised ground and excited states equilibrium geometries. The nomenclature S_0 , S_1 , S_2 , T_1 , T_2 , and T_4 follows the order of states at the ground state equilibrium geometry. All bond lengths (d) in pm units, angles (\angle) and dihedrals in degrees. Atoms are labeled according to Fig. 1.

	state symmetry	S_0 C_{2v}	S_1 C_2	S_2 C_2	S_3 C_{2v}	T_1 C_2	T_2 C_2	T_3 C_{2v}	T_4 C_{2v}
d	C_3 – S_7	163	167	168	170	166	167	171	172
d	N_2 – C_3	136	136	135	135	136	136	135	138
d	N_2 – H_1	100	100	100	101	100	100	100	100
d	C_3 – C_4	151	151	150	150	151	150	151	150
\angle	C_6 – N_2 – C_3	117	116	116	117	116	115	117	114
\angle	N_2 – C_3 – S_7	125	124	127	123	124	127	123	125
\angle	N_2 – C_3 – C_4	107	107	107	107	107	107	108	108
dihedral	H_1 – N_2 – C_3 – S_7	0	0	1	0	1	1	0	0
dihedral	N_2 – C_3 – C_4 – C_5	0	4	12	0	10	15	0	0
dihedral	C_3 – C_4 – C_5 – C_6	0	5	14	0	12	18	0	0

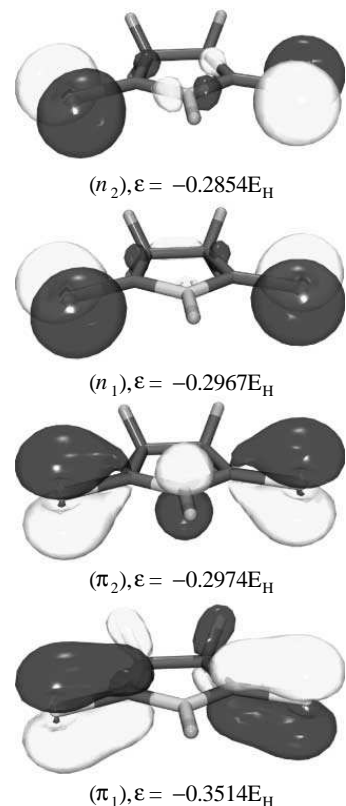


Fig. 2. The highest occupied n and π MOs. (S_0 geometry, TZVP basis, isoline = 0.050).

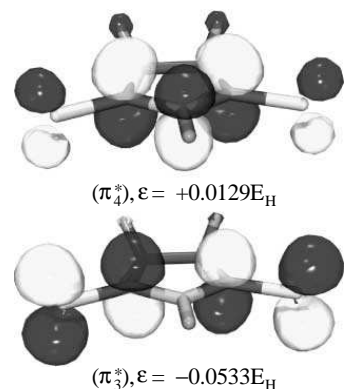


Fig. 3. The lowest unoccupied π^* MOs. (Other information as in Fig. 2).

pair orbitals arise. The b_2 symmetric one (for which the xz plane is a nodal plane) is found to be the highest occupied molecular orbital (HOMO, n_2). The other one transforms as a_1 and is the second-highest MO at the ground

state geometry (HOMO-1, n_1). As Fälth *et al.* already pointed out, the interaction of the lone pairs in these orbitals is mediated by symmetric and antisymmetric σ type contributions in the region of the C–N bonds [5]. Below these lone-pair orbitals, the two orbitals denoted π_1 and π_2 are found. The a_2 MO is recognised as the antisymmetric linear combination of two proper C=S group π orbitals, the symmetric counterpart of which is lower in energy and omitted in the figure. The other one of b_1 symmetry may alternatively be regarded as a linear combination of sulphur and nitrogen lone-pair orbitals which are perpendicular to the five-membered ring. However, we prefer to follow the symmetry argument and therefore account this orbital as being of π type. The lowest unoccupied MO (LUMO, π_3^*) is of a_2 symmetry and anti-bonding with respect to both C=S groups. It may be viewed as built from two π^* orbitals of isolated C=S groups by (negative) linear combination. Without diffuse functions in the AO basis, the second-lowest unoccupied MO (LUMO+1, π_4^*) also is of π^* type, exhibiting nodal planes perpendicular to and in the middle of the C–N bond axes. It possesses only minor contributions at the sulphur atoms. Concerning the TZVPP+Ryd basis set calculations, the second-lowest unoccupied MO corresponds to a totally symmetric Rydberg orbital. Further, the two lowest unoccupied b_1 orbitals exhibit mixed valence-Rydberg character. To be consistent with the nomenclature of the TZVP MOs, we denote the valence part of these mixed orbitals by π_4^* .

The calculated electric dipole moment for the ground state amounts to 2.14 D, pointing from the five-membered ring towards the N–H bond. For comparison, the thioformamide molecule exhibits approximately twice this value (4.46 D with B3LYP, 4.01 D from experiment) [31]. Surely, the lower polarity of dithiosuccinimide is related to its high molecular symmetry which results in cancellation of single contributions to the total dipole moment to some extent.

4.1.2 Vertical absorption spectrum and characterization of excited states

The computed vertical singlet and triplet spectra together with the experimental absorption maxima from Ref. [3] are shown in Tables 2 and 3. Upon using the TZVPP+Ryd basis set, the first Rydberg excitations are found at 5.11 eV within the triplet manifold and 5.23 eV within the singlet manifold, respectively. The physical meaning of all states above 5.1 eV computed in the TZVP basis set without diffuse functions is thus questionable. Therefore, they are omitted in the tables. Nevertheless, these states are incorporated into the set of intermediate states when the radiative lifetime of the T_1 state is determined by perturbation theory.

The DFT/MRCI calculations reveal that the first excited singlet state S_1 is of B_1 spatial symmetry, resulting from the $n_2 \rightarrow \pi_3^*$ (HOMO-LUMO) excitation. As expected for $n \rightarrow \pi^*$ transitions, its oscillator strength is rather

Table 2. Vertical singlet excitation energies ΔE [eV] and dipole transition oscillator strengths $f(r)$.

State	MR-MP2		TD-DFT		DFT/MRCI		experiment	
	TZVP		TZVP		TZVPP+Ryd			
	ΔE	ΔE	ΔE	ΔE	$f(r)$	dominant excitation(s)		
S_0 1^1A_1	0.00	0.00	0.00	0.00				
S_1 1^1B_1	2.58	3.13	2.68	2.65	$< 2 \times 10^{-4}$	$n_2 \rightarrow \pi_3^*$	2.77 ^a , 2.82 ^b	
S_2 1^1A_2	2.78	3.36	2.87	2.83	0.0	$n_1 \rightarrow \pi_3^*$	3.04 ^a , 3.08 ^b	
S_3 1^1B_2	3.87	4.72	4.18	4.14	0.714	$\pi_2 \rightarrow \pi_3^*$	3.96 ^a , 3.87 ^b	
S_4 2^1A_2	4.39	—	4.70	4.51	0.0	$n_2 \rightarrow \pi_4^*$		
S_5 2^1B_1	4.57	—	4.89	4.70	$< 9 \times 10^{-4}$	$n_1 \rightarrow \pi_4^*$		
S_6 2^1A_1	—	—	4.83	4.80	≈ 0.0	$n_1, n_2 \rightarrow \pi_3^*, \pi_4^*$		
S_7 3^1A_1	—	—	—	5.03	0.003	$\pi_2 \rightarrow \pi_4^*$		
S_8 2^1B_2	—	—	—	5.23	0.065	$n_2 \rightarrow R$		
S_9 4^1A_1	4.88 ^c	—	—	5.31	0.114	$\pi_1 \rightarrow \pi_3^*$	$\approx 4.96^d$	
S_{10} 3^1B_1	—	—	—	5.67	0.040	$\pi_2 \rightarrow R$		

^a from absorption in cyclohexane (Meskers *et al.* [3])^b from absorption in methanol (Meskers *et al.* [3])^c calculated as second root in A_1 symmetry^d tentative assignment as $1^1A_1(\pi \rightarrow \pi^*)$ by Meskers *et al.* [3]

small. The S_2 (1^1A_2) state with the leading configuration $n_1 \rightarrow \pi_3^*$ (HOMO-1, LUMO) is located only ≈ 0.2 eV above S_1 . The corresponding dipole transition $S_0 \leftarrow S_2$ is forbidden in C_{2v} symmetry. The results are corroborated by the MR-MP2 calculation that shows differences in excitation energy of approximately 0.1 eV for these states compared to DFT/MRCI. Concerning the assignment of S_1 and S_2 , we are thus in agreement with Meskers *et al.* who deduced the symmetry properties of these states from polarised phosphorescence excitation spectra [3]. However, our DFT/MRCI energies are slightly lower (≈ 0.1 –0.2 eV) than the absorption maxima observed in cyclohexane. In contrast, singlet excitation energies obtained from the TD-DFT treatment are systematically overestimated by about 0.5 eV. This may be related to the importance of double excitations for the correlation treatment in the present case.

Following Ref. [3], the source of intensity for the forbidden transition $S_0 \rightarrow S_2$ is vibronic coupling with the $\pi_2 \rightarrow \pi_3^*$ (HOMO-2, LUMO) excited state 1^1B_2 , giving rise to a strong absorption band at 3.96 eV. We find this state 0.2 eV higher in energy, at 4.14 eV in DFT/MRCI, whereas it comes out at 3.87 eV in the MR-MP2 calculation. A further relatively strong transition at ≈ 4.96 eV is mentioned in Ref. [3]. It may be associated with the S_9 (4^1A_1)

Table 3. Vertical triplet excitation energies ΔE [eV] and dipole transition oscillator strengths $f(r)$.

State	MR-MP2			TD-DFT			DFT/MRCI		experiment			
	TZVP		TZVP	TZVP		TZVPP+Ryd						
	ΔE	ΔE	ΔE	ΔE	$f(r)$	dominant excitation(s)						
T_1 1^3B_1	2.43	2.72	2.47	2.43		$n_2 \rightarrow \pi_3^*$		2.63 ^a				
T_2 1^3A_2	2.60	2.94	2.67	2.62	0.013	$n_1 \rightarrow \pi_3^*$						
T_3 1^3B_2	2.43	2.42	2.80	2.80	0.0	$\pi_2 \rightarrow \pi_3^*$						
T_4 1^3A_1	3.30	3.18	3.49	3.41	≈ 0.0	$\begin{cases} \pi_1 \rightarrow \pi_3^* \\ \pi_2 \rightarrow \pi_4^* \end{cases}$						
T_5 2^3A_2	4.34	—	4.75	4.53	0.131	$\begin{cases} n_2 \rightarrow \pi_4^* \\ n_1 \rightarrow \pi_3^* \end{cases}$						
T_6 2^3B_2	—	—	4.63	4.60	0.0	$n_1, n_2 \rightarrow (\pi_3^*)^2$						
T_7 2^3B_1	4.47	—	4.93	4.69	$< 4 \times 10^{-4}$	$n_1 \rightarrow \pi_4^*$						
T_8 2^3A_1	—	—	4.78	4.74	≈ 0.0	$n_1, n_2 \rightarrow \pi_3^*, \pi_4^*$						
T_9 3^3B_2	—	—	—	5.11	0.0	$n_2 \rightarrow R$						
T_{10} 3^3A_1	4.89 ^b	—	—	5.13	≈ 0.0	$\begin{cases} \pi_2 \rightarrow \pi_4^* \\ \pi_1 \rightarrow \pi_3^* \end{cases}$						
T_{11} 4^3A_1	—	—	—	5.33	0.003	$n_1 \rightarrow R$						
T_{12} 3^3B_1	—	—	—	5.59	≈ 0.0	$\pi_2 \rightarrow R$						
T_{13} 4^3B_2	5.27 ^c	—	—	5.62	0.0	$\pi_1 \rightarrow \pi_4^*$						

^a from absorption in cyclohexane, not observed in methanol (Meskers *et al.* [3])^b calculated as second root in A_1 symmetry^c calculated as second root in B_2 symmetry

state which results from $\pi_1 \rightarrow \pi_3^*$ excitation and also has a considerable oscillator strength in our calculation.

In the triplet manifold, the states corresponding to the $n \rightarrow \pi^*$ excited singlet states S_1 and S_2 are T_1 and T_2 . Again, the lowest state results from $n_2 \rightarrow \pi_3^*$ (HOMO-LUMO) excitation and thus exhibits B_1 spatial symmetry in accord with Ref. [3], where the phosphorescence is attributed to the 1^3B_1 state.

As expected, the singlet-triplet splitting is much larger for the $\pi_2 \rightarrow \pi_3^*$ (HOMO-2, LUMO) excited state T_3 (1^3B_2) than for the $n \rightarrow \pi^*$ ones T_1 and T_2 . As a consequence, T_3 gets so close to T_2 that one can hardly decide which of them is really the lower one in the vertical spectrum. And indeed, the energetic order of T_2 and T_3 is changed in the MR-MP2 calculation which reveals an excitation energy for T_3 almost equal to that of T_1 . TD-DFT even predicts the $\pi_2 \rightarrow \pi_3^*$ excited state to be the lowest triplet state. In the following we adopt the DFT/MRCI order of states, throughout.

Among the several further states below 5.0 eV, we only mention the $\pi_1 \rightarrow \pi_3^*$ excited triplet state T_4 (1^3A_1) at 3.41 eV which is the counterpart of S_9 (4^1A_1).

4.1.3 Geometries of excited states and spectral shifts in solution

Geometries of excited states were optimised with TD-DFT, allowing for C_2 and C_s symmetric distortions from the ground state geometry. For the obtained molecular geometries corresponding to minima on the potential energy surface, single-point DFT/MRCI calculations were carried out. The results are presented in Tables 4 and 5. The corresponding structural parameters are shown in Table 1.

In general, the minimum energies for C_2 and C_s symmetry are almost equal. This indicates that the molecule does not undergo a dramatic change in structure such as pyramidalization in the chromophore region for one of the states under consideration. Indeed, the only emerging deviation from C_{2v} symmetry is that the alkyl backbone is twisted somewhat out of plane. As the associated normal mode owes a very low frequency and the distortion is small, this comes along with an almost negligible relaxation of the energy.

More significant changes with respect to the ground state geometry are constituted by bond elongations in the chromophore region. For the $n \rightarrow \pi^*$ excited states T_1 and T_2 , the C=S bond lengths are 166 pm and 167 pm, respectively, which has to be compared with 163 pm for the ground state. The involved π_3^* MO exhibits a node along the C=S bond axis. The bond order may thus be reduced by $\frac{1}{4}$ for each C=S bond when this MO becomes singly occupied. For comparison: In simple thiocarbonyl systems such as thiophosgene, the C=S bond length in the $n \rightarrow \pi^*$ excited T_1 state is 174 pm *vs.* 162 pm in the ground state corresponding to a bond order reduction of $\frac{1}{2}$ [32]. The N–C bonds are not changed significantly. The amplitude of the π_3^* MO at the nitrogen atom vanishes and it can thus be considered as nonbonding in this region. The most prominent change in bond angle appears for the N–C–S angle which is enlarged by 2° at the T_2 equilibrium geometry. For the $n \rightarrow \pi^*$ excited singlet states S_1 and S_2 , the optimised structures are quite similar to the triplets. (The calculated oscillator strength for the $S_0 \rightarrow S_2$ electronic transition at the S_2 equilibrium geometry is $\approx 1 \times 10^{-5}$. This low value is related to the fact that the chromophoric symmetry is left unchanged in the excited state.)

For the $\pi \rightarrow \pi^*$ excited states, the elongation of the C=S bonds is even more pronounced. This is expected, as both π_1 and π_2 are bonding in this region. For the T_4 ($\pi_1 \rightarrow \pi_3^*$) state, a value of 172 pm is obtained. The N–C bonds are also noticeably lengthened in this state. This may be due to the admixture of a configuration in which π_4^* is occupied. This MO is strongly anti-bonding with respect to the N–C bonds. However, the qualitative picture of

Table 4. Relative energies ΔE [eV] of dithiosuccinimide at various molecular (triplet) geometries (DFT/MRCI, TZVP basis). The nomenclature S_0 , S_1 , S_2 , T_1 , T_2 , and T_4 follows the order of states at the ground state equilibrium geometry. Adiabatic TD-DFT energies in parentheses.

State	T_1 geometry	T_2 geometry	T_3 geometry	T_4 geometry
	$n_2 \rightarrow \pi_3^*$	$n_1 \rightarrow \pi_3^*$	$\pi_2 \rightarrow \pi_3^*$	$\pi_1 \rightarrow \pi_3^*$
	TD-DFT (C_2)	TD-DFT (C_2)	TD-DFT (C_s)	TD-DFT (C_s)
S_0	0.03	0.08	0.19	0.24
S_1	2.56	2.57	2.56	2.59
S_2	2.74	2.70	2.72	2.72
S_3	4.00	4.03	3.88	3.92
T_1	2.36 (2.66)	2.38	2.39	2.41
T_2	2.55	2.51 (2.83)	2.56	2.55
T_3	2.64	2.67	2.57 (2.16)	2.63
T_4	3.32	3.33	3.27	3.21 (2.87)

Table 5. Relative energies ΔE [eV] of dithiosuccinimide at various molecular (singlet) geometries (DFT/MRCI, TZVP basis). The nomenclature S_0 , S_1 , S_2 , T_1 , T_2 , and T_4 follows the order of states at the ground state equilibrium geometry. Adiabatic TD-DFT energies in parentheses.

State	S_1 geometry	S_2 geometry	S_3 geometry
	$n_2 \rightarrow \pi_3^*$	$n_1 \rightarrow \pi_3^*$	$\pi_2 \rightarrow \pi_3^*$
	TD-DFT (C_2)	TD-DFT (C_2)	TD-DFT (C_s)
S_0	0.03	0.08	0.13
S_1	2.56 (3.07)	2.57	2.56
S_2	2.73	2.70 (3.24)	2.73
S_3	3.97	4.01	3.89 (4.54)
T_1	2.36	2.38	2.38
T_2	2.55	2.51	2.56
T_3	2.62	2.65	2.58
T_4	3.31	3.31	3.28

orbital nodes surely is insufficient to describe the intricate force balancing in the five-membered ring.

Aside from total excitation energies, the single-point DFT/MRCI results support the TD-DFT findings: The lowest DFT/MRCI energy is always obtained at the TD-DFT minimum geometry of the respective state. Also, differences in vertical and adiabatic excitation energies are comparable in magnitude and trend. Both methods thus seem to agree concerning the local shape of the potential energy surface.

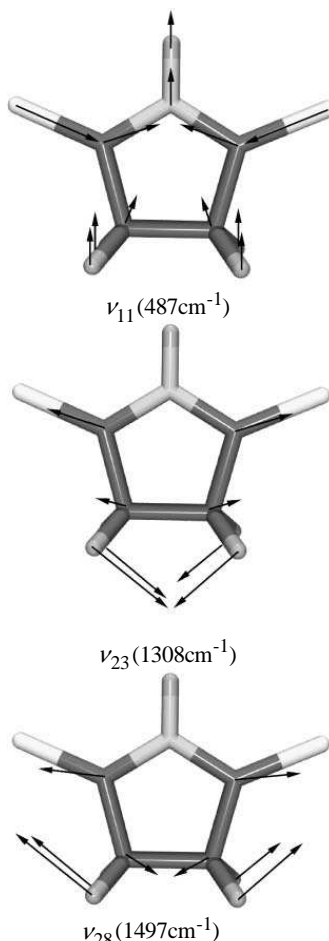


Fig. 4. Sketch of totally symmetric normal modes that are expected to be Franck–Condon active in the $S_0 \leftarrow T_1$ radiative transition and may contribute to the vibrational structure of the phosphorescence band (BH-LYP functional, TZVP basis).

The energetic relaxation is considerably larger for the $\pi \rightarrow \pi^*$ excited states than for the $n \rightarrow \pi^*$ states (approximately 0.3 eV vs. 0.1 eV). Therefore, at the T_3 geometry, T_2 and T_3 are predicted to be almost degenerate by the DFT/MRCI calculations. Overall, relaxation of the molecular structure in the lowest excited states is small due to the stiffness of the five-membered ring.

Vibrational normal modes along which the molecule is displaced with respect to S_0 in the T_1 state were obtained with the HOTFCHT programme. The totally symmetric normal modes that are expected to be important for the vibrational structure of the phosphorescence band are depicted in Fig. 4.

An estimate of the spectral shifts in polar aprotic solvents can be made from Table 6. The tabulated DFT/MRCI excitation energies are computed employing a one-particle basis which has been optimised together with the

Table 6. Relative energies ΔE [eV] of dithiosuccinimide states at various molecular geometries using COSMO solvation model ($\varepsilon = 32.60$, methanol) (DFT/MRCI, TZVP basis). The nomenclature S_0 , S_1 , S_2 , T_1 , T_2 , and T_4 follows the order of states at the ground state equilibrium geometry.

State	S_0 geometry (reoptimised)	T_2 geometry —	T_3 geometry —	absorption [3] (methanol)
S_0	0.00	0.07	0.15	
S_1	2.85	2.78	2.76	2.82
S_2	3.03	2.90	2.91	3.08
S_3	4.12	4.02	3.86	3.87
T_1	2.64	2.58	2.58	
T_2	2.84	2.71	2.74	
T_3	2.91	2.82	2.73	
T_4	3.59	3.46	3.39	

Table 7. Dipole moments μ [D] of dithiosuccinimide at the ground state geometry and at the equilibrium geometry of the respective state (DFT/MRCI, TZVP basis).

State	S_0 geometry	equilibrium geometry
$S_0, 1^1A_1$	2.14	2.14
$S_1, 1^1B_1$	1.35	1.45
$S_2, 2^1A_2$	1.23	1.14
$S_3, 1^1B_2$	1.43	1.86
$T_1, 1^3B_1$	1.30	1.36
$T_2, 1^3A_2$	1.18	1.06
$T_3, 1^3B_2$	0.94	1.21
$T_4, 1^3A_1$	1.54	1.67

surrounding screening charges in the COSMO model. For this purpose, the geometry of the ground state firstly was reoptimised at the uncorrelated level to get the minimum energy structure of the solvated system. However, no change compared to the vacuum ground state geometry emerged. Analogous single-point DFT/MRCI calculations at the vacuum equilibrium geometries of the T_2 and T_3 states are also presented in Table 6 as solvation effects may crucially influence the energetic order of these states. It is found that singlet and triplet $n \rightarrow \pi^*$ states exhibit a blue shift in our model of 0.16–0.20 eV. The energetic location of the S_3 ($\pi_2 \rightarrow \pi_3^*$) state is nearly left unchanged. At the ground state geometry, for example, it is shifted to lower energies by 0.06 eV. However, the $\pi \rightarrow \pi^*$ triplet states T_3 and T_4 appear to be blue-shifted by 0.1–0.16 eV. This contradicts the conventional rule of thumb that $n \rightarrow \pi^*$ states experience more

hypsochromic shifts with increasing solvent polarity whereas $\pi \rightarrow \pi^*$ states encounter bathochromic shifts. Table 7 shows the dipole moments for the states under consideration. It is seen that in our case the $\pi \rightarrow \pi^*$ excited states do not owe dipole moments much larger than the $n \rightarrow \pi^*$ ones. Also, the ground state value exceeds all others. Therefore, even for the $\pi \rightarrow \pi^*$ excited states hypsochromic shifts may occur. These shifts are more pronounced for the $n \rightarrow \pi^*$ excited states, however. Following Table 6, the near-degeneracy of T_2 and T_3 is not lifted by solvent effects.

The computed vertical excitation energies from Table 6 agree excellently with the experimental absorption data in methanol taken from Ref. [3]. It has to be kept in mind, however, that hydrogen bonding with protic solvents is not accounted for in this model.

4.1.4 Spin-orbit coupling

In Table 8, spin-orbit matrix elements for the low-lying electronic states of the dithiosuccinimide molecule are listed. In view of the subsequent discussion of the phosphorescence rate, the given values are computed at the equilibrium geometry of the T_1 state in C_2 spatial symmetry. However, the distortion from C_{2v} symmetry in the T_1 state is small, especially in the chromophore region where the largest contributions to spin-orbit interaction are expected. The matrix elements thus approximately obey C_{2v} symmetry selection rules: The coupling terms that vanish in C_{2v} symmetry do not exceed a few wave numbers at the T_1 state geometry.

Large spin-orbit matrix elements are found between the electronic ground state and triplet states of $n \rightarrow \pi^*$ type. The same applies to matrix elements between $n \rightarrow \pi^*$ and $\pi \rightarrow \pi^*$ excited states both for the singlet-triplet and for the triplet-triplet coupling case. On the other hand, the coupling between two $\pi \rightarrow \pi^*$ states is two orders of magnitude smaller than for the above-mentioned cases. The size of the coupling matrix element of two $n \rightarrow \pi^*$ states is intermediate, roughly one order of magnitude smaller than an $n \rightarrow \pi^*/\pi \rightarrow \pi^*$ coupling. This behaviour is widespread and is known as El-Sayed's rule [33].

Of particular importance concerning the radiative properties of the lowest triplet state is its spin-orbit coupling to the $S_3(\pi_2 \rightarrow \pi_3^*)$ state which gives rise to the most intense band in the absorption spectrum. Meskers *et al.* estimated the corresponding matrix element from the extinction ratio of the $S_0 \rightarrow T_1$ and $S_0 \rightarrow S_3$ absorption bands to approximately 150 cm^{-1} [3]. In contrast, our calculated value amounts to only 60.5 cm^{-1} . However, we obtain a large matrix element of 131.55 cm^{-1} between the S_3 and the T_2 state. This difference in coupling strength may be rationalised as follows: We consider the leading configurations which are $n_2 \rightarrow \pi_3^*$ for T_1 , $n_1 \rightarrow \pi_3^*$ for T_2 , and $\pi_2 \rightarrow \pi_3^*$ for S_3 . The coefficients of the corresponding CSFs in the DFT/MRCI wave functions approximately amount to 0.9 for all three states. As the mean-field spin-orbit operator is an effective one-electron operator, a non-zero matrix element is ob-

Table 8. Spin-orbit matrix elements (absolute values) [cm⁻¹] of the lowest singlet and triplet states, calculated at the T_1 geometry. The component of the spin-orbit Hamiltonian is indicated in parentheses.

$\langle T_1 \mathcal{H}_{\text{SO}} S_0 \rangle$	6.02(x)/182.95(y)
$\langle T_1 \mathcal{H}_{\text{SO}} S_1 \rangle$	0.36(z)
$\langle T_1 \mathcal{H}_{\text{SO}} S_2 \rangle$	14.28(x)/0.50(y)
$\langle T_1 \mathcal{H}_{\text{SO}} S_3 \rangle$	60.52(z)
$\langle T_2 \mathcal{H}_{\text{SO}} S_0 \rangle$	72.23(z)
$\langle T_2 \mathcal{H}_{\text{SO}} S_1 \rangle$	13.57(x)/1.30(y)
$\langle T_2 \mathcal{H}_{\text{SO}} S_2 \rangle$	0.08(z)
$\langle T_2 \mathcal{H}_{\text{SO}} S_3 \rangle$	0.39(x)/131.55(y)
$\langle T_2 \mathcal{H}_{\text{SO}} T_1 \rangle$	13.84(x)/1.70(y)
$\langle T_3 \mathcal{H}_{\text{SO}} S_0 \rangle$	0.02(x)/2.14(y)
$\langle T_3 \mathcal{H}_{\text{SO}} S_1 \rangle$	73.64(z)
$\langle T_3 \mathcal{H}_{\text{SO}} S_2 \rangle$	1.76(x)/170.36(y)
$\langle T_3 \mathcal{H}_{\text{SO}} S_3 \rangle$	0.55(z)
$\langle T_3 \mathcal{H}_{\text{SO}} T_1 \rangle$	71.67(z)
$\langle T_3 \mathcal{H}_{\text{SO}} T_2 \rangle$	1.57(x)/164.43(y)
$\langle T_4 \mathcal{H}_{\text{SO}} S_0 \rangle$	4.87(z)
$\langle T_4 \mathcal{H}_{\text{SO}} S_1 \rangle$	0.20(x)/135.00(y)
$\langle T_4 \mathcal{H}_{\text{SO}} S_2 \rangle$	54.60(z)
$\langle T_4 \mathcal{H}_{\text{SO}} S_3 \rangle$	0.11(x)/0.63(y)
$\langle T_4 \mathcal{H}_{\text{SO}} T_1 \rangle$	0.13(x)/133.84(y)
$\langle T_4 \mathcal{H}_{\text{SO}} T_2 \rangle$	55.53(z)
$\langle T_4 \mathcal{H}_{\text{SO}} T_3 \rangle$	0.01(x)/1.03(y)

tained only between configurations that are single excitations with respect to one another. If we neglect contributions from other configurations which are admixed with much smaller coefficients, the matrix element $\langle T_1 | H_{\text{SO},z} | S_3 \rangle$ is governed by the integral $\langle n_2 | H_{\text{SO},z} | \pi_2 \rangle$ whereas $\langle T_2 | H_{\text{SO},y} | S_3 \rangle$ is governed by $\langle n_1 | H_{\text{SO},y} | \pi_2 \rangle$. The lone-pair orbitals n_1 and n_2 are located almost exclusively at the sulphur sites. To a good approximation, they are linear combinations of sulphur 3p AOs which are lying in the yz plane and which are perpendicular to the C=S bond. In a local coordinate system at the sulphur centers, the orientation of the lone pairs with respect to the z axis is described by the rotation angle φ (Fig. 5). For the MOs n_1 and n_2 we thus get:

$$n_1 \approx \frac{1}{\sqrt{2}} (\cos \varphi p_{z,s8} + \sin \varphi p_{y,s8} + \cos \varphi p_{z,s7} - \sin \varphi p_{y,s7})$$

$$n_2 \approx \frac{1}{\sqrt{2}} (\cos \varphi p_{z,s8} + \sin \varphi p_{y,s8} - \cos \varphi p_{z,s7} + \sin \varphi p_{y,s7}) .$$

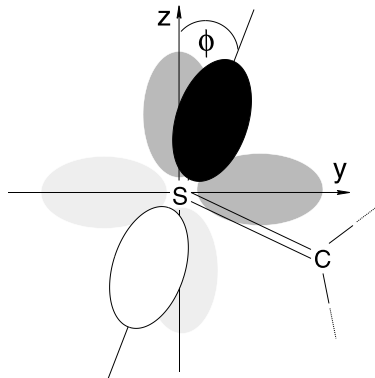


Fig. 5. Definition of the rotation angle ϕ in a local coordinate system at one of the sulphur centres.

For the π_2 MO we write

$$\pi_2 = \frac{1}{N} (p_{x,S8} + p_{x,S7} + \dots)$$

where the dots denote contributions from other centers and N is chosen to give the proper normalization. In the one-center approximation, the MO integrals are related to the symmetry equivalent AO integrals by:

$$\begin{aligned} \langle n_1 | H_{SO,y} | \pi_2 \rangle &\approx \frac{\sqrt{2}}{N} \cos \varphi \langle p_{z,S} | H_{SO,y} | p_{x,S} \rangle \\ \langle n_2 | H_{SO,z} | \pi_2 \rangle &\approx \frac{\sqrt{2}}{N} \sin \varphi \langle p_{y,S} | H_{SO,z} | p_{x,S} \rangle. \end{aligned}$$

As the coefficients of the leading configurations are comparable, this means that the ratio of the above matrix elements is determined to a good approximation solely by the angle φ :

$$\frac{\langle T_1 | H_{SO,z} | S_3 \rangle}{\langle T_2 | H_{SO,y} | S_3 \rangle} \approx \frac{\sin \varphi}{\cos \varphi} = \tan \varphi. \quad (1)$$

To illustrate this rule of thumb with numbers: At the T_1 state geometry, the spin-orbit integrals of interest amount to $\langle n_2 | H_{SO,z} | \pi_2 \rangle = 128.7 \text{ cm}^{-1}$ and $\langle n_1 | H_{SO,y} | \pi_2 \rangle = 292.4 \text{ cm}^{-1}$. The ratio of the integrals is thus $\langle n_2 | H_{SO,z} | \pi_2 \rangle / \langle n_1 | H_{SO,y} | \pi_2 \rangle = 0.440$. The angle φ is calculated from Table 1 to be 24° which leads to $\tan \varphi \approx 0.445$.

In turn, this means that these spin-orbit matrix elements strongly depend on the angle φ . Hence, they vary in magnitude upon deflection along the v_9 totally symmetric normal mode (see Fig. 6). The latter may be termed the scissoring mode of the two C=S groups. Similar considerations concerning the angle

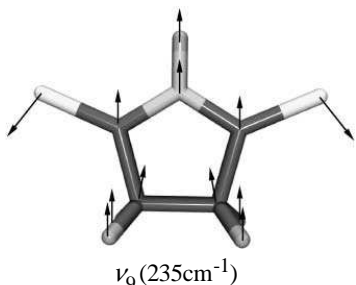


Fig. 6. Sketch of the scissoring mode of the two C=S groups (BH-LYP functional, TZVP basis).

φ apply to other spin-orbit matrix elements. This is shown in Fig. 7 together with a one-dimensional cut through the computed potential energy surfaces for the lowest excited states. The undistorted starting geometry in this case corresponds to the ground state equilibrium geometry for technical reasons. The matrix elements $\langle T_1 | H_{SO,z} | S_3 \rangle$ and $\langle T_2 | H_{SO,y} | S_3 \rangle$ become comparable for a curvilinear distortion of -40% of the normal mode unit vector. This corresponds to $\varphi \approx 41^\circ$ which is almost the value of 45° expected from our crude model.

For an estimate of inter-system crossing rates, we have determined potential energy curves of the ground and excited electronic states as one-dimensional cuts along the scissoring mode. Note, however, that these curves are not computed around the proper potential energy minimum of the particular excited state and do not take account of the correct Duchinski transformation of the normal modes. Their use for determining inter-system crossing rates is therefore somewhat questionable and the main intention here is to give a qualitative picture of the situation. The potential energy plots reveal almost equal slopes and equal minima positions for the pairs of states T_1/S_1 and T_2/S_2 , but displacements in minima and low-energy crossings for example for the pairs T_2/S_1 and T_3/S_2 . Anyway, the computation of proper inter-system crossing rates suffers from the limits in accuracy that are inevitably imposed on the calculated excitation energies. What can be said is: If T_3 is energetically located below S_2 , the inter-system crossing is expected to occur very fast. And if T_2 is located below S_1 , the corresponding radiationless transition will take place at a sizable rate despite the relatively small coupling matrix element. If we only consider the electronic coupling matrix elements, the rate of $S_2 \rightsquigarrow T_3$ inter-system crossing is expected to be about two orders of magnitude larger than that of $S_1 \rightsquigarrow T_2$.

The spin-orbit matrix element between the T_1 state and the electronic ground state S_0 is very large. However, this does not necessarily mean that the radiationless relaxation $T_1 \rightsquigarrow S_0$ is fast and efficient. Instead, a fast radiationless transition requires large Franck–Condon factors between the vibrational

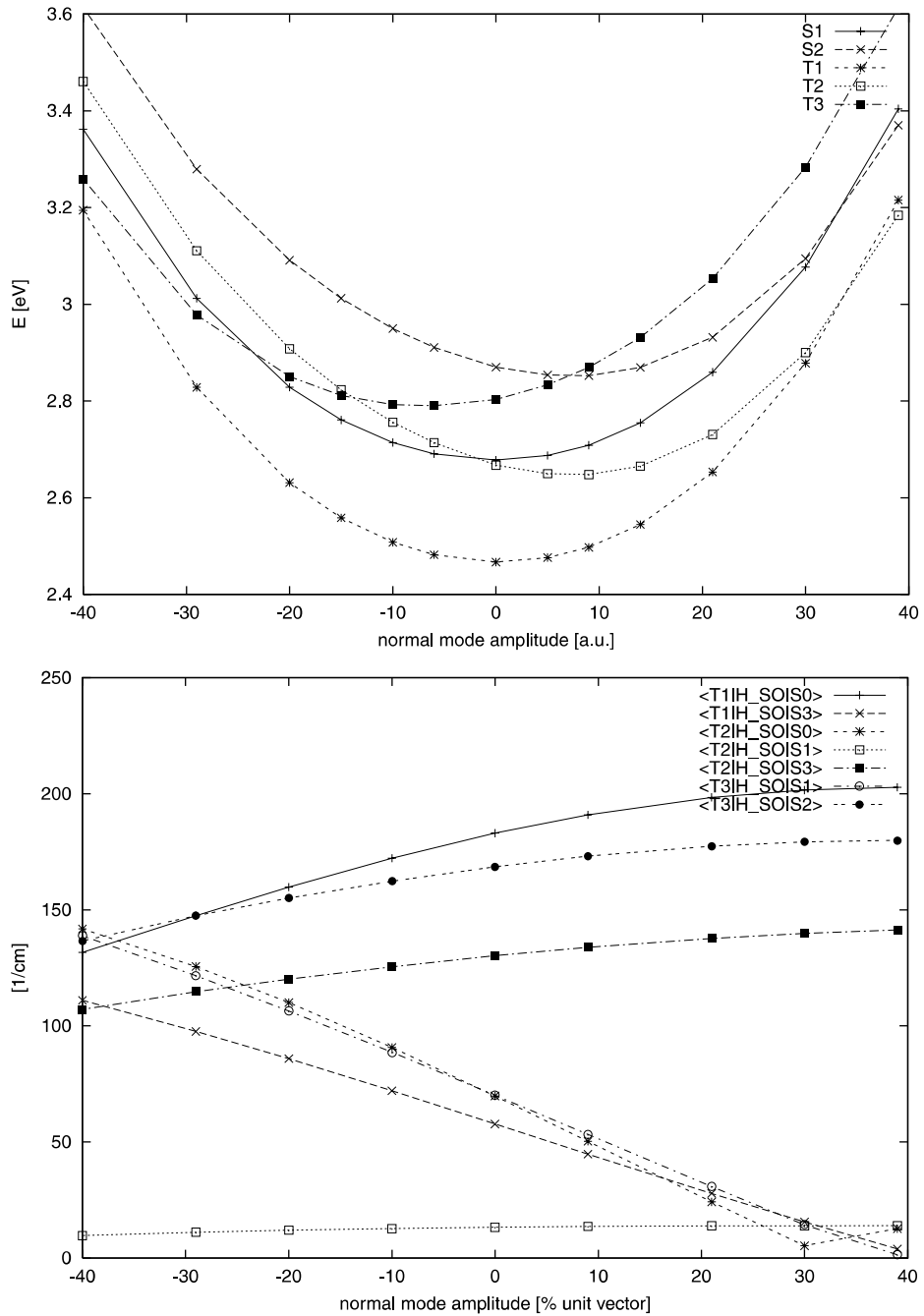


Fig. 7. DFT/MRCI excitation energies and spin-orbit coupling matrix elements (absolute values) for the lowest $n \rightarrow \pi^*$ states plotted against ν_9 normal mode elongation (C_{2v} symmetry, TZVP basis). A normal mode amplitude = 0 corresponds to the ground state geometry. The angle ϕ amounts to ≈ 41 degrees for -40% elongation and ≈ 6 degrees for $+40\%$ elongation.

zero level of the initial and isoenergetic excited vibrational levels of the final state as well. The equilibrium geometries of both states are rather similar and the energy gap is more than 2 eV. Therefore, it can be concluded that the overlap of these vibrational wave functions is small. The inter-system crossing $T_1 \rightarrow S_0$ thus will not be efficient. The totally symmetric normal modes ν_{11} , ν_{23} , and ν_{28} may act as accepting modes to which the electronic energy in the $T_1 \rightarrow S_0$ transition is initially transferred. However, they are only weakly accepting due to smallness of structural change in the excited state. The situation may be compared with thiocyclopentanone which also is planar in the T_1 state and phosphoresces with high quantum yield [2]. It has to be mentioned, however, that fluorescence is observed for this system in the gas phase, too.

4.1.5 Phosphorescence and singlet-triplet absorption

Probabilities and rates of spin-forbidden radiative transitions were obtained from the spin-free electric dipole operator matrix elements and the eigenvectors of the spin-dependent Hamiltonian in quasi-degenerate perturbation theory. Phosphorescence rates ($k_{p,\xi}$) and lifetimes ($\tau_{p,\xi}$) for individual sublevels of the lowest triplet state are given by the usual expression for spontaneous emission, applied to the spin-orbit coupled system:

$$k_{p,\xi} = \frac{1}{\tau_{p,\xi}} = \frac{4e^2}{3c^3\hbar^4} (E_{T_1} - E_{S_0})^3 |\mu_{el}(T_{1,\xi} \rightarrow S_0)|^2 .$$

Here, spin-orbit perturbed states are labelled by letters S, T in contrast to S , T for the Russel-Saunders coupled states (see Table 9 for more details). If there

Table 9. Vertical excitation energies [cm^{-1}] and transition dipole moments [D] for the lowest SO coupled triplet states at the T_1 state equilibrium geometry. States are labeled as $T_{i,\xi}$ where T_i denotes the corresponding pure triplet state and $\xi (=x, y, z)$ the dominant Cartesian spin component. The (main) polarization direction of the transition dipole moment is given in parentheses. Radiative lifetimes $\tau_{p,\xi}$ [ms] for the T_1 state sublevels.

(QDPT, 32 states)			(QDPT, 64 states)		
ΔE_{vert}	$\mu_{el}(T_{i,\xi} \rightarrow S_0)$	$\tau_{p,\xi}$	ΔE_{vert}	$\mu_{el}(T_{i,\xi} \rightarrow S_0)$	$\tau_{p,\xi}$
$T_{1,x}$	18 831.7	2.2×10^{-4} (z)	9670	18 805.6	3.0×10^{-4} (z)
$T_{1,z}$	18 833.5	4.1×10^{-2} (y)	0.28	18 807.5	4.8×10^{-2} (y)
$T_{1,y}$	18 834.5	1.8×10^{-2} (z)	1.45	18 808.6	1.8×10^{-2} (z)
$T_{2,x}$	20 260.3	3.9×10^{-3} (x)		20 231.8	4.5×10^{-3} (x)
$T_{2,z}$	20 261.2	7.8×10^{-3} (z)		20 232.3	6.3×10^{-3} (z)
$T_{2,y}$	20 293.5	1.2×10^{-1} (y)		20 263.8	1.2×10^{-1} (y)
$T_{3,y}$	21 037.4	8.3×10^{-3} (z)		21 025.0	8.6×10^{-3} (z)
$T_{3,x}$	21 107.9	1.0×10^{-3} (z)		21 094.9	8.0×10^{-4} (z)
$T_{3,z}$	21 112.9	1.0×10^{-2} (x)		21 100.6	1.1×10^{-2} (x)

is no pronounced fine-structure splitting and we are not concerned with very low temperatures, the triplet sublevels will be almost equally populated in thermal equilibrium. Under these circumstances, one can only observe the average of the individual phosphorescence rates which is termed the high-temperature limit of the phosphorescence rate $\bar{k}_{p,\text{high}}$:

$$\bar{k}_{p,\text{high}} = \frac{1}{3} (k_{p,x} + k_{p,y} + k_{p,z}) .$$

As already mentioned above, the chromophore exhibits almost C_{2v} symmetry in the T_1 state. Therefore, the mechanisms of $S_0 \rightarrow T_1$ absorption as well as $S_0 \leftarrow T_1$ emission can be understood applying C_{2v} symmetry selection rules. A detailed description of the coupling scheme which explains the intensity sources of spin-forbidden radiative transitions in the dithiosuccinimide molecule has been given in Ref. [34].

In summary, the $S_0 \leftarrow T_1$ transition is expected to occur fast from the z and y Cartesian spin states of the T_1 state, whereas the x sublevel merely does not emit:

- z sublevel: The sublevel $T_{1,z}$ interacts with singlet states of B_2 spatial symmetry. The most important of these is the S_3 state due to its large dipole transition moment and relatively small energy separation. The spin-orbit perturbed $T_{1,z}$ state thus exhibits the same polarization direction (y) for electric dipole transitions as the S_3 state. A further possible source of intensity for $T_{1,z}$ may be comprised by admixtures of A_2 symmetric triplet states to the ground state. The spin-orbit coupling in this case involves the z Cartesian spin component of the interacting triplet state of A_2 spatial symmetry. The polarization direction is y , too.

- y sublevel: The $T_{1,y}$ state contains an admixture of the S_0 ground state. Likewise, the $T_{1,y}$ sublevel appears in the spin-orbit perturbed S_0 ground state wave function. As a result, the dipole moment difference of the S_0 and T_1 states weighted by the perturbation coefficient $\langle T_1 | H_{\text{SO}} | S_0 \rangle / (E(T_1) - E(S_0))$ enters the dipole transition matrix element of the $T_{1,y}$ state. The corresponding radiative transition is thus z polarised. Interaction with excited totally symmetric singlet states and higher lying triplet states of B_1 spatial symmetry may also contribute to this z polarised transition.

- x sublevel: The third sublevel of T_1 with x Cartesian spin component can only interact with singlet states of A_2 spatial symmetry. Consequently, the transition $S_0 \rightarrow T_{1,x}$ is dipole forbidden in first-order perturbation theory and there occurs no emission from this state.

Our computed dipole transition probabilities (Table 9) reveal that the dominant polarization direction of the phosphorescence is y and that intensity borrowing from the S_3 ($\pi_2 \rightarrow \pi_3^*$) state is the main source. The same was found experimentally by Meskers *et al.* [3]. Emission from the $T_{1,y}$ state is of minor importance, despite of the large spin-orbit matrix element between T_1 and S_0 . The reason is that the dipole moment difference of T_1 and S_0 is only

moderate and that there are no further excited states of appropriate spatial symmetry (1A_1 , 3B_1) at low energies which owe a considerable oscillator strength. Our theoretical value for the high-temperature phosphorescence rate is $\bar{k}_{p,\text{high}} \approx 1.8 \times 10^3 \text{ s}^{-1}$ ($\tau_{p,\text{high}} \approx 0.5 \text{ ms}$) using a basis of 64 Russel–Saunders coupled states (32 singlets and 32 triplets) for the perturbation calculation. This agrees very well with experiment: Meskers *et al.* report a monoexponential decay of emission with a life time of $0.1 \pm 0.01 \text{ ms}$ in a glassy solvent (EPA) at 77 K and a quantum yield of luminescence of 0.5 ± 0.2 . From these values we deduce a pure radiative life time of approximately 0.2 ms. In view of the large sensitivity of the computed value to errors in energy and dipole transition matrix elements this agreement is quite satisfactory.

Upon looking at Table 9 and the experimental phosphorescence band in [3], one could ask whether the $T_{2,y}$ state contributes to the emission or not. The dipole transition moment of this state is larger than that of the $T_{1,z}$ state by a factor of approximately three. The y Cartesian spin sublevel of the T_2 state also derives its radiative intensity from coupling with the S_3 state. Hence, the polarization direction of emission from $T_{2,y}$ would be y , too. In addition, the computed energy difference between T_1 and T_2 is so small that it matches the separation of two strong maxima in the experimental band. However, it is generally accepted that emission only occurs from the lowest excited states of each multiplicity (Kasha's rule) [35]. The reason is that $S_n \rightsquigarrow S_1$ and $T_n \rightsquigarrow T_1$ radiationless transitions are generally (and in particular in the condensed phase) much faster than emission from higher excited states. Exceptions are quite scarce. The most prominent one is azulene which exhibits $S_0 \leftarrow S_2$ fluorescence which can be explained on the basis of a large $S_2 - S_1$ energy gap [35]. To our knowledge, the only reported case of $S_0 \leftarrow T_2$ emission are dimethylbenzaldehydes in mixed crystals which show an anomalously small energy gap (100 cm^{-1} or less) between $T_1(\pi \rightarrow \pi^*)$ and $T_2(n \rightarrow \pi^*)$, enabling thermal population of T_2 [36]. In the present case, however, this gap between T_1 and T_2 is much larger ($\approx 1400 \text{ cm}^{-1}$). Thermal population will thus not suffice for observable emission from T_2 at 77 K. Further, there is a sizable direct and indirect (via T_3) spin-orbit coupling between T_1 and T_2 (see Table 8). As there is no evidence for the $T_2 \rightsquigarrow T_1$ radiationless transition to be inefficient, we assign the whole band to T_1 phosphorescence. The two observed maxima may thus be constituted by the 0–0 origin band and a vibrational progression of the v_{23} or v_{28} totally symmetric vibrations.

In contrast to emission, $S_0 \rightarrow T_{2,y}$ absorption should be observable in experiment. The dipole transition moment is comparable to that computed for the $S_0 \rightarrow S_1$ transition (0.14 D). Indeed, in the experimental phosphorescence excitation spectrum the intensity ratio of the bands, assigned to the $S_0 \rightarrow S_1$ and $S_0 \rightarrow S_2$ transitions, changes with respect to the absorption spectrum [3]. The bands that were assigned to the $S_0 \rightarrow S_1$ transition by Meskers *et al.* are more intense in the excitation spectrum than the band of the forbidden $S_0 \rightarrow S_2$ transition whereas this ratio is inverted in absorption. The strongest phospho-

rescence excitation band in the region of the $S_0 \rightarrow S_1$ transition, is a γ polarised band (denoted “band 3” in Ref. [3]). Meskers *et al.* explain this band in terms of vibronic coupling of S_1 and S_3 and attribute the change in intensity to an unknown decay channel of S_2 . Our results, however, strongly suggest that this γ polarised band can be assigned to $S_0 \rightarrow T_2$ absorption. The puzzle of intensity change in phosphorescence excitation is thereby easily resolved as already the absorption ends up in a triplet state.

5. Conclusions

In this work, we have investigated the electronic spectrum of dithiosuccinimide and spin-orbit coupling phenomena occurring herein by means of quantum chemical methods. Our results are in very good agreement with recent experimental findings by Meskers *et al.* [3] and, moreover, provide an explanation for some puzzling details of the observed spectra.

Because of the two thiocarbonyl groups present in the molecule, dithiosuccinimide exhibits a dense spectrum of low-lying valence states. The first two excited singlet states (S_1 and S_2) originate from $n \rightarrow \pi^*$ excitations, with 1^1B_1 and 1^1A_2 separated by roughly 0.2 eV. These results corroborate the assignment by Meskers *et al.* [3] who deduced the symmetry characteristics of these states from polarised phosphorescence excitation spectra. As expected for $n \rightarrow \pi^*$ excited states, probabilities for a transition to or from the electronic ground state are small. The two strong absorption bands with maxima at 3.96 and 4.96 eV [3], respectively, are dominated by single excitations from high-lying occupied π orbitals to the lowest unoccupied π^* MO, giving rise to a 1^1B_2 (S_3) and a 1^1A_1 state. Several (dark) singlet states are located energetically between these strongly absorbing singlets. Quite remarkably, one of the intermediate states corresponds to a double excitation from the two highest occupied nonbonding orbitals to two π^* orbitals. We find three triplet states in the energetic neighbourhood of S_1 and S_2 , i.e., two $n \rightarrow \pi^*$ states (T_1 and T_2) as well as a $\pi \rightarrow \pi^*$ triplet excitation (T_3).

The electronic ground state and the low-lying $\pi \rightarrow \pi^*$ excited states exhibit C_{2v} symmetric equilibrium geometries. In the latter, C–S bonds are considerably longer than in the electronic ground state, a geometry relaxation yielding roughly 0.3 eV in energy. In contrast to $\pi \rightarrow \pi^*$ excitations, a C_2 symmetric twisted ring structure results from the first and second $n \rightarrow \pi^*$ excitations. Interestingly, the SC(NH)CS chromophore nearly retains its planarity also in the latter. The adiabatic and vertical excitation energies of the $\pi \rightarrow \pi^*$ states differ by merely 0.1 eV showing that their potential energy hypersurfaces are rather flat and the distortions are small.

We obtain large electronic spin-orbit coupling matrix element between $n \rightarrow \pi^*$ excited states on the one side and the electronic ground state or $\pi \rightarrow \pi^*$ excited states on the other side. The absolute size of T_1 and T_2 spin-

orbit matrix elements depends strongly on the scissoring angle $2\alpha = 180^\circ - 2\varphi$ between the two C=S groups, their ratio being approximately proportional to $\tan(\varphi)$. This finding is easily explained by a simple model that views the n_1 and n_2 nonbonding orbitals as linear combinations of pure sulphur p_y and p_z orbitals.

Phosphorescence from T_1 borrows intensity from two major sources. The z sublevel interacts heavily with the S_3 state which in turn exhibits a very strong dipole-allowed transition to the electronic ground state. The y sublevel is coupled directly by \mathcal{H}_{SO} with the S_0 state. Besides spin-orbit interaction, the coupling strength is determined by the dipole moment difference between T_1 and S_0 . Emission from the x sublevel is insignificant. A sum-over-states perturbation calculation including 64 singlet and triplet states yields a high-temperature phosphorescence lifetime of approximately 0.5 ms for the T_1 state, in qualitative agreement with the experimental total (radiative and nonradiative) lifetime of 0.1 ms and a luminescence quantum yield of 0.5 ± 0.2 from which we deduce an experimental radiative lifetime of approximately 0.2 ms. Because of its large spin-orbit matrix element with the S_3 state, dipole transition matrix elements between S_0 and T_2 are sizable. While emission is quenched efficiently by nonradiative processes, we predict the spin-forbidden transition from S_0 to T_2 to occur with a probability comparable to the spin-allowed $S_0 \rightarrow S_1$ absorption. We assign the y polarised band number 3 in the phosphorescence excitation spectrum [3] to this spin-forbidden transition, thus easily resolving the puzzle of intensity change with respect to the absorption spectrum.

Acknowledgement

Funding by the Deutsche Forschungsgemeinschaft (DFG) through project Ma 1051/5-1 is gratefully acknowledged. M. P. and S. G. wish to thank Dr. Filipp Furche for making his TD-DFT gradient available. Thanks are also due to Dr. Robert Berger for providing the HOTFCHT code.

References

1. A. Maciejewski and R. P. Steer, Chem. Rev. **93** (1993) 67.
2. D. C. Moule and E. C. Lim, J. Phys. Chem. A **106** (2002) 3072.
3. S. C. J. Meskers, T. Poloński, and H. M. Dekkers, J. Phys. Chem. **99** (1995) 1134.
4. M. Ratajczak-Sitarz, A. Katrusiak, and T. Poloński, J. Mol. Struct. **374** (1996) 357.
5. L. Fälth, U. Håkansson, and J. Sandström, J. Mol. Struct. (THEOCHEM) **186** (1989) 239.
6. U. Berg and J. Sandström, Act. Chem. Scand. **20** (1966) 689.
7. S. Grimme and M. Waletzke, J. Chem. Phys. **111** (1999) 5645.
8. A. D. Becke, J. Chem. Phys. **98** (1993) 1372.
9. C. Lee, W. Yang, and R. G. Parr, Phys. Rev. B **37** (1988) 785.

10. R. Ahlrichs, M. Bär, M. Häser, H. Horn, and C. Kölmel, Chem. Phys. Lett. **162** (1989) 165.
11. O. Treutler and R. Ahlrichs, J. Chem. Phys. **102** (1995) 346.
12. O. Vahtras, J. Almlöf, and M. W. Feyereisen, Chem. Phys. Lett. **213** (1993) 514.
13. F. Weigend and M. Häser, Theor. Chem. Acc. **97** (1997) 331.
14. F. Weigend, M. Häser, H. Patzelt, and R. Ahlrichs, Chem. Phys. Lett. **294** (1998) 143.
15. K. Eichkorn, O. Treutler, H. Öhm, M. Häser, and R. Ahlrichs, Chem. Phys. Lett. **240** (1995) 283.
16. S. Grimme and M. Waletzke, Phys. Chem. Chem. Phys. **2** (2000) 2075.
17. F. Furche and R. Ahlrichs, J. Chem. Phys. **117** (2002) 7433.
18. R. Ahlrichs, M. Bär, H.-P. Baron, R. Bauernschmitt, S. Böcker, M. Ehrig, K. Eichkorn, S. Elliott, F. Furche, F. Haase, et al., *Turbomole* (vers. 5.5), Universität Karlsruhe (2002).
19. R. Bauernschmitt and R. Ahlrichs, Chem. Phys. Lett. **256** (1996) 454.
20. M. Kleinschmidt, J. Tatchen, and C. M. Marian, J. Comp. Chem. **23** (2002) 824.
21. R. W. Wetmore and G. A. Segal, Chem. Phys. Lett. **36** (1975) 478.
22. M. Kleinschmidt, manuscript in preparation.
23. B. A. Heß, C. M. Marian, U. Wahlgren, and O. Gropen, Chem. Phys. Lett. **251** (1996) 365.
24. D. Danovich, C. M. Marian, T. Neuheuser, S. D. Peyerimhoff, and S. Shaik, J. Phys. Chem. A **102** (1998) 5923.
25. J. Tatchen and C. M. Marian, Chem. Phys. Lett. **313** (1999) 351.
26. AMFI is an atomic spin-orbit integral program written by B. Schimmelpfennig, University of Stockholm (1996).
27. B. A. Heß, C. M. Marian, and S. D. Peyerimhoff, in *Advanced Series in Physical Chemistry – Vol. 2, Modern Structure Theory, Part I*, ed. by C.-Y. Ng and D. R. Yarkony, World Scientific, 1995, pp. 152–278.
28. R. Berger, C. Fischer, and M. Klessinger, J. Phys. Chem. A **102** (1998) 7157.
29. A. Schäfer, C. Huber, and R. Ahlrichs, J. Chem. Phys. **100** (1994) 5829.
30. A. Klamt and G. Schüürmann, J. Chem. Soc. Perkin Trans. **2** (1993) 799.
31. E. M. Cabaleiro-Lago and J. R. Otero, J. Chem. Phys. **117** (2002) 1621.
32. D. C. Moule, I. R. Burling, H. Liu, and E. C. Lim, J. Chem. Phys. **111** (1999) 5027.
33. M. Klessinger and J. Michl, *Excited states and photochemistry of organic molecules*, VCH Publishers, Inc., Weinheim, Germany, 1995.
34. C. Marian, in *Reviews In Computational Chemistry*, vol. 17, ed. by K. Lipkowitz and D. Boyd, Wiley-VCH, Weinheim, 2001, pp. 99–204.
35. N. J. Turro, *Modern Molecular Photochemistry*, University Science Books, Sausalito, CA, 1991.
36. A. Despres, E. Migirdicyan, and L. Blanco, Chem. Phys. **14** (1976) 229.

4.4 Psoralene

In der Arbeit „Electronic excitation spectra and singlet-triplet coupling in psoraleen and its sulfur and selenium analogs“ („Elektronische Anregungsspektren und Singulett-Triplett-Kopplung in Psoralen und seinen Schwefel- und Selen-Analoga“) [53] wurden vertikale Anregungsspektren sowie erstmals auch Spin-Bahn-Matrixelemente des Psoralens und der Schwefel- und Selen-Analoga veröffentlicht.

Die berechneten Absorptionsspektren stehen in guter Übereinstimmung mit experimentellen Werten und Rechnungen mit zeitabhängiger Dichtefunktionaltheorie (TD-DFT) aus der Literatur. Bezuglich der Abhängigkeit der Energie eines bestimmten Zustands vom Substitutionsmuster mit Heteroatomen stellen die quantenchemischen Rechnungen Informationen über dunkle Zustände zur Verfügung, die experimentell schwer zugänglich sind. Die Energieunterschiede der tiefliegenden angeregten Zustände, die für das Singulett-Triplett ISC von großer Bedeutung sind variieren in den betrachteten Systemen erheblich. Die $n \rightarrow \pi^*$ Zustände werden bei Anwesenheit von Schwefel oder Selen im Pyronring stark abgesenkt. Die Absenkung der $\pi \rightarrow \pi^*$ Zustände ist weniger ausgeprägt. Dies führt dazu, dass in den Rechnungen für PSO(O-S)¹ und PSO(O-Se) die $n \rightarrow \pi^*$ Zustände zum S_1 nahezu entartet sind. Andererseits bleibt die Energie der $n \rightarrow \pi^*$ Zustände bei einer Substitution im Furanring nahezu unbeeinflusst, während der $\pi \rightarrow \pi^*$ Zustand S_1 energetisch leicht abgesenkt wird. Der Energieunterschied zwischen S_1 und den $n \rightarrow \pi^*$ Zuständen ist also im PSO(S-O) und PSO(Se-O) erhöht. Im MO-Bild können diese Befunde mit der starken Lokalisierung der n Orbitale in der Nähe der Cabonylgruppe in Verbindung gebracht werden. Gleichermaßen lässt sich der T_1 Zustand als Diradikal in den 5,6 Positionen des Pyronrings betrachten. Dies erklärt, dass die Energie dieses Zustands in allen betrachteten Psoralenen nahezu konstant ist.

In Verbindung mit den Anregungsenergien erlauben die Spin-Bahn-Matrixelemente, die wichtigsten Populationsmechanismen für Triplettzustände zu umreißen. Für die meisten Systeme gibt es mindestens drei Triplets mit $\pi \rightarrow \pi^*$ Charakter und einen mit $n \rightarrow \pi^*$ Charakter unter S_1 oder nahe entartet dazu. Obgleich die adiabatischen Anregungsenergien noch nicht bekannt sind, kann geschlossen werden, dass diese Zustände an ISC Prozessen beteiligt sind, die vom adiabatisch tiefstliegenden Singulett ausgehen. Letztere können abhängig vom System und wahrscheinlich auch vom Lösungsmittel sowohl $n \rightarrow \pi^*$ als auch $\pi \rightarrow \pi^*$ Charakter haben. Da alle Kopplungsmatrixelemente zwischen Singuletts und $\pi \rightarrow \pi^*$ -Triplets vernachlässigbar klein sind, ist es sehr wahrscheinlich, dass ${}^1(n \rightarrow \pi^*) \sim {}^3(\pi \rightarrow \pi^*)$ oder ${}^1(\pi \rightarrow \pi^*) \sim {}^3(n \rightarrow \pi^*)$ die dominanten Kanäle des ISC in die Triplets sind. Dabei muss jedoch berücksichtigt werden, dass alle $n \rightarrow \pi^*$ angeregten Zustände in polaren Lösungsmitteln eine erhebliche Blauverschiebung erfahren, sodass sie energetisch unter Umständen nicht erreichbar sind. Auf den ersten Blick widersprechen diese Befunde den experimentellen Ergebnissen, nach denen die Triplett-Quantenausbeute mit steigender Polarität des Lösungsmittels ansteigt.

Um diese offenen Fragen zu klären wurden von Jörg Tatchen weitergehende Untersuchungen zu den Geometrien angeregter Zustände, zu Schwingungsfrequenzen und Frack-Condon-Faktoren für strahlungslose Übergänge durchgeführt. [54; 15]

¹Für die Erklärung dieser Bezeichnungen sei auf die Veröffentlichung [53] hingewiesen.

4.4. PSORALENE



Available online at www.sciencedirect.com
SCIENCE @ DIRECT®

Journal of Photochemistry and Photobiology A: Chemistry 167 (2004) 201–212

Journal of
Photochemistry
and
Photobiology
A: Chemistry
www.elsevier.com/locate/jphotochem

Electronic excitation spectra and singlet–triplet coupling in psoralen and its sulfur and selenium analogs

Jörg Tatchen, Martin Kleinschmidt, Christel M. Marian*

Institute of Theoretical and Computational Chemistry, Heinrich-Heine-Universität, Universitätsstr. 1, D-40225 Düsseldorf, Germany

Received 23 April 2004; accepted 25 May 2004

Available online 23 July 2004

Abstract

We have calculated the vertical singlet and triplet excitation spectra and spin-orbit coupling matrix elements for psoralen and its derivatives resulting from the replacement of intracyclic oxygen by sulfur or selenium. Molecular ground state equilibrium geometries have been determined employing Kohn-Sham density functional theory. Electronic excitation energies and oscillatory strengths have been obtained utilizing a combined density functional/multi-reference configuration interaction method. Spin-orbit coupling matrix elements for correlated wavefunctions have been computed applying the efficient, purely non-empirical spin-orbit mean-field approximation.

The theoretical data allows for a detailed assignment of experimental absorption bands [J. Photochem. Photobiol. B: Biol. 35 (1996) 221]. The computed excitation energy of the first $\pi \rightarrow \pi^*$ singlet transition varies from 3.81 (7H-furo [3,2-g] [1] benzopyran-7-one) to 3.12 eV (7H-selenolo [3,2-g] [1] benzosenolopyran-7-one). The energy of the lowest triplet $\pi \rightarrow \pi^*$ state T_1 is remarkably constant in all cases (2.95–2.73 eV). The energies of the dark $n \rightarrow \pi^*$ states are found to be lowered considerably (up to ≈ 0.80 eV) upon replacing intracyclic oxygen at the pyrone side by sulfur or selenium, but much less upon hetero-atom substitution solely at the furan side. For all the heteropsoralens, additional low-lying $\pi \rightarrow \sigma^*$ states have been found that are important for photochemical ring opening reactions.

The spin-orbit coupling between the T_1 state and the ground state S_0 amounts to less than 2 cm^{-1} for all cases. Between $n \rightarrow \pi^*$ and $\pi \rightarrow \pi^*$ states appreciable spin-orbit coupling matrix elements are observed which indicate a probable channel for singlet-triplet radiationless transitions. Their size varies from several ten wavenumbers for those psoralens which have oxygen or sulfur in the pyrone ring to several hundred wavenumbers in the case when selenium is present in the pyrone ring.

© 2003 Elsevier B.V. All rights reserved.

Keywords: Spin-orbit coupling; Multi-reference configuration interaction; Excited states; Psoralen; Photodynamic therapy

1. Introduction

Psoralens (also called furocoumarins) are a class of photobiologically active substances which are of pharmaceutical use in many respects [1,2]. In a PUVA therapy (psoralen plus ultraviolet A or UV-A radiation) of skin diseases, oral or topical application of psoralens is combined with the exposure of the diseased skin to UV-A radiation [3]. This treatment is effective against, e.g., psoriasis and vitiligo [3]. In photopheresis, peripheral blood is the target of the photobiological action of psoralens in order to treat cutaneous T-cell lymphoma and other autoimmune disorders [3]. As some psoralens show antibacterial activity and also antiviral activity (among others against Herpes virus

and HIV type-1 virus), another possible field of application for psoralens is the purification of blood and blood products [4].

During the last 40 years, much effort has been spent in photobiological, photochemical, and photophysical research on clarifying the underlying mechanisms of the desired phototherapeutic effects and undesired side effects of psoralens (for reviews see [1,2,5]). It has been found that these heterocyclic carbonyl compounds can undergo photocycloadditions to biomolecules such as DNA and RNA or unsaturated fatty acids [3]. In the case of DNA, the psoralen is assumed to be intercalated between the two DNA strands first [6]. After photoexcitation, it may form photocycloadducts to pyrimidine bases (most effectively to thymidine) involving the C=C double bond of the furan ring (2, 3-position, see Fig. 1), the C=C double bond of the pyrone ring (5, 6-position, see Fig. 1), or both [3,6]. In the latter case, the resulting cross-links between the two DNA

* Corresponding author. Tel.: +49 211 81 13209;
fax: +49 211 81 13466.
E-mail address: christel.marian@uni-duesseldorf.de (C.M. Marian).

4. ANWENDUNGEN

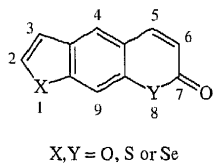


Fig. 1. Chemical structure of psoralens: in the parent compound: $X = Y = O$. In synthetic thio- and seleno-psoralens one or both of the intracyclic oxygen atoms is replaced by sulfur or selenium. We use the numbering for the parent compound throughout.

strands will inhibit the excessive mitosis of cells, causing a reduction of the proliferation which is characteristic, e.g., of psoriasis. This DNA reaction is also thought to be the active principle behind the antiviral and antibacterial activity of psoralens [5]. However, photoexcited psoralens may also take part in electron transfer reactions to molecular oxygen leading to the formation of superoxide ($O_2^{\cdot-}$) or hydroxyl (OH^{\cdot}) radicals (oxygen-dependent type I reactions) [7,8]. Additionally, they may produce singlet molecular oxygen $O_2 (^1\Delta_g)$ via excitation energy transfer (oxygen-dependent type II reaction) [5,7,8].

As some of the possible photoreactions (e.g. the oxygen-dependent type I and II reactions) of psoralens may cause severe side effects, many synthetic psoralens have been developed in order to minimize these effects and optimize the phototherapeutic use [1,9,10]. Among them, sulfur and selenium analogs of psoralen (Fig. 1 and Table 1) show enhanced light absorption in the UV-A region (400–320 nm, often a wavelength of 365 nm is used in practice) compared to the parent psoralen [11]. For some of these compounds (especially 7H-thiopyrano [3,2-f] [1] benzofuran-7-one), a high DNA-photobinding ability has been observed [12]. As nucleic acid bases are known to quench psoralen triplet states effectively [13], it seems likely that the reaction of psoralens with DNA proceeds via a triplet excited state. Further evidence is given by the excited state lifetimes which are much longer for triplet states than for singlet ones [4]. Concerning the heteropsoralens (HPS), an enhancement of the singlet-triplet intersystem crossing (ISC) rates and triplet formation quantum yields due to the heavy atom effect is expected to be at least in

part responsible for their increased reactivity. However, a definite answer to the question about the reacting state in the psoralen photocycloaddition to DNA is still missing (see, for example, Ref. [5]). For a similar discussion on the photodimerization of coumarin see Ref. [14].

Early spectroscopic studies of Song and coworkers on the parent psoralen ($X = Y = O$, Fig. 1) revealed a T_1 state of $\pi \rightarrow \pi^*$ type phosphorescing at $\lambda^P = 456$ nm with a life time of $\tau_P \approx 0.66$ s in ethanol at 77 K [15,16]. Fluorescence is observable in ethanol, too. However, the quantum yield of fluorescence ($\Phi_F \approx 0.019$) is much less than the one of phosphorescence ($\Phi_P \approx 0.13$) and the fluorescence band is very broad and shape-less. Mantulin and Song suspected an excited singlet state of $n \rightarrow \pi^*$ type near the lowest excited singlet state of $\pi \rightarrow \pi^*$ type to be involved in the fast radiationless depletion of the singlet $\pi \rightarrow \pi^*$ state to the electronic ground state S_0 [15]. Further studies on various psoralen derivatives, e.g. on 8-methoxysoralen by Lim and coworkers [17], showed a strong dependence of the fluorescence quantum yield on the solvent and on the temperature. The same applies to the triplet formation quantum yield. More precisely, both the quantum yields of fluorescence and triplet formation were found to decrease with decreasing solvent polarity or proticity and with increasing temperature. Lim and coworkers introduced the term “proximity effect” and suggested vibronic coupling of the $S_1(\pi \rightarrow \pi^*)$ state with a nearby $S_2(n \rightarrow \pi^*)$ state via an out-of-plane bending mode to be responsible for this behavior [17,18].

The absorption, fluorescence emission, and triplet-triplet absorption spectra for five HPS in various solvents such as benzene, ethanol, and trifluoroethanol (TFE) were investigated by Aloisi et al. [4]. In addition, they studied the quantum yield of singlet-oxygen production after photoexcitation in aerated solution. From these data, rate constants and quantum yields for various radiative and non-radiative transitions were derived. Collet et al. studied the photosensitized generation of hydroxyl radicals in water by ESR spin trapping techniques [11]. They also presented absorption spectra for all heteropsoralens in water, ethanol and mixtures of both [11]. In addition, the efficiency of photobinding to DNA for various heteropsoralens was evaluated by Collet et al. [12].

Table 1
Nomenclature of sulfur and selenium analogs of psoralen

X	Y	Heteroanalogs	Abbreviation ^a
O	O	7H-furo [3,2-g] [1] benzopyran-7-one	PSO(O-O)
O	S	7H-thiopyrano [3,2-f] [1] benzofuran-7-one	PSO(O-S)
O	Se	7H-selenopyrano [3,2-f] [1] benzofuran-7-one	PSO(O-Se)
S	O	2H-thieno [3,2-g] [1] benzopyran-2-one	PSO(S-O)
Se	O	2H-selenolo [3,2-g] [1] benzopyran-2-one	PSO(Se-O)
S	S	7H-thieno [3,2-g] [1] benzothiopyran-7-one	PSO(S-S)
S	Se	7H-selenopyrano [3,2-f] [1] benzothiophen-7-one	PSO(S-Se)
Se	S	2H-selenolo [3,2-g] [1] benzothiopyran-2-one	PSO(Se-S)
Se	Se	7H-selenolo [3,2-g] [1] benzoselenopyran-7-one	PSO(Se-Se)

^a Taken from Collet et al. [11].

So far, theoretical investigations on psoralen and its derivatives have been carried out solely by semiempirical methods [4] or time-dependent density functional theory (TD-DFT) [8,19]. The purpose of the current work is to elucidate mechanisms and trends in the photophysical properties of HPS utilizing more advanced quantum chemical methods. The questions to be dealt with are:

- (1) What is the effect of the hetero-atom substitution on the vertical electronic excitation spectra and the capability of absorption in the UV-A region?
- (2) Which spin-orbit matrix elements give rise to noticeable ISC from the singlet into the triplet manifold? How does spin-orbit coupling (SOC) between singlet and triplet states change when intracyclic oxygen is replaced by sulfur or selenium?
- (3) Is there a pronounced dependence of electronic excitation energies on the solvent polarity? What are the consequences with respect to intersystem crossing channels which are accessible upon UV-A excitation?

2. Methods and computational details

For the computation of electronic excitation spectra, a quantum chemical method has to be applied which allows for a balanced description of static and dynamic electron correlation and which brings about high computational expense. In order to minimize the latter, we decided to determine the potential energy surface minima of the electronic ground states at the level of density functional theory (DFT). The vertical electronic excitation energies and the dipole (transition) matrix elements were obtained from subsequent single-point calculations applying the combined density functional theory/multi-reference configuration interaction (DFT/MRCI) approach of Grimme and Waletzke [20]. Spin-orbit matrix elements (SOMEs) for the correlated DFT/MRCI wavefunctions were computed using the spin-orbit coupling kit SPOCK which has recently been developed in our laboratory [21].

In Sections 2.1–2.4 below, details of the various computational procedures are given. Unless noted otherwise, C_s symmetry constraints were imposed and TZVP basis sets from the TURBOMOLE library [22] were applied. For the parent psoralen ($X = Y = O$), additional calculations with a second basis set including diffuse functions were carried out in order to determine the energy regime of the lowest Rydberg states. This basis set called TZVP + Ryd consists of the original TZVP basis set and 3s, 3p, and 1d primitive diffuse Gaussians with origin at two dummy centers and exponents of 0.05, 0.02, 0.008 (s and p-Rydberg) and 0.015 (d-Rydberg). The two dummy centers were located inside the pyrone and the furan ring, respectively, and were allowed to adjust during the geometry optimization. The introduction of a third dummy center inside the central benzene ring was not found to change the results noticeably.

2.1. Geometry optimization

For the electronic ground states, geometry optimizations were performed applying the restricted Kohn-Sham DFT algorithm of the TURBOMOLE 5.6 program package [23]. The B3-LYP functional was used [24,25]. Harmonic vibrational frequencies were calculated analytically at the resulting geometries to ensure that they correspond to true minima of the potential energy surface. Utilizing the TZVP+Ryd basis set for the parent psoralen, a numerical grid, usually employed for the cesium atom, was chosen for the quadrature of the exchange correlation potential at the dummy centers.

2.2. Electronic spectra

The DFT/MRCI method of Grimme and Waletzke represents a very efficient and accurate means to obtain spin-free electronic spectra for large organic systems (errors in excitation energy usually less than 0.3 eV) [20]. The principal idea is to include major parts of dynamic electron correlation by density functional theory whereas static correlation effects are taken into account by short MRCI expansions. This MRCI expansion is built up from a one-particle basis of Kohn-Sham orbitals employing the BH-LYP functional [26,27]. Molecular orbitals were generated using the TURBOMOLE 5.6 program package [23]. The MRCI expansion is kept short by extensive configuration selection. For further details concerning the DFT/MRCI method we refer to the original publication of Grimme and Waletzke [20].

We calculated 12 roots for the A' and 8 roots for the A'' irreducible representation of the C_s symmetry group both for the singlet and the triplet multiplicity. Utilizing the TZVP basis set and applying standard selection thresholds, the dimension of the actual MRCI space ranged from approximately 1×10^5 to 7×10^5 configuration state functions (CSFs) per space and spin symmetry depending on the system under consideration. The size of the final reference space was approximately 100–200 CSFs per space and spin symmetry. Upon employing the TZVP + Ryd basis set for the parent psoralen, the dimension of the MRCI space was approximately 1.6×10^6 CSFs for the singlet case and 2.3×10^6 CSFs for the triplet case. The size of the reference space amounted to 100–130 CSFs, here.

2.3. Spin-orbit coupling

SOMEs in the basis of the DFT/MRCI wave-functions were computed using the recently developed SPOCK [21]. Key features of this program are: first, spin-coupling coefficients between CSFs for spin-dependent one-electron operators are determined fast [28]. Secondly, the one-center spin-orbit mean-field Hamiltonian is applied [29]. This non-empirical effective one-electron operator treats the expensive two-electron terms of the full Breit-Pauli Hamiltonian in a Fock-like manner [29]. The one-center approximation where the molecular mean-field is reduced to a sum

4. ANWENDUNGEN

Table 2

Vertical electronic excitation energies ΔE (eV) and oscillatory strengths $f(r)$ for the parent psoralen PSO(O–O) ($X = Y = O$, see Fig. 1) at the optimized equilibrium geometry of the ground state S_0

State	DFT/MRCI [TZVP]				DFT/MRCI [TZVP + Ryd]		TDDFT [19], ΔE (eV)	Experiment, ΔE (eV)
	Dominant excitation(s)	ϵ^2	ΔE (eV)	$f(r)$	ΔE (eV)	$f(r)$		
S_1 $2^1A'$	$\pi_H \rightarrow \pi_L^*$	0.75	3.81	0.168	3.81	0.166	3.77	3.76 ^a , 3.73 ^b , 3.70 ^c
S_2 $1^1A''$	$n_{H-3} \rightarrow \pi_L^*$	0.66	4.24	≈ 0	4.21	≈ 0	4.40	
S_3 $3^1A'$	$\pi_{H-1} \rightarrow \pi_L^*, \pi_H \rightarrow \pi_{L+1}^*$	0.69, 0.12	4.48	0.299	4.48	0.276	4.36	4.19 ^b , 4.35 ^b , 4.51 ^b , 4.19 ^c
S_4 $4^1A'$	$\pi \rightarrow \pi^*$ (mixed)		4.96	0.053	4.91	0.039	4.97	4.73 ^b
S_5 $5^1A'$	$\pi_H \rightarrow \pi_{L+1}^*, \pi_{H-1} \rightarrow \pi_{L+1}^*$	0.55, 0.22	5.26	0.756	5.20	0.775	5.24	5.00 ^b , 5.14 ^b , 5.10 ^c
S_6 $6^1A'$	$\pi_{H-2} \rightarrow \pi_L^*, \pi_{H-1} \rightarrow \pi_{L+2}^*$	0.43, 0.14	5.55	0.004	5.50	0.010	5.56	
S_7 $2^1A''$	–	–	–	–	5.50	0.003	–	
T_1 $1^3A'$	$\pi_{H-1} \rightarrow \pi_L^*, \pi_H \rightarrow \pi_L^*$	0.47, 0.33	2.95					
T_2 $2^3A'$	$\pi \rightarrow \pi^*$ (mixed)		3.28					
T_3 $3^3A'$	$\pi_H \rightarrow \pi_{L+1}^*, \pi_{H-1} \rightarrow \pi_L^*$	0.49, 0.19	3.79					
T_4 $1^3A''$	$n_{H-3} \rightarrow \pi_L^*, n_{H-3} \rightarrow \pi_{L+2}^*$	0.66, 0.12	4.08					
T_5 $4^3A'$	$\pi \rightarrow \pi^*$ (mixed)		4.37					
T_6 $5^3A'$	$\pi_{H-1} \rightarrow \pi_{L+1}^*, \pi_H \rightarrow \pi_{L+3}^*$	0.33, 0.20	4.56					
T_7 $6^3A'$	$\pi \rightarrow \pi^*$ (mixed)		4.61					

^a From absorption in ethanol at 77 K [15].

^b From absorption in cyclohexane [34] (multiple entries correspond to vibrational progressions).

^c From absorption in water–ethanol (volume ratio 95:5) [11].

of atomic contributions brings about considerable additional computational savings. Originally devised for heavy-metal compounds [29], this one-center mean-field approximation proved to cause only minor errors even in the case of light organic molecules [30].

2.4. Solvent effects

For the parent psoralen, spectral shifts due to electrostatic interactions in polar solvents were estimated employing the conductor-like screening model (COSMO) which is implemented in the TURBOMOLE package [31,32]. Of course, hydrogen bonding cannot be taken into account properly this way. A dielectric constant of $\epsilon = 78.54$ corresponding to water at a temperature of 298 K was chosen [33]. Electronic excitation energies are taken from DFT/MRCI calculations in the one-particle basis of COSMO optimized Kohn–Sham orbitals utilizing the TZVP basis set. Because of technical reasons, C_1 symmetry had to be used. 14 roots were computed for both singlet and triplet multiplicity. The geometry of the ground state was reoptimized.

3. Results and discussion

3.1. Vertical electronic excitation spectra and characterization of the low-lying excited states

3.1.1. The parent compound

For the parent psoralen ($X = Y = O$, see Fig. 1), electronic excitation energies from TD-DFT calculations applying the B3-LYP functional have recently been reported by Llano et al. [8] and Nakata et al. [19]. Nevertheless, we discuss the vertical electronic excitation spectrum of the par-

ent psoralen in some detail here, because this will pave the way for a discussion of the spectral changes occurring when sulfur or selenium is substituted for intracyclic oxygen. The vertical singlet and triplet spectra obtained from DFT/MRCI

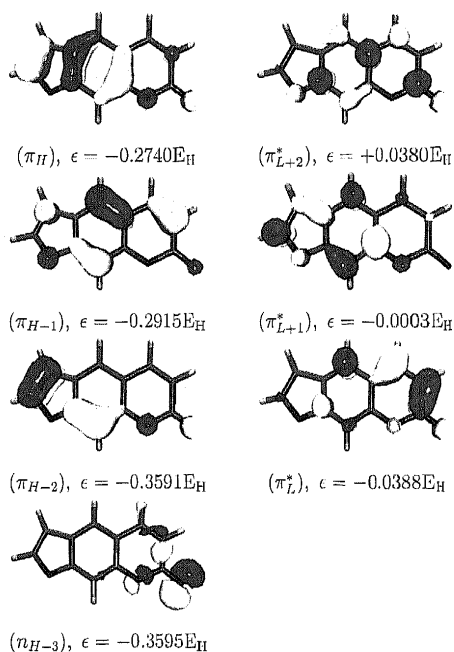


Fig. 2. The highest occupied and lowest unoccupied Kohn–Sham MOs for psoralen PSO(O–O) ($X = Y = O$, see Fig. 1, S_0 geometry, B3-LYP functional, TZVP basis, isoline = 0.050.)

4.4. PSORALENE

computations together with the TD-DFT values from Ref. [19] and some experimental absorption maxima from Refs. [15,34] are shown in Table 2.

The valence molecular orbitals which are involved in the dominant excitations listed in Table 2 are depicted in Fig. 2. With respect to the location of nodal planes, these valence molecular orbitals are in close agreement with those presented by Nakata et al. [19]. The lone-pair orbital (denoted n_{H-3} in Fig. 2) is localized almost exclusively around the carbonyl group of the pyrone ring. The occupied orbital π_{H-1} is completely delocalized and is bonding in the region of the 5–6 double bond in the pyrone ring. The highest occupied molecular orbital (HOMO, denoted π_H in Fig. 2) is mainly located at the furan side and the benzene ring. It is bonding with respect to the 2–3 double bond. The lowest unoccupied molecular orbital (LUMO, denoted π_L^* in Fig. 2) has major contributions in the pyrone ring and is antibonding with respect to the 5–6 double bond. The centroid of the virtual orbital π_{L+1}^* is (like that of the orbital π_H) directed towards the furan ring, but π_{L+1}^* is antibonding with respect to the 2–3 double bond. The 2–3 and the 5–6 double bonds are involved in the [2 + 2]-photocycloaddition reactions of psoralens to DNA bases.

At the equilibrium geometry of the ground state, our calculations predict the lowest-lying singlet excited state S_1 to be the $2^1A'$ state of $\pi \rightarrow \pi^*$ character. The dominant configuration for this state ($\pi_H \rightarrow \pi_L^*$) corresponds to the HOMO–LUMO transition. Our computed excitation energy of 3.81 eV is in excellent agreement with the experimental absorption maximum at 3.73 eV in cyclohexane [34] and the theoretical value of 3.77 eV obtained by Nakata et al. [19]. The S_2 state corresponds to the $n_{H-3} \rightarrow \pi_L^*$ excitation. Energetically, it is located at 4.24 eV, in good accord with the value 4.40 eV given in Ref. [19]. The TD-DFT calculations

of Nakata et al., however, predict it to be the third excited singlet state, slightly above another $\pi \rightarrow \pi^*$ excited state [19]. In our calculations, the latter state appears as S_3 at 4.48 eV. Both the S_1 and S_3 $\pi \rightarrow \pi^*$ excited states show a middle-sized oscillatory strength. Due to the energetic location, the practically important absorption in the UV-A region ranging from 320 to 400 nm may be addressed solely to S_1 . At higher energies of ≈ 5 eV, a strongly absorbing state is found in experiment [34]. We assign the transition between S_0 and $S_5(5^1A')$ at 5.26 eV with an oscillatory strength of 0.756 to this band. The energy of this $\pi \rightarrow \pi^*$ excitation is almost unchanged by the inclusion of diffuse functions in the basis set, confirming that it is a pure valence-type state.

In the triplet manifold, there are three states (T_1 – T_3) of $\pi \rightarrow \pi^*$ character in the vertical spectrum with energies below the first excited singlet state S_1 . As expected, the singlet–triplet splitting is much larger for the $\pi \rightarrow \pi^*$ excited states than for the $n \rightarrow \pi^*$ excited states. The $n_{H-3} \rightarrow \pi_L^*$ excited triplet state $T_4(1^3A'')$ is located above S_1 and only slightly below the corresponding singlet $n \rightarrow \pi^*$ state $S_2(1^1A'')$.

Remarkably, the spatial wave functions of the $\pi \rightarrow \pi^*$ excited triplet states differ considerably from their singlet counterparts. The lowest excited triplet state T_1 is not dominated by the HOMO–LUMO transition $\pi_H \rightarrow \pi_L^*$, in contrast to S_1 . Instead, it shows strong mixing of the configurations $\pi_H \rightarrow \pi_L^*$ and $\pi_{H-1} \rightarrow \pi_L^*$. From the shape of the MOs involved in the low-lying $\pi \rightarrow \pi^*$ transitions, one would assign a sizeable shift of electronic charge towards the pyrone ring and a reduction in bond strength both for the 2–3 and the 5–6 double bonds to the S_1 state. The charge displacement should be much less in the T_1 state for which a strong reduction in bond order in the 5–6 double bond but almost no change in the 2–3 double bond is expected.

Table 3
Vertical electronic excitation energies ΔE (eV) and oscillatory strength $f(r)$ for singlet states in parentheses for mono-substituted heteropsoralens (DFT/MRCI, TZVP basis, equilibrium geometry of the ground state)

State	X = O, Y = S	X = O, Y = Se	X = S, Y = O	X = Se, Y = O ^a
S_1	$2^1A' (\pi \rightarrow \pi^*)$			
	3.45 (0.081)	3.25 (0.059)	3.65 (0.028)	3.58 (0.005)
S_2	$1^1A'' (n \rightarrow \pi^*)$	$1^1A'' (n \rightarrow \pi^*)$	$3^1A' (\pi \rightarrow \pi^*)$	$3^1A' (\pi \rightarrow \pi^*)$
	3.62 (≈ 0)	$3.44 (2 \times 10^{-4})$	4.18 (0.370)	4.03 (0.340)
S_3	$3^1A' (\pi \rightarrow \pi^*)$	$3^1A' (\pi \rightarrow \pi^*)$	$1^1A'' (n \rightarrow \pi^*)$	$1^1A'' (n \rightarrow \pi^*)$
	4.16 (0.107)	4.06 (0.080)	$4.22 (3 \times 10^{-4})$	$4.23 (3 \times 10^{-4})$
S_4	$4^1A' (\pi \rightarrow \pi^*)$	$4^1A' (\pi \rightarrow \pi^*)$	$4^1A' (\pi \rightarrow \pi^*)$	$2^1A'' (\pi \rightarrow \sigma^*)$
	4.52 (0.076)	4.35 (0.067)	4.64 (0.315)	4.32 (≈ 0)
S_5	$5^1A' (\pi \rightarrow \pi^*)$	$5^1A' (\pi \rightarrow \pi^*)$	$5^1A' (\pi \rightarrow \pi^*)$	$4^1A' (\pi \rightarrow \pi^*)$
	4.83 (0.741)	4.65 (0.639)	5.02 (0.645)	4.49 (0.454)
T_1	$1^3A' (\pi \rightarrow \pi^*)$			
	2.85	2.78	2.91	2.87
T_2	$2^3A' (\pi \rightarrow \pi^*)$			
	3.13	3.02	3.16	3.15
T_3	$3^3A' (\pi \rightarrow \pi^*)$	$3^3A'' (n \rightarrow \pi^*)$	$3^3A' (\pi \rightarrow \pi^*)$	$3^3A' (\pi \rightarrow \pi^*)$
	3.45	3.29	3.53	3.38
T_4	$1^3A'' (n \rightarrow \pi^*)$	$3^3A' (\pi \rightarrow \pi^*)$	$1^3A'' (n \rightarrow \pi^*)$	$1^3A'' (\pi \rightarrow \sigma^*)$
	3.47	3.34	4.05	4.04

^a The $n \rightarrow \pi^*$ type state $2^3A''$ corresponds to T_6 and is located at 4.06 eV. The T_5 state at 4.05 eV originates from a $\pi \rightarrow \pi^*$ excitation.

4. ANWENDUNGEN

Table 4

Vertical electronic excitation energies ΔE (eV) and oscillatory strength $f(r)$ for singlet states in parentheses for di-substituted heteropsoralens (DFT/MRCI, TZVP basis, equilibrium geometry of the ground state)

State	X = S, Y = S	X = S, Y = Se	X = Se, Y = S ^a	X = Se, Y = Se ^b
S ₁	2 ¹ A' ($\pi \rightarrow \pi^*$) 3.34 (0.024)	2 ¹ A' ($\pi \rightarrow \pi^*$) 3.15 (0.027)	2 ¹ A' ($\pi \rightarrow \pi^*$) 3.29 (0.013)	2 ¹ A' ($\pi \rightarrow \pi^*$) 3.12 (0.022)
S ₂	1 ¹ A'' (n → π*) 3.58 (≈0)	1 ¹ A'' (n → π*) 3.41 (2 × 10 ⁻⁴)	1 ¹ A'' (n → π*) 3.58 (≈0)	1 ¹ A'' (n → π*) 3.41 (2 × 10 ⁻⁴)
S ₃	3 ¹ A' ($\pi \rightarrow \pi^*$) 3.95 (0.218)	3 ¹ A' ($\pi \rightarrow \pi^*$) 3.85 (0.188)	3 ¹ A' ($\pi \rightarrow \pi^*$) 3.85 (0.229)	3 ¹ A' ($\pi \rightarrow \pi^*$) 3.75 (0.214)
S ₄	4 ¹ A' ($\pi \rightarrow \pi^*$) 4.31 (0.142)	4 ¹ A' ($\pi \rightarrow \pi^*$) 4.19 (0.076)	4 ¹ A' ($\pi \rightarrow \pi^*$) 4.19 (0.234)	4 ¹ A' ($\pi \rightarrow \pi^*$) 4.09 (0.152)
S ₅	5 ¹ A' ($\pi \rightarrow \pi^*$) 4.67 (0.798)	5 ¹ A' ($\pi \rightarrow \pi^*$) 4.53 (0.770)	2 ¹ A'' ($\pi \rightarrow \sigma^*$) 4.21 (≈0)	2 ¹ A' ($\pi \rightarrow \sigma^*$) 4.17 (≈0)
T ₁	1 ³ A' ($\pi \rightarrow \pi^*$) 2.82	1 ³ A' ($\pi \rightarrow \pi^*$) 2.75	1 ³ A' ($\pi \rightarrow \pi^*$) 2.80	1 ³ A' ($\pi \rightarrow \pi^*$) 2.73
T ₂	2 ³ A' ($\pi \rightarrow \pi^*$) 2.97	2 ³ A' ($\pi \rightarrow \pi^*$) 2.85	2 ³ A' ($\pi \rightarrow \pi^*$) 2.95	2 ³ A' ($\pi \rightarrow \pi^*$) 2.83
T ₃	3 ³ A' ($\pi \rightarrow \pi^*$) 3.28	3 ³ A' ($\pi \rightarrow \pi^*$) 3.21	3 ³ A' ($\pi \rightarrow \pi^*$) 3.20	3 ³ A' ($\pi \rightarrow \pi^*$) 3.15
T ₄	1 ³ A'' (n → π*) 3.41	1 ³ A'' (n → π*) 3.25	1 ³ A'' (n → π*) 3.41	1 ³ A'' (n → π*) 3.24

^a 5¹A' ($\pi \rightarrow \pi^*$) at 4.59 eV with an oscillatory strength of 0.738.

^b 5¹A' ($\pi \rightarrow \pi^*$) at 4.48 eV with an oscillatory strength of 0.754.

Actually, the characterization of T₁ as a strongly localized diradical in the 5, 6-positions in the pyrone ring was already postulated by Song and coworkers in the early 1970s [15].

The different localization of electronic charge in the excited states brings about large differences in the excited state dipole moments (see Table 6). The dipole moment of the ground state S₀ amounts to 6.23 D, pointing from the furan ring towards the carbonyl group. Whereas the dipole mo-

ment of S₁ (8.66 D) is considerably increased with respect to the ground state value, this is not the case for the T₁ state (5.77 D). For the n_{H-3} → π_L* excited states S₂ and T₄, a shift of charge towards the furan ring results in a strong reduction of the dipole moment to 1.23 D. For the high-lying π → π* excited state S₅, a relatively moderate increase of the dipole moment compared to S₁ is observed, corresponding to a value of 7.21 D.

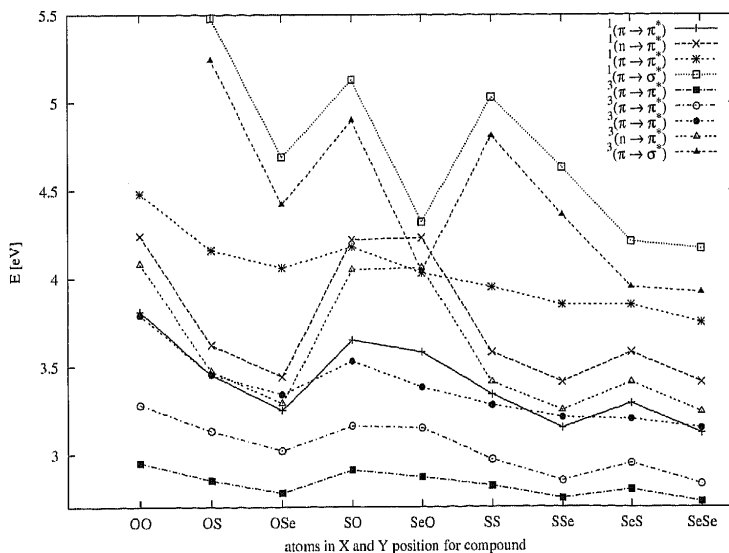


Fig. 3. Vertical excitation energies ΔE (eV) of heteropsoralens at the equilibrium geometry of the ground state S₀. (Abscissa encoding corresponding to Fig. 1. DFT/MRCI, TZVP basis, higher-lying states of $\pi \rightarrow \pi^*$ type are omitted.)

4.4. PSORALENE

3.1.2. Thio- and seleno-psoralens

For the mono- and di-substituted heteropsoralens, the vertical electronic excitation spectra are given in Tables 3 and 4, respectively. In addition, the excitation energies are represented graphically in Fig. 3.

A look at Fig. 3 reveals that the hetero-atom substitution in Y position has a large effect on the excitation energy of the singlet and triplet excited states of $n \rightarrow \pi^*$ character. In contrast, substitution in the X position does not introduce any noticeable change in the excitation energy of these states. For example, in PSO(O-Se) (X = O, Y = Se) the vertical excitation energy of the $n \rightarrow \pi^*$ type state $1^1A''$ is lowered by 0.80 eV compared to the parent psoralen whereas in PSO(Se-O) (X = Se, Y = O) this state is found at the same energy as in the parent psoralen. These findings are obviously related to the facts that the n orbital is strongly localized at the carbonyl group and that the LUMO π_L^* has only minor contributions in the 1-position at the furan side.

In contrast, the vertical excitation energy of the T_1 state, being of $\pi \rightarrow \pi^*$ type in all cases, is remarkably constant. For all the psoralens under study, this behavior supports the view of T_1 as a diradicaloid state which is localized in the 5–6 double bond of the pyrone moiety and is therefore nearly unaffected by hetero-atom substitution. In the S_1 state more prominent changes occur, in particular upon substitution in the six-membered pyrone ring. This state is appreciably lowered in excitation energy upon hetero-atom substitution (up to 0.69 eV for X = Y = Se). The different behaviors of S_1 and T_1 may be taken as an indication that, similar to the situation for the parent psoralen, the electronic structure of the

S_1 state is more ionic than that of the T_1 state for all these psoralens.

In Table 5, data of the experimental absorption spectra for all HPS in a water–ethanol mixture are given together with a tentative assignment of the bands to our computed electronic transitions. The experimental data are taken from the work of Collet et al. [11]. Our calculated excitation energies are in very good agreement with the experimental values. A maximum deviation of 0.31 eV is recognized in the case of the $S_0 \rightarrow S_3$ transition for PSO(O-S). For the parent psoralen and its analogs which are hetero-substituted at the pyrone side only, we assign the lowest $\pi \rightarrow \pi^*$ singlet states with moderate oscillatory strengths to long-wavelength shoulders given by Collet et al. For all psoralens which contain sulfur or selenium inside the five-membered ring, however, the lowest-lying singlet $\pi \rightarrow \pi^*$ states show very low oscillatory strengths (<0.03). For these compounds, we suggest the first pronounced band to result from an excitation of the second $\pi \rightarrow \pi^*$ excited state, whereas the lowest-lying $\pi \rightarrow \pi^*$ states may be associated to the broad long-wavelength tails appearing in the experimental spectra. Concerning practical application in PUVA, the marginal intensity of the $S_0 \rightarrow S_1$ transition has not necessarily to be a major drawback. Sufficient absorption in the UV-A region may be provided by the second $\pi \rightarrow \pi^*$ excited singlet states which are lowered in energy upon disubstitution down to 3.75–3.95 eV according to our calculations (Tables 3 and 4).

Quite remarkably, in the vertical spectra of all hetero-substituted psoralens, we find additional states of A'' symmetry in the energy regime below 5.5 eV that do not result

Table 5

Wavelengths λ_{\max} of experimental absorption maxima and corresponding extinction coefficients ϵ in water–ethanol (volume ratio 95:5) taken from Collet et al. [11] and assignment to our calculated gas phase transitions^a

X	Y	λ_{\max} (nm)	ΔE_{obs} (eV)	ϵ ($\text{dm}^3 \text{mol}^{-1} \text{cm}^{-1}$)	Assignment	ΔE_{calc} (eV)	$f(r)$
O	O	335 ^b	(3.70)	7600	$S_0 \rightarrow S_1$	3.81	0.168
		296	(4.19)	13900	$S_0 \rightarrow S_3$	4.48	0.299
		(243)	(5.10)		$S_0 \rightarrow S_5$	5.26	0.756
O	S	365 ^b	(3.40)	3300	$S_0 \rightarrow S_1$	3.45	0.081
		322	(3.85)	9700	$S_0 \rightarrow S_3$	4.16	0.107
		(259)	(4.79)		$S_0 \rightarrow S_5$	4.83	0.741
O	Se	375 ^b	(3.31)	2700	$S_0 \rightarrow S_1$	3.25	0.059
		323	(3.84)	9100	$S_0 \rightarrow S_3$	4.06	0.080
		(261)	(4.75)		$S_0 \rightarrow S_5$	4.65	0.639
S	O	316	(3.92)	13500	$S_0 \rightarrow S_2$	4.18	0.370
		(272)	(4.56)		$S_0 \rightarrow S_4$	4.64	0.315
S	S	336	(3.69)	10600	$S_0 \rightarrow S_3$	3.95	0.218
		(296)	(4.19)		$S_0 \rightarrow S_4$	4.31	0.142
S	Se	337	(3.68)	12000	$S_0 \rightarrow S_3$	3.85	0.188
		(295)	(4.20)		$S_0 \rightarrow S_4$	4.19	0.076
Se	O	323	(3.84)	13600	$S_0 \rightarrow S_2$	4.03	0.340
		(280)	(4.43)		$S_0 \rightarrow S_5$	4.49	0.454
Se	S	342	(3.63)	10500	$S_0 \rightarrow S_3$	3.85	0.229
		(298)	(4.16)		$S_0 \rightarrow S_4$	4.19	0.234
Se	Se	343	(3.62)	9900	$S_0 \rightarrow S_3$	3.75	0.214
		(301)	(4.12)		$S_0 \rightarrow S_4$	4.09	0.152

^a In parentheses, we give the corresponding excitation energies ΔE_{obs} and some additional approximate values for absorption maxima beyond the UV-A region which we obtained from the plotted spectra published by Collet et al.

^b Shoulder.

4. ANWENDUNGEN

Table 6
Dipole moments μ [D] of ground and excited states for mono-substituted heteropsoralens (DFT/MRCI, TZVP basis, equilibrium geometry of the ground state)

State	Dipole moments (μ)									
	X = O, Y = O	X = O, Y = S	X = O, Y = Se	X = S, Y = O	X = Se, Y = O ^a					
S ₀	X ¹ A'	6.23	X ¹ A'	6.11	X ¹ A'	5.82	X ¹ A'	5.90	X ¹ A'	5.80
S ₁	2 ¹ A'	8.66	2 ¹ A'	7.85	2 ¹ A'	7.08	2 ¹ A'	9.56	2 ¹ A'	10.44
S ₂	1 ¹ A''	1.23	1 ¹ A''	2.12	1 ¹ A''	2.15	3 ¹ A'	10.78	3 ¹ A'	10.98
S ₃	3 ¹ A'	9.92	3 ¹ A'	8.64	3 ¹ A'	8.08	1 ¹ A''	1.22	1 ¹ A''	1.16
S ₄	4 ¹ A'	6.77	4 ¹ A'	5.45	4 ¹ A'	5.60	4 ¹ A'	6.30	2 ¹ A'	6.37
S ₅	5 ¹ A'	7.21	5 ¹ A'	5.60	5 ¹ A'	4.26	5 ¹ A'	5.21	4 ¹ A'	6.60
T ₁	1 ³ A'	5.77	1 ³ A'	5.97	1 ³ A'	6.02	1 ³ A'	5.81	1 ³ A'	6.04
T ₂	2 ³ A'	7.45	2 ³ A'	7.24	2 ³ A'	6.85	2 ³ A'	8.03	2 ³ A'	8.15
T ₃	3 ³ A'	7.88	3 ³ A'	6.57	3 ³ A''	2.01	3 ³ A'	7.11	3 ³ A'	7.15
T ₄	1 ³ A''	1.23	1 ³ A''	1.97	3 ³ A'	5.29	1 ³ A''	1.30	1 ³ A''	6.22

^a Here, the states 1³A'' and 2¹A'' are of $\pi \rightarrow \sigma^*$ type. 2³A'' (not shown) is of n $\rightarrow \pi^*$ type.

from n $\rightarrow \pi^*$ excitations. These states correspond to single excitations from π -type MOs into virtual MOs of A' symmetry which we denote by σ^* in order to emphasize that they are valence like and not Rydberg like. The singlet-triplet splitting for these states is small (around 0.2–0.3 eV). The occurrence of states of this type at low excitation energies can be related to the questions of photostability and photo-reactivity of the psoralens. The lowest excitation energies (4.17 eV for the singlet and 3.92 for the triplet) of n $\rightarrow \sigma^*$ excited states are obtained for PSO(Se–Se). For PSO(Se–O), our calculations predict the lowest excited triplet state of A'' symmetry to be of $\pi \rightarrow \sigma^*$ type with an excitation energy of 4.04 eV below the nearly degenerate 2³A'' state of n $\rightarrow \pi^*$ type at 4.06 eV. In the case of PSO(O–Se), however, the lowest excited triplet state of n $\rightarrow \sigma^*$ type is located considerably higher at 4.42 eV. Thus, psoralens which contain selenium in the furan ring are expected to be least photostable in accord with chemical intuition. In the case of the parent psoralen, the lowest singlet state corresponding to an excitation from a π -type orbital into an orbital of A' symmetry (2¹A' at 5.50 eV employing the TZVP + Ryd basis set) is of s-Rydberg type at the ground state equilibrium geometry.

3.2. Solvent effects

Excitation energies of the parent compound in aqueous solution as mimicked by the COSMO solvation model are displayed in Table 8. The most pronounced changes compared to the vacuum values are observed for the n $\rightarrow \pi^*$ states. They are blue-shifted by 0.48 eV. For the $\pi \rightarrow \pi^*$ excited singlet state S₃, a red shift of 0.11 eV is obtained. Comparing the experimental absorption maxima in cyclohexane (median of vibrational progression at 4.35 eV, [34]) and water–ethanol mixtures (band maximum at 4.19 eV, [11]), an experimental estimate of 0.16 eV may be extracted for the bathochromic shift of the S₀ \rightarrow S₃ transition. The effect of solvation on the energy of the other $\pi \rightarrow \pi^*$ states is almost negligible within this model. In a simplified picture, the energetic stabilization or destabilization of the ground and excited states in polar solvents is connected to their dipole moments and the extent of polarization they induce in the surrounding solvent. Compared to the electronic ground state, the n $\rightarrow \pi^*$ states show dramatically reduced dipole moments. The dipole moment of the $\pi \rightarrow \pi^*$ state S₃ is noticeably increased, explaining the

Table 7
Dipole moments μ [D] of ground and excited states for di-substituted heteropsoralens (DFT/MRCI, TZVP basis, equilibrium geometry of the ground state)

State	Dipole moments (μ)							
	X = S, Y = S	X = S, Y = Se	X = Se, Y = S ^a	X = Se, Y = Se ^b				
S ₀	X ¹ A'	5.78	X ¹ A'	5.51	X ¹ A'	5.72	X ¹ A'	5.45
S ₁	2 ¹ A'	8.31	2 ¹ A'	7.28	2 ¹ A'	8.92	2 ¹ A'	7.73
S ₂	1 ¹ A''	1.64	1 ¹ A''	1.62	1 ¹ A''	1.49	1 ¹ A''	1.54
S ₃	3 ¹ A'	10.31	3 ¹ A'	9.96	3 ¹ A'	11.05	3 ¹ A'	10.91
S ₄	4 ¹ A'	5.36	4 ¹ A'	5.25	4 ¹ A'	5.96	4 ¹ A'	5.51
S ₅	5 ¹ A'	4.10	5 ¹ A'	2.62	2 ¹ A''	5.44	2 ¹ A''	4.93
T ₁	1 ³ A'	5.57	1 ³ A'	5.39	1 ³ A'	5.62	1 ³ A'	5.34
T ₂	2 ³ A'	8.49	2 ³ A'	7.76	2 ³ A'	9.35	2 ³ A'	8.54
T ₃	3 ³ A'	5.87	3 ³ A'	4.88	3 ³ A'	5.65	3 ³ A'	4.83
T ₄	1 ³ A''	1.55	1 ³ A''	1.52	1 ³ A''	1.41	1 ³ A''	1.45

^a Dipole moment of S₆ (5¹A'): 3.43 D.

^b Dipole moment of S₆ (5¹A'): 2.43 D.

4.4. PSORALENE

Table 8

Simulated electronic spectrum for psoralen PSO(O–O) assuming a solvent polarity corresponding to water ($\epsilon = 78.54$) using COSMO: vertical excitation energies ΔE (eV) and oscillatory strengths $f(r)$ (DFT/MRCI, TZVP basis, equilibrium geometry of the ground state reoptimized with COSMO)

State	Symmetry	Type	ΔE	$f(r)$
S_0	X^1A'			
S_1	$2^1A'$	$\pi \rightarrow \pi^*$	3.80	0.140
S_2	$3^1A'$	$\pi \rightarrow \pi^*$	4.37	0.381
S_3	$1^1A''$	$n \rightarrow \pi^*$	4.72	2×10^{-4}
S_4	$4^1A'$	$\pi \rightarrow \pi^*$	4.96	0.055
S_5	$5^1A'$	$\pi \rightarrow \pi^*$	5.30	0.636
S_6	$6^1A'$	$\pi \rightarrow \pi^*$	5.57	0.016
S_7	$7^1A'$	$\pi \rightarrow \pi^*$	5.71	0.083
T_1	$1^3A'$	$\pi \rightarrow \pi^*$	3.00	
T_2	$2^3A'$	$\pi \rightarrow \pi^*$	3.28	
T_3	$3^3A'$	$\pi \rightarrow \pi^*$	3.79	
T_4	$4^3A'$	$\pi \rightarrow \pi^*$	4.39	
T_5	$1^3A''$	$n \rightarrow \pi^*$	4.56	
T_6	$5^3A'$	$\pi \rightarrow \pi^*$	4.59	
T_7	$6^3A'$	$\pi \rightarrow \pi^*$	4.68	
T_8	$7^3A'$	$\pi \rightarrow \pi^*$	5.31	
T_9	$8^3A'$	$\pi \rightarrow \pi^*$	5.66	

calculated red-shift in polar solvents. The absence of any noticeable bathochromic shift for the other $\pi \rightarrow \pi^*$ excited states in our calculation is consistent with their moderately changed dipole moments compared to the ground state.

The dipole moments for the ground and low-lying excited states of all the HPS are shown in Tables 6 and 7. They are comparable to the corresponding ones for the parent psoralen. In a first approximation, we thus expect the solvent effects for these compounds to be very similar to the above findings. Remarkably, the dipole moments of the $\pi \rightarrow \sigma^*$ states ($2^1A''$ and $1^3A''$ for PSO(Se–O)), are somewhat larger than the ground state value.

3.3. Spin-orbit coupling

For the psoralens under investigation, SOMEs which were computed at the ground state equilibrium geometries are listed in Tables 9 and 10. We restrict our presentation to matrix elements between low-lying singlet and triplet states which may thus be important for intersystem crossing processes following photoexcitation in the UV-A region. For showing up trends, the matrix elements are also depicted in Fig. 4.

For all psoralens under investigation, the tabulated SOMEs between a triplet and a singlet $\pi \rightarrow \pi^*$ excited state as well as SOMEs between a triplet $\pi \rightarrow \pi^*$ state and the ground state do not exceed $1-2 \text{ cm}^{-1}$ and are often much less. On the other hand, the singlet-triplet coupling between a state of A' symmetry and a state of A'' symmetry typically is in the order of several tens per centimeter to several hundreds per centimeter. This applies to $n \rightarrow \pi^*/\pi \rightarrow \pi^*$ couplings, to those ones between $n \rightarrow \pi^*$ triplet states and the ground state S_0 , and also to couplings between $\pi \rightarrow \sigma^*$ excited states and states of A' symmetry. The observed proportions of $n \rightarrow \pi^*/\pi \rightarrow \pi^*$, $\pi \rightarrow \pi^*/\pi \rightarrow \pi^*$, and $n \rightarrow \pi^*/n \rightarrow \pi^*$ couplings are widespread in organic photophysics and are known as El-Sayed's rules [35].

Large changes in SOMEs are expected upon hetero-atom substitution because the atomic SOC constants increase strongly with the nuclear charge [36]. It becomes immediately evident from a look at Fig. 4 that the substitution of selenium for an intracyclic oxygen atom of the parent psoralen can cause an enormous increase of the SOMEs, indeed. Replacement of oxygen by sulfur causes less dramatic effects on the SOMEs and their order of magnitude is roughly the same as for the parent psoralen. More precisely, the extent of change in the singlet-triplet coupling which is induced by selenium substitution depends on the pair of states under consideration and the site of substitution (furan or pyrone moiety). Selenium substitution in the 8-position

Table 9

Spin-orbit matrix elements (absolute values) [cm^{-1}] of the lowest singlet and triplet states for the parent psoralen and mono-substituted heteropsoralens (DFT/MRCI, TZVP basis, equilibrium geometry of the ground state. The component of the spin-orbit Hamiltonian is indicated in parentheses.)

	$X = O, Y = O$	$X = O, Y = S$	$X = O, Y = Se$	$X = S, Y = O$	$X = Se, Y = O^a$
$(1^3A' H_{SO} X^1A')$	$5 \times 10^{-2} (z)$	$4 \times 10^{-2} (z)$	1.3 (z)	$4 \times 10^{-2} (z)$	0.4 (z)
$(1^3A' H_{SO} 2^1A')$	$7 \times 10^{-3} (z)$	$4 \times 10^{-2} (z)$	0.2 (z)	$1 \times 10^{-2} (z)$	0.3 (z)
$(2^3A' H_{SO} 2^1A')$	$5 \times 10^{-3} (z)$	$8 \times 10^{-2} (z)$	0.3 (z)	$2 \times 10^{-2} (z)$	0.2 (z)
$(3^3A' H_{SO} 2^1A')$	$5 \times 10^{-3} (z)$	$2 \times 10^{-2} (z)$	0.4 (z)	$4 \times 10^{-2} (z)$	0.3 (z)
$(1^3A'' H_{SO} X^1A')$	41.5 (x)/27.9 (y)	70.5 (x)/34.6 (y)	209.5 (x)/92.2 (y)	39.6 (x)/29.6 (y)	282.1 (x)/565.3 (y)
$(1^3A'' H_{SO} 2^1A')$	9.8 (x)/2.9 (y)	24.1 (x)/26.2 (y)	277.1 (x)/171.7 (y)	6.2 (x)/0.4 (y)	47.9 (x)/106.7 (y)
$(1^3A'' H_{SO} 3^1A')$	10.8 (x)/6.7 (y)	9.6 (x)/2.6 (y)	2.9 (x)/4.3 (y)	10.5 (x)/9.2 (y)	2.3 (x)/19.9 (y)
$(1^3A'' H_{SO} 1^1A')$	24.7 (x)/13.4 (y)	9.1 (x)/6.4 (y)	168.4 (x)/106.5 (y)	21.3 (x)/14.7 (y)	19.2 (x)/22.8 (y)
$(2^3A'' H_{SO} 1^1A'')$	4.2 (x)/0.3 (y)	25.8 (x)/21.6 (y)	202.9 (x)/113.2 (y)	11.0 (x)/3.6 (y)	11.3 (x)/0.4 (y)
$(3^3A'' H_{SO} 1^1A'')$	0.8 (x)/1.9 (y)	26.1 (x)/19.9 (y)	127.1 (x)/70.5 (y)	0.4 (x)/2.4 (y)	0.5 (x)/8.4 (y)
$(1^3A'' H_{SO} 1^1A'')$	$9 \times 10^{-2} (z)$	0.3 (z)	0.4 (z)	0.1 (z)	0.2 (z)
$(2^3A'' H_{SO} X^1A')$	15.5 (x)/7.2 (y)	27.8 (x)/125.6 (y)	197.7 (x)/621.8 (y)	38.9 (x)/114.3 (y)	41.3 (x)/20.0 (y)

^a Here, the state $1^3A'$ is of $\pi \rightarrow \sigma^*$ type, $2^3A''$ is of $n \rightarrow \pi^*$ type.

4. ANWENDUNGEN

210

J. Tatchen et al. / Journal of Photochemistry and Photobiology A: Chemistry 167 (2004) 201–212

Table 10

Spin-orbit matrix elements (absolute values) [cm^{-1}] of the lowest singlet and triplet states for di-substituted heteropsoralens (DFT/MRCI, TZVP basis, equilibrium geometry of the ground state. The component of the spin-orbit Hamiltonian is indicated in parentheses.)

	X = S, Y = S	X = S, Y = Se	X = Se, Y = S	X = Se, Y = Se
$\langle 1^3\text{A}' \mathcal{H}_{\text{SO}} X^1\text{A}' \rangle$	5×10^{-2} (z)	1.4 (z)	0.4 (z)	0.5 (z)
$\langle 1^3\text{A}' \mathcal{H}_{\text{SO}} 2^1\text{A}' \rangle$	9×10^{-3} (z)	0.2 (z)	0.2 (z)	0.2 (z)
$\langle 2^3\text{A}' \mathcal{H}_{\text{SO}} 2^1\text{A}' \rangle$	8×10^{-2} (z)	0.2 (z)	0.1 (z)	6×10^{-3} (z)
$\langle 3^3\text{A}' \mathcal{H}_{\text{SO}} 2^1\text{A}' \rangle$	3×10^{-2} (z)	0.2 (z)	0.3 (z)	0.5 (z)
$\langle 1^3\text{A}'' \mathcal{H}_{\text{SO}} X^1\text{A}' \rangle$	68.4 (x)/37.4 (y)	202.4 (x)/100.8 (y)	64.3 (x)/41.4 (y)	191.2 (x)/118.8 (y)
$\langle 1^3\text{A}'' \mathcal{H}_{\text{SO}} 2^1\text{A}' \rangle$	23.4 (x)/27.3 (y)	258.3 (x)/178.0 (y)	21.3 (x)/35.1 (y)	234.8 (x)/202.3 (y)
$\langle 1^3\text{A}'' \mathcal{H}_{\text{SO}} 3^1\text{A}' \rangle$	8.0 (x)/3.1 (y)	26.5 (x)/23.8 (y)	7.5 (x)/16.3 (y)	34.7 (x)/22.8 (y)
$\langle 1^3\text{A}'' \mathcal{H}_{\text{SO}} 1^1\text{A}'' \rangle$	14.8 (x)/0.2 (y)	158.5 (x)/110.8 (y)	14.7 (x)/5.6 (y)	138.3 (x)/118.7 (y)
$\langle 2^3\text{A}'' \mathcal{H}_{\text{SO}} 1^1\text{A}'' \rangle$	24.7 (x)/26.9 (y)	202.4 (x)/127.6 (y)	23.6 (x)/37.6 (y)	195.3 (x)/158.3 (y)
$\langle 3^3\text{A}'' \mathcal{H}_{\text{SO}} 1^1\text{A}'' \rangle$	16.7 (x)/13.7 (y)	67.4 (x)/41.3 (y)	11.9 (x)/13.6 (y)	30.4 (x)/23.9 (y)
$\langle 1^3\text{A}'' \mathcal{H}_{\text{SO}} 1^1\text{A}'' \rangle$	0.2 (z)	0.2 (z)	0.1 (z)	0.2 (z)
$\langle 2^3\text{A}'' \mathcal{H}_{\text{SO}} X^1\text{A}' \rangle$	33.5 (x)/86.4 (y)	161.3 (x)/609.8 (y)	269.6 (x)/546.4 (y)	211.3 (x)/453.6 (y)

in the pyrone ring ($X = \text{O}$, $Y = \text{Se}$) strongly increases the SOMEs between the lowest-lying $n \rightarrow \pi^*$ type singlet (triplet) state and $\pi \rightarrow \pi^*$ type triplet (singlet) states in many, but not all of the tabulated cases. For example, the matrix element $\langle 1^3\text{A}''(n \rightarrow \pi^*)|\mathcal{H}_{\text{SO},x}|2^1\text{A}'(\pi \rightarrow \pi^*) \rangle$ amounts to 277.1 cm^{-1} in PSO(O-Se) which corresponds to an increase of almost a factor of 30 compared to the parent psoralen. As the electronic coupling matrix element enters quadratically into the Golden Rule formula for radiationless transition rates, an increase by a factor of 1000 of the $S \rightsquigarrow T$ ISC rate for PSO(O-Se) compared to the parent psoralen seems plausible. The matrix element $\langle 1^3\text{A}''(n \rightarrow \pi^*)|\mathcal{H}_{\text{SO},x}|3^1\text{A}'(\pi \rightarrow \pi^*) \rangle$ is less influenced and shows a lowering down to 2.9 cm^{-1} for PSO(O-Se) from a value of

10.8 cm^{-1} for the parent psoralen. On the contrary, selenium substitution solely in the 1-position at the furan side ($X = \text{Se}$, $Y = \text{O}$) does not bring about any appreciable changes for those tabulated SOMEs which involve the lowest lying singlet ($S_3, 1^1\text{A}''$) or triplet ($T_6, 2^3\text{A}''$) state of $n \rightarrow \pi^*$ type. Instead, for PSO(Se—O) large SOMEs occur between the lowest triplet state of $\pi \rightarrow \sigma^*$ type ($T_4, 1^3\text{A}''$) and some $\pi \rightarrow \pi^*$ excited singlet states. A high matrix element of 565.3 cm^{-1} for $\mathcal{H}_{\text{SO},y}$ is also observed between T_4 and the ground state S_0 .

These findings are intimately related to the $1/r^3$ -dependence of the spin-orbit Hamiltonian: considerable spin-orbit integrals between two MOs will only arise if these MOs are located in the same spatial region. As the mean-field

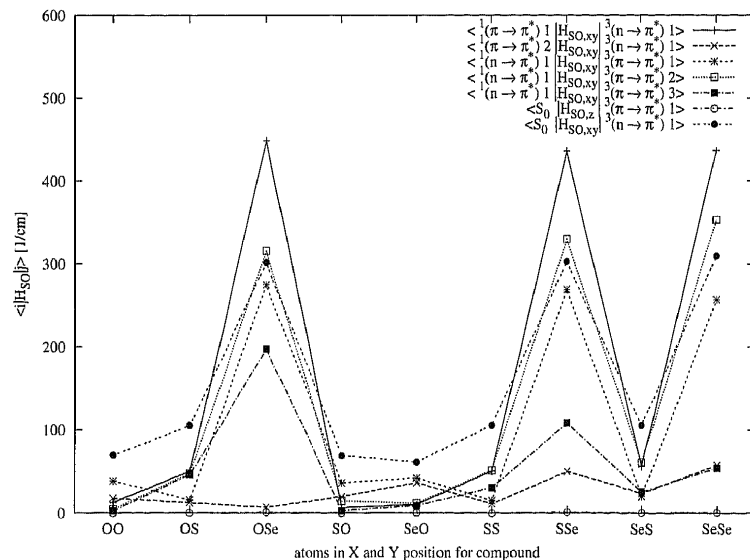


Fig. 4. Absolute values of spin-orbit matrix elements [cm^{-1}]. (Abscissa encoding corresponding to Fig. 1. If there is more than one nonvanishing Cartesian component of the spin-orbit Hamiltonian between to states the sum of their absolute values is depicted.)

4.4. PSORALENE

operator is an (effective) one-electron operator, non-zero matrix elements occur only between configurations that are singly excited with respect to one another.

SOMEs will thus be significantly increased upon selenium substitution only if the above conditions are fulfilled for the main configurations of the states involved. For example, the (highest occupied) n orbital is localized at the carbonyl group for all heteropsoraleins just as the MO n_{H-3} in Fig. 2. If the π orbital involved in the $\pi \rightarrow \pi^*$ excitation shows a noticeable amplitude in this region, the SOME between the lowest $n \rightarrow \pi^*$ excited states and this $\pi \rightarrow \pi^*$ excited state is expected to be very large, e.g. in PSO(O-Se). Similarly, the large SOME $\langle 1^3A''(\pi \rightarrow \sigma^*) | \mathcal{H}_{SO,y} | 1^1A'(S_0) \rangle$ in PSO(Se-O) can be explained by the amplitudes of the π and σ^* MOs at the 1-position in the furan ring.

Assuming that the shape and energetic order of the MOs and the electronic structure of the excited states are comparable for all the psoralens, a pronounced regularity in the size of the SOMEs is predicted. According to Fig. 4, this actually is the case to a large extent. One has to keep in mind, however, that these SOMEs are calculated at the respective ground state equilibrium geometry. Hetero-atom substitution may result in major changes in the adiabatic order of states. Hence, a similar regularity with respect to the time constants of spin-forbidden processes is by no means certain.

As discussed above, the $n \rightarrow \pi^*$ states are thought to be involved in the singlet-triplet ISC because of their appreciable SOMEs. At first sight, one might conclude that the ISC rate and as a consequence the triplet formation quantum yield will drop down sharply when the solvent polarity exceeds a certain value and the ISC channels involving the $n \rightarrow \pi^*$ states are not energetically accessible any more. Note, however, that Lim and others observed experimentally an increase of both the fluorescence and the triplet formation quantum yield upon increasing the solvent polarity or proticity. Of course, the quantum yield of triplet formation is a result of the competition of several processes. Among them, the internal conversion to the ground state plays a prominent role.

4. Conclusion

In this work, we have given a compilation of vertical electronic spectra and—for the first time—spin-orbit coupling matrix elements for psoralen and its sulfur and selenium substituted derivatives.

Our calculated absorption spectra are in close agreement with experimental values and previous TD-DFT calculations from the literature. Regarding the dependence of the energy of a specific state on the hetero-atom substitution pattern, our quantum chemical calculations are able to provide information about dark states which is difficult to access experimentally. More specific, the energy differences between low-lying excited states which are of great importance with respect to singlet-triplet ISC are found to vary strongly in

the systems under study. The $n \rightarrow \pi^*$ states are lowered in energy by a large amount, when sulfur or selenium is present in the pyrone ring. The lowering of the $\pi \rightarrow \pi^*$ state S_1 is less pronounced. As a result, the $n \rightarrow \pi^*$ states become nearly degenerate to S_1 in our calculated vertical spectra for PSO(O-S) and PSO(O-Se). On the other hand, substitution inside the furan ring does almost not affect the energy of the $n \rightarrow \pi^*$ excited states, but lowers slightly the $\pi \rightarrow \pi^*$ state S_1 in energy. The energy gap between S_1 and the $n \rightarrow \pi^*$ excited states is thus increased for PSO(S-O) and PSO(Se-O). In the MO picture, these findings may be related to the strong localization of the n orbital near the carbonyl group. Similarly, the view of the $\pi \rightarrow \pi^*$ T_1 state as a diradical in the 5, 6 positions of the pyrone ring may explain that the energy of this state is almost constant for all psoralens under study.

In all heteropsoraleins, low-lying $\pi \rightarrow \sigma^*$ excitations are found. We expect these states to be closely related to photochemical reactions involving bond cleavage and to the photostability of the psoralens.

In connection with the excitation energies, the calculated SOMEs allow to sketch the most important triplet state population mechanisms. For most of the systems, there are at least three triplet states of $\pi \rightarrow \pi^*$ and one of $n \rightarrow \pi^*$ character below or nearly degenerate to the S_1 state. Although the adiabatic excitation energies are unknown yet, we regard these states to be potentially involved in ISC processes starting from the adiabatically lowest excited singlet state. The latter may be of $\pi^* \rightarrow \pi^*$ or $n \rightarrow \pi^*$ type depending on the system and—probably—even the solvent. As all the coupling matrix elements between a singlet and a triplet $\pi \rightarrow \pi^*$ state in this energy regime are negligibly small, it is very likely that ${}^1(n \rightarrow \pi^*) \rightsquigarrow {}^3(\pi \rightarrow \pi^*)$ or ${}^1(\pi \rightarrow \pi^*) \rightsquigarrow {}^3(n \rightarrow \pi^*)$ are the dominant channels of ISC into the triplet state manifold. Note, however, that all $n \rightarrow \pi^*$ excited states exhibit a considerable blue shift in polar solvents and thus may not be accessible energetically. At first sight these findings contradict the experimental observation that the triplet quantum yield increases with increasing solvent polarity.

To resolve open questions which are connected with radiationless transitions in psoralens, a more detailed knowledge about the excited states in psoralens should thus be helpful. In a forthcoming publication we will discuss excited state equilibrium geometries, vibrational frequencies, and Franck-Condon factors for radiationless transitions. At the same time we will investigate the $\pi \rightarrow \sigma^*$ states in more detail.

Acknowledgements

Funding by the Deutsche Forschungsgemeinschaft (DFG) through project Ma 1051/5-1 is gratefully acknowledged. It is a pleasure to thank Stefan Grimme (Münster) and Mirko Waletzke for making their DFT/MRCI code available to us.

4. ANWENDUNGEN

References

- [1] D. Averbeck, *Photochem. Photobiol.* 50 (1989) 859–882.
- [2] W.M. Horspool, P.-S. Song (Eds.), *CRC Handbook of Organic Photochemistry and Photobiology*, CRC Press, Boca Raton, FL, 1995.
- [3] F. Dall'Aqua, D. Vedaldi, in: W.M. Horspool, P.-S. Song (Eds.), *CRC Handbook of Organic Photochemistry and Photobiology*, CRC Press, Boca Raton, FL, 1995, pp. 1357–1366.
- [4] G.G. Aloisi, F. Elisei, S. Moro, G. Miolo, F. Dall'Aqua, *Photochem. Photobiol.* 71 (2000) 506–513.
- [5] P.-S. Song, J.K.J. Tapley, *Photochem. Photobiol.* 29 (1979) 1177–1197.
- [6] Shim, in: W.M. Horspool, P.-S. Song (Eds.), *CRC Handbook of Organic Photochemistry and Photobiology*, CRC Press, Boca Raton, FL, 1995, pp. 1347–1356.
- [7] A. Harriman, in: W.M. Horspool, P.-S. Song (Eds.), *CRC Handbook of Organic Photochemistry and Photobiology*, CRC Press, Boca Raton, FL, 1995, pp. 1374–1378.
- [8] J. Llano, J. Raber, L.A. Eriksson, J. *Photochem. Photobiol. A: Chem.* 154 (2003) 235–243.
- [9] G. Mugesh, W.-W. du Mont, H. Sies, *Chem. Rev.* 101 (2001) 2125–2179.
- [10] S.R. Rajski, R.M. Williams, *Chem. Rev.* 98 (1998) 2723–2796.
- [11] M. Collet, M. Hoebelke, J. Piette, A. Jakobs, L. Lindqvist, A.V. de Vorst, *J. Photochem. Photobiol. B: Biol.* 35 (1996) 221–231.
- [12] M. Collet, E. Sage, J. Piette, *Photochem. Photobiol.* 66 (1997) 214–223.
- [13] R.V. Bensasson, E.J. Land, C. Salet, *Photochem. Photobiol.* 27 (1978) 273–280.
- [14] T. Wolff, H. Görner, *Phys. Chem. Chem. Phys.* 6 (2004) 368–376.
- [15] W.W. Mantulin, P.-S. Song, *J. Am. Chem. Soc.* 95 (1973) 5122–5129.
- [16] P.-S. Song, M.L. Harter, T.A. Moore, W.C. Herndon, *Photochem. Photobiol.* 14 (1971) 521–530.
- [17] T. Lai, B.T. Lim, E.C. Lim, *J. Am. Chem. Soc.* 104 (1982) 7631–7635.
- [18] E.C. Lim, *J. Phys. Chem.* 90 (1986) 6770–6777.
- [19] A. Nakata, T. Baba, H. Takahashi, H. Nakai, *J. Comput. Chem.* 25 (2004) 179–188.
- [20] S. Grimme, M. Waletzke, *J. Chem. Phys.* 111 (1999) 5645–5655.
- [21] M. Kleinschmidt, J. Tatchen, C.M. Marian, *J. Comp. Chem.* 23 (2002) 824–833.
- [22] A. Schäfer, C. Huber, R. Ahlrichs, *J. Chem. Phys.* 100 (1994) 5829.
- [23] R. Ahlrichs, M. Bär, H.-P. Baron, R. Bauernschmitt, S. Böcker, P. Deglmann, M. Ehrig, K.E. Chkorn, S. Elliott, F. Furche, F. Haase, M. Häser, C. Hättig, H. Horn, C. Huber, U. Huniar, M. Kattannek, A. Köhn, C. Kölmel, M. Kollwitz, K. May, C. Ochsenfeld, H. Öhm, A. Schäfer, U. Schneider, M. Sierka, O.T. Eutler, B. Unterreiner, M. von Arnim, F. Weigend, P. Weis, H. Weiss, *Turbomole* (vers. 5.6), Universität Karlsruhe, 2002.
- [24] A.D. Becke, *J. Chem. Phys.* 98 (1993) 5648–5652.
- [25] P.J. Stephens, F.J. Devlin, C.F. Chabalowski, M.J. Frisch, *J. Phys. Chem.* 98 (1994) 11623–11627.
- [26] A.D. Becke, *J. Chem. Phys.* 98 (1993) 1372–1377.
- [27] C. Lee, W. Yang, R.G. Parr, *Phys. Rev. B* 37 (1988) 785.
- [28] M. Kleinschmidt, C.M. Marian, *Chem. Phys.*, 2004, accepted for publication.
- [29] B.A. Heß, C.M. Marian, U. Wahlgren, O. Gropen, *Chem. Phys. Lett.* 251 (1996) 365–371.
- [30] J. Tatchen, C.M. Marian, *Chem. Phys. Lett.* 313 (1999) 351–357.
- [31] A. Klamt, G. Schüürmann, *J. Chem. Soc., Perkin Trans. 2* (1993) 799.
- [32] A. Schäfer, A. Klamt, D. Sattel, J.C.W. Lohrenz, F. Eckert, *Phys. Chem. Chem. Phys.* 2 (2000) 2187–2193.
- [33] R.C. Weast (Ed.), *CRC Handbook of Chemistry and Physics*, 66th ed., CRC Press, Boca Raton, FL, pp. 1985–1986.
- [34] H. Matsumoto, Y. Ohkura, *Chem. Pharm. Bull.* 26 (1978) 3433–3439.
- [35] M. Klessinger, J. Michl, *Excited States and Photochemistry of Organic Molecules*, VCH Publishers, Inc., Weinheim, Germany, 1995.
- [36] C. Marian, in: K. Lipkowitz, D. Boyd (Eds.), *Reviews in Computational Chemistry*, vol. 17, Wiley-VCH, Weinheim, 2001, pp. 99–204.

4.5 Porphin

Porphin ist die Stammverbindung für in vielen biologischen Prozessen wichtige Systeme. Es ist durch seine Struktur ein hervorragender Chelatligand, um Metallatome zu binden. Dabei bleiben über und unter der Ringebene zwei potentielle Bindungsstellen für weitere Liganden frei. An diesen Stellen können Moleküle gebunden werden oder Reaktionen stattfinden.

Beispielsweise ist im Blutfarbstoff Hämoglobin ein Eisenion an ein substituiertes, zweifach deprotoniertes Porphin koordiniert. Ein Sauerstoffmolekül kann an der freibleibenden Koordinationsstelle gebunden, und so transportiert werden. Im Chlorophyll ist in einem Porphyrinderivat Magnesium zu einem im sichtbaren Spektrum absorbierenden Komplex gebunden. Jeweils zwei dieser Komplexe bilden gemeinsam ein aktives Zentrum, das das eingefangene Licht an ein Redoxkette weitergibt.

Porphinderivate finden breite Anwendung als Tripletterzeuger. Diese sind durch hohe Triplet-Quantenausbeute und eine für Spinübertragung auf andere Moleküle ausreichend lange T_1 -Lebensdauer gekennzeichnet. So zerfallen nach optischer Anregung der intensiven Soret-Bande und interner Konversion in den S_1 Zustand nur 5% des Porphins durch Fluoreszenz. Die Triplettausbeute liegt bei nahezu 90%.

All diese Parameter machen das Porphinmolekül zu einem guten Studienobjekt, um daran nicht nur die Leistungsfähigkeit des neu entwickelten Programmpakets für größere Moleküle zu testen, sondern auch interessante Einblicke zu gewinnen.

Das Porphyrin fand Eingang in zwei Veröffentlichungen: In der Arbeit zu den Spinkopplungskoeffizienten wurden Berechnungen am freien Porphin, sowie an Metallporphyrinen durchgeführt und das Laufzeitverhalten von SPOCK.PT demonstriert. In der Publikation zum Spin-Bahn-CI-Teil wurde am freien Porphin in einer eingehenderen Untersuchung die Berechnung der Spin-Bahn-Kopplung mittels Störungstheorie und Spin-Bahn-CI gegenübergestellt.

4.5.1 Metallporphyrine

Untersucht wurde die freie Base des Porphins, sowie Magnesium-, Zink- und Galliumporphyrin. In diesen Metallporphyrinen sind jeweils die im Zentrum des Rings befindlichen Protonen durch ein entsprechendes Metallion ersetzt. Die Ergebnisse sind in der Veröffentlichung über die Spinkopplungen als Testfall veröffentlicht.[28]

In erster Linie wurden Zustände betrachtet, die energetisch unter oder nahe bei der intensiv absorbierenden Soret-Bande liegen, also die Singulett- und Triplet-Zustände in B_{2u} - und B_{3u} -Symmetrie etwa unterhalb von 3.5 eV. Die berechneten Energien der Q_x/Q_y und Soret-Banden stimmen mit den experimentellen Werten — soweit bekannt — sehr gut überein.

Unsere Erwartung, dass durch die Anwesenheit der Metalle deutlich größere Spin-Bahn-Matrixelemente als im freien Porphin auftreten könnten, wurde widerlegt. Im freien Porphin sind diese allesamt extrem klein: keines ist größer als 0.01 cm^{-1} . Zwar sind die entsprechenden Matrixelemente in den Metallporphyrinen deutlich größer als im freien Porphin, jedoch überschreitet nur eines die Grenze von 1 cm^{-1} : $\langle 2^3B_{3u}|H_{SO}(z)|2^3B_{2u}\rangle = 1.3\text{ cm}^{-1}$ im Zink-Porphyrin.

4.5.2 Lebensdauern im freien Porphin

In einer eingehenderen Untersuchung wurden Dipolübergangsmomente, Phosphoreszenzraten und Lebensdauern des ersten angeregten Triplettzustands im freien Porphin untersucht. Diese Ergebnisse sind als Anwendungsbeispiel in der Arbeit zu SPOCK.CI veröffentlicht.[52]

Zunächst wurden die Geometrien der ersten angeregten Singulett- und Triplettzustände S_1 und T_1 mit zeitabhängiger Dichtefunktionaltheorie im TZVP-Basisatz bestimmt. Eine Verzerrung der Geometrien aus der Planarität heraus könnte durch Symmetriebrüche zu deutlich größeren Spin-Bahn-Matrixelementen führen, als sie im Grundzustand gefunden wurden. Trotz deutlicher Verzerrung der Startgeometrien aus der Ebene heraus und Optimierung in C_1 Symmetrie kehrten jedoch alle diese Zustände im Laufe der Optimierung in D_{2h} -Symmetrie zurück. Alle folgenden Rechnungen wurden daher in D_{2h} -Symmetrie durchgeführt.

In der Veröffentlichung der Ergebnisse ist die Zuordnung der abgebildeten Orbitalen durcheinander geraten. Die korrekte Zuordnung der Orbitale und ihrer Bezeichnungen ist hier nochmals in Abbildung 4.1 zu sehen. Anhand der Besetzungsänderung der Orbitale konnten die Geometrieveränderungen im T_1 erklärt werden.

An den ermittelten Minimumsgeometrien der drei Zustände wurden DFT/MRCI-Rechnungen für acht Zustände in jeder Spinsymmetrie durchgeführt (insgesamt 64 Zustände). Die Übereinstimmung der berechneten Energien sowohl mit Ergebnissen anderer Rechnungen, als auch mit experimentellen Daten ist hervorragend.

Auch an den Geometrien der angeregten Zustände sind die berechneten Spin-Bahn-Matrixelemente der energetisch tief liegenden Zustände nicht signifikant größer als an der Grundzustandsgeometrie. Einige der Matrixelemente mit energetisch höher liegenden $n \rightarrow \pi^*$ -Zuständen, an denen das abgebildete nichtbindende Orbital $11b_{2u}$ (HOMO-9) beteiligt ist, erreichen jedoch etwa 20 cm^{-1} .

Eine Durchführung der Spin-Bahn-CI-Rechnungen ist mit der derzeitigen, noch nicht parallelisierten Version von SPOCK an einem derart großen System (114 korrelierte Elektronen in 516 Orbitalen) nur unter Einschränkungen möglich. Eine Reduzierung der Rechnung auf einen Zustand pro Spinsymmetrie bringt über das Selektionskriterium nach Energie der höchsten angeforderten Wurzel eine Verkleinerung des Konfigurationsraumes. Weiterhin zerfällt die Spin-Bahn-Hamiltonmatrix in zwei etwa gleich große Blöcke, da die geraden und ungeraden Symmetrien nicht gekoppelt sind. Jeder dieser beiden Blöcke hat eine Dimension von etwa $8.8 * 10^6$. Die gute Effizienz des Pakets aus DFT/MRCI und SPOCK zeigt sich deutlich in Tabelle VI der Veröffentlichung, die die Rechenzeiten zusammenfasst. So sind für den störungstheoretischen Teil (64 Zustände) für die Energien, Matrixelemente und Dichtematrizen lediglich knapp 3 Tage (70 Stunden) Rechenzeit vorausgesetzt, und für den variationellen Teil mit 16 Zuständen gut 1 1/2 Tage (39 Stunden). Die Rechnungen wurden auf einem inzwischen schon nicht mehr ganz aktuellen System mit 2.4 GHz Prozessor und 2 GB Arbeitsspeicher durchgeführt.

Phosphoreszenzraten, Dipolübergangsmomente und Lebensdauern der Komponenten des $T_{1,z}$ und $T_{1,x}$ des ersten angeregten Triplets wurden an der Grundzustandsgeometrie und an der T_1 -Geometrie sowohl störungstheoretisch, als auch variationell bestimmt. Da auch hierbei im Satz der Veröffentlichung ein Fehler auftrat, sind die Ergebnisse hier nochmals in Tabelle 4.1 aufgeführt. Die berechneten Werte der Hochtemperaturlebensdauer zwischen etwa 100 und 200 Sekunden stimmen sehr gut mit den experimentell ermittelten

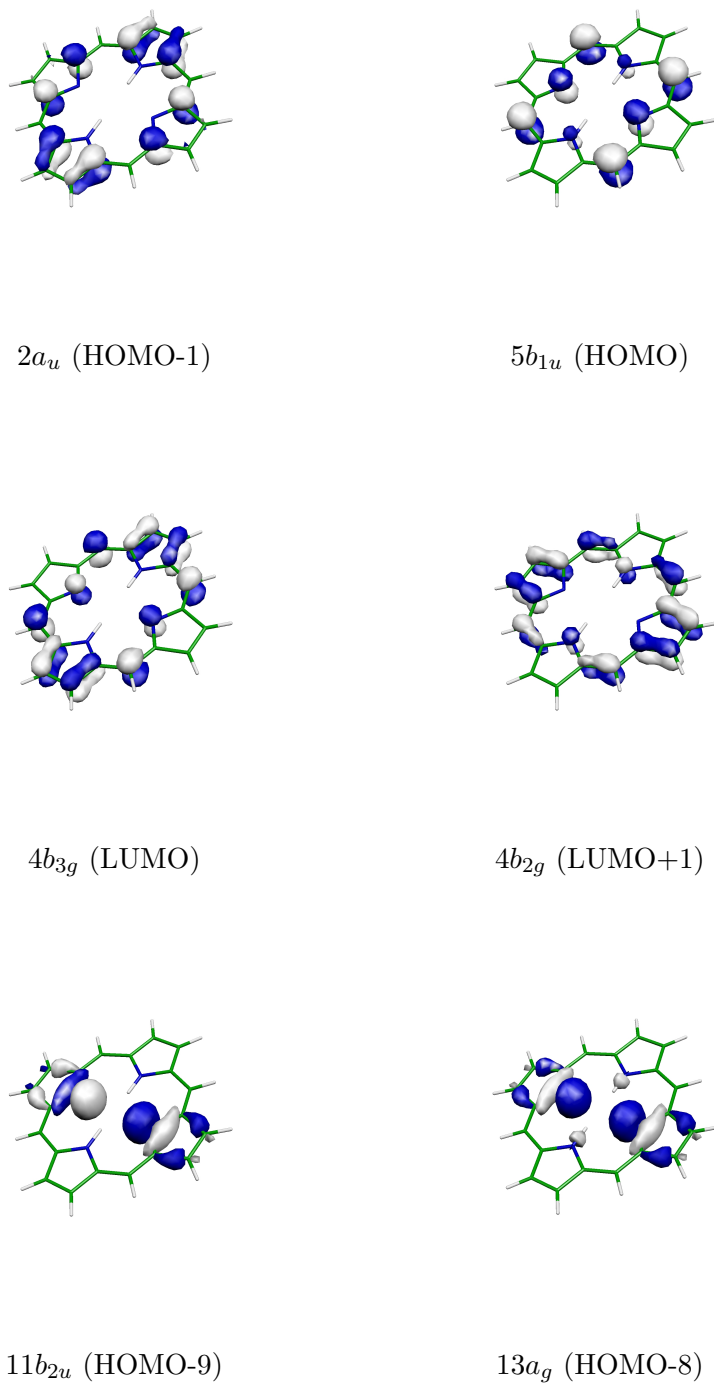


Abbildung 4.1: Orbitale des Porphins an der T_1 Geometrie

4. ANWENDUNGEN

Phosphoreszenzlebensdauern von 128 s [55] bzw. 80 s [56] überein. Für eine tiefer gehende Analyse der Daten sei auf die Veröffentlichung [52] hingewiesen.

	$\langle T_{1,z} x S_0 \rangle$ [ea ₀]	$\langle T_{1,x} z S_0 \rangle$ [ea ₀]	k_z [s ⁻¹]	k_x [s ⁻¹]	$\tau(T_{1,z})$ [s]	$\tau(T_{1,x})$ [s]	$\tau(T_1)$ [s]
QDPT_16(S ₀)	6.6*10 ⁻⁶	68.2*10 ⁻⁶	2.7*10 ⁻⁴	0.0289	3720	34.6	103
QDPT_64(S ₀)	4.4*10 ⁻⁶	62.4*10 ⁻⁶	1.2*10 ⁻⁴	0.0237	8470	42.1	126
SOCL_16(S ₀)	2.2*10 ⁻⁶	53.0*10 ⁻⁶	3.0*10 ⁻⁵	0.0175	33235	57.3	171
QDPT_16(T ₁)	4.2*10 ⁻⁶	68.7*10 ⁻⁶	5.6*10 ⁻⁵	0.0151	17700	66.2	198
QDPT_64(T ₁)	3.0*10 ⁻⁶	68.4*10 ⁻⁶	2.9*10 ⁻⁵	0.0150	34624	66.7	200
SOCL_16(T ₁)	0.5*10 ⁻⁶	91.8*10 ⁻⁶	8.1*10 ⁻⁷	0.0275	12000000	36.4	109

Tabelle 4.1: Dipoleübergangsmomente, Phosphoreszenzraten und Lebensdauern im Porphin an den S_0 und T_1 Geometrien mittels Quasientarteter Störungstheorie und Spin-Bahn-CI berechnet. $\tau(T_1)$ bezeichnet die gemittelte Lebensdauer der T_1 Feinstrukturniveaus im Hochtemperaturlimit; die nachgestellten Zahlen _16 und _64 geben die Zahl der berücksichtigten Zustände an.

Bemerkenswert sind die Ergebnisse bei Zeitmessungen, die in Tabelle 4.2 wiedergegeben sind. Da in der störungstheoretischen Rechnung viel mehr angeregte Zustände im DFT/MRCI berechnet werden müssen, um eine konvergierte Störsumme zu erreichen, dauert diese Rechnung insgesamt knapp doppelt so lange, wie die Spin-Bahn-CI-Rechnung, obwohl natürlich in diesem Fall die Berechnung der Spin-Bahn-Kopplung deutlich aufwendiger ist.

	dim(1 vector)	CPU time
MRCI (singlets, 4 Zust./Irrep)	1.1*10 ⁶	26.5h
MRCI (triplets, 4 Zust./Irrep)	1.9*10 ⁶	35.5h
1-RTDMs (32 Singulets + 32 Triplets)		2.5h
576 SOCMEs über 64 Zust.		5.5h
Gesamt (Störungstheorie)		≈70h
MRCI (Singletts, 1 Zust./Irrep)	0.4*10 ⁶	1.0h
MRCI (Tripletts, 1 Zust./Irrep)	0.6*10 ⁶	7.5h
MRSOCI (4 Wurzeln)	8.8*10 ⁶	25.0h
1-RTDMs (4 MRSOCI Vectoren)		4.8h
Gesamt (Variationsrechnung)		≈39h

Tabelle 4.2: Zeitmessung der verschiedenen Rechnungen am freien Porphin (D_{2h} symmetry) auf einem einzelnen Xeon 2.4 GHz Prozessor.

5

Zusammenfassung

In dieser Arbeit wurden neue Methoden zur Berechnung der Spin-Bahn-Wechselwirkung entwickelt, programmiert, getestet und auf mehrere größere organische Moleküle angewendet. Aufbauend auf dem semiempirischen DFT/MRCI-Ansatz, der Konfigurationswechselwirkung mit Dichtefunktionaltheorie kombiniert, wurden Module implementiert, mit denen die Spin-Bahn-Wechselwirkung entweder störungstheoretisch oder im Rahmen eines Spin-Bahn-CI voll variationell in der Berechnung berücksichtigt werden kann.

Die Hauptmerkmale des neuen Programmpakets SPOCK (SPin-Orbit-Coupling Kit) sind

- der schnelle DFT/MRCI-Ansatz
- die Einzentren-*mean-field*-Näherung für die Spin-Bahn-Integrale
- ein effizienter Anregungsmusteransatz zur Spinkopplung
- die RI-Näherung im Spin-Bahn-CI
- der *multi-root* Davidson Algorithmus im Spin-Bahn-CI

Durch die Kombination all dieser modernen Verfahren ist ein höchst effizientes Programm entstanden, das für die Berechnung der Spin-Bahn-Kopplung und daraus abgeleiteter Eigenschaften in großen Molekülen geeignet ist. Der Anregungsmusteransatz wurde im Rahmen dieser Arbeit auf spinabhängige Einelektronenoperatoren, sowie für den Zweielektronen-Spin-Bahn-Operator erweitert.

Das Programmpaket wurde ausgiebig getestet und liefert in allen Fällen, in denen ein Vergleich mit anderen Methoden möglich war, eine sehr gute Übereinstimmung der Ergebnisse bei wesentlich geringeren Rechenzeiten. Es konnte gezeigt werden, dass mit dem eigentlich aufwendigeren Spin-Bahn-CI eine Ersparnis an Rechenzeit erzielbar ist, da für die störungstheoretische Behandlung oft viele hoch liegende Zustände nur zum Zwecke der Konvergenz der Störsumme berechnet werden müssen. Im Spin-Bahn-CI reicht hingegen ein deutlich kleinerer Konfigurationsraum aus, um bereits gleich gute oder sogar bessere Ergebnisse wie mit einer langen Störentwicklung in einem größeren Konfigurationsraum zu erzielen.

In ersten Anwendungen wurden Thiophen, die DNS-Base Uracil, Dithiosuccinimid, das medizinisch bedeutsame Psoralen, sowie das in vielen biologischen Systemen anzutreffende Porphyrin untersucht. Die Berechnung von Spin-Bahn-abhängigen Eigenschaften wie z.B.

5. ZUSAMMENFASSUNG

Phosphoreszenzlebensdauern oder Dipolübergangswahrscheinlichkeiten ergeben in diesen Systemen — soweit bekannt — sehr gute Übereinstimmung mit experimentellen Daten.

Mit dem neu geschaffenen Programmpaket steht nun ein effizientes Werkzeug zur Verfügung, mit dem die Berechnung der Spin-Bahn-Kopplung in größeren Systemen zur Routineaufgabe werden kann. So beträgt die Rechenzeit im größten betrachteten System, dem Porphyrin mit 114 korrelierten Elektronen, lediglich etwa drei Tage auf einem PC der aktuellen Generation.

Weitere Steigerung der Effizienz und Anwendungsfelder des Programms sollen zukünftig erreicht werden durch

- eine Parallelisierung von SPOCK.CI
- die Einbettung in eine QM/MM-Umgebung
- die Implementierung von skalarrelativistischen Korrekturen in TURBOMOLE
- eine Parametrisierung des DFT/MRCI für Duplettzustände

6

Anhang

6.1 Inputbeschreibung

Bei den Eingabeparametern für SPOCK wird zwischen boolschen Parametern, die ein bestimmtes Verhalten des Programms ein oder ausschalten, und Parametern, die einen konkreten Wert übergeben unterschieden. Letztere verlangen nach einem Gleichheitszeichen (=) und dem entsprechenden Wert. Boolche Parameter können mit `on` und `off` geschaltet werden.

Allgemeine Parameter:

`$title=<STRING>`

Eine bis zu 80 Zeichen lange Zeichenkette als Titel für die Rechnung.

Vorgabe: leer

`$checkonly on/off`

Ist `checkonly` gesetzt, so werden alle Prüfungen auf Vorhandensein und Konsistenz der Dateien durchgeführt, jedoch vor der eigentlichen Rechnung angehalten.

Vorgabe: `off`

`$intfile=<STRING>`

Angabe des Dateinamens für die Spin–Bahn–Integrale.

Vorgabe: `SQUARE-igls`

`$printints on/off`

Ermöglicht die Ausgabe der Spin–Bahn–Integrale.

Vorgabe: `off`

`$print=<INTEGER>`

Ermöglicht eine Einstellung der Mitteilungsfreude von SPOCK. Derzeit sind nur die Werte 0 und 1 vergeben.

Vorgabe: 0

\$quiet on/off

Durch setzen von **\$quiet on** wird die Ausgabe auf das unbedingt notwendige reduziert.

Vorgabe: **off**

Parameter für die Matrixelementberechnung:

\$mes on/off

Ermöglicht das Abschalten der Matrixelementberechnung.

Vorgabe: **on**

\$largeme=<INTEGER>

Durch setzen dieses Parameters können die <INTEGER> größten Beiträge zu jedem Matrixelement ausgegeben werden (maximal 20).

Vorgabe: **0**

\$somefile=<STRING>

Die Matrixelemente werden in die Datei mit Namen <STRING> geschrieben. Dies wird benötigt für den Transfer der Matrixelemente zum Programm **soc_qdpt**. Der Aufbau der Datei ist selbsterklärend durch Kommentare dokumentiert.

Vorgabe: **SOMEs**

Parameter für die Störungstheorie

\$socqdpt on/off

Ermöglicht das Abschalten der störungstheoretischen Berechnung der Spin–Bahn–gekoppelten Zustände.

Vorgabe: **on**

\$printmat on/off

Ermöglicht die Ausgabe der Störungsmatrix vor der Diagonalisierung.

Vorgabe: **off**

\$usemp2 on/off

Nur in *ab-initio* Rechnungen:

Verwendung der MP2 Korrektur für nicht selektierte Konfigurationen bei den Energiewerten der Störungsmatrix.

Vorgabe: **off**

\$usedavid on/off

Nur in *ab-initio* Rechnungen:

Verwendung der Davidson–Korrektur bei den Energiewerten der Störungsmatrix.

Vorgabe: **off**

6.1. INPUTBESCHREIBUNG

Parameter für Störungstheorie und Spin–Bahn–CI:

\$complex on/off

Umschaltung zwischen der Verwendung komplexer (**on**) oder doppelt so grosser reeller (**off**) Matrizen. (siehe Abschnitt 3.3.2)

Vorgabe: **off**

\$printcomplex on/off

Für Fehlersuche können im Falle von **\$complex off** die artifiziellen entarteten Eigenwerte und -vektoren ausgegeben werden.

Vorgabe: **off**

\$stateshift=<int>

Die spinfreien CI–Zustände können mittels dieses Schalters verschoben werden, um die Energiewerte einer besseren Rechnung, oder eines Experiments nachzubilden. **<int>** gibt die Anzahl der zu berücksichtigenden Zustände an. In den folgenden Zeilen werden diese Zustände und ihre Energie näher spezifiziert. Jede Zeile besteht aus vier Einträgen:

<mult> <sym> <root> <energy>

Dabei ist

- **<mult>** die ausgeschriebene Multiplizität des Zustands (**singlet**, **doublet**, ...)
- **<sym>** die Symmetrie in TURBOMOLE-Notation
- **<root>** die Nummer der Wurzel und
- **<Energy>** die Energie in atomaren Einheiten

Der erste Zustand ist der Referenzzustand, zu dem die anderen in Relation verschoben werden. Beispiel:

```
$stateshift=3
singlet a1 1 0.0
triplet b1 1 0.1
triplet b2 1 0.1
```

Hier würden der erste 3B_1 und der erste 3B_2 Zustand auf den Wert 0.1 E_h relativ zum ersten 1A_1 verschoben werden.

\$shift_thresh=<real>

Da durch das Verschieben der Zustände die CI–Matrix vollständig gefüllt wird, kann mit diesem Parameter ein Selektionsschwellwert angegeben werden. Nur CSF mit grösseren Koeffizienten werden dann bei der Verschiebung berücksichtigt. (Dieser Parameter hat experimentellen Charakter!)

Vorgabe: 0.0

Parameter für das Spin–Bahn CI:

6. ANHANG

\$soci on/off

Ermöglicht das Anschalten des Spin–Bahn CI.

Vorgabe: off

\$nroots=<INTEGER>

Anzahl der Zustände, die im Spin–Bahn CI berechnet werden sollen.

Vorgabe: alle Wurzeln aus der Störungstheorie

\$nprintcomp=<INTEGER>

Bei der Ausgabe der Eigenvektoren des Spin–Bahn CI werden die <INTEGER> größten Koeffizienten ausgegeben.

Vorgabe: 5

\$davidtiming on/off

Detaillierte Zeitmessung der einzelnen Schritte während des Davidson–Algorithmus.

Vorgabe: off

\$spinorbit on/off

Zu Testzwecken kann der Spin–Bahn Operator ausgeschaltet werden. Die erhaltenen Energien und Vektoren entsprechen dann denen des spinfreien CI.

Vorgabe: on

\$restart on/off

Ermöglicht ein Fortsetzen der Rechnung mit den Vektoren einer vorherigen Rechnung als Startvektoren.

Vorgabe: off

\$startvec_only on/off

Ermöglicht Abbruch der Rechnung nach Erzeugung der Startvektoren.

Vorgabe: off

\$prec=<REAL>

Dieser Parameter steuert die Genauigkeit der Rechnung. Mögliche Werte liegen zwischen 1000 (geringste) und 0.001 (höchste). Er entspricht dem gleichnamigen Parameter im DFT/MRCI. Auswirkungen ergeben sich beim Konvergenzkriterium des Davidson–Algorithmus, sowie auf den Schwellwert für die Berücksichtigung von Matrixelementen im spinfreien Hamiltonoperator.

Vorgabe: 1.0

\$memvec=<int>

Zur Verfügung stehender Arbeitsspeicher für die Speicherung der CI–Vektoren in Megabyte. Minimalanforderung sind 2 komplexe Vektoren, also ist $2 \cdot 16^*$ (Dimension des Vektors).

Vorgabe: 512

6.2 Dateien und Datentransfer zu anderen Programmen

Der Informationstransfer zwischen den verschiedenen beteiligten Programmen läuft zum größten Teil über Dateien mit standardisierten Namen, die in entsprechenden Verzeichnissen auf der Festplatte vorliegen müssen:

Dateiname	Bedeutung
SQUARE-igls	Einelektronen-Spin-Bahn-Integrale, Name frei wählbar
control	TURBOMOLE-control-file, gelesen werden die Symmetriegruppe und DFT-Informationen
oneint	spinfreie Einelektronenintegrale
bkji	Dreiindexintegrale der RI-Näherung
scrat<mult>/	Unterverzeichnis aller Daten der Multiplizität <mult>
scrat<mult>/civec.<sym>	konvergierte spinfreie CI-Vektoren
scrat<mult>/HC.info.<sym>	Vernichter- und Erzeugerinformationen für die selektierten Konfigurationen der Symmetrie <sym>
scrat<mult>/energy.<sym>	spinfreie CI-Energien
scrat<mult>/refconf	Referenzen in Besetzungszahlschreibweise
scrat<mult>/mosort	Sortierung der MOs. (Abbruch wenn sie nicht in allen Multiplizitäten gleich ist)
scrat<mult>/ndimsym	Anzahl an Konfigurationen und CSFs im Referenzraum und im selektierten Raum
SOMEs	Spin-Bahn-Matrixelemente über die spinfreien CI-Wellenfunktionen. Das Format ist in der Datei selbsterklärend angegeben.
socivec	Spin-Bahn-CI-Vektoren

6. ANHANG

Danke!

Mein erster Dank gilt meiner Doktormutter Christel M. Marian. Sie hat mir dieses überaus interessante und herausfordernde Thema vermittelt. Von ihrem großen Erfahrungsschatz konnte ich in schwierigen Situationen immer wieder profitieren. Für das mir entgegengebrachte Vertrauen und ihre Geduld bedanke ich mich sehr herzlich!

Diese Arbeit entstand in enger und fruchtbarer Zusammenarbeit mit Jörg Tatchen. Die Entwicklung eines derart umfangreichen Programms kann allein von einer Person kaum bewerkstelligt werden. Gemeinsam habe wir oft an Lösungsdetails getüftelt, und immer wieder in Reaktion auf durchgeführte Rechnungen Probleme korrigiert und neue Funktionen eingebaut. Vielen Dank, Jörg!

Timo Fleig danke ich nicht nur für die Übernahme des Koreferats dieser Arbeit, sondern auch für viele Diskussionen über die Relativistik oder über Implementierungsfragen, über Wissenschaft im Allgemeinen und die Stellung der Chemie in ihr, sowie für den fast täglichen kleinen Fußballplausch.

Stefan Grimme und Mirko Waletzke haben die DFT/MRCI-Methode entwickelt und stellten den Quelltext des Programms zur Verfügung. Ich danke ihnen für die Einführung in den Code und für viele ergiebige Diskussionen in der Anfangszeit meiner Promotion.

Ich danke auch Bernd Schimmelpfennig für das AMFI-Integralprogramm, dessen Effizienz einen ganz wesentlichen Beitrag zum SPOCK-Paket liefert.

Im Institut für Theoretische Chemie herrscht ein ausgesprochen angenehmes Arbeitsklima. Allen Mitgliedern danke ich für diese freundliche Atmosphäre.

Der Deutschen Forschungsgemeinschaft DFG gilt mein Dank für die Förderung dieses Themas in einer Zeit, in der es nicht selbstverständlich ist, für Grundlagenarbeit entsprechende Mittel zur Verfügung zu haben.

6. ANHANG

Literatur

- [1] S. Grimme and M. Waletzke. *J. Chem. Phys.*, 111:5645–5655, 1999.
- [2] B. A. Heß, C. M. Marian, U. Wahlgren, and O. Gropen. *Chem. Phys. Lett.*, 251:365, 1996.
- [3] AMFI is an atomic spin-orbit integral program written by B. Schimmelpfennig, University of Stockholm, 1996.
- [4] “DIRAC04, a relativistic ab initio electronic structure program, Release dirac04.0 (2004)”, Written by H. J. Aa. Jensen and T. Saue and L. Visscher with contributions from V. Bakken and E. Eliav and T. Enevoldsen and T. Fleig and O. Fossgaard and T. Helgaker and J. Laerdahl and C. V. Larsen and P. Norman and J. Olsen and M. Pernpointner and J. K. Pedersen and K. Ruud and P. Salek and J. N. P. van Stralen and J. Thyssen and O. Visser and T. Winther., 2004.
- [5] P. Schwerdtfeger, editor. *Relativistic Electronic Structure Theory*, volume 1. Elsevier, 2002.
- [6] B.A. Heß and C.M. Marian. Relativistic effects in the calculation of electronic energies. In P.Jensen and P.R. Bunker, editors, *Computational Molecular Spectroscopy*, pages 169–219. John Wiley & Sons, Sussex, 2000.
- [7] W. Pauli. *Z. Phys.*, 43:601, 1927.
- [8] M. Douglas and N. M. Kroll. *Ann. Phys. (N.Y.)*, 82:89–155, 1974.
- [9] B. A. Heß. *Phys. Rev. A*, 33:3742, 1986.
- [10] G. Jansen and B. A. Heß. *Phys. Rev. A*, 39:6016, 1989.
- [11] A. D. Becke. *J. Chem. Phys.*, 98:1372, 1993.
- [12] C. Lee, W. Yang, and R. G. Parr. *Phys. Rev. B*, 37:785, 1988.
- [13] S. Grimme. private Mitteilung.
- [14] C. M. Marian. private Mitteilung.
- [15] J. Tatchen. Dissertation, Universität Düsseldorf, 2006.
- [16] R. Pauncz. *The Unitary Group in Quantum Chemistry*. Elsevier, 1986.
- [17] R. Pauncz. *The Symmetric Group in Quantum Chemistry*. CRC Press, 1995.
- [18] B. Liu and M. Yoshomine. *J. Chem. Phys.*, 74:612, 1981.
- [19] R. J. Buenker and R. A. Phillips. *J. Mol. Spectrosc. (THEOCHEM)*, 123:291, 1985.
- [20] B. A. Heß. *Habilitationsschrift*. Universität Gesamthochschule Wuppertal, 1986.

LITERATUR

- [21] D. R. Yarkony. *J. Chem. Phys.*, 84:2075, 1986.
- [22] S. Yabushita, Z. Zhang, and R. M. Pitzer. *J. Phys. Chem. A*, 103:5791, 1999.
- [23] N. Flocke, M. Barysz, J. Karowski, and G. H. F. Diercksen. *Int. J. Quantum Chem.*, 61:1, 1997.
- [24] N. Flocke, M. Barysz, J. Karowski, and G. H. F. Diercksen. *Int. J. Quantum Chem.*, 61:11, 1997.
- [25] N. Flocke, M. Barysz, J. Karowski, and G. H. F. Diercksen. *Int. J. Quantum Chem.*, 61:21, 1997.
- [26] N. Flocke. *Int. J. Quantum Chem.*, 61:747, 1997.
- [27] R. W. Wetmore and G. A. Segal. *Chem. Phys. Lett.*, 36:478, 1975.
- [28] M. Kleinschmidt and C. M. Marian. Efficient generation of matrix elements for one-electron spin-orbit operators. *Chem. Phys.*, 311:71, 2005.
- [29] R. McWeeny. *J. Chem. Phys.*, 42:1717, 1965.
- [30] I. L. Cooper and I. Musher J. *J. Chem. Phys.*, 57:1333, 1972.
- [31] R. Pauncz. *Spin Eigenfunctions, Construction and Use*. Plenum Publ. Co., 1979.
- [32] S. Grimme and M. Waletzke. *Phys. Chem. Chem. Phys.*, page 2075, 2000.
- [33] N. Gilka. private Mitteilung.
- [34] M. Kleinschmidt, J. Tatchen, and C. M. Marian. Spin -orbit coupling of dft/mrci wavefunctions: Method, test calculations, and application to thiophene. *J. Comp. Chem.*, 23:824, 2002.
- [35] J. Tatchen, M. Waletzke, C.M. Marian, and S. Grimme. *Chem. Phys.*, 264:245, 2001.
- [36] BNSOC is a spin-orbit coupling program package developed by B. A. Hess and C. M. Marian, with contributions from P. Chandra, S. Hutter, F. Rakowitz, and R. Samzow.
- [37] R. J. Buenker and S. D. Peyerimhoff. *Theoret. Chim. Acta*, 35:33, 1974.
- [38] R. J. Buenker and R. A. Phillips. *J. Mol. Struct. THEOCHEM*, 123:291, 1985.
- [39] S. Brownridge and F. Grein. *J. Phys. Chem. A*, 107:7969, 2003.
- [40] F. Grein. *Chem. Phys.*, 296:71, 2004.
- [41] M. Kleinschmidt. Diplomarbeit, Universität Bonn, 1999.
- [42] F. Rakowitz and C. M. Marian. *Chem. Phys. Lett.*, 257:105, 1996.
- [43] Z. Bai, J. Demmel, J. Dongarra, A. Ruhe, and H. van der Vorst, editors. *Templates for the Solution of Algebraic Eigenvalue Problems: A Practical Guide*. SIAM, Philadelphia, 2000.
- [44] E. R. Davidson. *J. Comput. Phys.*, 17:87, 1975.
- [45] W. Butscher and W. E. Kammer. *J. Comp. Phys.*, 20:313, 1975.
- [46] B. Liu. In C. Moler and I. Shavitt, editors, *Numerical Algorithms in Chemistry*. LBL-8158 Lawrence Berley Laboratory, 1978.

LITERATUR

- [47] M. Crouzeix, B. Philippe, and M. Sadkane. *J. Sci. Comput.*, 15:62, 1994.
- [48] S. Hutter. Dissertation, Universität Bonn, 1994.
- [49] J. Tatchen, M. Kleinschmidt, and C. M. Marian. Quantum chemical investigation of spin-forbidden transitions in dithiosuccinimide. *Z. Phys. Chem.*, 217:205, 2003.
- [50] S. Salzmann. Diplomarbeit, Universität Düsseldorf, 2005.
- [51] S. C. J. Meskers, R. Poloński, and H. M. Dekkers. *J. Phys. Chem.*, 99:1134, 1995.
- [52] M. Kleinschmidt, J. Tatchen, and C. M. Marian. Spock.ci: A multireference spin-orbit configuration interaction method for large molecules. *J. Chem. Phys.*, 124:124101, 2006.
- [53] J. Tatchen, M. Kleinschmidt, and C. M. Marian. Electronic excitation spectra and singlet-triplet coupling in psoralen and its sulfur and selenium analogs. *J. Photochem. Photobiol. A*, 167:201, 2004.
- [54] J. Tatchen and C. M. Marian. *Phys. Chem. Chem. Phys.*, 8:2133, 2006.
- [55] M. P. Tsvirko, K. N. Solovev, A. T. Gradyushko, and S. S. Dvornikov. *Opt. Spectrosc.*, 38:400, 1975.
- [56] M. Gouterman and G.-E. Khalil. *J. Mol. Spectr.*, 53:88, 1974.

Die hier vorgelegte Dissertation habe ich eigenständig und ohne unerlaubte Hilfe angefertigt. Die Dissertation wurde in der vorgelegten oder in ähnlicher Form noch bei keiner anderen Institution eingereicht. Ich habe bisher keine erfolglosen Promotionsversuche unternommen.

Düsseldorf, den 2. Juni 2006

(Martin Kleinschmidt)